State Limits of Peloids

Zur Erlangung des akademischen Grades eines

DOKTOR-INGENIEURS

von der Fakultät für

Bauingenieur-, Geo- und Umweltwissenschaften
am Karlsruher Institut für Technologie (KIT)

genehmigte

DISSERTATION

von

Dipl.-Ing. Michael Külzer
aus Gerlingen

Karlsruhe, 2015

Contents

Chapter 1

Introduction

1.1 The Rissa landslide

In 1978, at the western Norwegian coastline close to Trondheim a severe landslide occurred, which became prominent in the geotechnical field since it was exeptionally well documented by eyewitnesses and accidentally present amateur photographers. This landslide took place at Rissa, a typical Norwegian farming community made up of small farms and single family homes, located at the shore of Lake Bothen (GREGERSEN 1981).

The landslide was initiated by excavation work for the deliberated extension of an existing farm, with the surplus masses placed at the shoreline to extend the land area of the farm. All of a sudden 70-90 m of the shore line slid out into the bay, including half of the recently placed 700 m^3 earth fill. Subsequently, the slide developed retrogressively towards the backlands, which was inclined by only 6°. Successive minor slides took place, each resulting in a complete soil liquefaction with the debris pouring into the lake like streaming water. At this point the real catastrophe started. A large, flake-type slide was initiated within an area of 150 m x 200 m including a building and was moving monolithically towards the bay. A series of flake-type slides with similar size started successively, and after 5 minutes duration the landslide came to its rest. Altogether 7 farms and 5 single family homes were taken by the slide. Only one out of 40 people within the slide area was killed, the others could escape under partially dramatic circumstances. At the end, the total slide area covered 330000 m^2 with a maximum distance to the initial excavation of 1.5 km (GREGERSEN 1981).

The region of Trondheim is one of two large marine sediment areas in Norway. According to ROSENQVIST (1966), ROSENQVIST (1972) and GREGERSEN (1981), the sediments were formed by rapid access of electrically charged clay minerals to salt water so that the fine

Figure 1.1: Bird's-eye view of the Rissa 1978 landslide (by courtesy of Norwegian Geotechnical Institute NGI)

fractions flocculated and precipitated together with the coarser particles. By sedimentation, stable gels were formed with comparatively high water contents. After the melting of glaciers these soft sediments were uplifted above sea level. Subsequent reduction of the salinity by fresh water led to a collapsible skeleton of hydrolyzed particles, which was destroyed by disturbance. Consequently, the soil was turned to a liquid.

The example of the Rissa landslide impressively illustrates that the mechanical behaviour of fine-grained sediments with pore water highly depends on the interparticle surface forces. The present treatise is intended to contribute to the clarification of these surface effects and the consequences for the mechanical behaviour of such sediments, and a suggestion is given for the incorporation of the interparticle surface forces to the concept of state limits. The findings are then applied to a re-interpretation of the Rissa landslide.

1.2 Concept of state limits

State limits are states of a granular material which are asymptotically attained by proportional deformation paths with constant strain rate directions (GUDEHUS 2011). They can be defined by relations of

- the void ratio e

- the mean skeleton pressure p_s

- and a shear stress invariant τ

and can be reached from a range of initial states (described by e_0, p_{s0} and τ_0) by a sufficient proportional deformation.

Four kinds of state limits can be identified and can be illustrated in a e-$\ln p_s$-diagram (Fig. 1.2a). Isotropic compression (i) requires the principal skeleton stresses $p_{s1} = p_{s2} = p_{s3}$, therefore $\tau = 0$. An increase of p_s yields a decrease of e, which can mean the highest possible e of a particle assembly. Oedometric compression (o) leads to $p_{s2} = p_{s3} = K_0 p_{s1}$ with the earth pressure coefficient at rest K_0, therefore $\tau \neq 0$. e is lower for the same p_s, resulting in the o-line below the i-line. A so-called critical state (c) is reached by sufficient shear deformation. Then τ gets stationary, and e lies on the c-line below the o-line. A maximum density (d) can be achieved by cyclic shearing with small amplitudes and constant p_s. All state limits in e-$\ln p_s$-plots have horizontal asymptotes $e = e_0$ for $p_s \to 0$ and $e \to 0$ for $p_s \to \infty$. Consequently, the range enclosed by the i- and the d-line represents every possible state (e, p_s, τ) of particle skeletons in TERZAGHI's (1925) sense.

Transitions from possible initial states (e_0, p_{s0}, τ_0) towards state limits can partly be illustrated in e-$\ln p_s$-plots. During isotropic compression (Fig. 1.2b) the i-line is asymptotically reached after sufficient deformation. By oedometric compression with subsequent drained shearing (Fig. 1.2c) the o-line is initially approached, subsequent shearing with constant p_s yields a decrease of e down to the c-line. Then, stationarity is reached, and (e_c, p_{sc}, τ_f) remain unchanged with further shear deformation. During undrained shearing (Fig. 1.2d), e remains constant but p_s tends towards the c-line. Stationarity can only be reached for $e < e_{c0}$, otherwise p_s vanishes and liquefaction occurs. Cyclic shearing (Fig. 1.2e) yields densification down to the d-line if drainage is enabled, otherwise p_s decreases with constant e until the d-line is reached. For $e \geq e_{d0}$ again p_s vanishes and the skeleton decays. Consequently, fine-grained soils of rather high density can be mobilized during earthquakes (cyclic mobility), but for $e < e_{c0}$ larger monotonous deformations yield a recovery of p_s and therefore a re-stabilization.
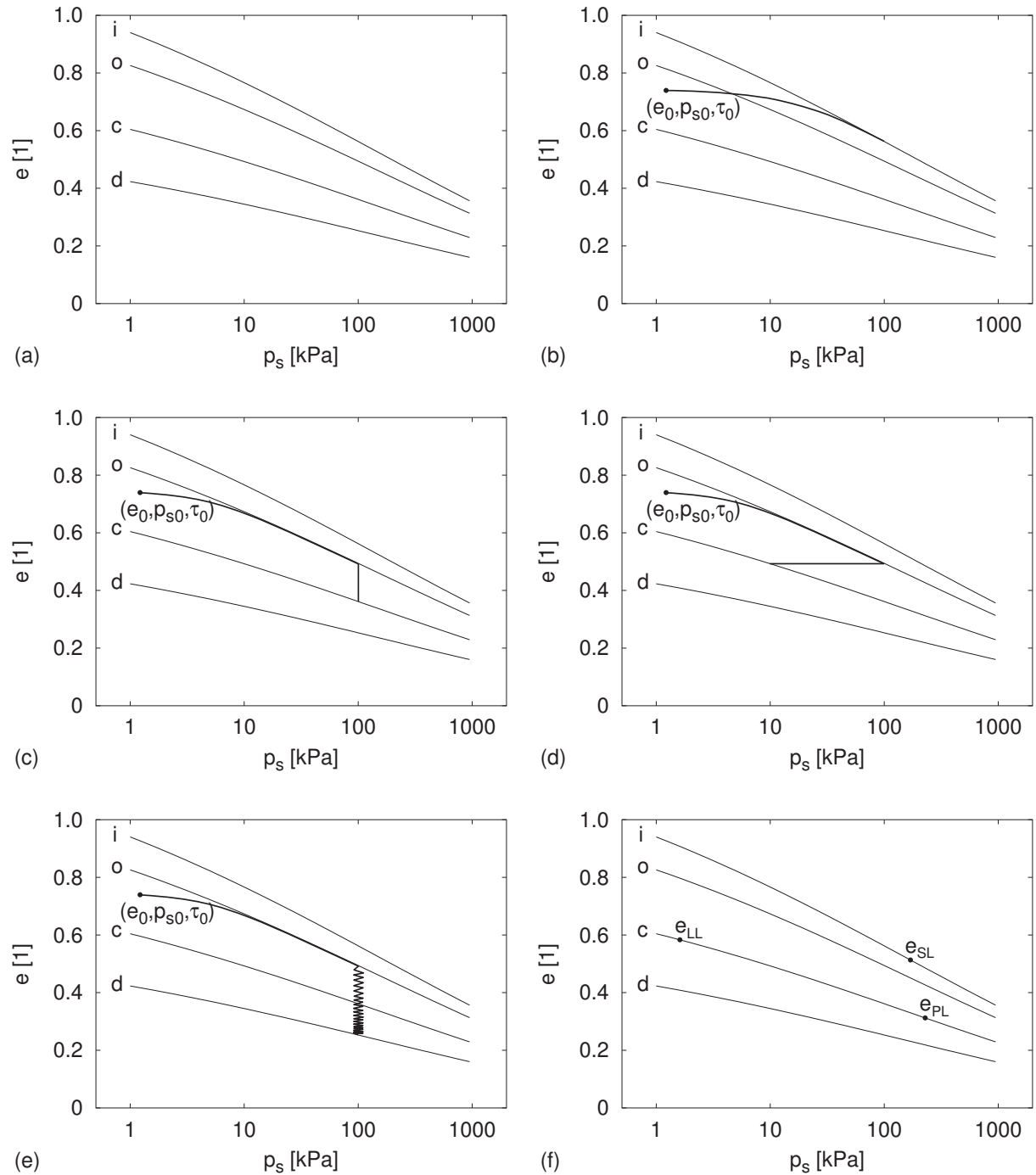
Figure 1.2: Examples of state limits of isotropic compression, oedometric compression, critical and densest state (a). Asymptotical transitions from (e_0, p_{s0}, τ_0) due to isotropic compression (b), oedometric compression and drained shearing (c), oedometric compression and undrained shearing (d), oedometric compression and cyclic shearing (e). Interpretation of conventional liquid, plastic and shrinkage limits (f).

Conventional Atterberg limits can be incorporated into the concept of state limits (Fig. 1.2f). According to the Casagrande method, the liquid limit is determined by a specimen placed into a cup and the repeated drop of the cup up to the closure of a groove. During this procedure, the specimen is subjected to repeated shearing with a very low p_s. The corresponding e_{LL} may therefore be located on the c-line with an estimated p_s in the range of a few kPa. The plastic limit is determined by rolling a thread of soil on a filter paper up to crumbling at a diameter of 3 mm. This test is based on intensive shearing of the specimen during the generation of suction pressure, thus e_{PL} may be located on the c-line. The corresponding p_s evolves from the suction pressure and can range from about 100 kPa for silts to much more for clays. The shrinkage limit is obtained by pore water evaporation of a specimen of high initial water content and the related generation of isotropic suction pressure (cf. Sec. 4.4.1). Therefore e_{SL} may be located on the i-line with the corresponding p_s ranging from about 100 kPa for silts to far more for clays.

State limit void ratios can be approximated by BAUER's (1996) formula

$$\frac{e_i}{e_{i0}} = \frac{e_o}{e_{o0}} = \frac{e_c}{e_{c0}} = \frac{e_d}{e_{d0}} = \exp\left[-\left(\frac{3p_s}{h_s}\right)^n\right] \quad , \tag{1.1}$$

providing a function for the void ratio e with dependence on the mean skeleton pressure p_s and the direction of the associated proportional deformation path. n and h_s in (1.1) are material constants, with the exponent n ranging from ca. 0.1 for very angular to ca. 0.6 for round particles and a so-called solid hardness h_s ranging from ca. 0.5 MPa for soft to ca. 10 GPa for very hard solid particles. (1.1) provides horizontal asymptotes for $p_s \to 0$ and $p_s \to \infty$ in an e-$\ln p_s$-plot. The path direction enters via the denominator e_{i0} etc.

Viscosity, i.e. rate-dependency, can be allowed for by means of

$$h_s = h_{sr}\left[1 + I_v \ln\left(\frac{\dot{\varepsilon}}{D_r}\right)\right] \tag{1.2}$$

with the viscosity index I_v, a reference granular hardness h_{sr} at a reference deformation rate D_r, and the invariant strain rate intensity $\dot{\varepsilon}$. (1.2) is similar to an equation proposed by LEINENKUGEL (1976) introduced for the strain-rate dependency of the undrained cohesion.

The combination of (1.1) and (1.2) is illustrated in Fig. 1.3 for strain-controlled oedometric compressions with subsequent undrained shearing. Starting from a possible initial state (e_0, p_{s0}, τ_0), oedometric compression with constant deformation rate $\dot{\varepsilon} = D_r$ (0-1) shows an asymptotical approach to the o-line of D_r. Due to a sudden decrease of the deformation
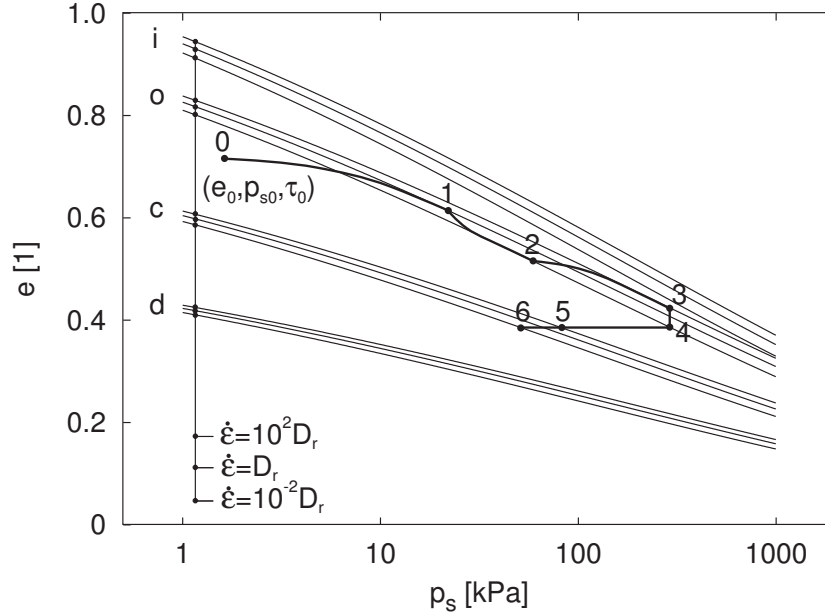
Figure 1.3: Example of state limits with respect to the deformation rate $\dot{\varepsilon}$

rate by factor 100 (1-2) the o-line for $\dot{\varepsilon} = 0.01 D_r$ is approached. By subsequent increase to $\dot{\varepsilon} = 100 D_r$ the corresponding o-line is reached (2-3). During creep, i.e. constant p_s, the creep rate decreases (3-4). Undrained shearing with $\dot{\varepsilon} = 100 D_r$ yields a transition to the corresponding c-line (4-5). Decrease of the shear rate yields a decrease of p_s (5-6). With the latter and with $c_u = p_s \tan \varphi_c$ the above-mentioned rate-dependency of the undrained cohesion can be explained, which becomes relevant e.g. in the consideration of vane shear tests with regard to a geotechnical design.

By sufficient proportional deformation of a granular volume element, state limits need not be attained all over the entire element volume. Even for uniform initial conditions e_0, p_{s0} and τ_0, proportional deformation along the element boundaries may yield a non-uniform distribution of the local deformations within the element, e.g. by the spontaneous formation of shear band patterns. Then, the concept of state limits should be applied for the localized shear bands, since there much bigger deformations occur.

This restriction was already perceived by HVORSLEV (1937) after executing stress-controlled drained shear tests with remoulded saturated cohesive soils. He determined the critical void ratio via the water content of a minute specimen taken directly from the shear plane. CASAGRANDE (1936) introduced the term 'critical void ratio' for the state of sand showing no further changes of volume after a sufficient drained shear deformation. He ignored shear bands and did not outline why he named this state 'critical'. ROSCOE *et al.* (1958) compared the results of drained and undrained shear tests and found one

unique line to which all paths in a $(p,\ e,\ \tau)$ space converge, the so-called critical void ratio (C.V.R.) line. These results were integrated by means of triaxial tests into Critical State Soil Mechanics (CSSM) by SCHOFIELD & WROTH (1968). They postulate three limit void ratios for isotropic and oedometric compression and for the critical state to decrease with $\ln p$ with the same slope λ. Other than (1.1) this requires lower and upper cutoffs. Within hypoplasticity (GUDEHUS 1999), state limits appear as attractors of a rate-type constitutive relation and are approximated by (1.1), with the advantage of objective reference values e_{i0}, e_{o0}, e_{c0}, e_{d0}, h_s and n (the ones in CSSM are not). Rate-dependency is not covered by CSSM, but can be allowed for within visco-hypoplasticity via (1.2) and the objective parameters I_v, h_{sr} and D_r. More about the concept of state limits can be found elsewhere, e.g., in GUDEHUS & MAŠÍN (2009), GUDEHUS (2005) and HERLE (1997). In KRIEG (2000) the influence of the temperature is incorporated to the concept of state limits. ZOU (1998) investigated the influence of ions on the mechanical behaviour of fine-grained soils, but a comprehensive concept of state limits with regard to the influence of ions cannot be found in the literature until present.

It is emphasized that state limits of peloids appear as *attractors* (i.e. asymptotes) of certain evolutions. The nature of these geotechnical state limits is different to the one of thermodynamical state limits, since the latter are describing *transitions*.

1.3 The term *peloid*

For unification and demarcation purposes, the term *peloid* (Greek: $\pi\eta\lambda\acute{o}s$ = clay) was introduced by GUDEHUS (2011) for denoting mixtures of hydrophilic fine mineral particles and water with ions. All types of minerals are included, and also mixtures of different mineral types, as long as they are hydrophilic, i.e. the mineral surface is wettable. Since the minerals are tiny fragments, they possess a significant specific surface area. Therefore surface effects have to be considered. The type of ions is not further specified; they are omnipresent in a rather low concentration and can be decisive for the mineral's interaction. Gas bubbles, enclosed in the particle skeleton, may occur as well as additives, e.g. polymers for stabilization of the solid particle skeleton.

1.4 Scope and outline

The present study aims at the origin and effects of surface forces and its influence on the state limits of peloids. One aim is the merge of fundamentals describing the interaction

of charged mineral particles in aqueous electrolytes. Another aim is the experimental investigation of well-defined model peloids in order to determine its state limits and to link the results with fundamentals. A further aim is the transfer of the findings to other natural fine-grained soils. The incorporation into constitutive relations and numerical simulations are beyond the scope.

In this introductory Chapter the issue of particle interactions was illustrated by means of the quick-clay landslide of Rissa in 1978. The concept of state limits was presented and a definition of the term "peloid" was given. After the scope of this work the content of the present treatise is outlined as follows.

Chapter 2 contains fundamentals of the particle interaction. A synopsis on mineralogy is given for an understanding of mineral particles. The specific surface area is studied with respect to particle size and shape. The origin of particle surface charges is treated more extensively, providing a key for subsequent investigations. The interaction of charged particle surfaces with aqueous electrolytes and the interaction of charged particles in an electrolyte are presented.

In Chapter 3 the materials investigated in experiments are introduced. Aluminium oxide and laponite powders are used as model materials for the representation of silts and clays, respectively. These well-defined model peloids can be reproducibly prepared and contain less impurities than natural soils.

In Chapter 4 sample preparation and testing devices are presented. With respect to the peculiarity of the model peloids, experimental investigations require the modification of standard testing devices and the development of new devices.

Chapters 5 and 6 represent the principal part of the present work, viz. experimental results obtained with the model peloids. Sedimentation tests aim at the choice of an adequate preparation technique and the principal characteristics of particle interaction. Oedometric and isotropic compression tests as well as drained and undrained shear tests were executed for the examination of the state limits. Some further tests which could not be executed successfully are also presented. The test results are interpreted, and a summary of the findings is given.

In Chapter 7 experimentally determined state limits are presented and an example for the transferring to other minerals is given. The introductory example of the Rissa landslide is revisited by an interpretation of quick clay based on own findings.

With Chapters 8 and 9 the treatise is closed by a summary and an outlook in English and German.

Chapter 2

Fundamentals

As already briefly outlined, the soil mechanical behaviour of peloids is highly affected by surface forces acting between fine particles. This realm is rather outside conventional soil mechanics. For a deeper understanding, also other disciplines like e.g. colloidal physics have to be employed in order to prepare fundamentals for the interpretation of observations, which partially appear strange at first glance.

In this chapter, an overview is given on the mineralogical composition of the solid component of peloids. With a discussion of the specific surface, the influence of surface forces on the mechanical behaviour of peloids is indicated. The origin of charges at the particle surface is related to the mineralogy and to chemical reactions with the pore water. An explanation is given for the interaction of a charged particle with electrolytes, subsequently the interaction of two charged particles in an electrolyte is discussed.

2.1   A synopsis on mineralogy

2.1.1   Mineralogical classification scheme

About ca. 4000 minerals are known, which are classified into groups based on common properties. Depending on the aim this classification can be carried out e.g. by the type of genesis or by characteristic properties like crystal shape, hardness, brightness or density. Scientifically, minerals are classified by their chemical composition and structural assembly. Different schemes are existing, wherein the classification scheme by Dana, established in 1854 and preferably used in the United States, and the classification scheme by Strunz, established in 1941 and used worldwide, are of highest significance. According to Strunz' scheme, the minerals are assigned to ten classes (STRUNZ & NICKEL 2001), with each

Table 2.1: Scientific classification of minerals (STRUNZ & NICKEL 2001) with represent (KLEIN & HURLBUT 1993)

Class	Denomination	Represent
1	Elements	Gold, Platinum, Iron
2	Sulfides and Sulfosalts	Cinnabar, Molybdenite
3	Halides	Halite, Fluorite
4	Oxides	Corundum, Hematite, Goethite
5	Carbonates and Nitrates	Calcite, Dolomite, Niter
6	Borates	Borax
7	Sulfates	Anhydrite, Gypsum
8	Phosphates, Arsenates, Vanadates	Turquoise
9	Silicates	*see Tab.* 2.2 *on page* 12
10	Organic Compounds	Amber

class further subdivided into divisions, subdivisions and groups. Tab. 2.1 provides an overview on the top-level classification of minerals with some representatives.

From a soil mechanical point of view, the oxides of the 4th class, the carbonates of the 5th class, the sulfates of the 7th class and the silicates of the 9th class are of major interest, since they include the minerals most soils chiefly consist of. In the present work, focus is set on oxides and silicates, as they represent typical silts and clays. Hence, a more detailed consideration of these classes is given for oxides in Sec. 2.1.2 and for silicates in Sec. 2.1.3.

2.1.2   Class of oxides

Oxide minerals consist of a chemical combination of oxygens and one or more metals and therefore are grouped as simple oxides and multiple oxides. The simple oxides are of the types XO, X_2O and X_2O_3 with a metal X and oxygen O. In contrast, multiple oxides are of the type XY_2O_4 with non-equivalent metals X and Y and oxygen O (KLEIN & HURLBUT 1993).

Since the bond type in oxide structures is generally strongly ionic, the minerals of the oxide group are relatively hard and dense (KLEIN & HURLBUT 1993). Aluminium oxide (Al_2O_3, corundum), a prominent representative of the X_2O_3 simple oxide type, is after diamond the second hardest natural mineral, showing a Moh's hardness of 9 (with Moh's hardness ranging from 1 for talc to 10 for diamond). The structure of aluminium oxide
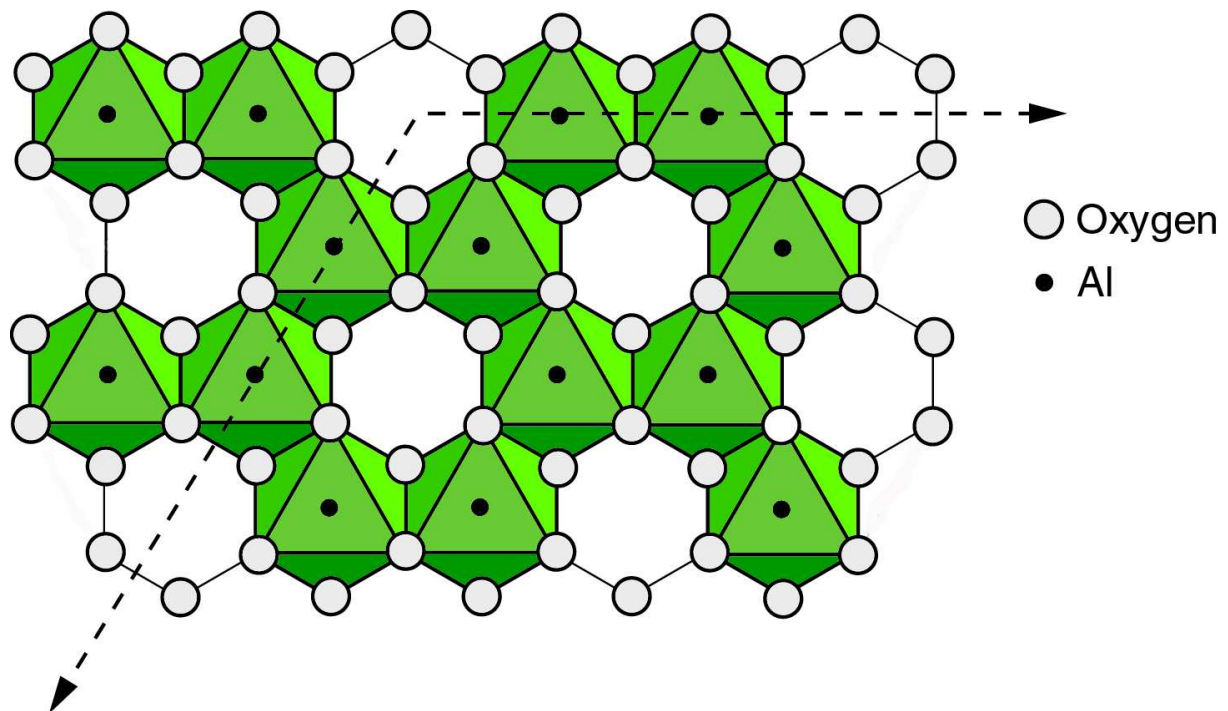
Figure 2.1: Mineralogical structure of aluminium oxide (KLEIN & HURLBUT 1993, modified)

consists of the fundamental unit of a regular octahedron, with the hexagonal closest packing of six O^{2-} and one Al^{3+} at the center (KLEIN & HURLBUT 1993). These octahedra are combined via shared oxygens, with one octahedron vacant for every two octahedra filled with Al^{3+} at the center (Fig. 2.1). This mineralogical configuration, also termed α-alumina, is the only thermodynamically stable phase of Al_2O_3 up to its melting point at 2050°C and atmospheric pressure (BAUMGART *et al.* 1984). Hence, corundum is comparatively hard and preferably used as abrasive and refractory.

The classification of the oxide group shows a notable peculiarity: quartz (SiO_2), the most common of all oxides, is not classified as an oxide mineral but is mineralogically attributed to the division of tectosilicates of the silicate group (Sec. 2.1.3). This is due to the close relation of the SiO_2 unit cells to other Si-O-compounds (KLEIN & HURLBUT 1993) and to the consequent application of the Strunz' classification scheme. Nevertheless, the chemical composition of quartz is similar to the one of aluminium oxide. This gains significance in the consideration of the surface chemism for the particle charge (Secs. 2.3.1 and 2.3.2).

2.1.3   Class of Silicates

The mineralogical class of silicates is the most significant one, since well over 90% of the Earth's crust is constituted by silicate minerals. The structure of all silicates is based on the fundamental unit of a regular tetrahedron, with four O^{2-} located at the apices and one Si^{4+} at the center (see below for details). These tetrahedra can be linked via shared oxygens, giving raise to a diversity of structural configurations (KLEIN & HURLBUT 1993). Hence, the structural variety of the silicates lead to a further subclassification of the Silicate group into nine divisions (Tab. 2.2):

Table 2.2: Divisions of the silicate class (STRUNZ & NICKEL 2001) with represent (KLEIN & HURLBUT 1993)

Class	Denomination	Represent
9.A	Nesosilicates	Olivine
9.B	Sorosilicates	Hemimorphite
9.C	Cyclosilicates	Beryl
9.D	Inosilicates	Pyroxene
9.E	Phyllosilicates	Kaolinite, Muscovite, Chlorite, Vermiculite, Montmorillonite, Laponite
9.F	Tectosilicates without zeolitic H_2O	Quartz, Orthoclase
9.G	Tectosilicates with zeolitic H_2O	Opal
9.H	Unclassified silicates	./.
9.I	Germanates	./.

The denomination of the silicate divisions is derived from the mineral structure due to the linking of the SiO_4 tetrahedra. Silicates without linked SiO_4 tetrahedral groups are called nesosilicates (Greek: *nesos*, island). Silicates with two linked SiO_4 groups are classed as sorosilicates (Greek: *soros*, heap). Silicates with more than two linked tetrahedra may form either closed ring-like structures, the cyclosilicates (Greek: *kyklos*, circle), or theoretically infinite single chains, the inosilicates (Greek: *inos*, thread). If three of the oxygens of a tetrahedron are shared by adjoining tetrahedra, flat sheets of theoretically infinite extension are formed, termed phyllosilicates (Greek: *phyllon*, leaf). If all four of the oxygens of a tetrahedron are shared by adjoining tetrahedra, a three-dimensional network composed by unit cells results, denoted tectosilicates (Greek: *tecton*, builder) (KLEIN & HURLBUT 1993).

Out of these nine divisions, the phyllosilicates division with the clay minerals and the

tectosilicates division with the quartz minerals are in the focus of the present work.

The phyllosilicates, also termed *layer silicates*, consist of a combination of two or three layers with each layer being periodically assembled by unit cells. Two types of unit cells, the (silicate) tetrahedron and the octahedron, can be distinguished. By two-dimensional assembly of one type of these unit cells, a tetrahedron layer or an octahedron layer with theoretically infinite two-dimensional extensions is obtained. Since the dimensions of the tetrahedral and octahedral unit cells are rather similar, composites of tetrahedral and octahedral layers is readily formed by hydrogen bonding. Combination of a tetrahedron and an octahedron layer yields so-called two-layer phyllosilicates; combination of a tetrahedron, an octahedron and a tetrahedron layer yields so-called three-layer phyllosilicates (GRIM 1962).

Out of the tectosilicates, quartz is the most prominent representative. It consists of a three-dimensional assembly of silicate tetrahedra (HEANEY *et al.* 1994).

In the following the silicate tetrahedron and the octahedron unit cells are discussed. Subsequently the mineralogical composition of some significant phyllosilicates and of quartz are presented.

Tetrahedral unit cell and unit layer

The basic unit cell of the silicates is the SiO_4-tetrahedron (Fig.2.2). The Si^{4+}-cation in the center of the tetrahedron is chemically bounded to four O^{2-} anions at its apexes (HEIM 1990). The tetrahedral assembly results from the condition of equidistance of the silicon to the oxygens. The height of the unit cell, i.e. the distance from the base to the tip, counts 4.93 Å, determinable geometrically via the ionic radii or experimentally via x-ray diffraction (XRD). Since the charge balance of the SiO_4-tetrahedron yields a net charge of $4e^-$, the existence of a single unit cell is quite unlikely (GRIM 1962).

By arrangement of the unit cells to a hexagonal unit layer, with the tips of all pointing in the same direction, the oxygens in the base plane of a specific unit cell are shared with the ones from the adjacent unit cells, forming an extended layer of the composition $Si_4O_6(OH)_4$. In this network, the charges at the concatenation plane are fully compensated. Nevertheless, the excess charges at the tips of the tetrahedra still remain unsaturated with a net charge of $1e^-$ per single unit, making the existence of a single layer also unlikely (GRIM 1962).
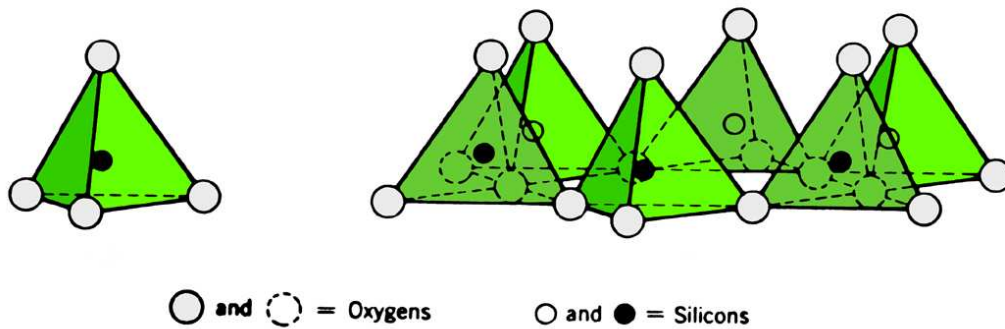
Figure 2.2: SiO$_4$-tetrahedral unit cell and its arrangement to a hexagonal unit layer (GRIM 1962, modified)

Octahedral unit cell and unit layer

Another basic unit cell related with layer silicates is the octahedron (Fig. 2.3). It consists of two sheets of closely packed hydroxyls with embedded aluminum, iron, or magnesium cations. By octahedral coordination, these central cations are equidistant to six hydroxyls. The height of the unit cell counts 5.05 Å (GRIM 1962).

Again, by two-dimensional combination of the octahedral unit cells a regular unit layer is formed with the unit cells linked by common hydroxyls at the tips. Since the central cation of the octahedral cell can be divalent or trivalent, two cases of the octahedral layer structure have to be distinguished: With Al^{3+} as the central cation, only two-thirds of the possible positions are occupied, and the layer is called dioctahedral; with Mg^{2+} as the central cation, all possible positions are occupied, and the layer is called trioctahedral. In both cases the structure is electrically balanced (GRIM 1962), giving support to the existence of a single octahedral layer. However, the dioctahedral or trioctahedral structure
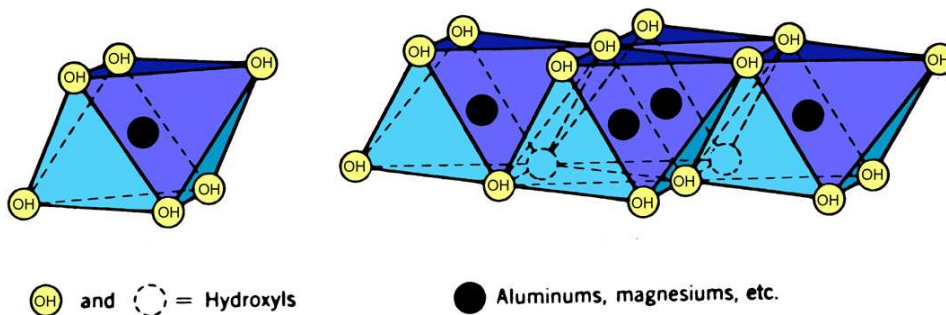
Figure 2.3: Octahedral unit cell and its arrangement to a unit layer (GRIM 1962, modified)

of the layer will have consequences for the type of layer silicate formed by the combination of tetrahedral and octahedral layers, as outlined below.

Kaolinite

The simplest combination of two different unit layers is the dioctahedral 1:1 layer silicate kaolinite (Fig. 2.4). Its name is derived from the Chinese hill's name *kauling*, where the mineral is obtained from (KLEIN & HURLBUT 1993).
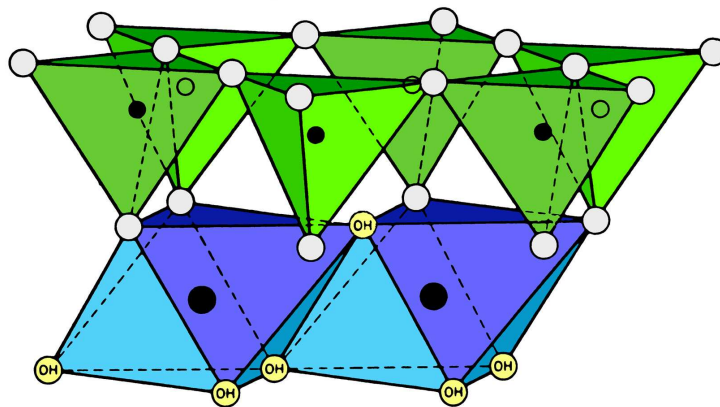
Figure 2.4: Dioctahedral 1:1 layer silicate kaolinite (GRIM 1962, modified)

Kaolinite is composed of a silicon tetrahedral and an alumina octahedral layer. In this unit the tips of the tetrahedrons and the ones of the octahedral sheet form a common layer, with all the tips of the tetrahedra pointing towards the center of the layer (GRIM 1962).

Only two-thirds of the unit cells of the octahedral layer are occupied by aluminium (dioctahedral). Two-thirds of the linking atoms are shared by the silicons and aluminiums, and are oxygens instead of hydroxyls (GRIM 1962).

The height of the two-layer kaolinite structure counts 7.2 Å. Since the net charge of a kaolinite structure is zero, its faces are electrically neutral. Therefore kaolinite minerals can be stacked like coin columns, showing a basal spacing of 7.2 Å.

Pyrophyllite

Another combination of two different unit layers is the dioctahedral 2:1 layer silicate pyrophyllite (Fig. 2.5). The mineral's name is derived from Greek: *pyros*, fire and *phyllos*, leaf, since pyrphyllite exfoilates on heating and thereby exhibits its layer structure (KLEIN & HURLBUT 1993).
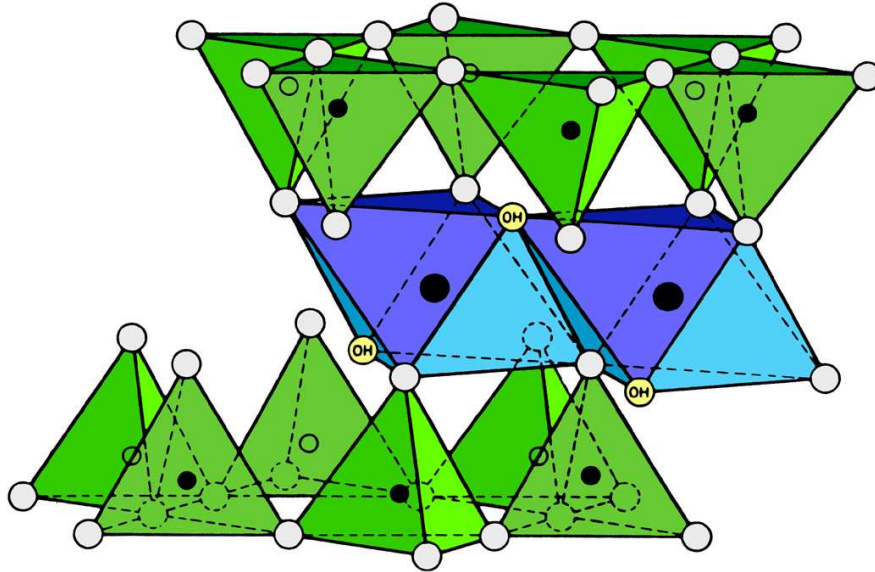
Figure 2.5: Dioctahedral 2:1 layer silicate pyrophyllite (GRIM 1962, modified)

Pyrophyllite is a comparatively rare mineral, it represents the perfect composition of an aluminium octahedral layer covered by an upper and a lower silicon tetrahedral layer. Like in the Kaolinite structure, only two-thirds of the unit cells of the Pyrophyllite's octahedral layer are occupied by aluminiums (dioctahedral, KLEIN & HURLBUT 1993).

The height of the pyrophyllite structure counts 9.2 Å. Since the pyrophyllite structure is electrically neutral, the minerals can also be stacked like coin columns, yielding a basal spacing of 9.2 Å.

Muscovite

The dioctahedral 2:1 layer silicate muscovite (Fig. 2.6) is termed after Muscovy, a substitute for glass in Old Russia (KLEIN & HURLBUT 1993).

Muscovite consists of a pure aluminium octahedral (dioctahedral) layer sandwiched by an upper and a lower tetrahedron layer. In both tetrahedra layers, some of the silica are replaced by further aluminiums. Additionally, potassium ions are incorporated at the centers of the hexagon, which is formed by the silicon tetrahedra assembly (GRIM 1962).

The replacement of some silica of the tetrahedra layers by aluminums leads to an electrical charge imbalance of the entire layer. This electrical charge imbalance is compensated by the incorporation of the potassiums, hence the whole assembly appears electrically neutral.

The height of the muscovite structure counts 10 Å and therefore is about 0.8 Å larger than
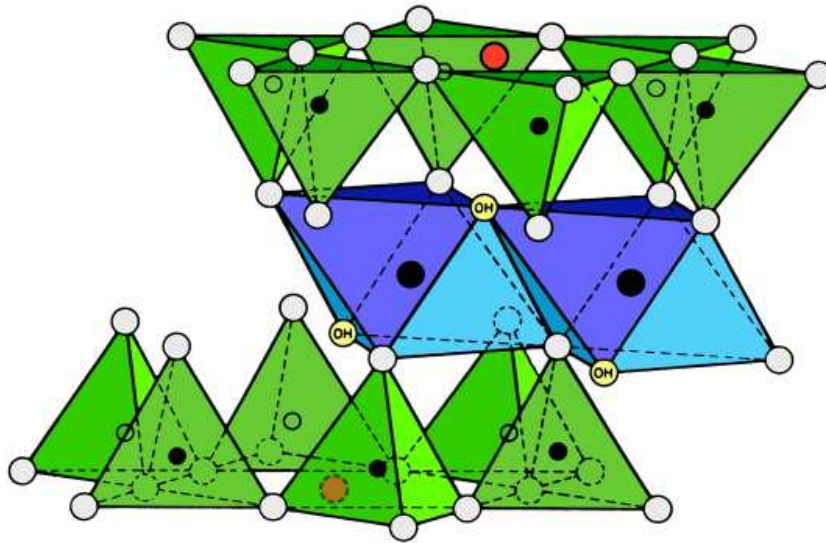
Figure 2.6: Dioctahedral 2:1 layer silicate muscovite (GRIM 1962, modified)

regular three-layer silicates. This increased thickness of the muscovite layer is attributed to the potassiums, towering from the silicon tetrahedra. Under consideration of the mineral's electrical neutrality, the muscovite layers may be stacked like coin columns with a basal spacing of 10 Å, requiring an in-plane offset of each mineral by half the diameter of the hexagon ring (GRIM 1962).

Montmorillonite

The dioctahedral 2:1 layer silicate montmorillonite (Fig. 2.7) is termed after the French city *Montmorillon* with its large deposits of this type of mineral (KLEIN & HURLBUT 1993).

Montmorillonite shows the typical three-layer structure with an octahedral layer covered by an upper and a lower silicon tetrahedral layer. Other than pyrophyllite, the octahedral layer of montmorillonite contains not only aluminium, but some magnesium substituting the former. The height of the montmorillonite structure counts 9.2 Å and therefore equals the height of regular three-layer minerals (GRIM 1962).

Due to the cation substitution in the octahedral layer, the structure exhibits a negative electrical charge at its faces. Therefore the montmorillonite structure reveals the outstanding feature that water and other polar molecules can enter between the unit layers, causing the lattice to expand into the direction perpendicular to the mineral's face. Additionally, so-called exchangeable cations may also enter between the unit layers. The
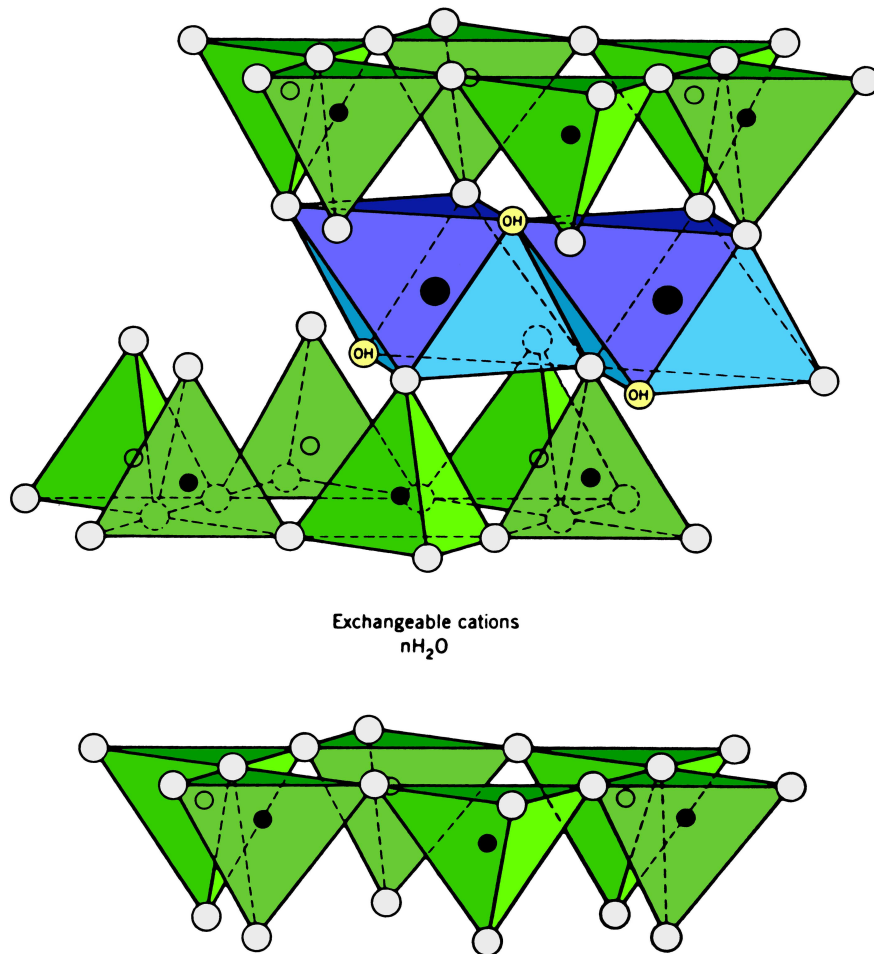
Figure 2.7: Dioctahedral 2:1 layer silicate montmorillonite (GRIM 1962, modified)

thickness of the water layers between the unit layers depends on the nature of these exchangeable cations: A montmorillonite with sodium as the exchangeable cation frequently has one molecular water layer and therefore a basal spacing of about 12.5 Å, a montmorillonite with calcium as the exchangeable cation frequently has two water layers and therefore a basal spacing of about 15.5 Å. The expansion is reversible by substitution of the exchange cations (GRIM 1962).

These interlayer sheets of polar molecules may develop with a thickness of many molecular layers. Therefore the basal spacing of montmorillonite varies from 9.2 Å, when no polar molecules are between the unit layers, to a complete separation of the mineral layers (GRIM 1962).

Laponite

The trioctahedral 2:1 layer silicate laponite is a synthetically produced mineral. Its appellation is derived from the mineral's producer name *Laporte*. Though this mineral does not occur in nature, it is itemized in this section since it was used as model material for experimental investigations within the present treatise.

Laponite shows a similar mineralogical configuration like montmorillonite. It consists of an octahedral layer covered by an upper and a lower silicon tetrahedral sheet. In the octahedral layer three-thirds (trioctahedral) of the unit cells are occupied by magnesiums, with some magnesiums substituted by lithiums and some unit cells of empty spaces (LAPORTE 2000).

The height of the laponite structure of 9.2 Å is identical with the one of montmorillonite. An infinitely extended laponite sheet carries electrical face charges and shows a similar inter-layer behaviour like montmorillonite. The diameter of a real laponite particle is about $d = 25$ nm (LAPORTE 2000, Sec. 3.2) and is about 2 decades smaller than montmorillonite particles.

Laponite provides wide technical applications as rheological additive, e.g. for surface coatings, paper and polymer films, and for personal care and household products. It can also be used for ceramics and enamels and in oilfield applications (LAPORTE 2000).

Summary for the division of phyllosilicates

Recapitulating the mineralogy of phyllosilicates, they consist of a combination of two unit layers, each composed of a flat assembly of either tetrahedral or octahedral unit cells. Depending on the kind of the unit layer's central cations and the composition of unit layers to the layer silicate, various types of minerals are obtained. An overview on the presented minerals is provided by Tab. 2.3.

Table 2.3: Mineralogical composition of Phyllosilicates

Mineral	Layer type		Tetrahedron	Octahedron	swellable
Kaolinite	1:1	dioctahedral	Si	Al	no
Pyrophyllite	2:1	dioctahedral	Si	Al	no
Muscovite	2:1	dioctahedral	Si & Al / K	Al	no
Montmorillonite	2:1	dioctahedral	Si	Al & Mg	yes
Laponite	2:1	trioctahedral	Si	Mg & Li	yes

Kaolinite and pyrophyllite with pure silicon tetrahedra and aluminium octahedra are perfect 1:1 and 2:1 layer silicates, respectively. Their faces are electrically neutral and therefore non-swellable. Other layer silicates with some of the silicons and aluminium partially substituted by other cations show deviations from the perfect structure, and hence carry electrical charges at their faces. These electrical charges give rise to the swelling properties of that types of minerals.

Quartz

The tectosilicate quartz (SiO_2) is one of the most common minerals of the earth's crust. Its mineral name is presumably derived from Saxon: *Querkluftertz*, cross-vein ore.

The quartz mineral may exist in various polymorphs, depending on the ambient temperature and pressure. Below 573°C and 20 kbar, the so-called α-quartz is the only thermodynamically stable configuration (HEANEY *et al.* 1994) and hence referred to in the following.

The structure of quartz consists of the fundamental tetrahedral unit cell of a silicon in the center and four oxygens at the apexes, as characteristic for the silicates class and already presented above. The unit cells are helically assembled to a hexagonal crystal structure (Fig. 2.8), yielding to a three-dimensional network. The crystal structure of quartz depends on the clock- or counterclockwise orientation of the tetrahedral helices
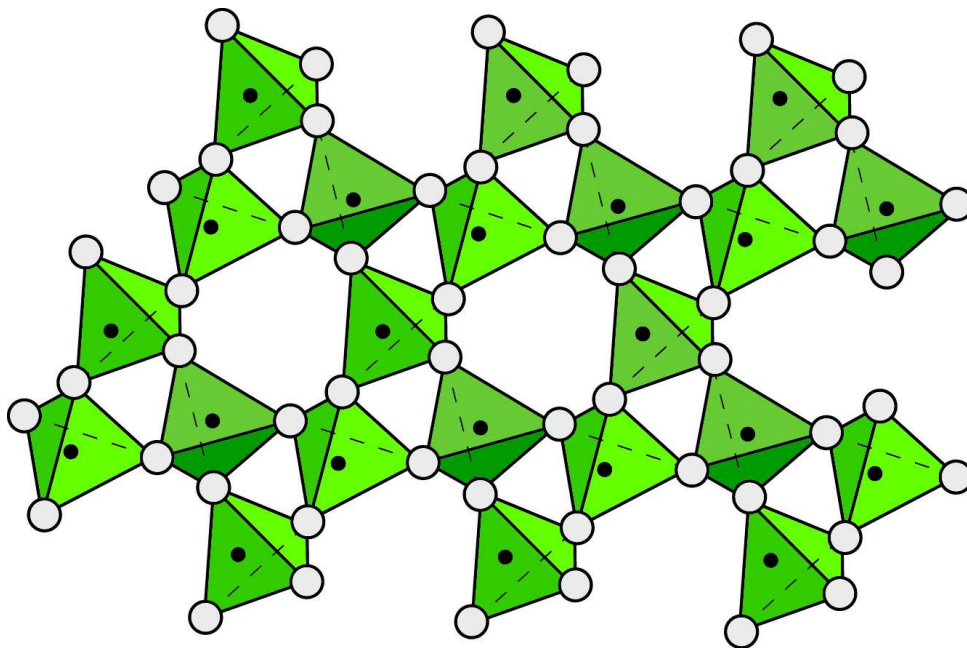
Figure 2.8: Mineralogical structure of quartz (KLEIN & HURLBUT 1993, modified)

(HEANEY *et al.* 1994). Due to this crystal structure, quartz particles show a rather compact particle shape, with sharp edges if freshly broken or smooth edges if abrased.

Quartz exhibits a Moh's hardness of 8 and is therewith about 4 times weaker than corundum (KLEIN & HURLBUT 1993, see Sec. 2.1.2). Quartz is industrially used, e.g. as raw material for glasses, enamels and overglazes or as filler material for tyres, erasers or emulsion paints. The piezoelectrical properties of quartz are utilized in electronics.

As already mentioned in Sec. 2.1.2, quartz is mineralogically classified to the group of silicates, since it consists of unit cells of SiO_2-tetrahedrons. Nevertheless, it is again pointed out that quartz and corundum exhibit similar physical and chemical properties.

2.2 Specific surface area of particulate materials

Since the particle interaction due to surface effects is subject of investigation, the surface area is important. The specific surface area is defined as the surface area of a particle referred to its mass. The higher the specific surface area, the more dominant surface effects will influence the mechanical behaviour.

2.2.1 Geometrical approach

For silts with compact particles, a sphere of diameter d and given mass density ρ is considered as first approximation. With the surface area $A = \pi d^2$ and the mass $m = \pi \rho d^3/6$, the specific surface area

$$\frac{A}{m} = \frac{6}{\rho d} \tag{2.1}$$

increases with the inverse of the diameter.

Fig. 2.9 shows the course of (2.1) with reasonable axis scaling, i.e. for particle diameters between the one of large blocks down to nanopowders, and for the range of the typical specific surface area of silts (cf. Tab. 2.4). For particle diameters below ca. 10^{-4} m, a remarkable increase of the specific surface area is obtained, with a progressive increase of A/m with decreasing d. On the other hand, A/m is negligible for spheres of large d.

For layer silicates with platelet-like particle shape, a disc of diameter d and thickness h with density ρ is considered. With the surface area $A = \pi d(d/2 + h)$ and the mass $m = \pi \rho d^2 h/4$, the specific surface area

$$\frac{A}{m} = \frac{2}{\rho} \left(\frac{2}{d} + \frac{1}{h} \right) \tag{2.2}$$
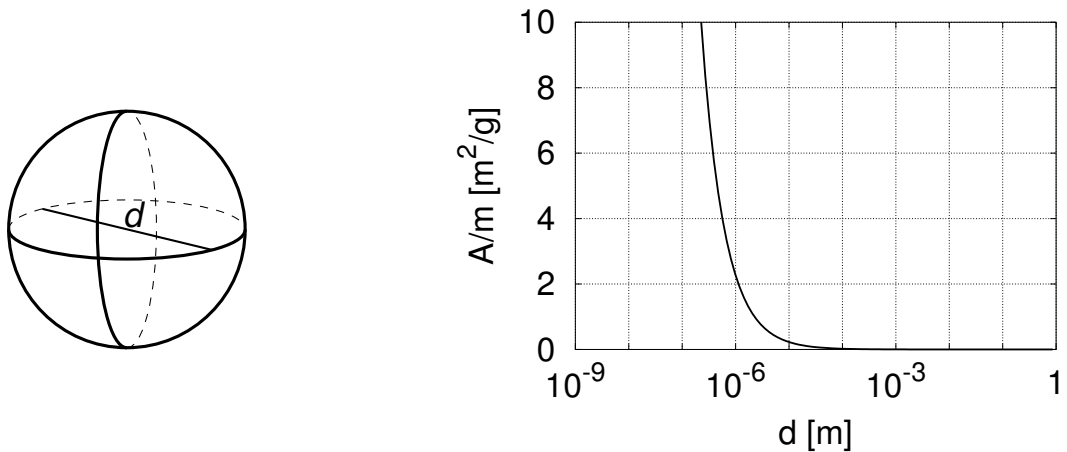
Figure 2.9: Specific surface area A/m of a sphere of density $\rho = 2.65$ gcm^{-3} with respect to the diameter d

is the sum of the specific surface area of the face $A_F/m = 2/(\rho h)$ and the edge $A_E/m = 4/(\rho d)$. A/m increases with the inverse of d and the inverse of h.

For a given thickness of the disk $h = 0.92$ nm, matching the typical thickness of a 2:1 layer silicate (cf. Sec. 2.1.3), the course of A/m is plotted in Fig. 2.10. For large d, A/m is nearly independent from d since A_F/m is constant and the contribution of A_E/m is low. The latter is only remarkably contributing for $d < 10^{-6}$ m, leading to an increase in A/m with decreasing d. For discs, i.e. for cylinders with $d \gg h$, there is therefore a lower limit of the specific surface area $A/m \geq 2/(\rho h)$; consequently even for larger d the specific surface area is by no means negligible for plate-like particles.
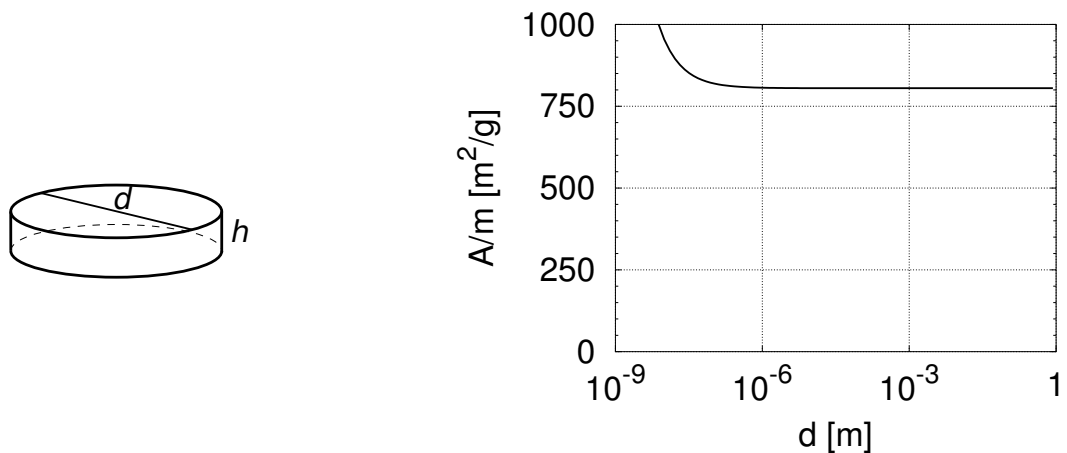
Figure 2.10: Specific surface area A/m of a disk of thickness $h = 0.92$ nm and density $\rho = 2.70$ gcm^{-3} with respect to the diameter d

The ratio of the face surface area A_F and the edge surface area A_E of a disk

$$\frac{A_F}{A_E} = \frac{d}{2h} \tag{2.3}$$

is obtained from the specific surface area of the face $A_F/m = 2/(\rho h)$ and the edge $A_E/m = 4/(\rho d)$. A_F/A_E increases with increasing d and decreasing h. For a constant $h = 0.92$ nm of a 2:1 layer silicate, the course of (2.3) is plotted in Fig. 2.11, again with reasonable axis scaling. It can be concluded, e.g., that the surface area of the face of a montmorillonite particle with $d = 10^{-6}$ m is about 600 times the one of the edge.
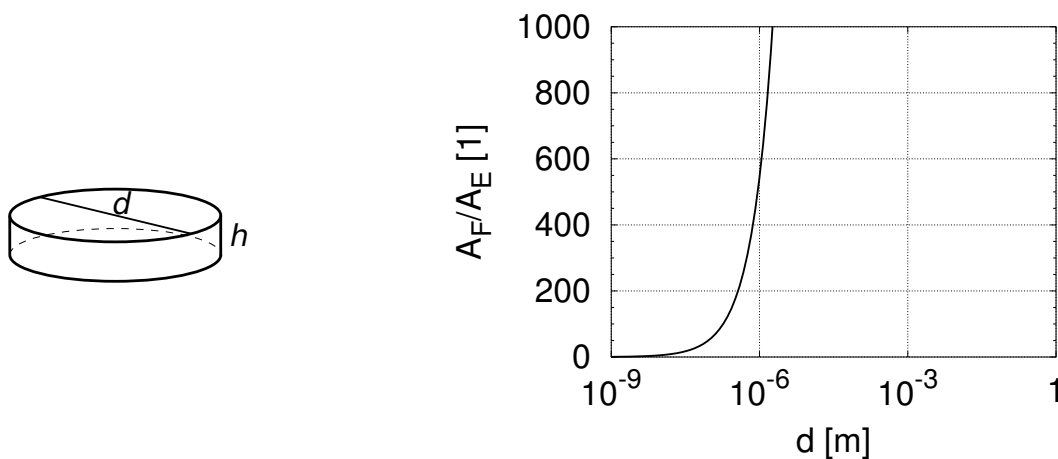
Figure 2.11: Ratio of the face and edge surfaces A_F/A_E of a disk of height $h = 0.92$ nm with respect to the diameter d

2.2.2 Experimental approach

The specific surface area can be also be determined experimentally. A common procedure is to measure the amount of gas physically adsorbed by dry particles. According to the so-called B.E.T. method, termed after the researchers' surname initials Brunauer, Emmett and Teller, the adsorbed volume of a gas V_g at low temperature is recorded versus the partial gas pressure p_g up to the saturation pressure of the gas p_{g0}. Typically, these adsorption isotherms start with an approximately linear course at $p_g/p_{g0} \approx 0.05$. The three authors stated that at this point the entire surface is just covered by a complete unimolecular layer of adsorbed gas. Via V_g and the molecular diameter of the gas, the corresponding surface area is obtained by back-calculation. Different types of gases are used at specific temperatures, with the most common nitrogen N_2 used slightly above its boiling point at atmospheric pressure and -195.8°C (Brunauer *et al.* 1939).

2.2.3 Examplary data

A collection of specific surface areas of some granulates, determined by the B.E.T. method, is provided in Tab. 2.4. Thus fine sand shows an estimated surface area in the range of a letter paper per gram. Quartz powder has a surface area of about half the size of a standard window per gram. The surface area of one gram of corundum powder equals about two times the area of a ping-pong table. Laponite shows a surface area per gram of about three halfs of a tennis court.

Table 2.4: Specific surface area B.E.T. of selected granulates according to product data sheets (*estimated*, [†]Mikrosil LS300, [◇]Alcoa CT3000SG, [⋆]Laponite RD) and reference areas for comparison

Material	A/m [m^{2}g^{-1}]		Reference area	A [m^2]
Fine sand[*]	< 0.1		Letter paper	0.06
Quartz powder[†]	0.55		Standard window	1
Corundum powder[◇]	7.0		Ping-pong table	4.16
Laponite powder[⋆]	370		Tennis court	260

2.3 Origin of particle surface charges

Minerals were presented in Sec. 2.1 for the case of infinite mineral extension. It was shown that pure aluminium oxide (corundum), pure silicium dioxide (quartz) and some of the pyrophyllites (clays) are electrically balanced, whereas other pyrophyllites carry face charges according to their mineralogical composition.

Now finite extensions of these minerals, i.e. discrete particles, are considered. They can emerge by fracturing of larger mineral assemblies. Fresh surfaces arise, and the broken chemical bonds will be saturated almost immediately by physical adsorption of omnipresent ions, even at ultra high vacuum conditions (HEANEY *et al.* 1994).

According to the aims of the present work, the surface charge of the above-mentioned hydrophilic minerals immersed into water is considered more in detail. It will be shown that the surface charge of these minerals is due to physico-chemical acid-base reactions in the uni-molecular vicinity of the particles, and depends on the pH of the water.

2.3.1 Surface charge of corundum particles immersed into water

The raising of surface charges of corundum particles due to immersion into water is described by several authors (e.g. HIDBER 1993, BAADER 1995, REED 1995). Since the entire process is rather complex, it is explained in a simplified manner.

When a corundum particle (Fig. 2.12A) is immersed into water, the particle surface becomes wetted. By closer look in a molecular scale, the aluminum molecules at the surface with its unsaturated bonds will attract adjacent polar water molecules, leading to a hydration of the particle surface, i.e. a physical adsorption of water (Fig. 2.12B).
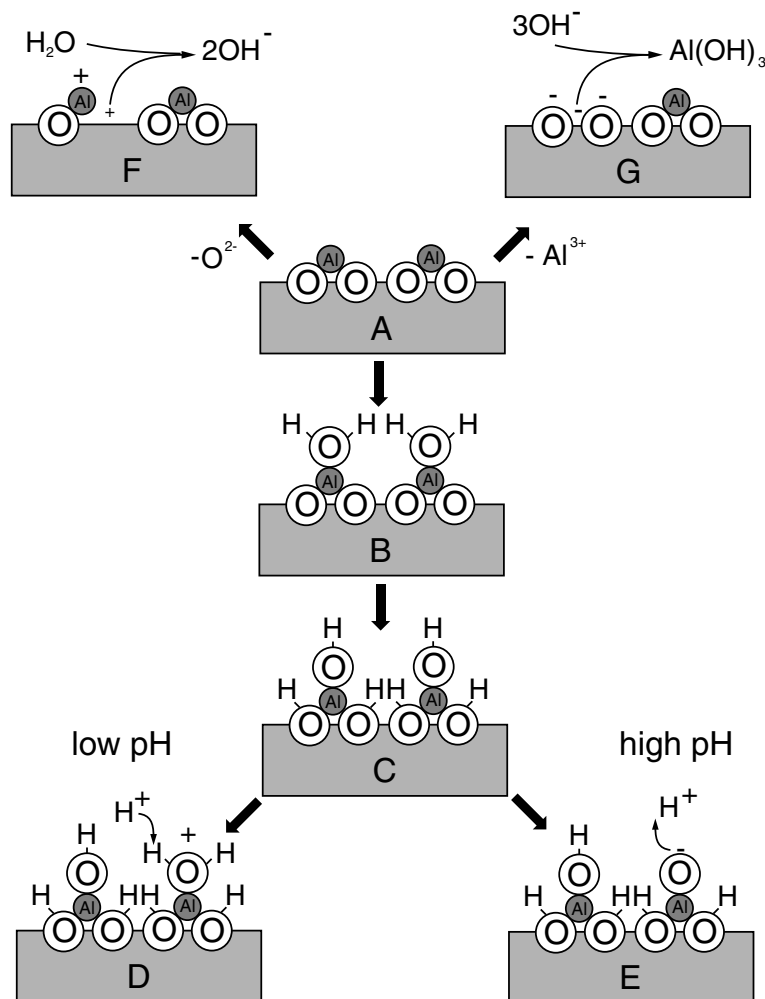
Figure 2.12: Schematical mechanisms leading to charged particle surfaces of aluminum oxide (after HIDBER 1993).

Subsequently, chemisorption of water molecules results in a hydroxylation of the aluminiums (Fig. 2.12C), since chemisorption is energetically more favourable than hydration. This adsorption was confirmed by IR-spectroscopy (HIDBER 1993).

Depending on the current pH, i.e. on the availability of H_3O^+ and OH^- ions, the OH-groups will accept (Fig. 2.12D) or donate (Fig. 2.12E) protons (H^+) in order to achieve an acid-base-equilibrium. At low pH, i.e. a high concentration of H_3O^+, the OH-groups will accept protons, leading to a positive surface charge of the particle. At high pH, i.e. a high concentration of OH^-, the OH-groups donate protons, leading to a negative surface charge of the particle. In between, at a distinct pH, the surface charge vanishes. This distinct pH is called *isoelectric point* (IEP, cf. Sec. 2.4.3 and 3.1.2). The processes of acceptance or donation of protons are reversible, i.e. by each shifting of pH a new equilibrium is reached with a correspondingly changed surface charge.

In spite of the marginal solubility of corundum in water, the detaching of Al^{3+} or O^{2-} ions from the particle surface is also contributing to the formation of surface charges. At low pH, O^{2-} is detached from the particle surface and forms hydroxyls ($2OH^-$) by chemical reaction with H_3O^+ from the water, resulting in a positive surface charge (Fig. 2.12F). At high pH, Al^{3+} is detached from the particle surface and forms aluminium hydroxyl ($Al(OH)_3$) by chemical reaction with OH^- from the water, resulting in a negative surface charge (Fig. 2.12G). In both cases there is a loss in particle mass, and reversibility is not given. The solved ions can again precipitate, preferentially at particle contacts (RICHTER 2006).

Since H_3O^+ and OH^- ions cause the generation of surface charges, they are called *potential determing* ions. During the described processes, H_3O^+ and OH^- is consumed or released, respectively. Consequently, by immersion of corundum particles into water, the initial pH is changed up to the point where equilibrium is reached, and the particles then show a distinct surface charge. In order to modify a surface charge, acids or bases may be added. The adding of acids or bases results in an increase of the ion concentration of the bulk water.

2.3.2   Surface charge of quartz particles immersed into water

The described mechanisms of raising surface charges on aluminium oxide particles (Sec. 2.3.1) are principally transferable to other oxide materials (HEANEY *et al.* 1994). This generalization is referred to the chemical group of oxides, and is therefore not restricted to the mineralogical class of oxides (Sec.2.1.2), but it is particularly valid for tectosilicates of the silicate class (Sec.2.1.3).

Therefore the surface charge of quartz, the most prominent representative of the tecto-silicates, can also be explained by the hydration and hydroxylation of unsaturated silicon bonds, and the subsequent protonation or deprotonation of hydroxyls according to the

bulk water pH (HEANEY *et al.* 1994). Since silicon instead of aluminium is involved, the IEP of quartz differs from the one of corundum (Sec. 3.1.2).

2.3.3 Surface charge of phyllosilicate particles immersed into water

The above described mechanisms with surface charge due to immersion into water can be transfered to phyllosilicates if the mineralogical structure is allowed for. In Sec. 2.1.3 it was shown that phyllosilicates consist of a two-dimensional assembly of tetrahedral and octahedral unit layers. The faces of these unit layers are electrically neutral (dioctahedral assembly with Al^{3+} as central cation or trioctahedral assembly with Mg^{2+}) or electrically charged by the substitution of some central cations. In both cases the oxygens of the tetrahedrons and the hydroxyls of the octahedrons are chemically bonded to the central cations. Therefore the surface charges at the faces of phyllosilicates are permanent (LAGALY 1997) and not affected by the immersion into water.

However, the regular two-dimensional assembly of tetrahedral and octahedral unit layers is disturbed at the edges of the particles. There, some of the valencies of the central cations (Si^{4+}, Al^{3+} and substitutes) and the corresponding anions (O^{2-}, OH^-) remain unsaturated. If immersed into water, protonization and deprotonization as indicated in Sec. 2.3.1 and Sec. 2.3.2 proceed, with the consequence of positively charged edges in an acid regime and negatively charged edges in a basic regime of bulk water (LAGALY 1997).

2.4 Interaction of charged particles and electrolytes

In Sec. 2.3 the raising of surface charges of mineral particles immersed into water was discussed. It was shown that surface charges are generated by chemical reactions at the mineral surface. The interaction of charged particles with proximate water molecules and dissolved ions is now discussed.

2.4.1 Interaction of charged particles and water molecules

Due to the dipole character of water molecules, the surface charge of a particle will affect the water molecules near the particle surface. In soil mechanics, this type of water is called 'bound pore water', and particular properties like increased viscosity and density are ascribed to it. This topic is under vital discussion in several disciplines, thus the

following statements about water in the proximity of charged particles may contribute to clarification.

HOLZ (2002) examined the translational and rotational motion of a water molecule on a path from the bulk water towards a charged particle surface with a NMR device. It could be shown that the translational motion of a water molecule remains nearly unaffected, whereas the rotational motion is strongly hindered if the water molecule is nearby a charged particle surface.

Since a system of higher order normally exhibits a higher density, the water in the proximity of a charged particle surface should be denser than the one in the bulk. Several authors have reported on this phenomenon. Presumably the first was TERZAGHI (1920). He performed experiments with a thin water film enclosed by glass sheets, and observed that the water evaporated rapidly until several wet spots remained, surrounded by Newton's rings. A microscopical examination of the wet spots yielded a certain number of 'crystal-leaves' in every water spot. Hence he concluded that a water film of a thickness below 100 μm has properties which are different from the ones of the bulk water.

RENDULIC (1937) performed triaxial tests with saturated clay and systematically observed a minute excess of expelled pore water as against the quantity expected due to the test control. Initially he assigned this excess pore water volume to the swelling of the rubber membrane, but even after a more detailed investigation of the rubber membrane's water absorption this phenomenon could not be explained. Consequently, he concluded that the pore water within the specimen is affected by molecular forces and therefore has a higher density, which is reduced at the moment of outflow from the specimen, leading to an increase in pore water volume. He supported this hypothesis by a quotation of Harkins (no reference given), who stated the mean density of water in the pores of charcoal in the range of 1.2 gcm^{-3}. By back-calculation via the expelled pore water volume, Rendulic finally determined the mean pore water density as ca. 1.05 gcm^{-3}.

MARTIN (1962) collected and re-examined experimental data concerning adsorbed water in clay, which had been published by other authors within the precedent 20 years. Regarding the density of adsorbed water on Na-montmorillonite (Fig. 2.13) he gives a minimum density of 0.97 gcm^{-3} at a water content of 0.7 g H_2O/g clay (approx. the plastic limit). For lower water contents the density rapidly rises to about 1.4, for higher water contents the density gradually rises until at a water content of about 5 the density of the adsorbed water equals that of normal liquid water.

DERJAGUIN & CHURAYEV (1971a) reported on investigations with condensation of water vapour in glass capillaries, performed by Fedyakin. Herein the appearance of condensate columns was observed with modified properties like depressed water vapour pressure and
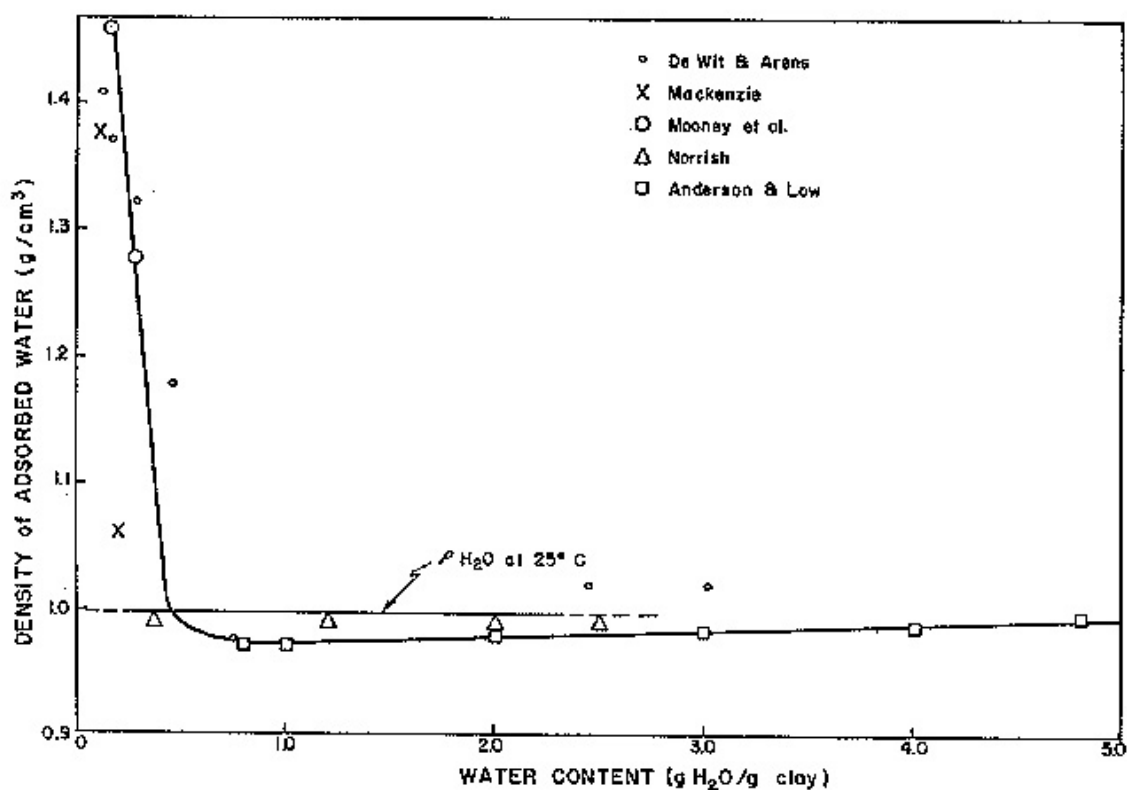
Figure 2.13: Adsorbed water density on Na-montmorillonite (MARTIN 1962).

increased thermal expansion as compared with normal water. This caused the authors to introduce the terms "normal" and "anomalous" water, the latter also termed "water II", "modified" or "polywater". The authors measured the density of the anomalous water by discharging drops into a density-gradient tube containing a vertically graded mixture of mineral oil and tetrachloro-ethylene and observing the equilibrium level at which the drops stopped. From these experiments densities of anomalous water up to 1.4 g/cm^3 were derived. Those results have been validated by the same authors via phase separation tests of mixtures of "water I" and "water II" at sub-zero temperatures.

From the date of publishing this work was subject of a vigorous discussion. DERJAGUIN & CHURAYEV (1971b) faced the criticism that the properties of "anomalous water" may be attributed to contamination, e.g. by silica gel. The authors replied by stating that even by the very sensitive electron probe method no silicon atoms were detectable within the water samples. They once again pointed out that only the condensation of water vapour led to the formation of "anomalous water" and stated that further experiments regarding the distillation of anomalous water resulted in no loss of anomaly up to temperatures

<500°C, but a loss of anomaly above 700°C. The authors concluded that molecules of anomalous water also exist in the vapour phase and that the observations cannot be explained by the presence of impurities.

Two years later DERJAGUIN & CHURAYEV (1973) had to withdraw their hypothesis of anomalous water, after an increased concentration of sodium and silicon atoms within the anomalous water samples could be clearly detected by the neutron activation analysis method. They found that there were no condensates both free of impurity atoms and simultaneously exhibiting anomalous properties. The previously observed anomaly was therefore ascribed to the presence of molecular-dissolved compounds, thereafter the theoretical interpretation by a stable bulk phase of water molecules, the so-called "polywater" hypothesis, was abandoned. This withdrawal became famous in the scientific community and is up to nowadays referred to as the *error of Derjaguin.*

Nevertheless the research on this topic was continued. DERJAGUIN *et al.* (1986) published experimental results on the thermal expansion of water. In these tests, capillaries with 2 mm diameter were filled with silica gel of pore sizes in the order of 50Å. Then, the relative thermal expansion of the pore water was determined by the dilatometric method. Within the temperature range from 0 to 70°C, the thermal expansion of the pore water differed from the one in the bulk phase, whereas in the range from 70 to 90°C no difference in thermal expansion was determinable. Based on these results, it was concluded the water in pores exhibits an increased density up to 2% higher than in the bulk. In the temperature range from 0 to 8°C, more precise measurements with a dilatometer of a capillary of 0.3 mm diameter yielded no maximum of the water density at 4°C, which states another remarkable peculiarity.

FRIPIAT *et al.* (1982) studied the behaviour of water in suspensions of swelling smectites (hectorite and laponite) and non-swelling phyllosilicate (kaolinite) over a large range of solid concentration. By means of nuclear magnetic resonance (NMR) and calorimetric heats of immersion measurements they found that the water molecules in these phases are distributed in two phases. Phase a contains the so-called free water between secondary particles resulting from the aggregation of primary particles (individual sheets) of smectites or between the individual kaolinite crystals. Phase b contains the water molecules influenced by the surface force fields of the primary particles. With rotational correlation times of the water molecules of about two orders of magnitude lower than those of liquid water the authors estimated the zone thickness of phase b to about three water molecules, and concluded that the forces acting on the water molecules in phase b are of short range. The authors stated that the water molecules of phase b would cover the primary particles of kaolinite crystals and the secondary particles of smectites.

TOPOLNICKI (1987) carried out biaxial tests with saturated Goldhausen clay, a remoulded kaolin clay (see Sec. 4.9 for details of the biaxial device). Kaolin powder was mixed with water under vacuum to a slurry with 82% water content. The slurry was sucked from the mixer with vacuum and pumped into the membrane bag of the biaxial device. This method led to almost homogeneous and fully saturated specimens. Initial consolidation of the slurry was executed by strain-controlled uniaxial compression of the specimen in either 1- or 2-direction with $\dot{\varepsilon}_1 = 0.5\%/h$. After reaching a specified pressure p_q up to 800 kPa this compression was stopped, and the decay of excess pore water pressure was awaited for ca. 0.5 h. Subsequently the specimen was subjected to isochoric shear deformation, i.e. with volumetric strain $\varepsilon_v = \varepsilon_1 + \varepsilon_2 = 0$. In so-called *active* tests the sign of $\dot{\varepsilon}_1$ was kept, in *passive* tests the sign of $\dot{\varepsilon}_1$ was changed after initial compression. During all tests the modulus of strain rate was maintained constant, $\dot{\varepsilon}_m = (\dot{\varepsilon}_1^2 + \dot{\varepsilon}_2^2)^{0.5} = 0.5\%/h$, in order to exclude viscous effects, and all tests were conducted under a back pressure of 200 kPa.
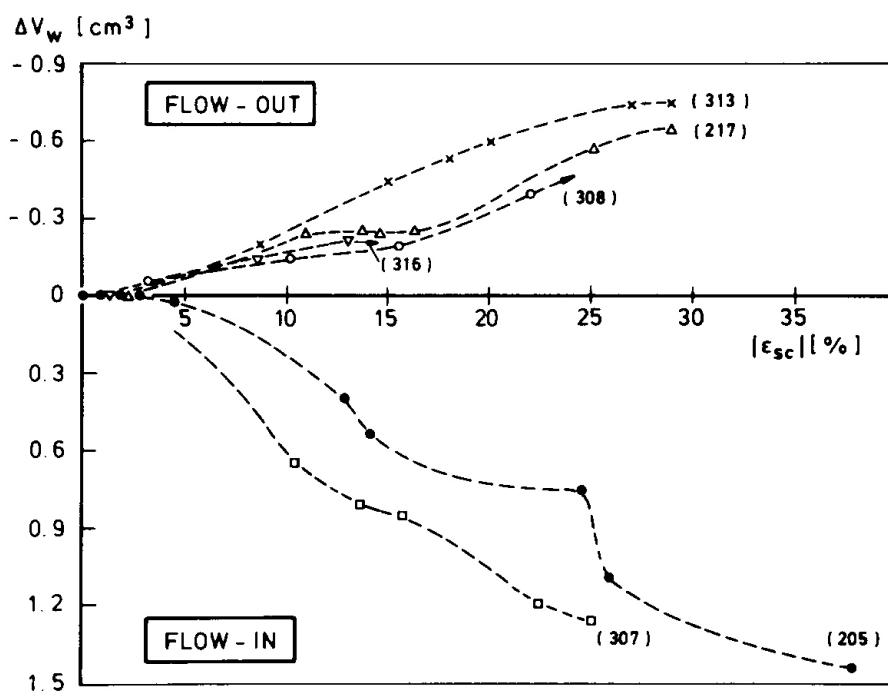
Figure 2.14: Changes of pore water volume with shear strain, observed during drained isochoric biaxial tests with Goldhausen clay (TOPOLNICKI 1987)

Full drainage was enabled during isochoric deformation. In case of active shear deformation an outflow of pore water up to 0.8 cm³, in case of passive shear deformation an inflow up to 1.4 cm³ was observed (Fig. 2.14), which comes up to about 1% of the total pore water volume. In active tests steady states were apparently reached at $\varepsilon_{sc} \approx 30\%$ deviator strain. Reproducibility was shown with four active and two passive tests. Topolnicki

was of opinion that Fig. 2.14 cannot be explained by inaccuracies of control operations, nor by elastic volume changes of water and soil particles. The results could neither be explained by errors of the displacement transducers, penetration of water through the rubber membrane nor elastic deformation of the horizontal upper plate. It was concluded that the results were due to changes of pore water density. This was explained with the density difference of adsorbed water at the particle surface as compared with bulk water, especially in structure and density, due to surface forces.

Zou (1996) ascribed the non-linear hydraulic permeability of fine-grained soils to dielectric properties of the pore liquid, with the latter representing the polarizability of the water molecules and the ion concentration of the pore liquid. Since the counter-ion concentration and the number density of polarized water molecules in the diffuse layer of a charged particle are higher towards the particle surface, the viscosity of the liquid in the diffuse layer is higher than the one in the bulk, and is spatially variable. The motion of water molecules due to shear forces being partly rotational, this additional rotation should lead to a decrease of the polarizability. With the permeability relation proposed by Zou (1996) linear and non-linear hydraulic conductivity can be described.

2.4.2   Interaction of charged particles and ions

When a charged particle is immersed in an electrolyte, the dissolved ions of the electrolyte interact with the electrical field generated by the surface charge of the particle. In this section the arrangement of the ions and the consequences for the electrical field are discussed. Macroscopic relative motion between the particle and the solution is excluded, but microscopic motion of the electrolyte's ions is allowed for. Processes are described in time averages as a snapshot.

Owing to the mobility of the ions, a charged particle is surrounded by counter-ions (i.e. ions of opposite sign) due to electrostatic attraction whilst the number of co-ions (i.e. ions of the same sign) is diminished by electrostatic repulsion. Viewn from a sufficient distance, the particle surface charge is then balanced by the counter-ions and the particle appears electrically neutral (Hunter 1993). This system with electrical charges on the particle surface and counter- and co-ions of the electrolyte is termed *electrical double layer*, introduced by Helmholtz (1853). He submitted a theory on the structure of the electrical double layer, assuming that the entire surface charge is compensated by a single layer of balancing counter-ions (Fig. 2.15a). Consequently, the thickness of the electrical double layer would have the size of the counter-ions.

Gouy (1910) and Chapman (1913) introduced (independently of each other) another ap-
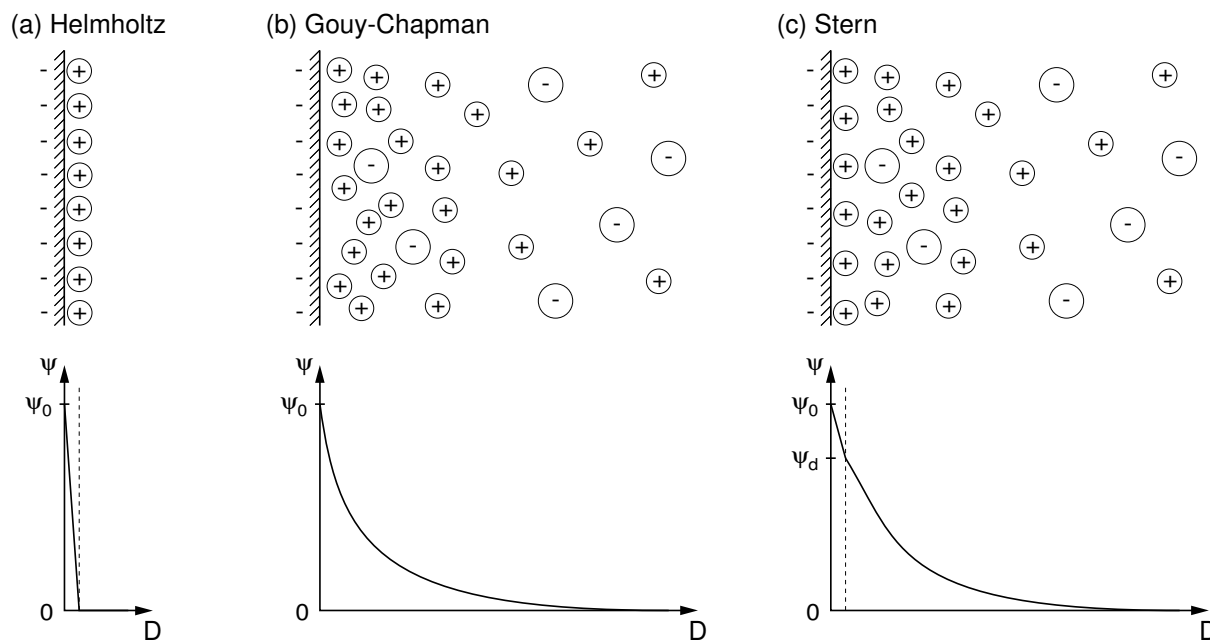
Figure 2.15: Models of the electrical double layer with electrical potential course in the order of historical development

proach. They considered the thermal agitation of the ions and postulated a cloud of ions surrounding the particle, the so-called *diffuse layer* (Fig. 2.15b). Again, the particle charge is fully compensated, but across a thicker electrical double layer. The Gouy-Chapman model predicts unrealistically high ion concentrations at the particle surface, which is due to the assumption of vanishing ion dimensions.

Stern (1924) combined the merits of the Helmholtz and Gouy-Chapman models by allowing for finite ion dimensions. He assumed a "plane of closest approach" where a portion of the counterions reside and attached to this a Gouy-Chapman type "diffuse layer."

Grahame (1947) introduced a further distinction of the boundary layer by separating two regions, called inner and outer Helmholtz layer. Both contain ions which are restricted in motion. Within the inner Helmholtz layer the ions are assumed to be non-hydrated, whereas the outer Helmholtz layer contains hydrated ions. Another opinion was published by HUNTER (1993), taking into account that cations tend to remain hydrated whereas many anions do not.

There are further models like the triple-layer theory, providing further refinement especially on the structure of the compacted layer. Since these theories are beyond the scope of the present treatise they are left aside.

Gouy and Chapman independently derived the potential distribution of a diffuse layer

under the assumption of a homogeneous charge distribution in an ambient liquid of homogeneous relative dielectricity constant ε_r and with substitution of the ions by point charges. Assuming a Boltzmann distribution for the charge, the concentration $n_{f,i}$ of the counter-ions in the diffused layer in relation to the counter-ion concentration of the bulk solution $n_{f,i0}$ can be obtained via (REED 1995)

$$\frac{n_{f,i}}{n_{f,i0}} = \exp\left(-\frac{E_i}{k_B\,T}\right) \tag{2.4}$$

with the potential energy of the counter-ion E_i, the Boltzmann constant k_B and the absolute temperature T. E_i depends on the valency z_i of the ion and on the electrical potential ψ at this position according to

$$E_i = z_i\,e\,\psi \tag{2.5}$$

with the elementary charge e. For surface potentials $\psi_0 \leq 100$ mV

$$\psi = \psi_0 \exp\left(-\frac{a}{\kappa^{-1}}\right) \tag{2.6}$$

holds with the Debye-length κ^{-1}, representing the distance of the particle surface to the plane with $\psi/\psi_0 = \exp(-1)$. The Debye-length κ^{-1} is also termed *double layer thickness* and can be calculated by

$$\kappa^{-1} = \sqrt{\frac{\varepsilon_0\,\varepsilon_r\,k_B\,T}{N_A\,e^2\,\sum n_{f,i0}\,z_i^2}} \tag{2.7}$$

with the dielectricity constant of vacuum ε_0, the relative dielectricity constant ε_r, the Boltzmann constant k_B, the absolute temperature T, the Avogadro number N_A, the elementary charge e and the ion concentration $n_{f,i0}$ of the ions i with valency z_i in the bulk. The order of magnitude of κ^{-1} therefore depends only on the properties of the bulk liquid (ε_0, ε_r, T, $n_{f,i0}$, z_i), but is independent of the particle properties (e.g. ψ_0).

With (2.6) and (2.7), the normalized potential ψ/ψ_0 for aqueous electrolytes at room temperature can be plotted versus the distance to the particle surface (Fig. 2.16). For a constant $n_{f,i0}$, the normalized potential decreases with increasing a. Asymptotes can be found with $\psi/\psi_0 = 1$ at $a = 0$ and $\psi/\psi_0 \to 0$ at $a \to \infty$.

The influence of $n_{f,i0}$ is exemplarily shown for a symmetrical 1:1 electrolyte, say NaCl, in Fig 2.16a. The higher $n_{f,i0}$, the more rapidly ψ/ψ_0 decreases. The corresponding Debye-length, graphically obtainable at $\psi/\psi_0 = \exp(-1) \approx 0.37$, decreases with increasing $n_{f,i0}$.
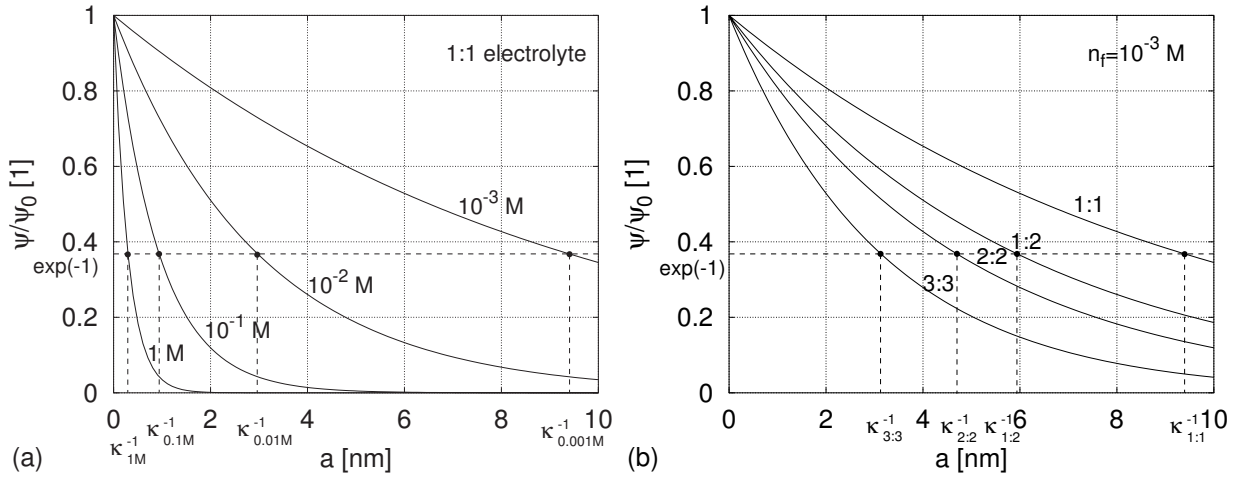
Figure 2.16: Normalized potential ψ/ψ_0 versus distance to the particle surface a for (a) 1:1 electrolytes of various ion concentrations n_f and (b) for different x:y electrolytes of ion concentration $n_{f,i0} = 10^{-3}$ M. Constants: $\varepsilon_0 = 8.854 \cdot 10^{-12}$ C^{2}J^{-1}m^{-1}, $\varepsilon_r = 78.5$, $k_B = 1.381 \cdot 10^{-23}$ JK^{-1}, $T = 293$ K, $N_A = 6.022 \cdot 10^{23}$ mol^{-1}, $e = 1.602 \cdot 10^{-19}$ C.

E.g., $n_{f,i0} = 0.001$ M (M = mole per liter) yields $\kappa^{-1} = 9.62$ nm, whereas $n_{f,i0} = 1$ M yields $\kappa^{-1} = 0.304$ nm. This decrease in Debye-length with increasing ion concentration is referred to as the so-called *double layer compression*.

The influence of the ion valency z_i is shown in Fig. 2.16b. For a constant ion concentration $n_{f,i0} = 10^{-3}$ M, increasing ion valency leads to a decrease of κ^{-1}. For an aqueous symmetrical 1:1 electrolyte, (2.7) yields $\kappa^{-1} = 9.62$ nm in contrast to a 3:3 electrolyte with $\kappa^{-1} = 3.20$ nm of the same bulk ion concentration.

It should be kept in mind that the term 'Debye-length' per definition only describes a length scale for a specified decay of ψ_0, but not the total extent of the double layer. Thus the term 'double layer thickness' is misleading. Strictly speaking the total extent of the double layer is infinite as outlined above. For practical applications the extent of the double layer may be regarded as the reach of the surface potential up to the particle distance where ψ/ψ_0 falls below an arbitrarily chosen threshold value, say $\psi/\psi_0 < 1\%$. Thus, (2.6) yields a reach of the double layer of ca. $5\kappa^{-1}$.

The distribution of the counter- and co-ion concentration across the double layer can be calculated with (2.4), (2.5) and (2.6), leading to

$$n_{f,i} = n_{f,i0} \exp\left[-\frac{z_i \, e \, \psi_0 \exp\left(-\dfrac{a}{\kappa^{-1}}\right)}{k_B T} \right] \tag{2.8}$$
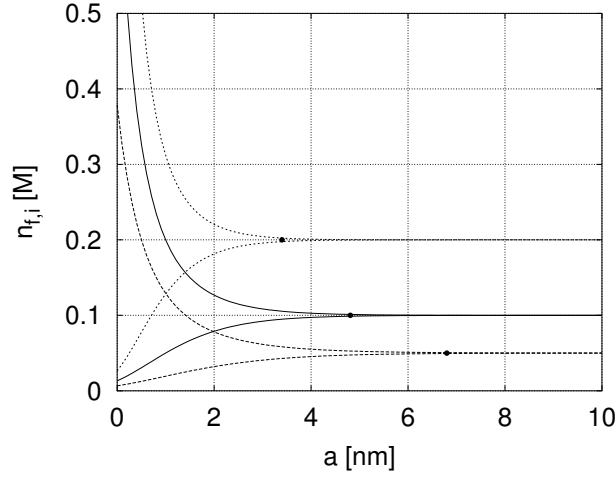
Figure 2.17: Concentration of counter- and co-ions n_i with respect to the distance from the particle surface a for 1:1 electrolytes of concentration $n_{i0} = 0.05$, 0.1 and 0.2 M in the bulk. Constants: $\varepsilon_0 = 8.854 \cdot 10^{-12}$ $C^2 J^{-1} m^{-1}$, $\varepsilon_r = 78.5$, $k_B = 1.381 \cdot 10^{-23}$ JK^{-1}, $N_A = 6.022 \cdot 10^{23}$ mol^{-1}, $e = 1.602 \cdot 10^{-19}$ C, $T = 293$ K, $\psi_0 = 50$ mV.

with κ^{-1} according to (2.7). In (2.8) the elementary charge e, the Boltzmann constant k_B, the dielectricity constant of vacuum ε_0, the relative dielectricity constant ε_r and the Avogadro number N_A are constants. For a given temperature T, (2.8) can be plotted with respect to the distance a to the particle surface, the surface potential ψ_0 and the ion concentration of the bulk solution $n_{f,i0}$ with valency z_i (Fig. 2.17). With increasing a the concentration of the counter-ions decreases, and the concentration of the co-ions increases asymptotically up to $n_{f,i0}$ in the bulk. For $a \to 0$ and z_i appropriately signed, (2.8) yields the finite counter- and co-ion concentration $n_{f,i} = n_{f,i0} \exp[-(z_i\,e\,\psi_0/k_B T)]$ at the particle surface. The higher the bulk ion concentration, the more pronounced is the gradient $\partial n_{f,i}/\partial a$ in the utmost proximity to the particle surface.

The above-mentioned practical reach of the double layer of ca. $5\kappa^{-1}$ is denoted with respect to $n_{f,i0}$ by filled dots in Fig. 2.17. The precision of this estimation Δ can be calculated via

$$\Delta = 1 - \frac{n_{f,i}}{n_{f,i0}} = 1 - \exp\left[-\left(\frac{z_i\,e\,\psi_0\,\exp(-5)}{k_B\,T}\right)\right] \tag{2.9}$$

with the results of (2.9) being graphically depicted in Fig. 2.18. An increase in ψ_0 leads to a loss in precision which is independent of $n_{f,i0}$. For 1:1 electrolytes and surface potentials $\psi_0 < 100$ mV the loss in precision is below 3%. For symmetrical electrolytes of higher valency and the same restriction of ψ_0, (2.9) yields $\Delta \approx 5\%$ for $|z_i| = 2$ and $\Delta < 8\%$ for $|z_i| = 3$. Hereby it is shown that the proposed estimation of the double layer extension is sufficient to get an idea about the range of action of the particle charges.
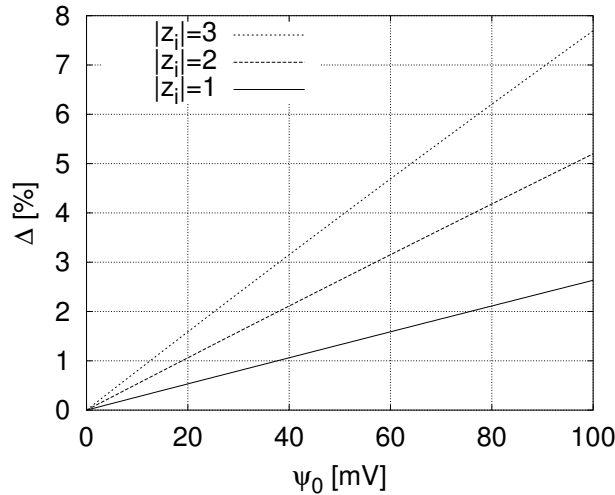
Figure 2.18: Deviation $\Delta = 1 - n_{f,i}/n_{f,i0}$ of the ion concentration $n_{f,i}$ at the distance to the particle surface $5\kappa^{-1}$ and the ion concentration of the bulk $n_{f,i0}$ with respect to the surface potential ψ_0 for the valencies $|z| = 1$, $|z| = 2$ and $|z| = 3$. Constants: $k_B = 1.381 \cdot 10^{-23}$ JK^{-1}, $T = 293$ K, $e = 1.602 \cdot 10^{-19}$ C.

2.4.3 The zeta-potential

Up to now the charged particle and the electrolyte solution have been regarded for thermodynamical equilibrium, i.e. in macroscopically motionless states. In this section, the formation of the electrical double layer is considered, and subsequently a relative motion between the charged particle and the electrolyte solution is induced.

By inducing motions of a charged particle relative to the electrolyte solution, part of the diffuse layer will move alongside the particle whilst another part of it will be *stripped*. Within this representation the formation and structure of the transition range is not considered, rather a shear zone of vanishing thickness within the diffuse layer is assumed. Since the stripped part of the diffuse layer does not contribute to the electrical neutrality anymore, the charged particle with the Stern layer and the convected part of the diffuse layer will exhibit an electrical potential relative to the bulk potential, termed *zeta-potential* ζ (REED 1995, Fig. 2.19).

Other than the surface potential ψ_0 and the Stern potential ψ_d, which both are not accessible by measurements, the zeta-potential is experimentally determinable (see below for methods). Since ζ correlates with ψ_0 and ψ_d in magnitude and sign, it is a welcome measure for the assessment of the particle's surface charge properties.

Unfortunately, the location of the slip plane is experimentally unaccessible and therefore remains unknown. Hence a back-calculation of ψ_0 or ψ_d, based on the measured ζ and with
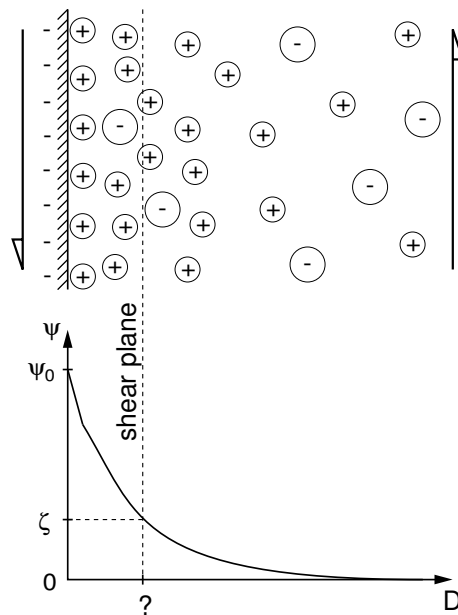
Figure 2.19: Definition of the ζ-potential (after REED 1995, modified)

(2.6), e.g., would require an appropriate estimation of the slip plane location. Although schemes for the analysis can be found in literature, the ignorance of the slip plane location is a major drawback in the usage of the zeta-potential in general. Other uncertainties in the derivation of the surface potential are viscous influences of the dragging velocity as well as the ion species and concentration on the zeta-potential. Nevertheless the measurement of the ζ-potential is a useful tool to gain information about the particle surface charge. Although ζ and ψ_0 are not precisely correlated, both are identical in the case of vanishing particle surface charges, i.e. at $\zeta = \psi_0 = \psi_d = 0$. This special case is used for the determination of the so-called isoelectric point (IEP), i.e. the value of pH for electrical neutrality of the particle surface (Sec. 2.3).

A typical dependence of the ζ-potential on pH is shown for goethite in Fig. 2.20. In general, the course shows positive ζ for low pH and negative ζ for higher pH. At $\zeta = 0$ the IEP is located. Regarding the influence of salts, it was shown in Sec. 2.4 that by the presence of salt ions the surface charge is screened and the double layer is compressed. Consequently, a higher ion concentration of the bulk water causes a weaker ζ-potential. The location of the IEP is not affected by the salt concentration since salts are non-potential-determing ions.

The measurement of the ζ-potential can be performed by utilizing the electrokinetic phenomenon. This generic term describes the behaviour of liquids and solids under relative motion along a boundary layer, viz. an inhomogeneous charge distribution within the media resulting in the raise of an electrical potential difference and vice versa (NEY 1973).
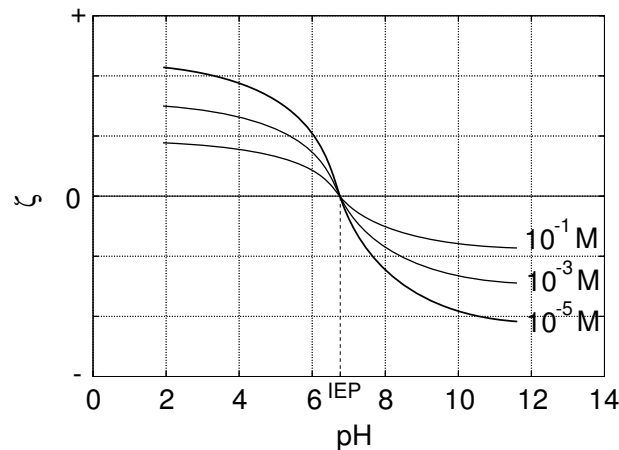
Figure 2.20: Typical ζ-potential course of goethite with respect to the ion concentration in the bulk water (after REED 1995, modified)

In other words, the electrokinetic phenomenon may appear in two types, (a) by motion in consequence of a potential difference and (b) by potential difference in consequence of a motion. These two types can be further subdivided into (a1) *electrophoresis* and (a2) *electroosmosis* as the relative movement of suspended charged particles in a suspension due to an electrical field, (b1) *sedimentation potential* as a result of suspended particles settling in the gravitational field and (b2) *streaming potential* as a result of a flowing liquid passing motionless solid surfaces. Though the results of ζ-potential measurements depend on the applied procedure and therefore may differ, this uncertainty is no major drawback for the present application since ψ_d and ζ are only correlated with the IEP and this is determined with sufficient precision in all procedures.

2.5 Particle-particle interactions in electrolytes

The interaction of a charged particle and an electrolyte solution was discussed above. Now attention is given to the interaction of two charged identical particles in an electrolyte solution. Forces arise by the approach of two particle surfaces. Their origin is the inter-molecular interaction of atoms of the bodies and the interstitial media. The most important interatomic forces can be classified by means of their range (HORN 1990):

- Van-der-Waals forces, long-ranged as compared to the atomic size,

- Coulomb forces, long-ranged as compared to the atomic size, and

- forces due to the exchange or non-exchange of electrons (covalent bonds), hydrogen bonds and Born repulsion, short-ranged as compared to the atomic size.

The long-ranged van-der-Waals and Coulomb forces will be taken into consideration in the subsequent outline, whereas the short-ranged forces are left aside.

2.5.1   Van-der-Waals forces

The van-der-Waals–force is ubiquitous and always attractive. It arises by interaction of atomic and molecular electrical dipoles and is based on three different mechanisms (Horn 1990, Atkins 1996):

- Keesom-Interaction:
  A permanent dipole is generating an electrical field which may orientate other permanent dipoles so that they are attracted by the former.

- Debye-Interaction:
  A permanent dipole is inducing another dipole in a polarizable atom or molecule. The induced dipole is aligned so that both dipoles are attracting each other.

- London-Interaction:
  Non-polar molecules have no permanent dipole moment. Nevertheless, fluctuations of the electron density distribution give rise to an ephemeral dipole moment, polarizing adjacent molecules and consequently inducing dipole moments. The current dipole moment of the former molecule is steadily changing its direction, but the induced dipole moments of the adjacent molecules are following these changes. Therefore the interaction is not eliminated for an averaged time, and a permanent attraction between the molecules arises.

For a pair of spherical particles of identical size the attractive interaction potential can be obtained via (Israelachvili 1991)

$$W_A = -\frac{AR}{12\,D} \tag{2.10}$$

with the Hamaker constant A, the radius of the particles R and the separation of the particle surfaces D. By first approximation A is independent from the electrolyte concentration of the dispersion and the separation of the particle surfaces (Lagaly 1997). The attractive interaction force F_A is the partial derivative of (2.10) with respect to D

$$F_A = \frac{\partial W_A}{\partial D} = \frac{AR}{12\,D^2} \quad , \tag{2.11}$$

meaning an increase of F_A with the inverse square of the particle separation D.

2.5.2   Coulomb forces

The repulsive interaction potential of a pair of like-charged spherical particles of identical size in an electrolyte is, according to the Derjaguin-proximity (ISRAELACHVILI 1991),

$$W_R = \frac{64\,\pi\,k_B\,T\,R\,\rho_\infty\,\gamma^2}{\kappa^2}\exp\left(-\kappa\,D\right) \tag{2.12}$$

with the Boltzmann constant k_B, the absolute temperature T, the particle radius R, the ion concentration of the bulk electrolyte ρ_∞, the Debye-length κ^{-1} and the separation of the particle surfaces D. Via the auxiliary variable $\gamma = \sinh(ze\psi_0/4k_BT)$ the particle surface charge is considered with respect to the surface potential ψ_0, the elementary charge e and the valency z. Note that κ^{-1} is also affected by the particle surface charge. Analogously, the repulsive force F_r is the partial derivative of the interaction potential (2.12) with respect to D

$$F_R = \frac{\partial W_R}{\partial D} = -\frac{64\,\pi\,k_B\,T\,R\,\rho_\infty\,\gamma^2}{\kappa}\exp\left(-\kappa\,D\right) \quad, \tag{2.13}$$

meaning that F_R increases with the inverse exponent of D.

2.5.3   The DLVO-theory

Starting from the situation that both particles are separated sufficiently so that their double layers are entirely developed and don't interfere, particles with surrounding ion clouds in a collective can be regarded as electrically neutral (Sec. 2.4). Consequently, the Coulombic repulsion between the particles vanishes. Simultaneously, the remaining ubiquitous van-der-Waals attraction acts between the particles, causing them to move closer together. Decreasing particle separation leads to interferences of both double layers, giving rise to a counteracting Coulombic repulsion. Decrease in particle separation continues until equilibrium of attractive and repulsive forces is achieved.

A mathematical formulation of this force equilibrium was published by Derjaguin and Landau (1941) and by Verwey and Overbeek (1948), independently (REED 1995). In this so-called DLVO-theory, termed after the first characters of the publishers surnames, the interparticle interaction potential $W(D)$ with respect to the particle separation D was derived by the addition of the attractive van-der-Waals interaction potential $W_A(D)$ and the repulsive Coulombic interaction potential $W_R(D)$ according to (2.12) and (2.10),

reading

$$
\begin{aligned}
W(D) &= W_A(D) + W_R(D) \\
&= -\frac{A}{6\,D}\frac{R_1\,R_2}{R_1 + R_2} + \frac{64\,\pi\,k_B\,T\,R\,\rho_\infty\,\gamma^2}{\kappa^2}\exp\left(-\kappa\,D\right) .
\end{aligned}
\tag{2.14}
$$

The interparticle force interaction $F(D)$ is then obtained by differentiation of (2.14) with respect to D, yielding

$$
\begin{aligned}
F(D) &= \frac{\mathrm{d}W(D)}{\mathrm{d}D} \\
&= \frac{A}{6\,D^2}\frac{R_1\,R_2}{R_1 + R_2} - \frac{64\,\pi\,k_B\,T\,R\,\rho_\infty\,\gamma^2}{\kappa}\exp\left(-\kappa\,D\right) .
\end{aligned}
\tag{2.15}
$$

The plots of (2.14) and (2.15) in Fig. 2.21 for different ψ_0 and constants given in the caption show some peculiarities. For $\psi_0 = 0$ mV (Fig.2.21a), i.e. for uncharged particle surfaces, the total interaction potential decreases monotonically with decreasing particle separation. Since the repulsive potential vanishes, the total and the attractive potential are identical. Therefore the total interaction force increases monotonically with decreasing particle separation. Practically spoken, if two uncharged particles are immersed in a liquid, they get attractive, approach and consequently are even more attractive. This process cascades up to the point the particles are getting into contact, i.e. at vanishing particle separation. Then a permanent finite attraction force is established.

For $\psi_0 = 30$ mV (Fig. 2.21b), i.e. for weak particle surface charges, a significant repulsive potential is present, increasing with decreasing particle separation. Nevertheless the attractive potential, present as in the previous case, stays predominant. Therefore the total interaction potential again decreases monotonically with decreasing particle separation. Hence, the total interaction force it attractive over the entire particle distance range with the consequences outlined above.

For $\psi_0 = 50$ mV (Fig. 2.21c), i.e. for higher charged particle surfaces, the system behaviour changes remarkably. The addition of the attractive and repulsive potential energy results in a no longer monotonic course of the total interaction potential. An energy barrier and a local energy minimum is obtained. Consequently, starting at a large particle separation the total interaction force is increasingly attractive with decreasing particle separation. Then, the interaction force decreases down to the zero-crossing ($D \approx 6$ nm in Fig. 2.21c2), becomes increasingly repulsive (2 nm $< D <$ 6 nm), subsequently decreasingly repulsive (1.5 nm $< D <$ 2 nm), and after a second zero-crossing increasingly attractive with decreasing particle separation.
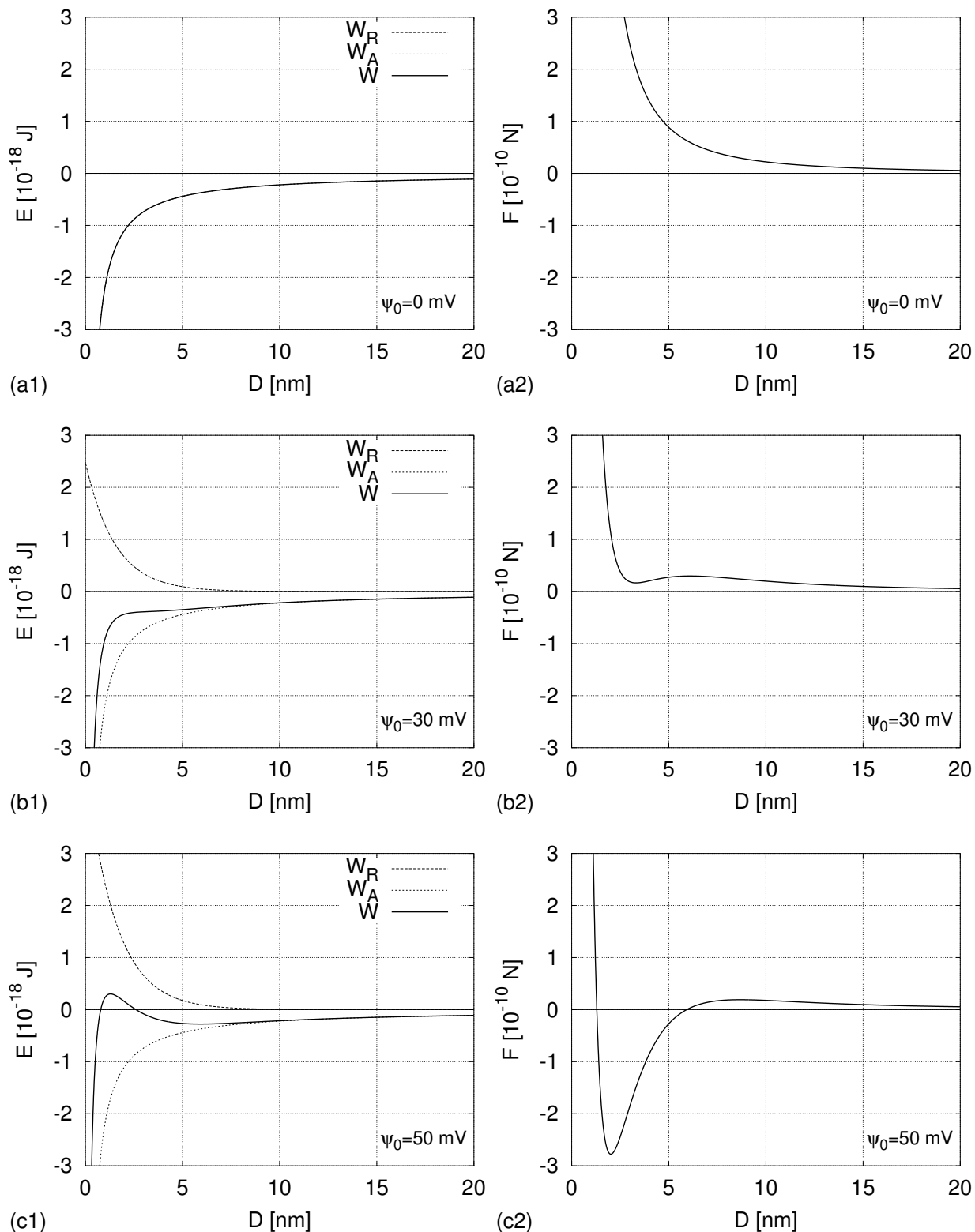
Figure 2.21: Particle interaction potential $W(D)$ and force interaction $F(D)$ according to (2.14) and (2.15) versus particle surface separation D for surface potentials (a) $\psi_0 = 0$ mV, (b) $\psi_0 = 30$ mV and (c) $\psi_0 = 50$ mV. Constants: $R = 0.5 \cdot 10^{-6}$ m, $n_f = 4 \cdot 10^{-2}$ M, $\rho_\infty = 2.409 \cdot 10^{25}$ m^{-3}, $z = 1$, $e = 1.602 \cdot 10^{-19}$ C, $\varepsilon_0 = 8.854 \cdot 10^{-12}$ C^{2}J^{-1}m^{-1}, $\varepsilon_r = 78.5$, $k_B = 1.381 \cdot 10^{-23}$ JK^{-1}, $T = 298$ K, $N_A = 6.022 \cdot 10^{23}$ mol^{-1} and $A = 5.3 \cdot 10^{-20}$ J.

For initially highly separated and thus free particles, the attractive interaction force initially causes the particles to move together up to the particle separation of $D \approx 6$ nm, where the interaction force vanishes. Since the interaction force becomes repulsive for a further decrease of particle separation, ongoing compression then requires the supply of work. At the point the external work exceeds the energy barrier (Fig. 2.21c1), the interaction force becomes progressively attractive again, leading to the above described cascading process of particle approach up to particle contact.

The energy barrier can be overcome e.g. by applying a compression force or by thermal vibration of the particles. The latter is Boltzmann-distributed, stating that some of the particles show a high agitation while others show an agitation according to the mean thermal energy.

This particular case of interacting repulsive and attractive potential is the more pronounced, the higher ψ_0 and A and the lower ε_0 and T.

So far, the variation of ψ_0 was discussed. Now the influence of n_f is considered, which also has an effect on the total interaction potential and therefore on the interaction force. As stated earlier, dissolved salt has no effect on the attractive potential but on the repulsive potential according to (2.12). Herein, R_∞, γ and κ^{-1} are affected by the salt concentration. In consequence, (2.14) is modified, although by a more complicated relation than via ψ_0.

Fig. 2.22 illustrates the influence of a 1:1 electrolyte on the interaction potential and
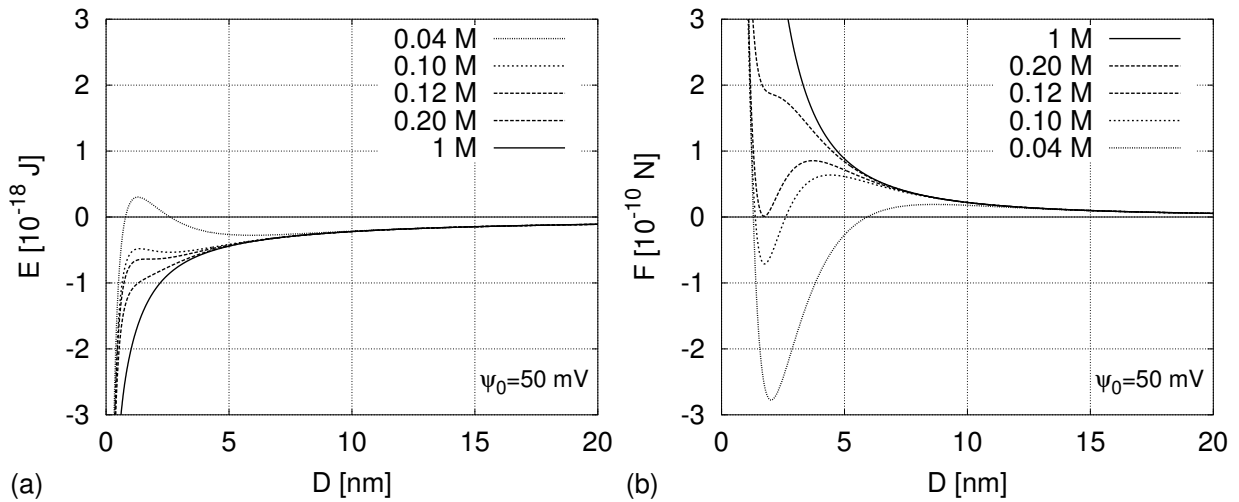
Figure 2.22: Particle interaction potential $W(D)$ and force interaction $F(D)$ according to (2.14) and (2.15) versus particle surface separation D with respect to the ion concentration $n_{f,i0}$. Constants: $R = 0.5 \cdot 10^{-6}$ m, $\psi_0 = 50$ mV, $\rho_\infty = 2.409 \cdot 10^{25}$ m^{-3}, $z = 1$, $e = 1.602 \cdot 10^{-19}$ C, $\varepsilon_0 = 8.854 \cdot 10^{-12}$ C^{2}J^{-1}m^{-1}, $\varepsilon_r = 78.5$, $k_B = 1.381 \cdot 10^{-23}$ JK^{-1}, $T = 298$ K, $N_A = 6.022 \cdot 10^{23}$ mol^{-1} and $A = 5.3 \cdot 10^{-20}$ J.

interaction force for a constant $\psi_0 = 50$ mV. For low n_f, the system behaviour is qualitatively the same like presented in Fig. 2.21c. For $n_f = 0.12$ M a transition from repulsive DLVO-behaviour to pure attraction occurs – the critical coagulation concentration (ccc) is reached. By further n_f-increase the particle interaction is increasingly attractive. In general, an increase of n_f shows the same effects like a decrease of ψ_0, although this observation is based on different mechanisms as outlined.

Chapter 3

Materials selected for experimental investigations

An experimental program was performed with well-defined synthetic model materials in order to provide reproducible testing conditions. Aluminium oxide powder was used as representative for silts, laponite powder was used as representative for clays. In this chapter these materials are introduced and their properties are presented.

3.1 Aluminium oxide

Aluminium oxide powder (corundum, α-Al$_2$O$_3$), labelled Alumina CT 3000 SG SQR, was obtained from Alcoa Chemie GmbH, Ludwigshafen, Germany. The material was delivered in paper bags of 25 kg each and transferred immediately after arrival to sealed PE buckets in order to avoid moisturization during storage. Having approximately 550 kg of aluminium oxide powder in stock initially, this amount was sufficient for the entire experimental program, ensuring the tests to be performed with the same production charge.

The aluminium oxide powder is synthetically produced from bauxite by the *Bayer process.* Herein, the aluminium compounds are dissolved in soda lye at elevated temperatures and pressures, whereas impurities remain undissolved and can be separated by filtration. By subsequent seeding and cooling of the solution, aluminium hydroxide is precipitated and transformed into the oxide by calcination (BAUMGART *et al.* 1984). Finally, the aluminium oxide is <u>s</u>uper <u>g</u>rounded (denomination "SG" in the product name) and classed.

3.1.1 Physical and chemical properties

Typical product properties of aluminium oxide were provided by the manufacturer (AL-COA 1998). According to the data sheet, grain size ranges from 0.2 to 2 μm without giving any comments on the method of testing and the test conditions. For the representation of the particle size range and distribution (Fig. 3.1), the conventional diagram used in the field of Soil Mechanics was extended towards a finer range, since the area of interest exceeds the conventional range. Usually this extended range is not covered by standard methods for the determination of particle size distribution, e.g. sedimentation or sieving, and is therefore not employed. With the grain diameters $d_{60} = 0.8$ μm and $d_{10} = 0.4$ μm at 60% and 10% mass portion obtained by Fig. 3.1, the material would be characterized by the grain size distribution curve and the coefficient of uniformity $U = d_{60}/d_{10} \approx 2$ as uniformly graded silty clay.
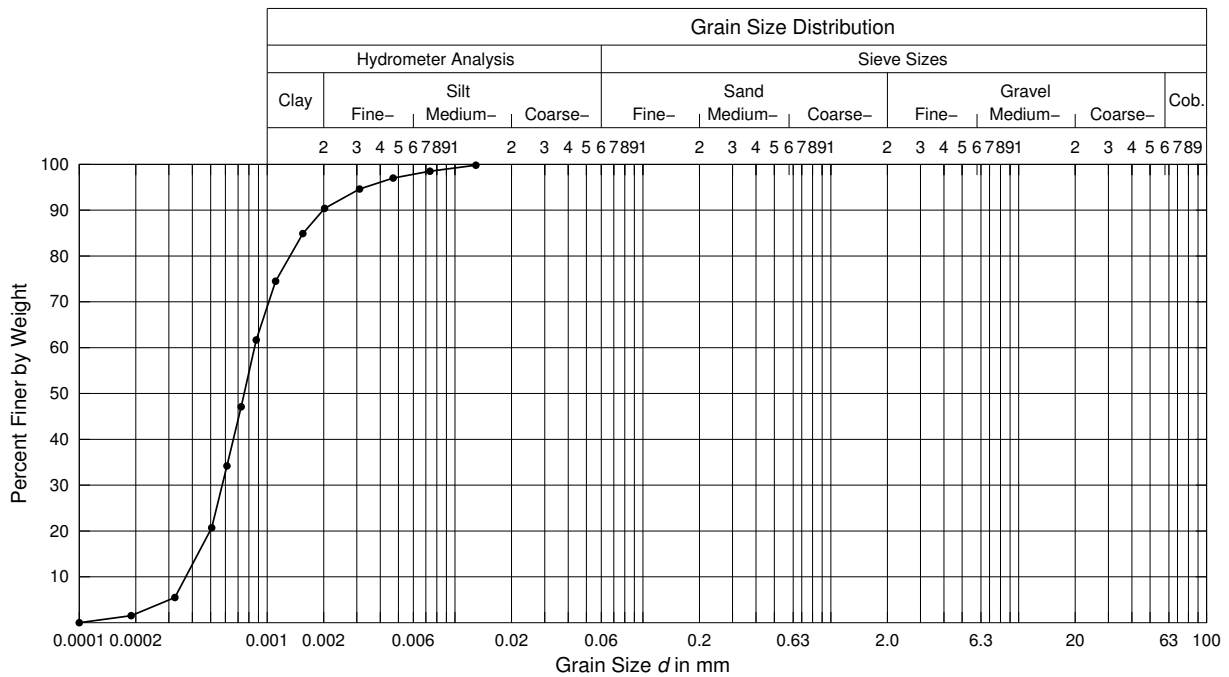
Figure 3.1: Grain size distribution of aluminium oxide CT 3000 SG as provided by the manufacturers data sheet (ALCOA 1998).

In Fig. 3.2 a scanning electron micrograph of a dry secondary (i.e. agglomerated) aluminium oxide CT 3000 SG particle is presented in shipped state. According to the scale, it consists of primary particles (i.e. grains) with grain diameters well below 0.1 μm and up to above 1 μm. Based on a comparison of Figs. 3.1 and 3.2 it is assumed that the given grain size distribution curve is representing the material in dispersed state (i.e. primary particles). The shape of the primary particles can be characterized as angular and com-
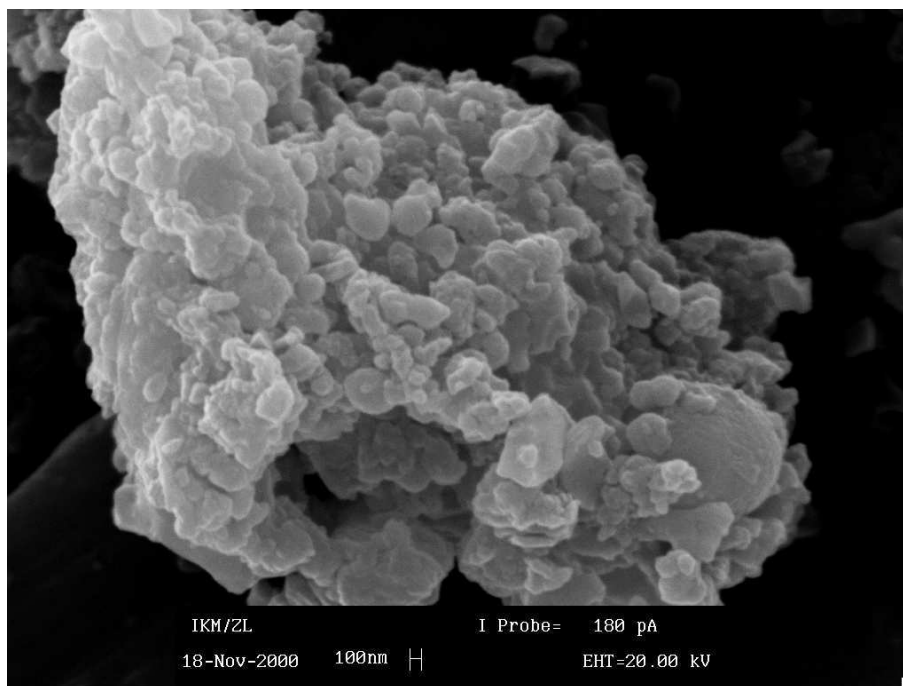
Figure 3.2: Scanning electron micrograph (SEM) of a dry secondary aluminium oxide CT 3000 SG particle in shipped state (Reinshagen 2000).

pact, which is attributed to the mineral's crystal structure (Sec. 2.1.2) and the grinding during the manufacture process.

The specific gravity of aluminium oxide counts $\gamma_s = 39.3$ kNm^{-3} (Alcoa 1998). Compared with the one of typical silts ($\gamma_s = 26.5$ kNm^{-3}) the grain density of aluminium oxide is thus about 50% higher. The specific surface area $S_m = 7.0$ m^{2}g^{-1} (Alcoa 1998, Sec. 2.2.3) is comparatively high, which can be illustrated by approx. 30 g of aluminium oxide equaling the area of a tennis court.

From the chemical composition as given in Tab. 3.1, aluminium oxide CT 3000 SG con-

Table 3.1: Chemical composition of aluminium oxide CT3000SG (Alcoa 1998).

Al_2O_3	≥ 99.5 m%
Na_2O	≤ 0.10 m%
Fe_2O_3	≤ 0.03 m%
SiO_2	≤ 0.07 m%
CaO	≤ 0.03 m%
MgO	≤ 0.09 m%

tains traces of impurities in the range of <0.5 m%. The presence of magnesium oxide is noteworthy; it is necessary as crystal growth inhibitor during the manufacturing process of high-purity aluminium oxide powders with an Al_2O_3-content above 99% (BAUMGART *et al.* 1984). This magnesium oxide is partially dissolved when the particles are immersed into water and raises the ion concentration of the water remarkably. Another peculiarity of aluminium oxide, which is generally seen as chemically inert, is the solubility of small amounts of aluminium oxide in water (Sec. 2.3.1). The dissolved aluminium oxide can be precipitated at grain contacts, which then leads to a true cementation of the grain skeleton. This effect may influence the results of long-term experiments, especially in low acid and high basic pH-regimes (RICHTER 2006). Since the experiments in the present treatise were performed in a comparatively short period of time, these cementation effects can be neglected.

3.1.2   Zeta-potential

The dependence of the ζ-potential of aluminium oxide on pH results from electrophoresis measurements with the Zetasizer 3000HS (Malvern Instruments).
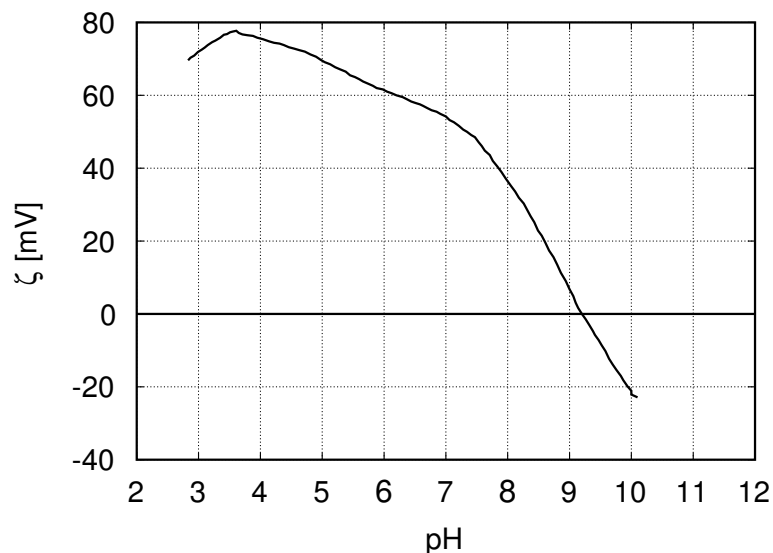
Figure 3.3: ζ-potential of aluminium oxide CT3000SG with respect to pH (REINSHAGEN 2000, modified).

According to Fig. 3.3, electrical neutrality of the particle surface is reached at pH9.2 (IEP). For pH towards the acid regime, the particle surface becomes increasingly positive charged with a maximum surface charge in the range of pH4. Shifting pH towards the basic regime leads to an increasingly negative particle surface charge.

3.1.3 Phase diagram

Due to the pH-dependent surface charge (Sec. 2.3.1), the resulting ζ-potential with its dependence on the present ions (Sec. 2.4.3 and 3.1.2) and the interaction of van-der-Waals–attraction and osmotic repulsion according to the DLVO-theory (Sec. 2.5.3), a phase diagram of aluminium oxide in water with respect to pH and ion concentration can be obtained either theoretically or experimentally (Fig. 3.4).
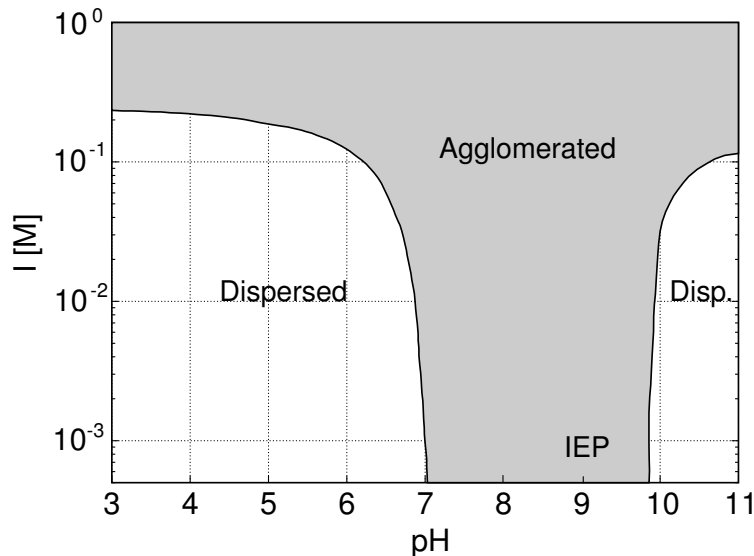
Figure 3.4: Phase diagram of aluminium oxide CT3000SG with respect to pH and the ion concentration (GRAULE *et al.* 1994, modified).

In this phase diagram two regions of agglomerated and dispersed states can be distinguished. In agglomerated states, pure interparticle attraction yields a pasty-like peloid (cf. Fig. 2.21a and b), whereas in dispersed states DLVO-interaction yields a fluid-like peloid (cf. Fig. 2.21c). The experimental investigation of aluminium oxide peloids (Sec. 5) was performed for an agglomerated state at pH9 and for a dispersed state at pH4. In the latter case the ionic concentration has to be taken into account, whereas in the former case the state is independent of pH.

3.2 Laponite

Laponite, labelled Laponite RD, was obtained from Solvay Soda Deutschland GmbH, Rheinberg, Germany. The material was delivered in polyethylene lined cardboard boxes because of its hygroscopic properties. 50 kg of dry laponite powder was kept in stock, sufficient for the performance of all tests with the same production charge.

3.2.1   Physical and chemical properties

Laponite is a synthetic trioctahedral 2:1 layer silicate and therefore comparable with the natural and swellable mineral montmorillonite (Sec. 2.1.3). Laponite consists of disk-like particles of 25 nm in diameter and 0.92 nm in height as first approximation (LAPORTE 2000, LAGALY 1997) and is therefore by decades smaller in diameter as compared to montmorillonite.
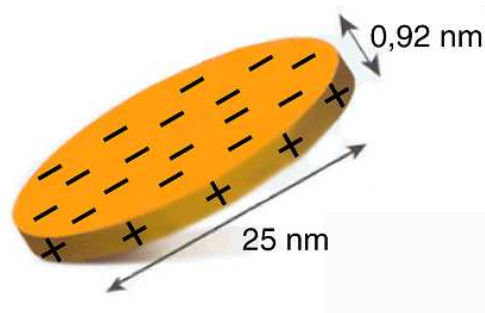
Figure 3.5: Sketch of a laponite particle (taken from a product data sheet of ROCKWOOD ADDITIVES LTD.)

Since individual laponite particles are hardly to detect, a specification of the particle size distribution is almost impossible. The specific gravity of laponite counts $\gamma_s = 26.5$ kNm^{-3} (LEVITZ *et al.* 2000), which is in the typical range of natural clay particles. Laponite shows a specific surface area of $S_m = 370$ m^{2}g^{-1} BET and a calculative $S_m = 900$ m^{2}g^{-1} (LAPORTE 2000, Sec. 2.2).

Table 3.2: Chemical composition of Laponite RD (LEVITZ *et al.* 2000).

SiO$_2$	65.82 m%
MgO	30.15 m%
Na$_2$O	3.20 m%
LiO$_2$	0.83 m%

The chemical composition of laponite is reflected by the empirical formula

$$[\mathrm{Si}_8\,(\mathrm{Mg}_{5.45}\mathrm{Li}_{0.4})\,\mathrm{H}_4\mathrm{O}_{24}]^{-0.75}\,\mathrm{Na}^{+0.75}$$
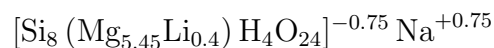
(LEVITZ *et al.* 2000). Herein, the part in square brackets represents the laponite mineral and the sodium the corresponding counter-ion. This empirical structure formula is also supported by chemical analysis (Tab. 3.2).

The chemical stability of laponite particles immersed into water depends on pH. For pH<10 minor amounts of silicates, Na^+, Li^+ and Mg^{2+} ions are dissolved according to the chemical formula

$$Si_8Mg_{5.45}Li_{0.4}H_4O_{2.4}Na_{0.7}+12H^++8H_2O \Rightarrow 0.7Na^++8Si(OH)_4+5.45Mg^{2+}+0.4Li^+$$
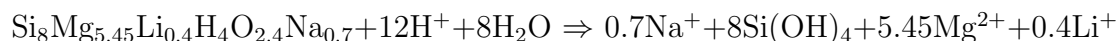
(MOURCHID & LEVITZ 1998). By this long-term process, the ionic strength of the water is gradually raised, particularly due to the solution of bivalent magnesium ions. This may effect the stability of laponite peloids in general, but will not become relevant for the present treatise (cf. Sec. 3.2.3).

3.2.2 Zeta-potential

The dependence of the ζ-potential of laponite with respect to pH was determined by electrophoresis measurements with the Zetasizer 3000HS (Malvern Instruments).
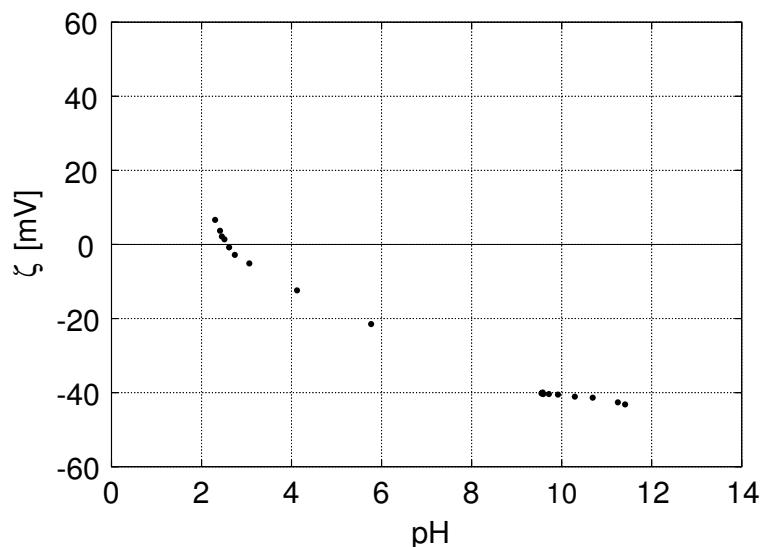
Figure 3.6: ζ-potential of laponite with respect to pH (BUGGISCH 2003)

Regarding the test results shown in Fig. 3.6, a vanishing ζ-potential is obtained for pH2.5. Below this pH the ζ-potential becomes increasingly positive; above the ζ-potential becomes increasingly negative.

Electrophoresis measurements provide the presented dependence of the ζ-potential on pH as an integral result. Therefore Fig. 3.6 represents the ζ-potential of the entire particle but neither the ζ-potential of the particle face nor of the edge. At pH10, the faces are negatively and the edges are positively charged.

3.2.3 Phase diagram

The interaction of charged laponite particles immersed into water depends on the solid mass concentration and the ionic strength of the water and can be illustrated by an experimentally derived phase diagram (MOURCHID *et al.* 1998, Fig. 3.7), with four different phases to be distinguished:
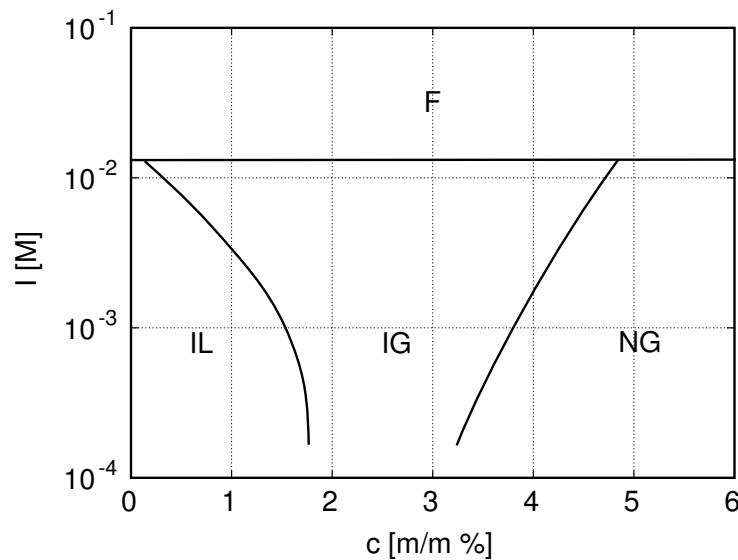
Figure 3.7: Phase diagram of Laponite with respect to mass concentration and ion strength (MOURCHID *et al.* 1998, modified)

F Flocculated phase: For ion strengths above ca. 0.17 M laponite particles flocculate (house-of-card-structure) and settle, i.e. a separation of water and peloid can be observed. For a given solid mass concentration the height of the sediment decreases with increasing ionic strength. This phase is not transparent.

IL Isotropic liquid phase: Aggregates, consisting of several particles, are suspended in water. The size and density of these aggregates depends on the ionic strength via the Debye-length. Regularly the size of the aggregates is too small for the scattering of visible light, therefore the liquid appears transparent. The viscosity of the liquid depends on the ionic strength and solid mass concentration.

IG Isotropic gel phase: The gel shows a randomized particle orientation which depends on the ionic strength. At low ionic strength the gel is transparent. With increasing ionic strength chain aggregates are bundled, showing aggregate sizes in the range of some μm and turning the gel opaque, consequently.

NG Nematic gel phase: The particles of the gel are evenly orientated, similar to the orientation in liquid crystals.

Phase transitions from isotropic liquid to isotropic gel and isotropic gel to nematic gel proceed without macroscopic phase separation. In contrast to these cases, phase transition from isotropic liquid, isotropic gel and nematic gel to the flocculate phase lead to macroscopic phase separation, i.e. the formation of separate sediment and water layers.

In conjunction with the above mentioned chemical stability of laponite particles, the long-term process of ion solution (especially of the bivalent Mg^{2+}) can lead to a phase transition towards the isotropic gel or the flocculated phase. Furthermore, mixing of laponite powder and distilled water will introduce Na^+ counter-ions into the mixture. LEVITZ *et al.* (2000) examined the ionic strength of these mixtures and specified $I \approx 2 \cdot 10^{-4}$ M as a lower threshold. Nevertheless, with the chosen ion concentrations and the limited test durations, the effects of the long-term ion solution could be neglected in the present treatise.

Chapter 4

Sample preparation and testing devices

For the experimental investigation of the mechanical properties of peloids reproducible sample preparation techniques were required, which are introduced in Sec. 4.1. The effectiveness of the sample preparation techniques and the fabric genesis of the peloids were investigated in sedimentation tests. Their procedure is described in Sec. 4.2.

Regarding the oedometric compression behaviour, a standard device was applied (Sec. 4.3). The isotropic compression behaviour was investigated with a newly designed shrinkage device (Sec. 4.4). Standard cone penetration tests were performed for a fast determination of the undrained shear strength (Sec. 4.5). For the investigation of the undrained shear strength with respect to the deformation and deformation rate, vane shear tests were executed with a customized rotational viscosimeter (Sec. 4.6). The drained shear strength was investigated in a standard direct shear apparatus, and also with a new thin-layer technique (Sec. 4.7). A newly designed coupled tumble-shrink apparatus (Sec. 4.9) was targeting at the densest state of the specimen. With a re-assembled biaxial device (Sec. 4.9) existing results regarding the changes of the pore water density were verified and further tests were performed.

4.1   Sample preparation

Each specimen was prepared by pouring dry mineral powder into demineralized water under severe mixing. Subsequently, acids/bases and salts were added for the preset of a desired pH and ionic concentration whilst mixing was continued. All preparations were executed at room temperature.
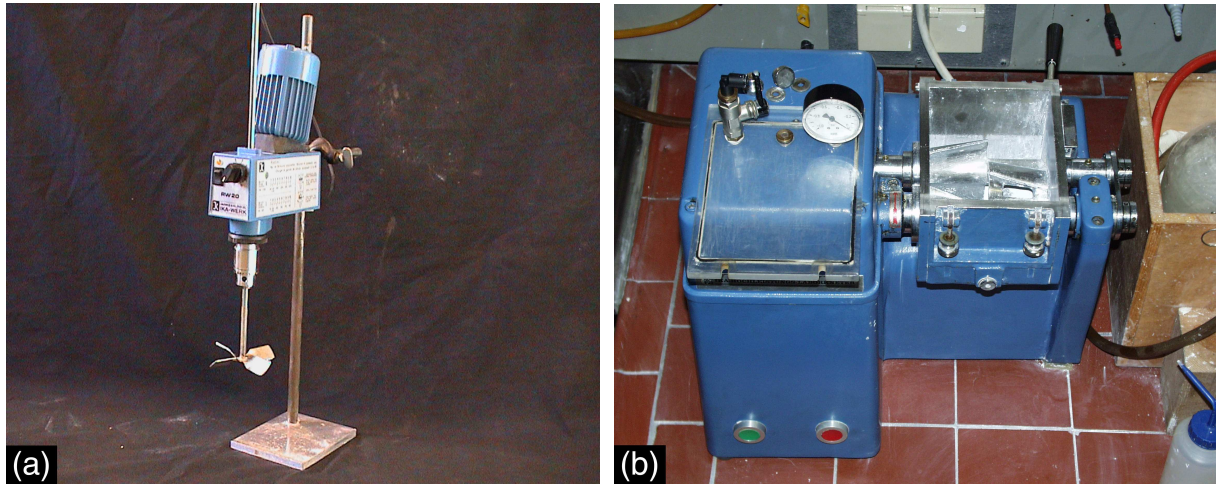
Figure 4.1: Propeller mixer (a) and lab kneader (b) for the preparation of the specimen

Two methods of mixing, either with a propeller mixer or a lab kneader, were employed (Fig. 4.1). With the propeller mixing method, the specimen was stirred under atmospheric pressure by a four-leaved stainless steel propeller with a comparatively high revolution speed of $n \approx 250 \text{ min}^{-1}$, whereas with the lab kneader method the specimen was kneaded under vacuum (≈ -0.85 bar referred to atmospheric pressure) by stainless steel blades with a rather low revolution speed of $n \approx 50 \text{ min}^{-1}$.

The actual pH was measured either by pH-paper or by a pH-meter with a KCl electrode. The desired pH was adjusted via the successive adding of either 2M HCl acid or 1M NaOH base, and was repeatedly controlled during the entire preparation process. The duration of mixing was determined by attaining a constant pH and therefore ranged between several hours and some days.

4.2   Sedimentation test setup

Sedimentation tests were performed in order to study the pH-dependent particle interaction in suspension, the subsequent sediment genesis, and the effectiveness of the applied mixing methods.

The sedimentation tests were executed according to German Standard DIN 18123–6. The suspensions were prepared by mixing demineralized water and successive adding of mineral powder up to the desired solid volume fraction. Mixing method and pH control were identical with the ones described in Sec. 4.1. Additionally, the standard mixing method by shaking as described in the German Standard was also applied. In contrast to the German Standard, no anti-coagulants were added. After finishing the preparation of

suspensions with 1000 ml in volume, they were poured into perspex cylinders of approx. 1100 ml capacity each.

During the test, the specific gravity of the suspension was measured by a hydrometer with respect to the elapsed sedimentation time and the temperature of the suspension. Back-analyses, based on Stokes' law with allowance for the temperature-depending viscosity of water, yielded lump size distribution curves of the mineral powder. After the standard 24h-duration of the sedimentation tests, the observation of the settlement behaviour was continued. Finally, the porosity of the sediment was derived via the sediment volume and the particle mass.

4.3 Oedometric compression apparatus

The uniaxial compressibility of peloids was investigated with an oedometer device. Herein, a cylindrical specimen was axially loaded, while radial spreading was prevented and axial drainage was allowed for. During the test, the axial load was altered stepwise and the corresponding variation in axial length was recorded with respect to the time.

This type of test is typically performed to determine the oedometric stress-strain, con-solidation and creep behaviour of soils. It is of practical relevance for the settlement prediction of widespread loadings on comparatively thin soil layers and for the parameter determination for numerical calculations.

4.3.1 Mechanical design

The main item of the device was the oedometer cell (Fig.4.2). It contained the cylindrical specimen (A) with typically dimensions of 20 mm in initial height and either 76 mm or 100 mm in diameter. The specimen was axially enclosed between filter papers and filter plates (B) and was radially prevented from spreading by a ring of comparatively high stiffness (C). For the sake of dewatering, the base (D) and the head plate (E) were provided with channels. With the perspex ring (F) applied, the whole assembly could be flooded to prevent saturated specimens from evaporation. Besides the perspex ring, all parts in contact with the specimen or the pore water were made of stainless steel.

Since it was intended to perform some tests with specimens of initially liquid state, the device had to meet some additional requirements. A guided head plate system was chosen for the smooth lowering of the head plate and the continuous recording of its vertical
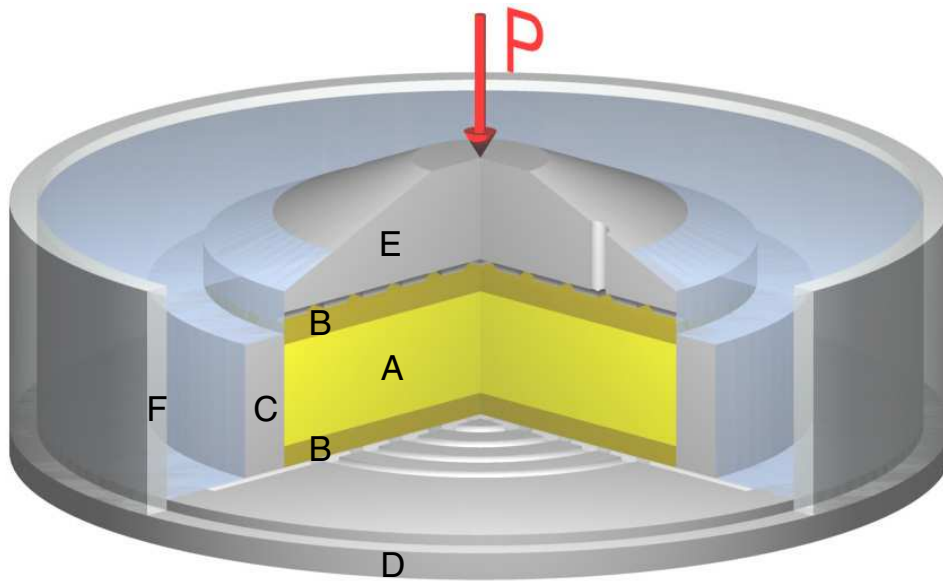
Figure 4.2: Oedometer beaker with specimen (A), filter plates (B), steel ring (C), base
(D) and head (E) plate, perspex ring (F)

position during the preparation and testing procedure. Moreover, during the test a twist
of the head plate could be excluded.

The prevention of the liquid specimen from passing through gaps came up as a challenge.
Regarding the gap between the steel ring and the base plate, both were replaced by a
beaker. According to the consolidation theory this results in a 4-times higher consolidation
time. Regarding the gap between the ring and the top plate, radial swelling of the filter
paper due to wetting was considered for the specification of the filter paper's diameter in
dry state. In conjunction with accurate cutting this technique led to a sealing of the gap
without generating stick-slip-resistance between the ring and the top plate. With these
improvements, about half of all tests could be finished successfully.

After preparation, the entire oedometer beaker was inserted into a cantilever loading
frame with a ratio of 1:10. With respect to the force limits of the loading frame and
the geometry of the oedometer beaker, vertical pressures up to about 1500 kPa could be
imposed.

The vertical position of the top plate was measured in relation to the base plate by an
electronic dial gauge (Mitutoyo Digimatic ID-C, Range 30 mm). The readings of the dial
gauge were continuously recorded by a data acquisition routine running on a personal
computer under MS-DOS. Vertical loading by dead weights was recorded manually. In
beforehand, calibration tests of the vertical force transition were performed with a load
cell replacing the oedometer cell.

4.3.2 Testing procedure

After mounting the apparatus, reference measurement of the top plate's vertical position was taken with an aluminium block of 20 mm in height inserted into the beaker. Then, the beaker was removed from the loading frame and filled up to the level of the lower filter plate surface with water of the same pH and salt concentration like the one of the prepared specimen. Subsequently, the specimen was poured or pasted, whilst the water level was correspondingly raised ahead of the specimen's level. With this method, the beaker was filled up to ca. 1 mm below the horizontal rim.

The filled beaker then was set into the loading frame, and the upper filter paper was centred in the steel ring. After lowering the head plate almost down to the level of the specimen, the beaker was flooded with water. For initial contact the top plate was loaded with a 100 g piece of weight. Data acquisition was subsequently started, and the compression test was executed.

After the test was finished, the specimen was removed and the water content of the specimen was determined. Subsequent analysis included the back-calculation of the corresponding void ratios via the final void ratio, the vertical position of the top plate and under assumption of full saturation. By this method, an unnoticed expulsion of the initially liquid specimen at low vertical pressure levels would not affect the test results in the higher pressure range.

4.4 Isotropic compression apparatus

The isotropic compression apparatus is a self-developed device for a simple investigation of the isotropic compression behaviour of saturated peloids. During the test, shrinkage of a hemispherical specimen due to evaporation of the pore water is observed by a continuous measurement of the pore water's suction pressure and the loss in weight of the specimen.

4.4.1 Principle of compression by shrinkage

If a fully water-saturated specimen is exposed to a non water-saturated atmosphere, the specimen tends to desiccate. In physical terms more water molecules per time unit pass from liquid to gas than vice versa, i.e. the evaporation rate is higher than the condensation rate. In the course of time, desiccation causes the liquid/gas interface to adapt to the specimen's surface (Fig. 4.3). The pressure difference $\Delta p = p_a - p_w$ between the

atmospheric pressure p_a and the pore water pressure p_w, both related to vacuum, is then obtained by the Kelvin equation (e.g. SCHUBERT 1982)

$$p_a - p_w = \frac{RT}{v_L} \ln\left(\frac{p_v^0}{p_v}\right) \tag{4.1}$$

with the universal gas constant $R = 8.314$ JK^{-1}mol^{-1}, the absolute temperature T, the molar volume of water $v_L = 1.8 \cdot 10^{-5}$ m^{3}mol^{-1}, the saturation vapour pressure above a curved liquid/gas interface p_v and the saturation vapour pressure above a plane liquid/gas interface p_v^0.

The pressure difference Δp is also determined by the curvature and the surface tension of the liquid/gas interface. With the Young-Laplace equation (e.g. SCHUBERT 1982)

$$p_a - p_w = \gamma_L \left(\frac{1}{r_1} + \frac{1}{r_2}\right) \tag{4.2}$$

the pressure difference is obtained from the surface tension of water $\gamma_L \approx 7 \cdot 10^{-5}$ kN/m and the principal radii of curvature r_1 and r_2, to be measured in perpendicular planes (Fig. 4.3).
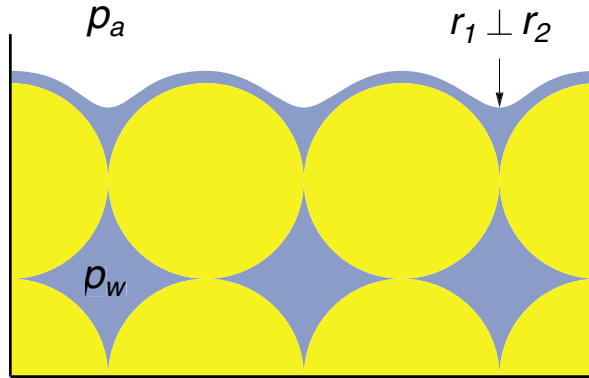
Figure 4.3: Curved liquid/gas interface

Introducing the mean radius of curvature $r_m = 2r_1r_2/(r_1 + r_2)$ and the relative humidity $\psi = p_v/p_v^0$, comparison of (4.1) and (4.2) yields

$$r_m = \frac{2\gamma_L v_L}{RT \ln\left(\frac{1}{\psi}\right)} \tag{4.3}$$

with the consequence of $r_m \to \infty$ for full saturation of the atmosphere ($\psi = 1$). Then the liquid/gas interface is plane. Only a minor decrease in ψ results in a drastic decrease of r_m and therefore in a drastic increase of $p_a - p_w$.

Capillary entry occurs if $p_a - p_w$ according to (4.1) reaches the capillary entry pressure p_{ce} according to (4.2). This is the case when the relative humidity is so low that r_m is in the range of the pore radius. Then the liquid/gas interface enters the pores, which is also visually observable by the change in colour and brilliancy of the specimen surface.

Allowing for the atmospheric pressure and for full saturation of the specimen ($S_r = 1$), Terzaghi's principle of effective stress can be written as

$$\sigma = \sigma' + p_w - p_a \tag{4.4}$$

with the total pressure σ, the grain skeleton pressure σ' and the pore pressure $p_w - p_a$. For capillarity, (4.1) and (4.2) yield $p_w - p_a < 0$. If σ is zero, then $\sigma' = -(p_w - p_a)$. Therefore, in the shrinkage test the effective pressure equals the suction pressure of the pore water relative to the atmospheric pressure. Since the suction pressure acts isotropically, the shrinkage test represents an isotropic compression if the boundary conditions are properly chosen.

Isotropic compression leads to a densification of the grain skeleton. Assuming full saturation of the specimen ($S_r = 1$) initially, the void ratio e is obtained via the water content w according to

$$e = \frac{\gamma_s}{\gamma_w} w \tag{4.5}$$

with the specific gravity of the solid γ_s and water γ_w, respectively. Evaporation leads to a decrease in w and, pursuant to (4.5), proportionally to a decrease in e.
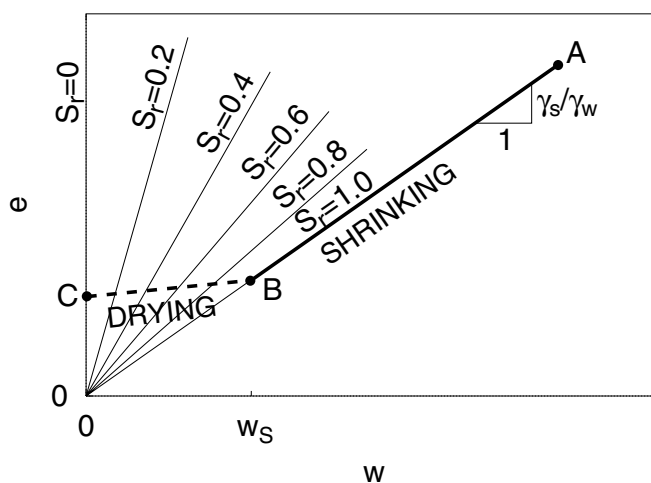
Figure 4.4: On the definition of shrinking and drying

In Fig. 4.4 the relation between void ratio e and water content w is illustrated. The line A-B represents the decrease in e due to the evaporation of pore water of a fully saturated specimen between the starting point A of water content w_A, say close to the liquid limit w_L, and point B, indicating the water content at shrinkage limit w_S. Herein, full saturation is maintained through compensation of the pore water volume loss by densification of the grain skeleton. This process is termed *shrinking*. With further decrease of the water content below w_S, the pore water volume loss cannot be entirely compensated anymore by densification of the grain skeleton (line B-C). Capillary entry occurs, and the specimen is no longer fully saturated ($S_r < 1$). This process is termed *drying*. Since σ' and e can then hardly be determined, the course of line B-C is not considered any further.

4.4.2   Mechanical design

The shrinkage apparatus (Fig. 4.5) consisted of a smooth perspex plate (A) with a central filter stone (B), where the hemispherical specimen (C) was centrically placed on. At the bottom side of the filter stone a pressure transducer (D) was located for the measurement of the pore water pressure. The entire assembly was suspended by nylon strings, adjustable in length for the horizontal alignment of the plate. These strings were mounted to a strain-gauge beam (E) for the measurement of the entire assembly weight.

The absolute atmospheric pressure was additionally recorded in order to allow for barometric variation. The tests were executed under stable environmental conditions in an air-conditioned laboratory with constant temperature of 20°C and constant humidity of ca. 60%.

The apparatus was equipped with a strain gauge beam (Hottinger Baldwin Z6FD1, range 5 kg) and two absolute pressure transducers (Transamerica BHL, range 25 bar). Data acquisition was realized by a multimeter (Hewlett Packard HP34709A) and an individual software (within a Hewlett Packard HP-VEE environment) running on a personal computer, providing data online-visualization. Minor changes in supply voltages were taken into consideration, yielding a remarkable improvement of the readings' precision.

4.4.3   Testing procedure

In preparation for the test, the porous filter stone was initially dismantled. A beaker was filled with deionized water and set into a vacuum chamber. The filter stone was put onto the top of a frame, the latter located over the beaker. After sealing the vacuum chamber, deionized water and the filter stone were degassed by evacuating the vacuum chamber
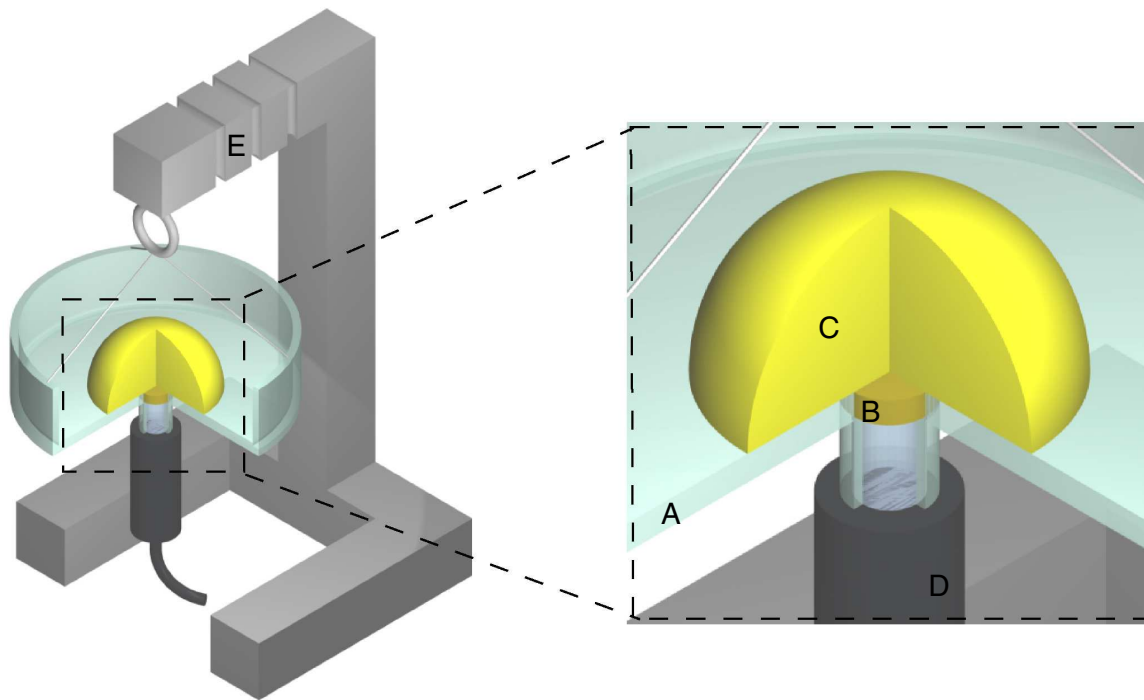
Figure 4.5: Shrinkage apparatus

down to the absolute atmospheric pressure of $p_a \approx 0.15$ bar. Subsequently the filter stone was tossed into the beaker by slightly tilting the vacuum chamber, and saturation of the filter stone was awaited for ca. 10 minutes. Then the evacuation was terminated, and the beaker was removed from the vacuum chamber.

After mounting the pressure transducer to the bottom of the plate, the swallowing capacity of the pressure transducer was filled with degassed water by a syringe. The filter stone was taken off the beaker and instantaneously moulded into its position on the top of the plate, ensuring no gas bubbles were trapped in the swallowing capacity. Finally a drop of water was put on top of the filter plate to avoid desiccation, and adjustment to the ambient temperature was awaited.

Subsequently, the top of the plate was lubricated with silicone grease and data acquisition was started in order to take initial readings. Then the specimen was formed stepwise by successive adding of material onto the top of the filter stone. This procedure was continued until a hemispherical specimen with a diameter of approx. 6 cm was achieved. From that moment onwards, no further action was needed for the execution of the test.

The initial water content was determined at the beginning of the test with excessive material from preparation, and at the end of the test with the specimen itself.

4.5   Cone penetration apparatus

The cone penetration apparatus is a standard device for a fast estimation of the undrained cohesion c_u of soft soils. In the test the penetration depth s_k of a cone with an apex angle α and mass m_k into the specimen is recorded. By empirical correlation (e.g. HANSBO 1957) c_u can be obtained via

$$c_u = \frac{K_\alpha\, m_k\, g}{s_k{}^2} \tag{4.6}$$

with g denoting the gravity acceleration and K_α a form factor depending on α.

Tables of correlation, provided by the manufacturer, lead to similar results as (4.6). Results of cone penetration tests are in a good agreement with the one of vane shear and uniaxial pressure tests (HANSBO, 1957). Advantage of the apparatus is a fast and easy procedure. Viscosity effects according to the penetration rate are not taken into account.

4.5.1   Mechanical design

The apparatus is shown in Fig.4.6. It consisted of a base plate with a vertical shaft and a height-adjustable cantilever. At the tip of the cantilever, a magnetic release mechanism was mounted for the suspension and the release of the cone. The release mechanism was additionally equipped with a scale for the measure of the cone's penetration depth.
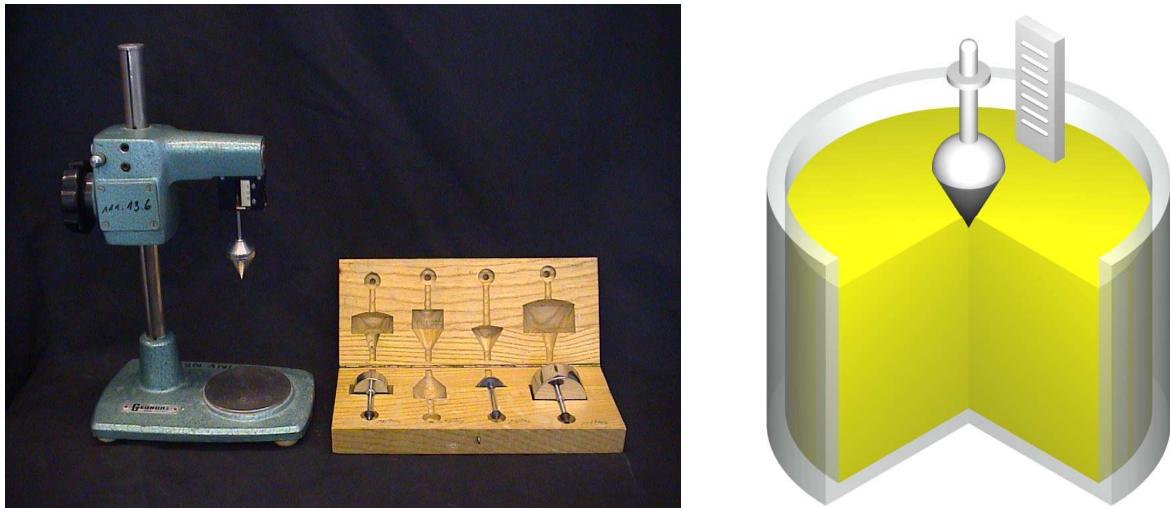
Figure 4.6: Cone penetration apparatus

Four cones with variation in apex angle and mass were provided. According to the consistency of the specimen, a cone with a reasonable penetration depth had to be chosen for the testing procedure. Thus, a range of ca. $0.1 < c_u < 10$ kPa could be covered.

4.5.2 Testing procedure

A beaker, filled with prepared material, was set on the base plate of the apparatus. According to the consistency of the material, an appropriate cone was chosen and attached to the release mechanism. By lowering the cantilever via a hand-wheel, the tip of the cone was levelled down to the the specimen's surface. By disengaging the magnetic release mechanism, the cone was penetrating the specimen's surface due to its dead load and gravity acceleration. Finally, reading of the cone's penetration depth was taken directly after test execution.

4.6 Vane shear apparatus

Another method for a fast determination of the undrained shear resistance c_u is the vane shear test. In contrast to the cone penetration test, the vane shear test also enables the investigation of the c_u-dependence on the shear strain and the shear rate.

4.6.1 Principle and mechanical design

The testing principle is based on the torsion of a submerged vane, producing the twist of a cylindrical element inside the specimen (Fig. 4.7a). Hereby, shear resistance is generated along the element's surface and is integrally measured via the corresponding torque. During the rather rapid test, drainage is negligible. Under consideration of the vane geometry, the measured torque yields the undrained shear resistance c_u.
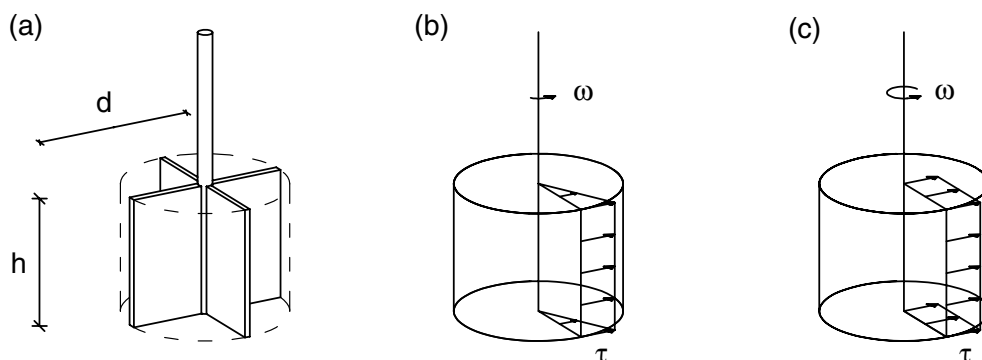
Figure 4.7: Vane shear apparatus: (a) Four-blade vane, (b) triangular and (c) rectangular distribution of mobilized shear resistance τ

For the analysis of the test results, the generation of the shear resistance and its distribution at the cylindrical surface has to be considered (SILVESTRI *et al.* 1993). According to

the local shear strain due to initial torsion ω, the highest shear resistance τ is generated at the mantle of the cylinder, whereas the shear resistance at the faces may be assumed as triangularly distributed for the sake of simplicity (Fig. 4.7b). With ongoing torsion, the shear resistance at failure $\tau_f = c_u$ is reached at the mantle and the faces, assuming a rectangular distribution of shear strains and stresses (Fig. 4.7c). Then, the undrained cohesion c_u is obtained via

$$c_u = \frac{M}{\frac{\pi d^2 h}{2}\left(1 + \frac{d}{3h}\right)} \qquad (4.7)$$

with the measured torque M and the diameter d and height h of the vane.

Standard lab vane shear devices usually cover a range of ca. $3 \leq c_u \leq 100$ kPa. Since the expected c_u of unconfined peloids was below this range and a sufficient precision was also needed, a more sensitive method had to be developed. Therefore a rotational viscosimeter (Haake Rotovisco RV20) was modified and equipped with a data acquisition system. Herewith, the torque at the vane's axis due to torsion with constant revolution speeds of $8{\cdot}10^{-4} \leq n \leq 8\,\mathrm{s}^{-1}$ could be measured continuously. By acquisition of the torque in time intervals of 0.2 s via a personal computer, data sets were obtained which could be back-analyzed towards c_u-ω-diagrams. With the maximum torque of the viscosimeter $M_{max} = 5{\cdot}10^{-2}$ Nm and a four-blade stainless steel vane of $d = 16.0$ mm and $h = 32.0$ mm, a range of $c_u \leq 3.33$ kPa could be covered.

4.6.2   Testing procedure

The material was prepared in a beaker under specified conditions. Then, the filled beaker was located under the modified viscosimeter and fixed to the tripod of the viscosimeter in order to avoid twist of the entire beaker. By lowering the viscosimeter unit, the vane was penetrating into the specimen. Hereby, a penetrating depth of two times the vane height was aspired to ensure a sufficient vertical cover of the vane. Subsequently, a period of ca. 0.5 h was awaited for the decay of excess pore pressures due to the vane's penetration. After starting the data acquisition, shearing was induced and the evolution of the corresponding torque was observed online. Subsequent tests were performed at different locations of the specimen.

4.7 Direct shear apparatus

For the investigation of the drained shearing resistance with regard to the deformation direct shear tests were performed. The direct shear apparatus is a standard device in a soil mechanical lab, but in some of the tests the usual procedure was modified by performing *thin-layer tests* with specimen heights of ca. 2 mm. Additionally, mechanical and electronic modifications were made for the execution of cyclic densification tests.

4.7.1 Mechanical design

The cuboidal specimen (A) with a square base of 60 mm in length was vertically enclosed by filter papers and an upper (B) and a lower (C) porous filter stone (Fig. 4.8), enabling the vertical drainage of pore water during the entire test. Horizontal enclosure of the specimen was provided by a splitted box. The whole assembly was flooded in order to maintain full saturation of the specimen.
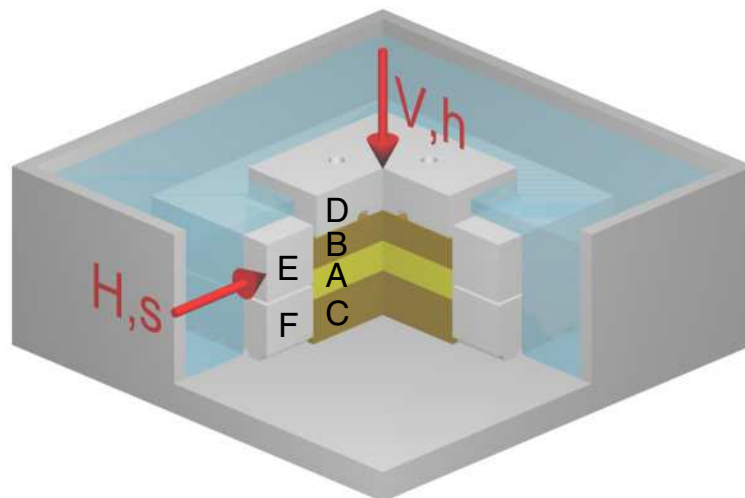
Figure 4.8: Direct shear box

For initial consolidation of the specimen, vertical loading was provided by a moveable top plate (D). By this principle, K_0-conditions were applied (oedometrical compression). Tilting of the top plate and the upper filter stone was enabled by applying the vertical load to a steel sphere, located in the centre of the top plate.

Subsequent shearing was induced by a relative horizontal displacement of the upper frame (E) with respect to the lower one (F), initiated by a drive of constant speed. With a proper combination of gear wheels, horizontal shear velocities in the range of 0.03 to 73 mm/h

were applicable. With this setup, horizontal displacements up to 10 mm could be reached. For cyclic densification the upper frame was connected to the drive by a push/pull rod.

The device was equipped with a force transducer for the measurement of the horizontal shear force H (HBM load cell U2A, range 100 kg and 1000 kg), a transducer for the determination of the horizontal shear deformation s (Novotechnik Linopot, range 25 mm) and a dial gauge for the measurement of the change in vertical height Δh of the specimen (Mitutoyo Digimatic ID-C, Range 30 mm). Data readings were automatically taken and stored by a personal computer for subsequent analysis.

For cyclic densification a separate control program was developed, enabling the change of the shearing direction by reaching a limit value either in horizontal displacement or horizontal force, or due to the occurence of dilatancy as detected by the height measurement.

4.7.2   Testing procedure

For the determination of the specimen height, the lower filter paper was placed and an aluminium block of 20 mm in height was inserted into the device. After placing the upper filter paper, the upper filter stone and the top plate, the level of the top plate was taken in relation to a reference height. This procedure was required to obtain a reference level for the height measurement in order to determine the height of the specimen during the test and for the subsequent analysis. After detaching the aluminium block, the assembly was flooded up to the level of the lower filter stone with demineralized water of identical pH and ion concentration like in the specimen.

Typically, direct shear tests are performed with specimen heights of ca. 20 mm. The above noted modification of the standard testing procedure is referred to tests with slim specimens of only ca. 2 mm in height. According to the consolidation theory, this reduction in specimen height yielded a reduction of the consolidation time by the factor 100. Low consolidation times in association with non-isochoric shearing at a properly chosen shear rate can keep the pore water pressure almost at hydrostatic level. Therefore the recording of excess pore water pressures became obsolete and the effective stresses could directly be determined. Furthermore, direct shearing of thin specimens provided the advantage of a high portion of the specimen to be captured by shear. This was also helpful in the subsequent void ratio determination.

Preparation was continued by filling the specimen into the frame up to a precalculated fill level. This precalculation was based on the results of anticipated oedometric compression tests and targeted at a sufficient specimen height at the end of the last consolidation step in order to avoid blocking of the frame by the filter stone. During the filling, the water

level was raised above the top level of the specimen. Then the upper filter stone and the top plate were carefully placed, the vertical dial gauge was mounted, and the data acquisition was started.

In the subsequent consolidation the specimen was vertically loaded by a stepwise application of deadweights. During each load step, full consolidation was awaited for. Therefore the required consolidation time was preestimated, and the consolidation process was followed via the readings of the vertical settlement. After full consolidation at the last load step, the height of the specimen was finally controlled in order to avoid blocking of the frame by the filter stone.

Finally shearing was induced by starting the drive. The test was continued until either a steady state was reached or the maximum horizontal displacement of ca. 10 mm was approached. After the test, the water level was lowered, the assembly dismantled, and the specimen was extracted for the determination of the void ratio.

4.8   Tumble-shrink apparatus

The so-called *tumble-shrink apparatus* was developed to investigate the cyclic densification of a specimen. The principle of this device consists of the superposition of shrinking (cf. Sec. 4.4.1) and cyclic shearing.

4.8.1   Mechanical design

The device (Fig. 4.9) consists of a base plate (A) with a filter stone (B) located at the centre. The cylindrical specimen (C) of 50 mm in diameter and height is enclosed by a rubber membrane and a thick-walled rubber tube (D) along its mantle.

The specimen is subjected to shrinkage due to the evaporation of pore water at its top face. Additionally, radial cyclic deformation is induced by the pairwise pneumatic loading of rubber hemispheres (E and F, respectively). The deformation amplitude is controlled by regulation of the air pressure, the cycle duration by programmable electro-pneumatic valves (Festo). The suction pressure $p_a - p_w$ is recorded via the filter stone and a relative pressure transducer (G; Transamerica BHL, range 16 bar).
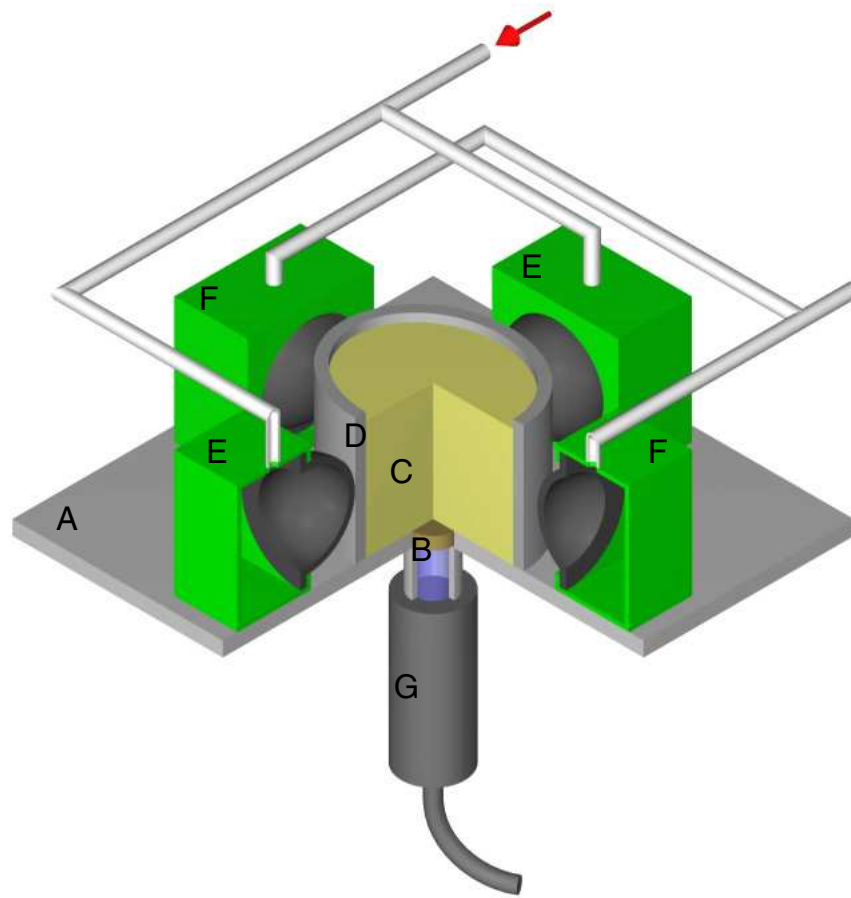
Figure 4.9: Tumble-shrink apparatus

4.8.2   Testing procedure

After covering the filter stone with a filter paper, the specimen was carefully filled into the tube. Via a simple data acquisition system the development of pore water suction pressure was awaited. Then pneumatic loading was started, initially with a deformation amplitude of ca. 5 mm of the rubber hemispheres. With ongoing test duration, the deformation amplitude was successively lowered down to ca. 1 mm in order to avoid unintended dilatancy of the specimen. The applied cycle duration was in the range of 2 seconds and was kept constant throughout the entire test. At the end of the test, the hardened specimen didn't show any further deformation due to the pneumatic loading. Then, the specimen was dismantled and cut into pieces for the subsequent determination of the void ratio.

4.9 Biaxial apparatus

With the biaxial device the deformation of a cuboidal specimen is enabled in two directions whilst deformation in the third direction is prevented. Deformations can be achieved either strain or stress controlled. With this assembly the boundaries of the sample remain plane and parallel, and right angles are maintained during deformations. Therefore the strain rates and pressures are principal components.

4.9.1 Mechanical design

The biaxial device was originally designed and set up by KUNTSCHE (1982) and was improved by TOPOLNICKI (1987) and later by the author. Cuboidal samples, enclosed and sealed by a rubber membrane, were constrained between two horizontal rigid smooth steel plates with a distance of 50 mm. The vertical faces of the specimen were each in contact with one of four movable rigid smooth steel plates (Fig. 4.10), which could change the two horizontal dimensions of the sample (direction 1 and 2) between 133 and 45 mm. Each plate could be moved with a continuously adjusted speed up to 0.03 mm/s.

For continuous measurement of pore water volume changes with sufficient accuracy, a device consisting of 1 ml- and 25 ml-burettes and a differential pressure transducer was developed. This device was connected to a filter stone at the bottom of the specimen.

The biaxial apparatus was located in an air-conditioned laboratory with temperature of 20±1°C in order to minimize thermal influences on the specimen and the transducers.

Transducers and data acquisition

The biaxial apparatus was equipped with eleven transducers for the measurement of displacements, forces and pressures. Horizontal displacements of the movable plates in the direction of the drive were registered for each plate separately by four inductive displacement transducers (Novotechnik Linopot, range 50 mm). Horizontal forces, acting normally on the movable plates in the direction of the drive, were recorded by load cells (Moser-Scholle MSSD, range 5 kN), which were decoupled from transversal forces by means of roller bearings. Vertical forces, acting normally on the horizontal upper plate, were measured by three load cells (Hottinger Baldwin S9, range 10 kN) in 120 degree assembly. The pore water pressure was recorded by a relative pressure transducer (Gems, range 16 bar), i.e. the measurand was independent from atmospheric pressure changes. For the continuous acquisition of the fill level of the burettes a differential pressure transducer
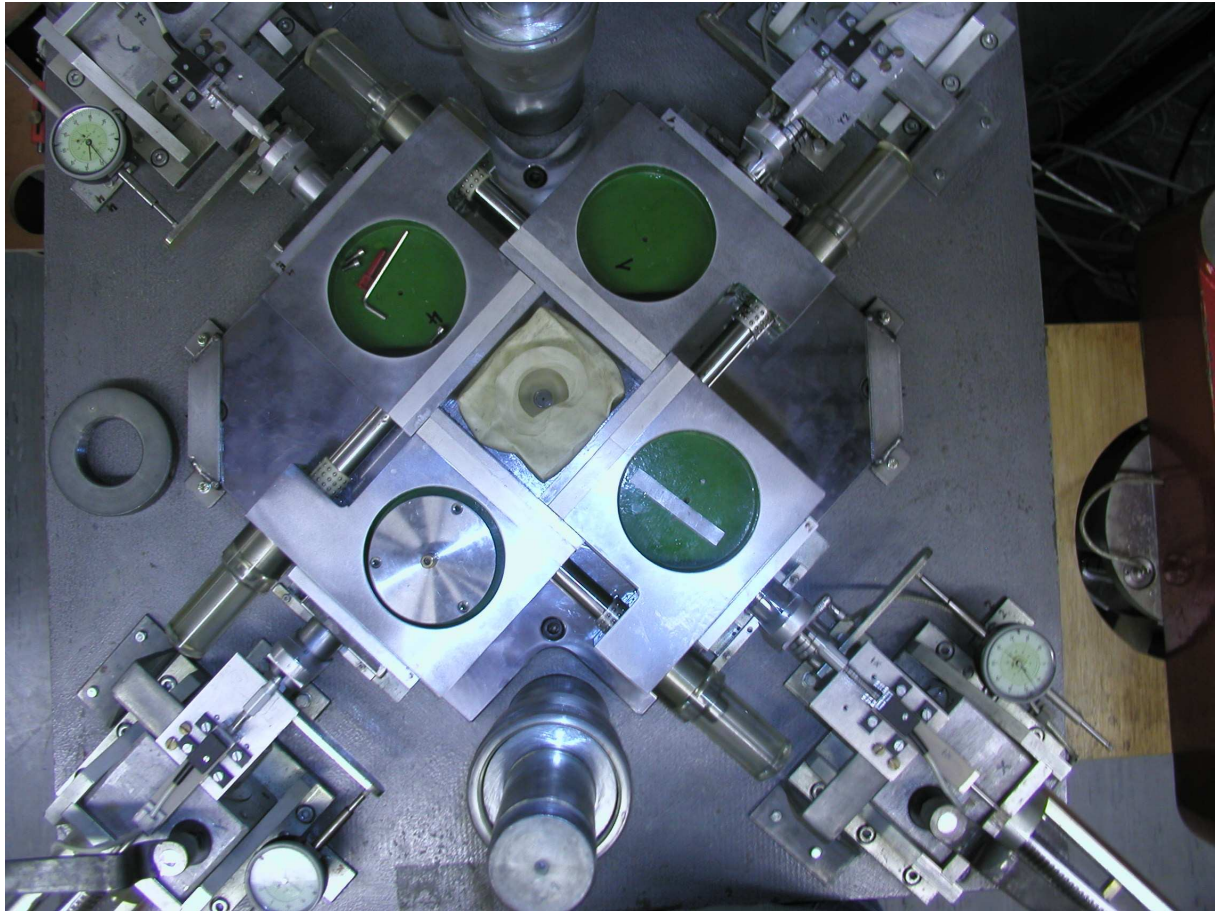
Figure 4.10: Top view of the biaxial apparatus (partially dismantled).

(Siemens Teleperm, range 13..130 mbar) was used. Herewith, the fill level of the burettes was measured by the hydrostatic pressure of the burette's water column in relation to a water column of fixed height. With the 25 ml-burette an accuracy of $4 \cdot 10^{-3}$ ml with a resolution of $3.3 \cdot 10^{-4}$ ml was achieved (Fig. 4.11), with the 1 ml-burette the precision was even ca. 20 times higher.

The transducers were supplied by a 20-channel voltage unit. The transducer output voltages were transferred to a digital multimeter (HP Agilent 34970A), reading a set of values in loops of ca. 1 s duration at minimum. Changes in the supply voltage have been allowed for a correction of the transducer readings. Herewith, a remarkable increase in readings precision could be achieved.

Drive control

The drive was either remote-controlled or manually operated, the former during the regular testing procedure and the latter in case of pre- and post-testing operations or emer-
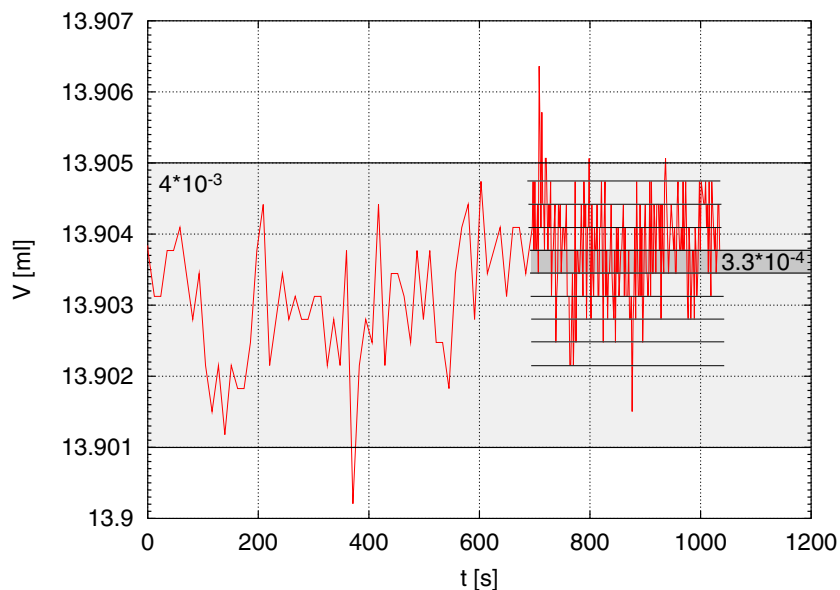
Figure 4.11: Accuracy and resolution of the volume measurement device at constant level of the 25 ml burette.

gency interventions. The direction commands were executed by applying voltages to each of the two engine control units separately. Therefore 'Forward', 'Stop' and 'Back' commands were encoded as potentials of 10 V, 0 V and -10 V, generated by the power supply and switched by actuators of the HP Agilent 34970A multifunction module. The revolution speed commands were encoded as 64128 step digits between 0 and 10 V, each generated by a HP36789 power supply separately. Within the engine control units these commands were interpreted by contactors for switching the power circuit and by integrated circuits for the desired engine revolution. By the simultaneous reading of the actual engine revolution via tachometer and comparison with the target value, the velocities could be precisely controlled via the integrated circuits.

The former test control via a HP-86B microcomputer was substituted by a personal computer running Windows98 and the software package HP-VEE, the latter operating as the test control (Fig. 4.12). The control program was communicating with the HP 34970A multimeter and actuator modules via a RS232-interface and with the HP36789 power supply via HP–IL-interface.

Control and data acquisition software was developed for uniaxial compression ($\dot{\varepsilon}_1 = const$, $\dot{\varepsilon}_2 = 0$), biaxial compression ($\dot{\varepsilon}_1 = \dot{\varepsilon}_2 = const$), consolidation ($\dot{p}_1' = \dot{p}_2' = 0$) and isochoric deformation with constant deformation rate ($\varepsilon_1 = -\varepsilon_2$, $\sqrt{\dot{\varepsilon}_1^2 + \dot{\varepsilon}_2^2} = const$).
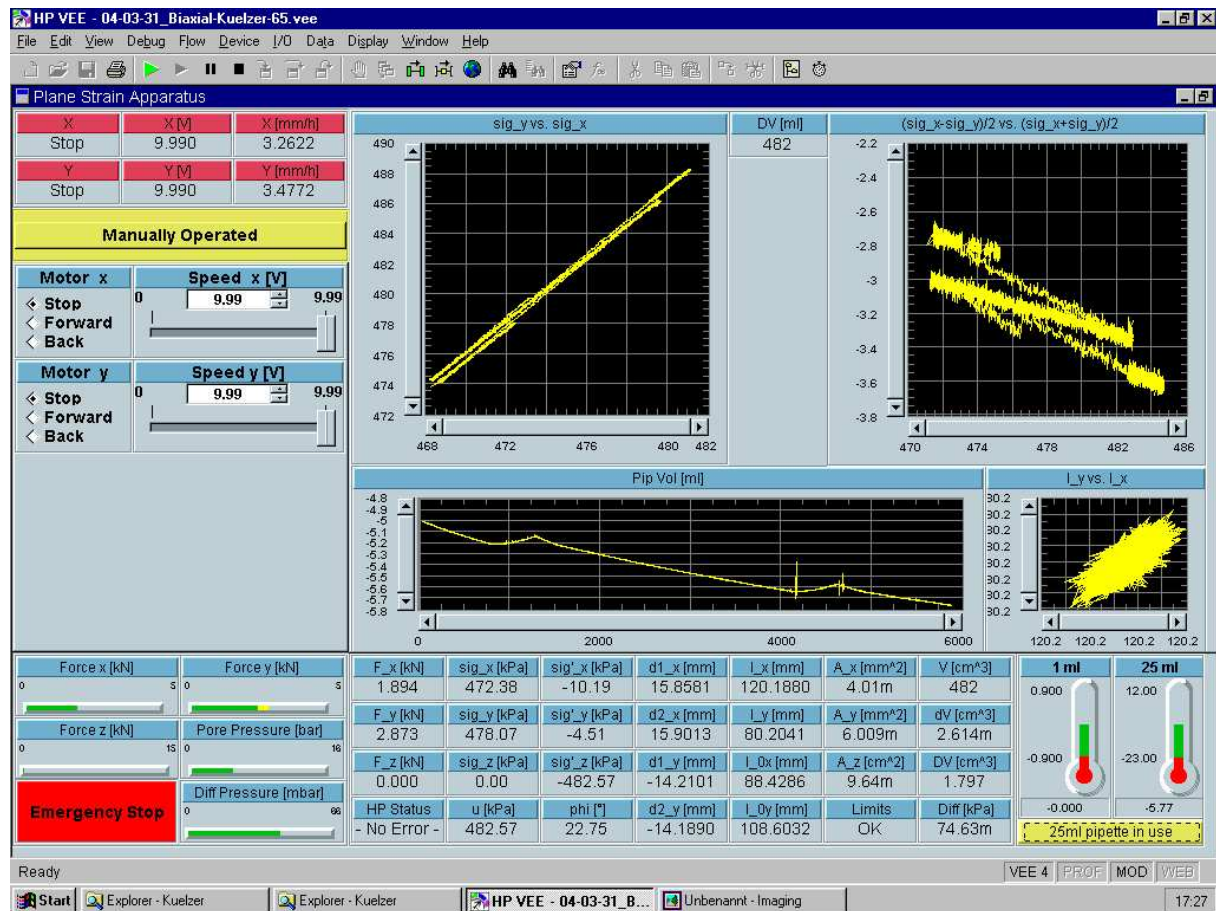
Figure 4.12: Screenshot of the control program for the biaxial device.

4.9.2   Testing procedure

All biaxial tests were executed with remoulded peloid specimens, which were mixed with water under vacuum, then sucked from the mixer by vacuum and finally pumped into the evacuated membrane bag in the box formed by the plates. This procedure led to highly homogeneous and almost fully saturated specimens.

Initial compression of the slurry was executed by strain-controlled compression of the specimen in 1-direction. After reaching a specified p', consolidation was awaited according to the readings of the burette level. Subsequently the specimens were subjected to isochoric deformation. In so-called *active* tests the sign of $\dot{\varepsilon}_1$ was kept, in *passive* tests the sign of $\dot{\varepsilon}_1$ was changed after initial compression. During the entire tests the deformation rate was maintained constant in order to exclude viscous effects, and the preselected back pressure remained unchanged.

Chapter 5

Experimental results with aluminium oxide peloids

In this section experimental results with aluminium oxide peloids are presented. Initially, the sedimentation behaviour was investigated for the study of interparticle forces, genesis of the sediment fabric and effectiveness of several preparation techniques (Sec. 5.1). Subsequent tests aimed at the compressibility under oedometric (Sec. 5.2) and isotropic (Sec. 5.3) conditions under variation of interparticle forces. With drained shear tests the determination of the critical void ratio and the critical friction angle were studied with regard of the particle interaction (Sec. 5.4). Undrained shear tests yielded an integral measure of the interparticle pressure (Sec. 5.5). Other tests, which could not be conducted successfully for any reason, are also reported (Sec. 5.6). The results are summarized in Sec. 5.7.

5.1   Sedimentation tests

As a preliminary, sedimentation tests were performed in order to study the influence of surface effects on the settlement behaviour. Herein, the influence of the preparation method was also studied. The sedimentation behaviour was assessed by the rapidness in particle settling and by the height of the obtained sediment. From the settling behaviour grain size distribution curves were derived. For a general description of the test setup see Sec. 4.2.

5.1.1   Sedimentation behaviour with respect to the particle charge

Sedimentation states of aluminium oxide suspensions with respect to pH are shown in Fig. 5.1(a) after 2 weeks of settling. Each cylinder contains an aluminium oxide suspension, prepared with the propeller mixer (Sec. 4.1), with a solid volume fraction of $\alpha_s = 5m\%$ each. By presetting pH, a range from pH4 to pH9 was covered.
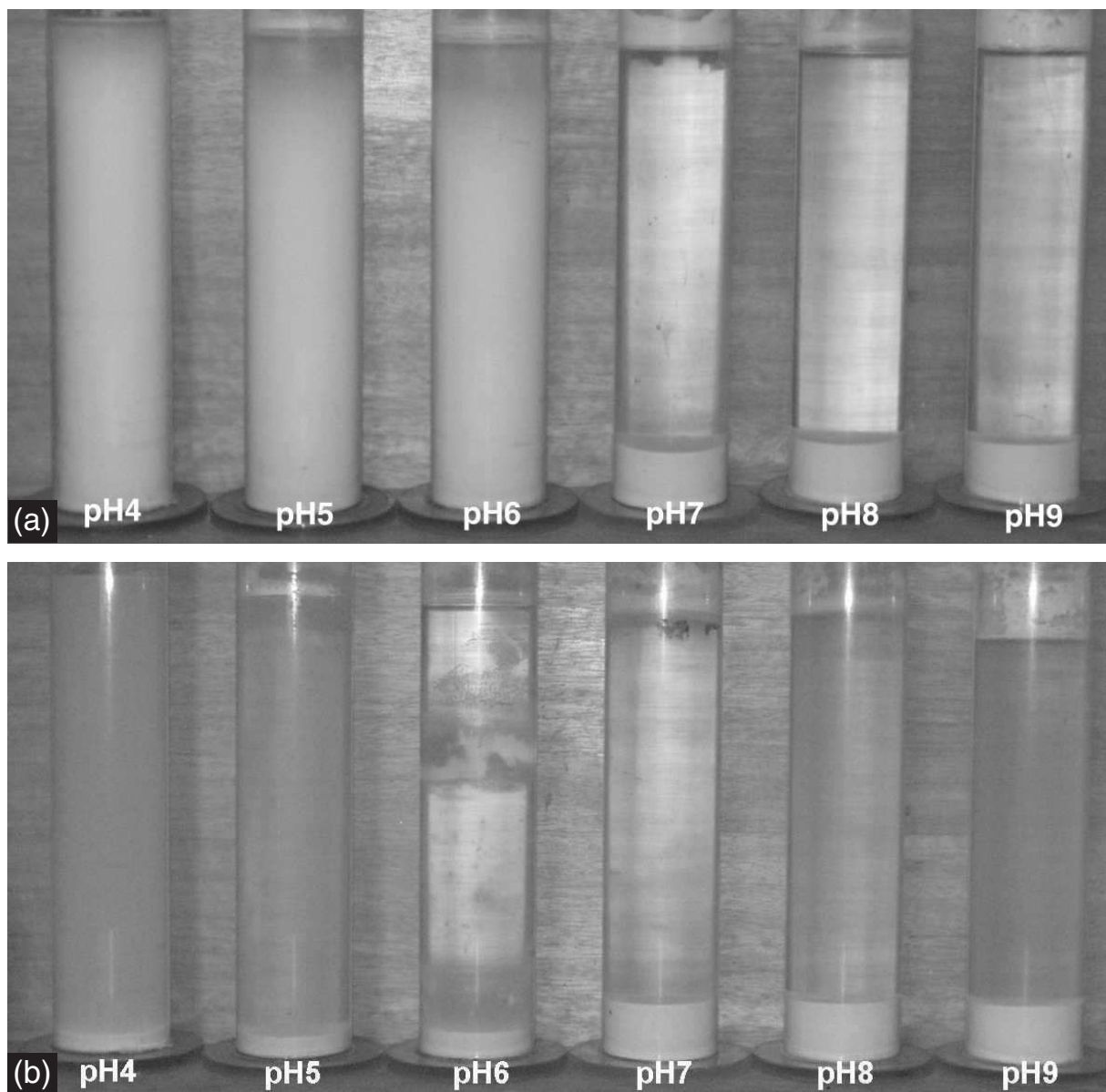
Figure 5.1: Sedimentation states of aluminium oxide suspensions with different pH (a) after 2 weeks and (b) after 4 months of settlement duration

The dependence of the sedimentation behaviour on pH is clearly visible. For pH9 to pH7 the sedimentation seems to be almost finished, which is derived from the clear water column, and the sediments show an equal height. For pH6 to pH4 the sedimentation is still ongoing, as indicated by the cloudy water column. The opaqueness of the water column is more pronounced for pH4 and less for pH6. The development of the sediment is hardly visible.

Fig. 5.1(b) shows the sedimentation state after a duration of 4 months. At pH6 the sedimentation is also completed, the water column is clear. At pH5 and pH4 the sedimentation is still ongoing, as indicated by the slightly opaque water column. At pH6 to pH4 sediments are obtained which show markedly smaller sediment heights as compared to pH9 to pH7.

The solid volume fractions and void ratios of the sediments were determined via the height and diameter of the sediment bodies and the mass of the grains. Therefore the remaining portion of still suspended particles at pH4 and pH5 was neglected, since it wouldn't contribute notably to the sediment height. Tab. 5.1 shows that the void ratio of the sediment may vary in wide amounts, viz. ranging from $e = 1.22$ at pH4 to $e = 5.66$ at pH9.

Table 5.1: Solid volume fraction α_s and corresponding void ratio e of the sediments with respect to pH.

pH	4	5	6	7	8	9
α_s	0.45	0.42	0.39	0.15	0.15	0.15
e	1.22	1.38	1.56	5.66	5.66	5.66

5.1.2 Settlement behaviour with respect to the preparation method

For the investigation of the influence of the preparation technique, aluminium oxide suspensions with $\alpha_s = 5\%$ solid fraction were prepared with the propeller mixer and the lab kneader (Sec. 4.1). Additionally, the standard preparation method by DIN 18123-6 was applied: The dry powder was mixed with demineralized water by a rotational motion of the sealed cylinder with a revolution speed of approx. $1\ \mathrm{s^{-1}}$ for a duration of 24 hours. No anti-coagulatives were added. These tests were performed at pH4 and pH9 only, since at these pH the most prominent differences in sedimentation behaviour were observed before (Sec. 5.1.1). Tests results were analyzed with regard to the grain size distribution.
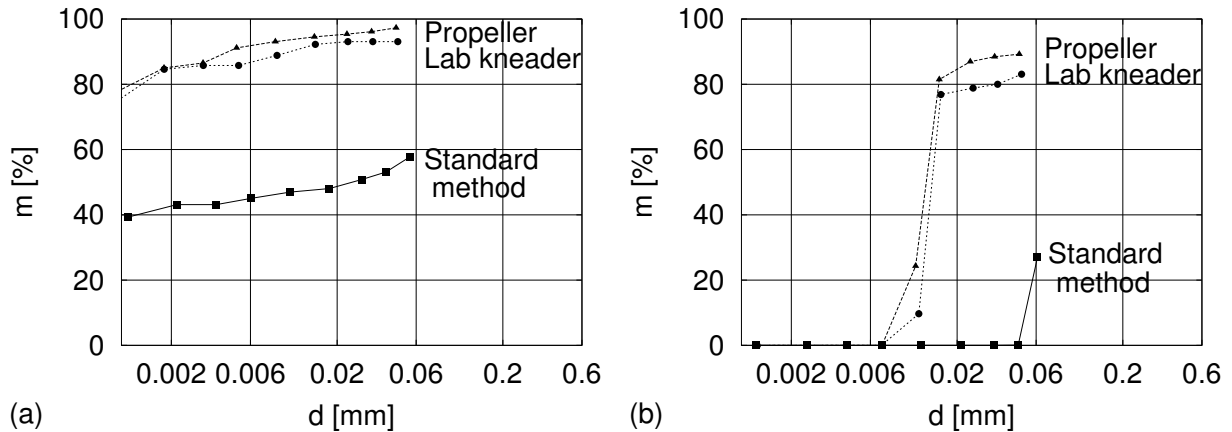
Figure 5.2: Grain size distribution according to different preparation techniques at (a) pH4 and (b) pH9

In Fig. 5.2 the grain size distributions of aluminium oxide at pH4 and pH9 are presented for the different preparation techniques. For suspensions prepared at pH4 with the propeller mixer and the lab kneader, the fraction of grain sizes with an equivalent diameter of $d < 1$ μm is about 80 m%, and the fraction of grain sizes with an equivalent diameter of $d > 60$ μm is below 10 m%. For suspensions prepared with the standard preparation method at pH4, the fraction of $d < 1$ μm is solely 40 m%, the one for $d > 60$ μm ca. 60 m%.

Contrary to these findings the suspensions prepared with the propeller mixer and lab kneader at pH9 contain no fraction of equivalent diameters of $d < 6$ μm, and the fraction of $d > 60$ μm can reach 20 m%. For suspensions of pH9 prepared by the standard preparation method the lower limit of equivalent grain size appears to be only 45 μm, and the fraction of $d > 60$ μm with 75 m% is comparatively high.

5.1.3   Interpretation

The test results impressingly illustrate the influence of the surface forces and the preparation technique on the sedimentation behaviour of the suspension and the fabric of the sediment.

The pH-dependent sedimentation behaviour can be explained with the interparticle interactions. Uncharged particles at pH9 (IEP) agglomerate due to van-der-Waals–attraction and form secondary particles, which sink rapidly due to their comparativly large size. According to the DLVO-theory, charged particles, e.g. at pH4, attract each other up to the distance where the interaction force vanishes (local potential energy minimum). By

further approach repulsive interaction forces will arise, so an interaction force equilibrium is only reached at the distance of the local energy minimum. Therefore, the particles won't agglomerate, but remain in dispersed state. According to Stoke's law, they settle much slower.

Now the transition range of the sedimentation behaviour between pH9 and pH4 is focused. The sedimentation behaviour can be divided into two classes, with one of rapid sedimentation between pH9 and pH7 and another with slow sedimentation between pH6 and pH4. For rapid sedimentation the interparticle forces are attractive, as outlined above. Even a small attractive force causes the particles to agglomerate. For slow sedimentation, different sedimentation rates were observed with the highest at pH6 and the lowest at pH4. This can be explained with the increasing particle charge towards the acid regime. According to the DLVO-theory, the energy barrier to be overcome with further particle approach increases with the particle charge. Boltzmann distributed thermal oscillation and Brownian motion provide the energy for activation, with dependence on the absolute temperature and independence of pH. Therefore the probability to exceed the energy barrier is higher if the energy barrier is low, causing the particles to rather agglomerate at pH6.

The transition from attractive to repulsive behaviour can also be used for the estimation of a 'critical' ζ-potential. With a transition at approx. pH6.5, Fig. 3.3 yields $\zeta = 55$ mV. The actual ζ-potential will be somewhat lower, since the ion concentration was not allowed for in this estimation. Fig. 3.4 yields $n_f \approx 5 \cdot 10^{-2}$ M for the transition range at pH6.5, which is presumably due to small portions of impurities of the demineralized water and the aluminium oxide powder.

Regarding the fabric genesis of the sediment, the above described mechanisms are also relevant. Attractive particles at pH9 to pH7 sink as agglomerates, with the latter maintaining their attractive properties. When the agglomerates reach the sediment surface,
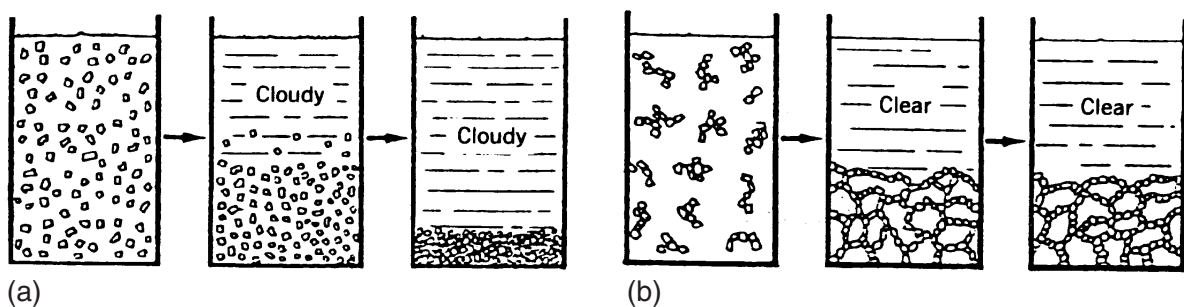
Figure 5.3: Sinking and fabric genesis of (a) repulsive and (b) attractive particles (REED 1995)

they are kept in position due to attraction, particle contact and friction at the contacts. Therefore a honeycomb– or house-of-card–like loose sediment is obtained with macropores (Fig. 5.3b), whereas repulsive particles slowly sink as primary particles or tiny aggregates. When they reach the sediment surface, they approach each other only up to the distance according to the local energy minimum. Since they won't get into particle contact, there is no friction or shear resistance between the particles. Thermal oscillation acts as a kind of permanent vibrator on the entire sediment, causing a further densification of the latter and a more homogeneous fabric with ongoing time (Fig. 5.3a).

The above findings are seemingly contradictary, since attractive particles yield a loose but repulsive particles a dense fabric. From the viewpoint of soil mechanics, one could expect the opposite, hence a grain skeleton subjected to effective pressure should be denser than without. The validity of the interpretation with Fig. 5.3 is supported by means of Kryo-SEM analyses of the fabric, but only if the micrographs are carefully interpreted. Therefore the sample preparation and analysing procedure has to be taken into account in order to avoid an inconsistency.

Fig. 5.4 shows two Kryo-SEMs of aluminium oxide suspensions with identical solid volume fraction of $\alpha_s = 0.35$ and different pH. Both suspensions were extensively stirred and then filled into tiny hollow cylinders. Subsequently, the cylinders were set into the Kryo-SEM and shock frozen by liquid nitrogene down to a temperature of -196°C. Then, the hollow cylinders were broken and exposed to high vacuum, causing the ice to sublimate. After sputtering the freshly broken surface with a thin layer of gold atoms the surface was irradiated by an electron beam, and the micrographs were obtained by scanning and
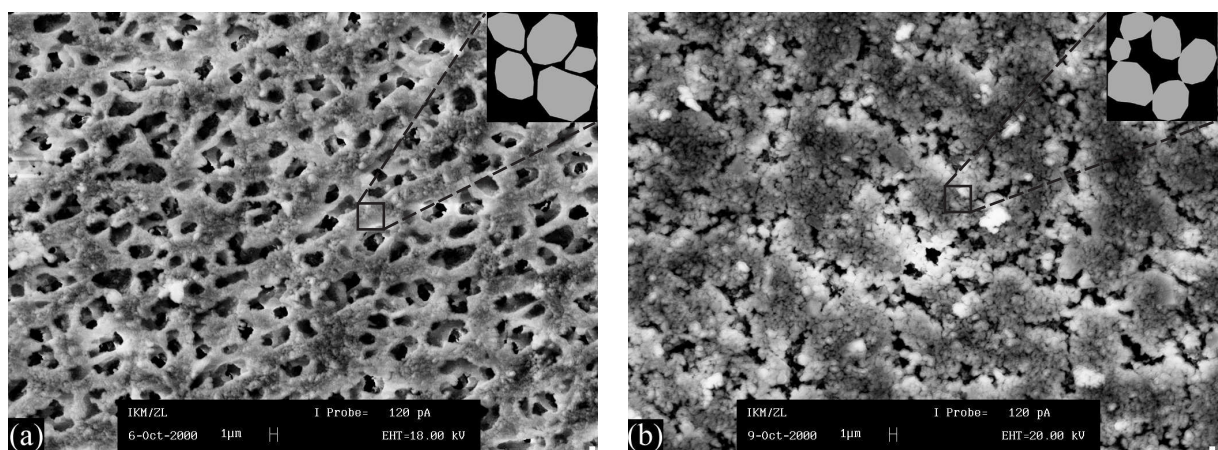
Figure 5.4: Kryo-SEM of aluminium oxide suspensions with solid volume fraction $\alpha_s = 0.35$ and (a) repulsive (pH4) and (b) attractive (pH9) particle interaction (REINSHAGEN 2000)

analysis of the secondary electrons.

At first sight, the micrographs show large macropores for repulsive particles (Fig. 5.4a), but only smaller macropores for attractive particles (Fig. 5.4b). This findings would be inconsistent with the above given DLVO-based interpretation of suspension and sediment, but by closer look at small representative areas of the fabric with the scale of some particle diameters (square markers in Fig. 5.4) the inconsistency can be eliminated. Within these representative areas, a dense fabric for repulsive particles and a loose fabric for attractive particles is obtained, which agrees with the DLVO-interpretation given above.

The difference in the macro-scale fabric of Fig. 5.4 can be also explained with the DLVO-theory and under consideration of the identical solid volume fraction. For charged particles at pH4, $\alpha_s = 0.35$ in the micrograph is lower than in the sediment ($\alpha_s = 0.45$, Tab. 5.1), i.e. Fig. 5.4a shows a suspension of charged particles after severe stirring and successive shock-freezing. Since the particles were highly separated and evenly distributed after stirring, they approached each other according to the DLVO-attraction, but could not sink to form a sediment before shock-freezing. Therefore large pores (formerly filled with water) are detectable, which would have vanished during full sinking of the particles if not been conserved by shock-freezing. For attractive particles, $\alpha_s = 0.35$ in the micrograph is higher than in the sediment ($\alpha_s = 0.15$, Tab. 5.1), i.e. Fig. 5.4b shows a precompacted sediment of uncharged particles. Consequently, the macropores appear smaller than they would in an uncompacted sediment.

In this context the question arises, why micrographs of representative sediment states have not been taken in order to avoid this temporary confusion. Answer is given by the high occupancy rate of the Kryo-SEM, which did not allow an own investigation programme as wished. Hence, existing micrographs had to be used and interpreted carefully.

Finally the influence of the preparation technique on the degree of dispersion is discussed. According to Fig. 5.2 the best dispersion results are achieved independently of pH by the propeller mixer. This method provides the highest input of mechanical energy into the suspension, which is necessary for the breaking of secondary particle bonds. The latter will presumably be smashed by the impact of the propeller blades and the high shearing gradient. The lab kneader also provides good dispersion results, which is attributed to high shearing gradients in the closest proximity of the meshing blades, whereas the standard mixing method appears non-sufficient for a satisfactory dispersion of aluminium oxide suspensions. This is attributed to the comparatively low input of mechanical energy and low shearing gradient in the suspension. Consequently, the propeller mixing method was chosen for the preparation of the specimen for subsequent tests.

5.2 Oedometric compression tests

Oedometric compression tests were performed with uncharged aluminium oxide peloids at pH9 and positively charged aluminium oxide peloids at pH4, since these pH represent the most prominent agglomerated and well-dispersed states, respectively. Additionally, the influence of NaCl on the oedometrical compression behaviour of uncharged and charged aluminium oxide peloids was also investigated.

5.2.1 Oedometric compression with uncharged particles

The oedometric compression behaviour of a saturated aluminium oxide peloid with uncharged particles (pH9) is shown in Fig. 5.5. During the test, vertical drainage was allowed at both sides of the specimen. Test duration was 10 days.

Starting at $e = 2.2$, presetted by the water content during the sample preparation, an increase in the vertical effective stress σ_v' leads initially to no significant compression (step 1-2 in Fig. 5.5a). From the corresponding time-compression curve (Fig. 5.5b), with the time in logarithmic scale, a creep-like compression behaviour is obtained, which cannot definitely be attributed to a response of the specimen, since in this low stress range friction of the cantilever system may influence the test results.

With further stepwise loading (Fig. 5.5a), compression of the grain skeleton is observed. Since the increment of ε decreases with the load steps (Fig. 5.5b), the stiffness of the specimen increases. The inclination of the compression curve in the e-$\ln \sigma_v'$-diagram can be represented by the compression index $C_c = -\Delta e / \ln(\sigma_v'/\sigma_{ref})$, which visibly decreases with the loading.

During each load step the settlement is delayed. The plot of the corresponding strain ε over the logarithm of time (Fig. 5.5b) shows in the primary section a typical S-type course, indicating the dissipation of excess pore water pressures according to TERZAGHI's (1925) consolidation theory. The consolidation time t_{98} decreases with increasing σ_v'. Since the consolidation index $c_v = d^2/t_{98}$ is almost constant for a specific type of soil, the decrease of t_{98} is attributed to a reduction in the thickness d of the specimen.

The secondary section of (Fig. 5.5b) shows a linear decrease of ε with the logarithm of time. This represents compression creep, which is characterised by ongoing densification under constant σ_v' without development of significant excess pore water pressure.

Fig. 5.6 shows a series of compression tests performed with uncharged particles at pH9. The initial void ratios arise from the specimen preparation with different water contents.
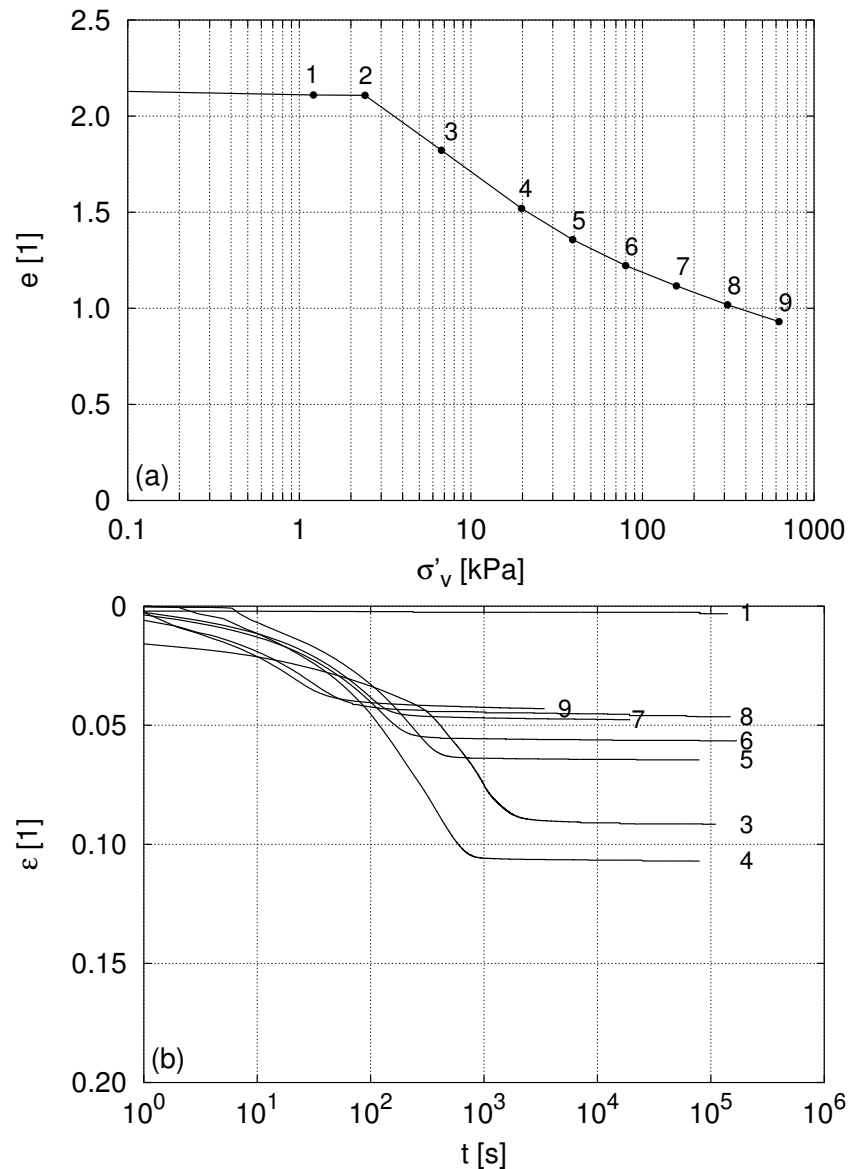
Figure 5.5: Void ratio e vs. effective vertical pressure σ'_v (a) and vertical strain ε vs. time t (b) of an aluminium oxide peloid at pH9

The upper bound of the attainable initial void ratio is given by the void ratio obtained by sedimentation (Tab. 5.1), and at the lower bound by the void ratio the specimen was just homogeneously mixable.

The compression behaviour shows that independently of the initial void ratio all curves coincide for higher σ'_v. This coincidence ranges over nearly two decades in σ'_v and starts from $\sigma'_v \approx 10$ kPa. In the transition range before, the decrease in void ratio is evidently higher for larger initial void ratios; then the specimen shows a higher compressibility.

Figure 5.6: Void ratio e vs. effective vertical pressure σ'_v for a set of compression tests of aluminium oxide peloids at pH9 (uncharged particles)

5.2.2　Oedometric compression with charged particles

The compression behaviour of aluminium oxide peloids with positively charged particles (pH4) is presented in this section. The testing conditions of Sec. 5.2.1 were adopted.

Remarkably, these tests were performed with material in initially liquid state. As expected, an expulsion of material through the gaps between the top and base plates and the horizontal ring was observed in some of the tests at low pressure levels. Thus some oedometer tests have been started which had to be prematurely terminated. Remedy was searched for, e.g. by applying minor load step increments at the early stages of the test or by sealing the gaps with plasticine, both without success. An effective remedy arose by replacing the base plate and the ring by a beaker and by the precise tailoring of the dry filter paper on top of the specimen, allowing for the radial swelling due to watering up to the dimensions of the ring diameter and therefore sealing the gap (cf. Sec. 4.3.1). By this method, two successful tests could be carried out with only minor expulsion of material.

The void ratio e was determined by back-analysis after the finalization of the tests via the mass m_s of the oven-dried specimen. Since for a fully saturated specimen $e = V \cdot \rho_s / m_s$, loss in m_s leads to an apparent increase in e for all earlier steps by back-calculation, whereas the subsequent course of the compression curve is not affected by inkscape grichischthis evaluation.

Fig. 5.7 shows the compression behaviour of a specimen with an apparent initial void ratio
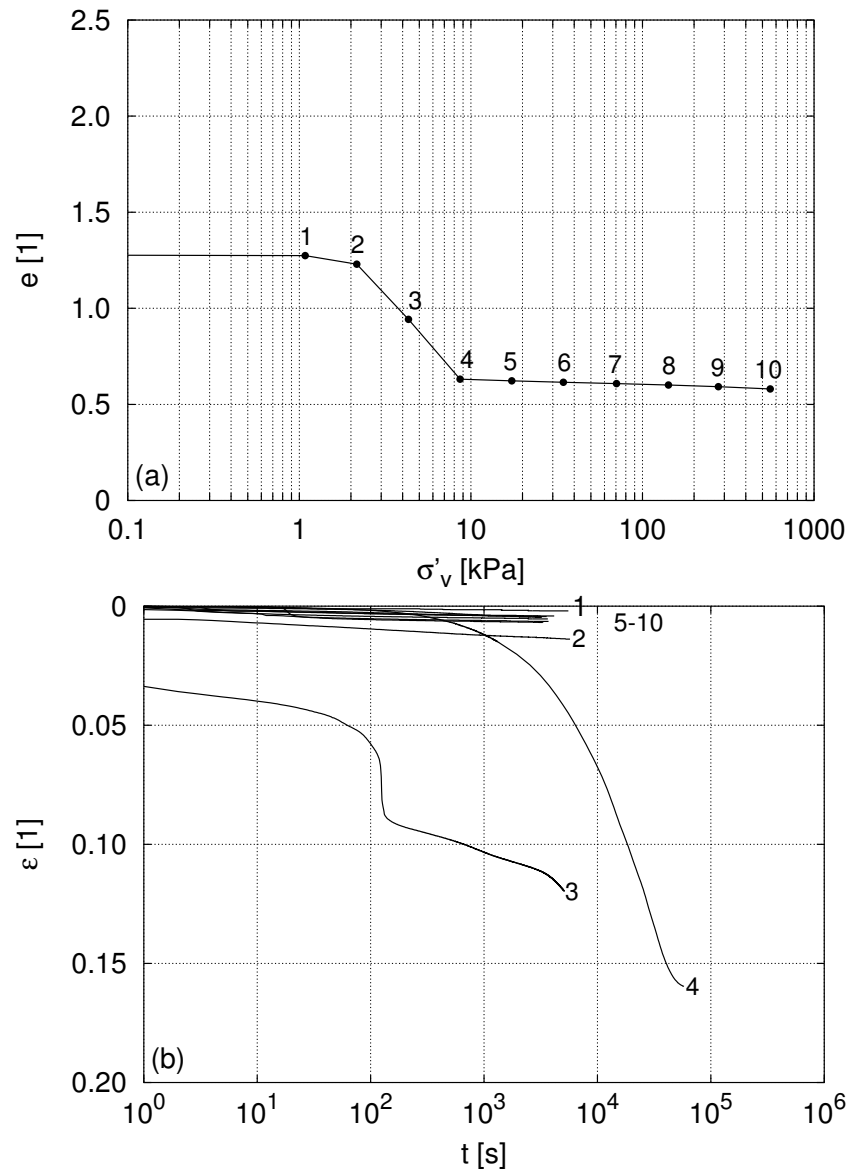
Figure 5.7: Void ratio e vs. effective vertical pressure σ'_v (a) and vertical strain ε vs. time t (b) of an aluminium oxide peloid at pH4

of $e = 1.28$. Initial loading of the specimen (step 1 and 2) yields a creep-like behaviour (Fig. 5.7b), which again cannot definitely be attributed to a response of the specimen (cf. Sec. 5.2.1).

Further σ'_v-increase (step 3) leads to a substantial compression, but the course of the time-dependent strain reveals that this compression step is only partially due to consolidation. The irregularity at approx. 100 s represents the above mentioned expulsion of material. From the back-analysis, the initial void ratio and the void ratios of steps 1 and 2 become tendencially higher: E.g. with $e_0 = 1.28$, the initial void ratio is slightly above $e = 1.22$
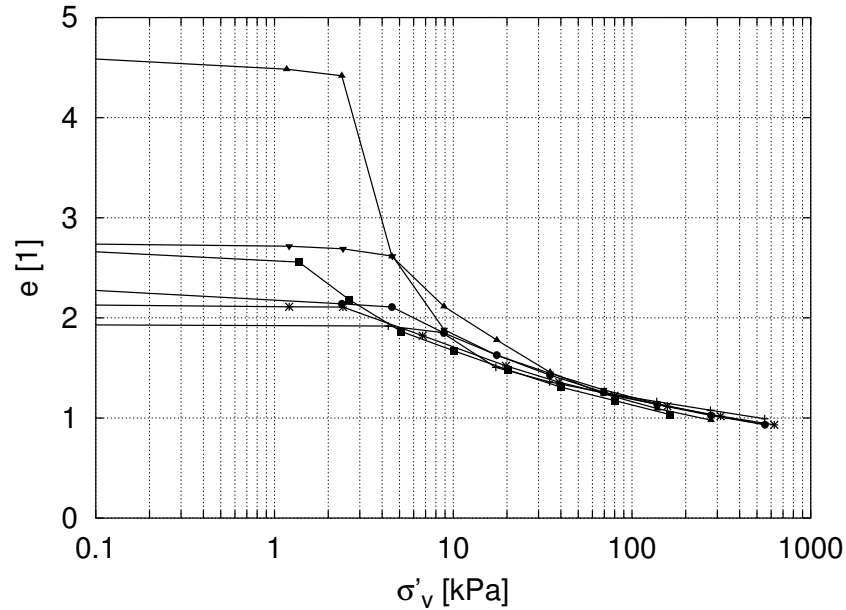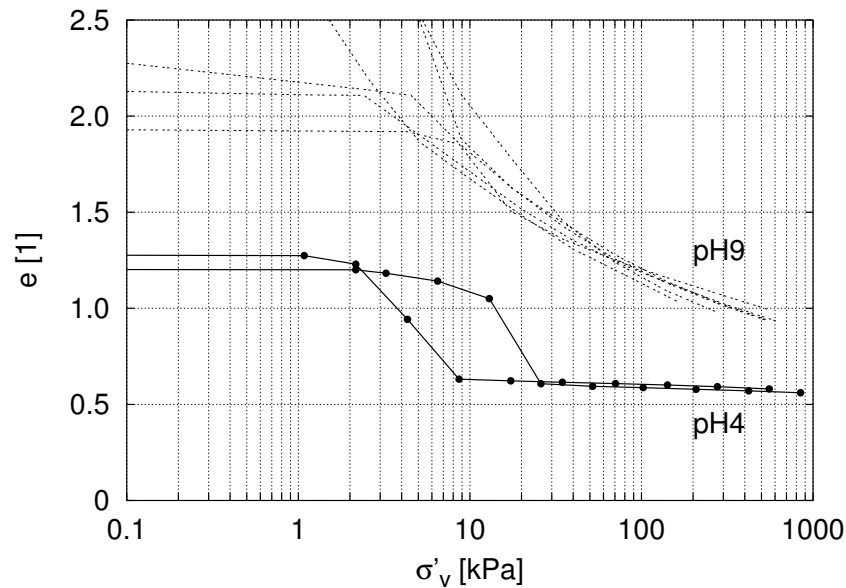
Figure 5.8: Void ratio e vs. effective vertical pressure σ'_v for a set of compression tests of aluminium oxide peloids with positively charged particles (pH4)

of the sediment (Sec. 5.1.1).

With step 4, no further expulsion of material was observed and the typical consolidation behaviour was regained, accompanied by a rather high compression and therefore decrease of e.

Subsequent steps 5-10 reveal a different time-dependent compression behaviour of the specimen. Apparently no significant consolidation delay can be registered, not even within the first seconds after load increment. At these load steps it appears that compression is only due to creep. The decrease in void ratio is rather low for increasing σ'_v, i.e. the specimen shows a low compressibility in this stress range.

In Fig. 5.8 results of two successful compression tests with aluminium oxide peloids of charged particles are presented. Both compression curves coincide in the higher vertical effective stress range. The divergence of both curves in the range of $\sigma'_v \approx 10$ kPa is attributed to jamming of the filter paper in the gap between the top plate and the ring and therefore friction between them. For higher stress levels, this friction is rather negligible.

Comparison with the results obtained with uncharged particles (Sec. 5.2) shows that even at higher σ'_v of the observed stress range the compression curves of uncharged and charged particles do not coincide. The corresponding void ratio is considerably higher for uncharged particles, and also a prediction of the σ'_v-range for the merge of all curves is hardly to give.

5.2.3 Oedometric compression with uncharged particles and NaCl added

Fig. 5.9 shows the compression behaviour of aluminium oxide peloids of uncharged particles (pH9) in the presence of Na^+ and Cl^- ions. The peloids were prepared by dissolving NaCl in water to achieve an ion concentration of $n_f = 1.35$ M. Subsequently the required amount of aluminium oxide powder was added for an initial void ratio of $e_0 = 2.18$. These mixtures were then subjected to oedometric compression. For comparison, previous results obtained with uncharged and charged particles without salt (Sec. 5.2.1 and 5.2.2) are included in Fig. 5.9.
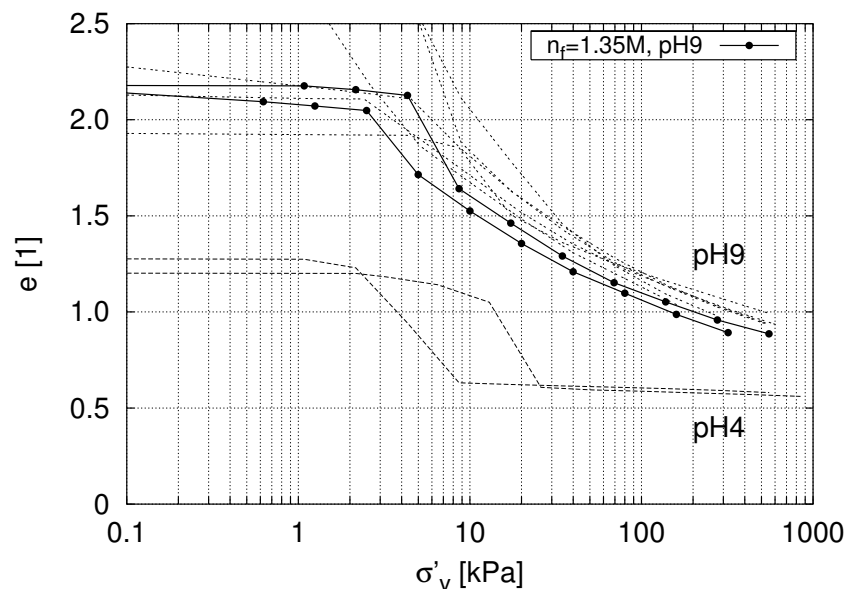
Figure 5.9: Void ratio e vs. effective vertical pressure σ'_v of aluminium oxide peloids with uncharged (pH9) particles and an ion concentration of $n_f = 1.35$ M NaCl of the pore water

Test results yielded no characteristic influence of Na^+ and Cl^- ions on the compression behaviour of uncharged aluminium oxide peloids. The courses of both compression curves follow the one obtained without salts.

5.2.4 Oedometric compression with charged particles and NaCl added

For the investigation of the compression behaviour of aluminium oxide peloids with positively charged particles (pH4) in the presence of Na^+ and Cl^- ions, the preparation method

of Sec. 5.2.3 was adopted. Test results are sorted by two different conditions: In Fig. 5.10a tests with identical initial void ratio but different ion concentration, in Fig. 5.10b tests with different initial void ratio but identical ion concentration are presented.

Regarding the results with identical initial void ratio $e_0 = 1.40$, different compression curves are obtained with respect to the ion concentration (Fig. 5.10a). For the representative range of the vertical effective pressure $\sigma'_v > 10$ kPa, a cross-section at an arbitrarily chosen σ'_v yields a higher void ratio for increasing ion concentration, and the compression
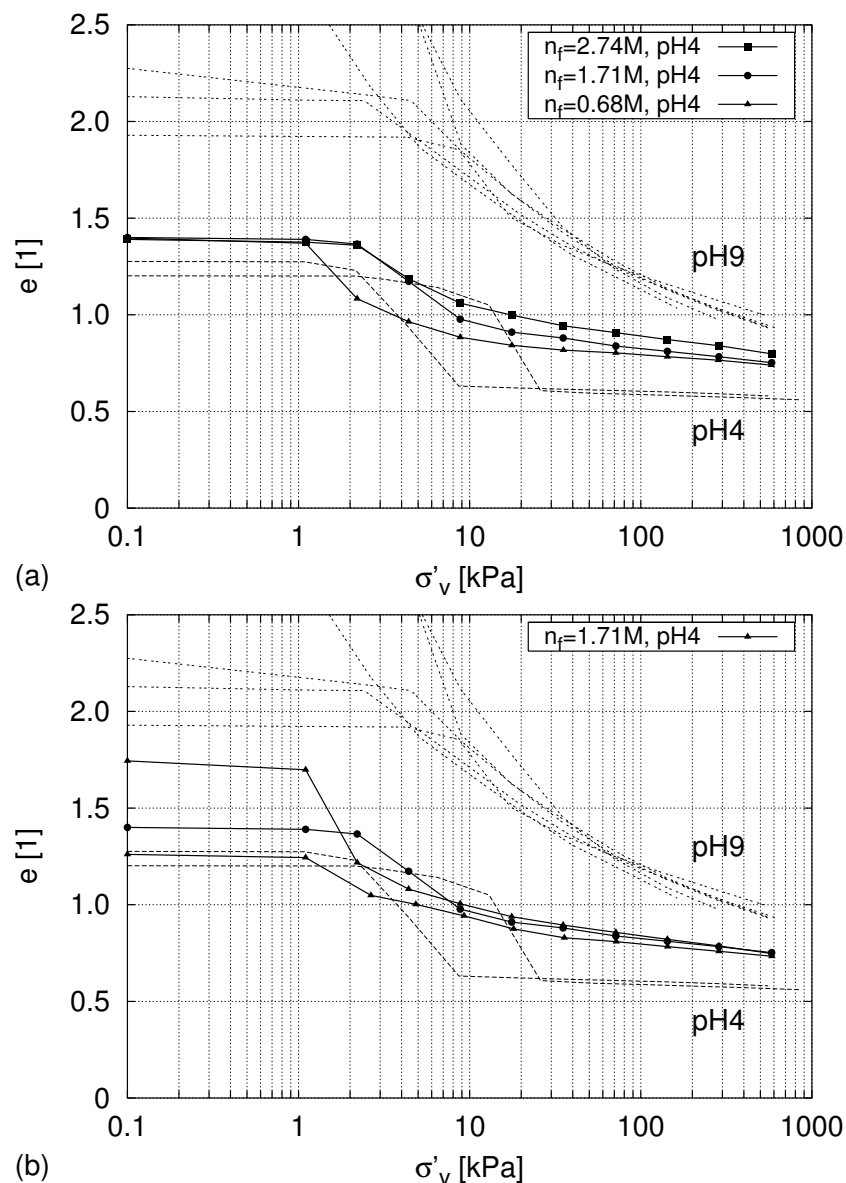

Figure 5.10: Void ratio e vs. effective vertical pressure σ'_v of aluminium oxide peloids with charged particles (pH4): Variation of ion concentration of NaCl of the pore water (a) and variation of initial void ratio (b)

behaviour tends towards the one of uncharged particles. Also for high effective vertical pressures up to the range of $\sigma'_v \approx 1000$ kPa the influence of the ion concentration remains detectable. In the representative σ'_v-range the compressibility is higher with increasing ion concentration. Regarding the results with different initial void ratios but identical ion concentration, the compression curves again coincide for a vertical effective stress range of $\sigma'_v > 10$ kPa.

It is also noteworthy that in these tests there was no expulsion of material (cf. Sec. 5.2.2).

5.2.5 Interpretation

The oedometric compression behaviour of aluminium oxide peloids shows a high dependence on particle charge and ion concentration. This dependence is not only observable in the low vertical effective pressure range, but also shows its imprint for vertical effective pressures of up to 1000 kPa.

For an interpretation of this behaviour it is worth taking a closer look at the specimens' initial structure at the start of the compression tests, since it slightly differs from the one obtained by sedimentation (Sec. 5.1). During the preparation of the specimen for the compression tests, the initial void ratio was presetted by mixing the appropriate amounts of aluminium oxide and water. In general these void ratios were different from the ones obtained by sedimentation: At pH9 the void ratio by preparation was smaller than the one by sedimentation, at pH4 vice versa. This is just the situation captured by Fig. 5.4, hence the specimen's initial structure is qualitatively represented by the micrographs. Consequently at pH4 the repulsive particles are suspended, and the suspension contains comparatively large macropores filled with water. Whereas, at pH9 the attractive particles form a precompacted sediment with comparatively small water-filled macropores (cf. Sec. 5.1.3).

In the following interpretation of the compression behaviour, particle strength and stiffness are considered as comparatively high. In the observed stress range there is only, if any, non-significant particle fraction, and merely minor particle deformations occur. With this simplification, any compaction is only due to rearrangement of the particle fabric.

Oedometric compression of aluminium oxide peloids with attractive particles (pH9) due to stepwise loading (Sec. 5.2.1) causes a successive densification of the particle fabric. Each load step is accompanied by a delayed consolidation, indicating a noteworthy decrease in pore volume. During the corresponding excess pore water pressure reduction, the particle fabric seems to be considerably rearranged, finding a new configuration to withstand the load. This configuration seems not to be significantly altered during the subsequent creep

phase. The corresponding void ratios are still comparatively high and can only be justified with the existence of lattices. These lattices consist of secondary particles, the latter formed by primary particles under the presence of attractive forces between the particle contacts and shear resistance via friction. The secondary particles are also attractive and form a three-dimensional network due to the same properties at their contacts. This meta-stable assembly can develop a remarkable bearing capacity despite of rather low physico-chemical contact forces (see Sec. 5.5 for an estimation of the interparticle pressure). If these physico-chemical contact forces could be neutralized, the particle network would collapse.

Results of a set of oedometric compression tests with uncharged particles (pH9) show that independently of the initial void ratio e_0 the subsequent compression behaviour is very similar. After sufficient load increments the same compression curve is reached, indicating that the corresponding particle network configuration is reproducible. Hence it is concluded that a representative compression curve is existing, which is asymptotically reached during load increase. This representative compression curve describes the course of the lowest possible density to withstand oedometrical loading, its characteristics seem only to depend on pH.

Oedometric compression of aluminium oxide peloids with charged particles (pH4) due to stepwise loading (Sec. 5.2.2) shows a different densification behaviour. As a result of the sample preparation, the specimens are suspended at the beginning of the test. Initial load steps give rise to a filtering of these suspensions, indicated by a delayed compaction due to the necessary flow of pore water. During this compaction, the particles are free of local translational and rotational motion (cf. Sec. 5.1.3), with the consequence that a rather dense sediment is obtained after completion of the filtration process. This sediment shows only a low compressibility with further load increment, and no significant consolidation delay. The corresponding creep rate is significantly higher than the one of uncharged particles, giving raise to the assumption that the particles are not in contact (cf. Sec. 2.5.3) in the observed vertical stress range. Therefore the particle fabric can be rearranged more easily under constant vertical load, with this rearrangement driven by thermal oscillation.

Results of a set of oedometric compression tests with charged particles (pH4) again show that after sufficient load increments the same compression curve is reached, hence the corresponding particle fabric configuration is reproducible. The compression behaviour can be described by means of a representative compression curve for the course of the loosest possible density to withstand oedometrical loading, again asymptotically reached during load increase. The characteristics of this representative compression curve seem only to depend on pH.

Oedometric compression of aluminium oxide peloids with uncharged particles (pH9) and substantial NaCl-concentration of the pore water show the same results like without salt. This is totally in agreement with the theory, since there is no specific attraction of the counter-ions towards the particle surface and no surface charge to shield (Fig. 2.20, IEP). The dissociated Na^+ and Cl^- will be evenly distributed in the pore water without any further effect on the mechanical behaviour of the peloid. Therefore the above said for uncharged particles (pH9) without salts remains valid.

In contrast, oedometric compression of aluminium oxide peloids with charged particles (pH4) and substantial NaCl-concentration of the pore water shows a considerable dependence of the densification behaviour on the presence of ions. For same initial void ratio e_0, lower n_f results in a denser particle network at the same vertical stress level. This can be theoretically substantiated by the increase of the ζ-potential with decreasing n_f (Fig. 2.20, pH4). With higher ζ-potential the particles appear higher charged, therefore the representative compression curve tends towards the one of maximum charged particles (pH4, $n_f = 0$). For the same ion concentration n_f, vertical loading with different e_0 yields the same representative compression curve. Again, this is in agreement with above findings of pH4 and pH9 peloids without salts.

In summary, the representative oedometric compression curve for the lowest possible density is characterized by the particles' ζ-potential. Herewith the influence of pH and ion concentration is covered.

5.3 Isotropic compression tests

The investigation of the isotropic compression behaviour was executed with a newly developed device (Sec. 4.4). Principally, a saturated specimen was isotropically compressed by suction pressure of the pore water due to evaporation of the latter. Therefore isotropic compression results from the increase of isotropic pore water suction pressure and is therefore a stress-controlled method.

5.3.1 Isotropic compression with uncharged particles

In Fig 5.11a the typical time development of the specimen's mass during an isotropic compression test with an aluminium oxide peloid of uncharged particles (pH9) is presented. The apparent jump in mass at $t = 0$ represents the placement of the specimen onto the plate, enabling the determination of the specimens total mass at the beginning of the test.

With ongoing time, the mass of the specimen decreases due to evaporation of the pore
water.

Fig 5.11b shows a typical development of the suction pressure $p_a - p_w$ during the test,
expressed as the difference between the absolute atmospheric pressure p_a and the absolute
pore water pressure p_w. At initialization of the test, $p_a - p_w = 0$ indicates full saturation of
the specimen with no suction pressure. With ongoing evaporation $p_a - p_w$ decreases, first
accompanied by an increasing rate of suction pressure. At $p_a - p_w \approx -20$ kPa a kink in
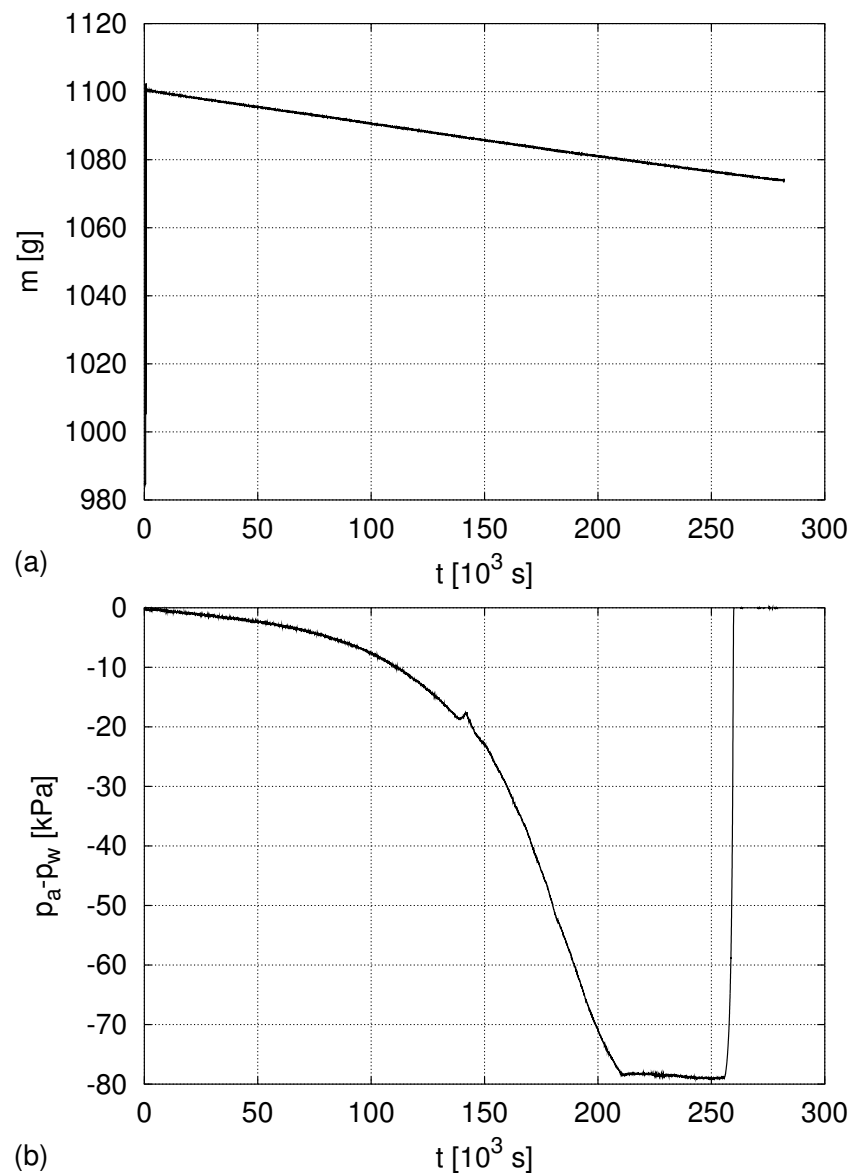
Figure 5.11: Development of (a) the mass m and (b) the suction pressure $p_a - p_w$ of the
specimen with time t during an isotropic compression test with an aluminium oxide peloid
of uncharged particles (pH9)

suction pressure development is observed, which is attributed to a stick-slip motion of the specimen relative to the base plate. At $p_a - p_w \approx -80$ kPa the maximum suction pressure is recorded at the transducer and kept almost constant for approx. $50 \cdot 10^3$ s. In this period of time gas bubbles develop in the dead volume of the pressure transducer. Although the suction pressure within the specimen is further increasing, it is not detected any longer by the transducer due to expansion of the gas bubbles. Finally, a sudden percolation due to capillary entry led to a total loss of suction. After the tests, a break-through channel between the specimen and the base plate could be clearly identified.

From Fig 5.11a and b, a compression curve can be derived by means of the recorded data. The void ratio is determined by e_0 at the beginning of the test and the loss of pore water during evaporation, under the assumption of full saturation of the specimen. The effective pressure is equal to $p_a - p_w$ (cf. Sec. 4.4).
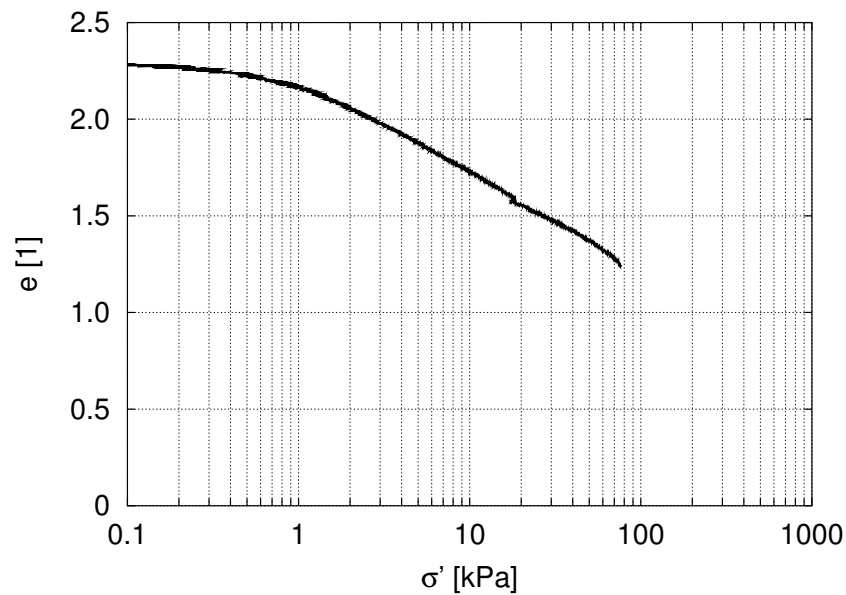
Figure 5.12: Translation of Fig. 5.11 into a e-ln σ'-diagram (isotropic compression of an aluminium oxide peloid at pH9

The isotropic compression curve (Fig. 5.12) shows, after a precursory transition range, an almost linear decrease of the void ratio with increasing logarithmic effective pressure up to $\sigma' \approx 80$ kPa. At this point the compression curve is cut off due to capillary entry.

Results of several tests with uncharged aluminium oxide particles and different initial void ratios are shown in Fig 5.13. In general, all curves show a similar behaviour as described above. For all investigated initial void ratios e_0, the curves tend to coincide for increasing σ'.
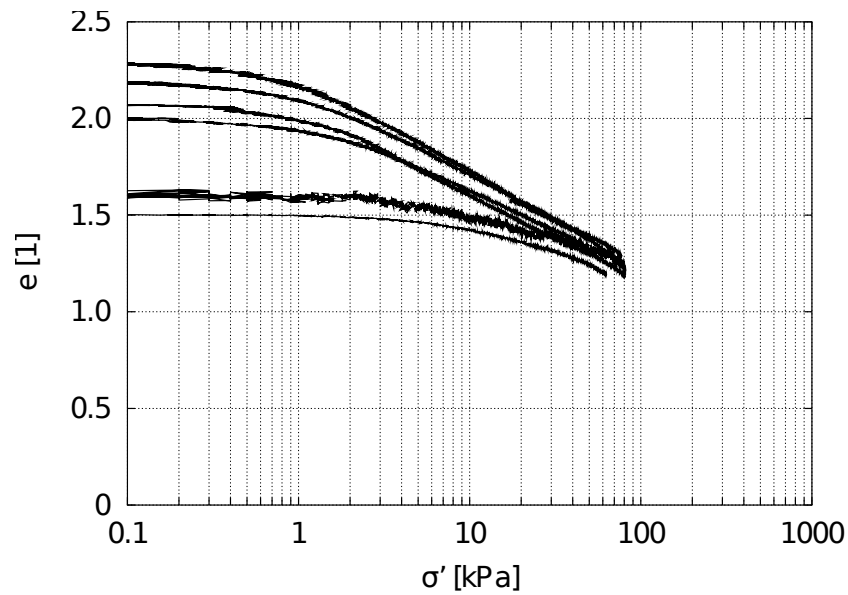
Figure 5.13: Isotropic compression of a set of aluminium oxide peloids at pH9

5.3.2   Isotropic compression with charged particles

The tests with aluminium oxide peloids of positively charged particles (pH4) were performed like described in Fig. 5.3.1. To prevent spreading of the initially liquid-like specimen, a flexible ring of approx. 5 cm in diameter and height was applied. The ring was set centrical to the filter stone and the gap between ring and base plate was sealed with silicone grease. Nevertheless, only one reliable test could be performed successfully.

Figure 5.14: Isotropic compression of an aluminium oxide peloid at pH4

Fig 5.14 illustrates the isotropic compression behaviour of aluminium oxide peloids of positively charged particles (pH4). The compression curve is nearly horizontal, i.e. the compressibility is very low. Comparison with the also plotted results obtained with uncharged particles (pH9) show that the compression curves for the charged and uncharged particles are far away from each other, at least in the effective pressure range up to $\sigma' \approx 80$ kPa.

5.3.3 Interpretation

Isotropic compression tests of saturated specimens induced by suction pressure due to evaporation of pore water represent a feasible method for the study of the compression behaviour. In contrast to the problems with friction of the oedometers' cantilever system, the isotropic compression apparatus generates the load in a very gentle manner. This especially enables the investigation of the compression behaviour in the range of very low effective pressures.

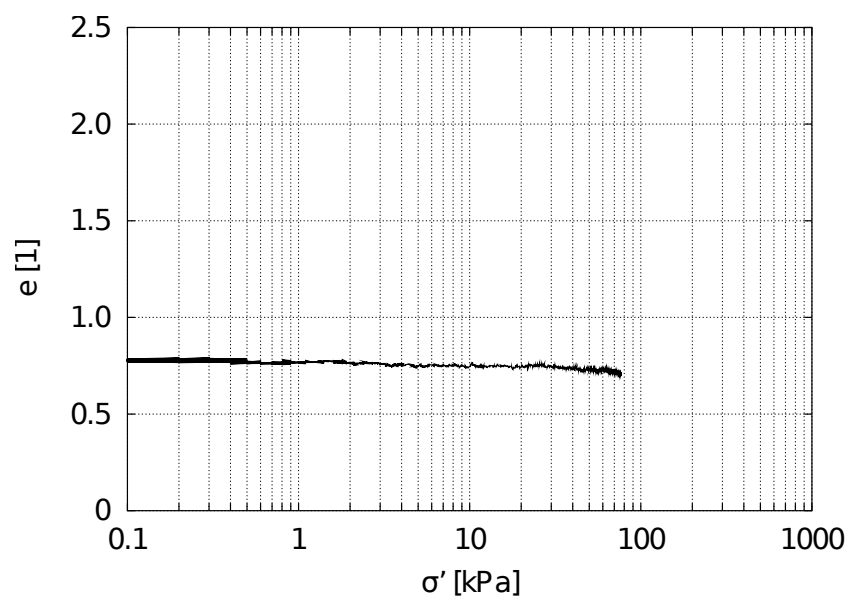As expected, the isotropic compression behaviour of aluminium oxide peloids shows a high dependence on the particle charge. Tests with uncharged particles (pH9) reveal a comparatively high stiffness in the very low effective pressure range (Fig. 5.12). This indicates that the lattice structure of the peloid is able to carry minor loads without considerable rearrangement of the attractive particles. Further increase of the effective pressure gradually yields a compression and therefore rearrangement of the particle fabric. Interestingly, the corresponding compression curve follows a straight line in the e-$\ln \sigma'$-diagram, indicating the lowest possible density of the particle fabric for the carriage of isotropic loading (cf. Sec. 1.2).

Further tests with aluminium oxide peloids of uncharged particles (pH9) show the same compression behaviour (Fig. 5.13). Results with lower initial void ratios e_0 show a larger effective pressure range of high stiffness at the beginning, indicating that the lattice structure possesses a sufficient bearing capacity to carry the loads without considerable rearrangement. With further effective pressure increase all compression curves are approaching the curve of lowest possible density asymptotically.

Results of the isotropic compression test with an aluminium oxide peloid of charged particles (pH4) yield a very high stiffness throughout the entire effective stress range. Densification of the suspension towards a sediment cannot be seen in Fig. 5.14 since it takes place without the generation of noteworthy suction pressure. As already discussed in Sec. 5.1.3 and 5.2.5, further densification of the sediment is quite low due to the comparatively dense arrangement of the charged particles during the transition from suspension

to sediment.

Above results of isotropic compression can be compared with the ones of oedometric compression (Sec. 5.2) via the mean skeleton pressure

$$p_s = \frac{p_{s1} + p_{s2} + p_{s3}}{3} \tag{5.1}$$

with the principal pressures p_{s1}, p_{s2} and p_{s3}. For oedometric conditions, $K_0 = p_{s2}/p_{s1} = p_{s3}/p_{s1} = 1 - \sin \varphi_c$ holds. Due to symmetry of the oedometer, p_{s1} represents the vertical effective pressure σ'_v. Herein, DLVO particle interaction p_n is neglected, since it would not significantly contribute at least in the higher p_s-range (cf. Sec. 5.5 for the range of p_n). Anticipating $\varphi_c = 38°$ from direct shear test results (Sec. 5.4) the mean skeleton pressure for oedometric conditions becomes

$$p_s = \sigma'_v \frac{1 + 2(1 - \sin \varphi_c)}{3} = 0.590 \, \sigma'_v \quad . \tag{5.2}$$

For isotropic compression $p_s \equiv \sigma'$ holds.

Comparison of the isotropic and oedometric compression test results is shown in Fig. 5.15. Independent of pH the isotropic compression curves are always above the ones for oedometric compression. This is explained with the difference in principal pressures $p_{s1} = \sigma'_v$ and $p_{s2} = p_{s3} = K_0\sigma'_v$ and the corresponding deviatoric stress during the oedometric compression, yielding a minute shearing of the grain skeleton during compaction. Isotropic
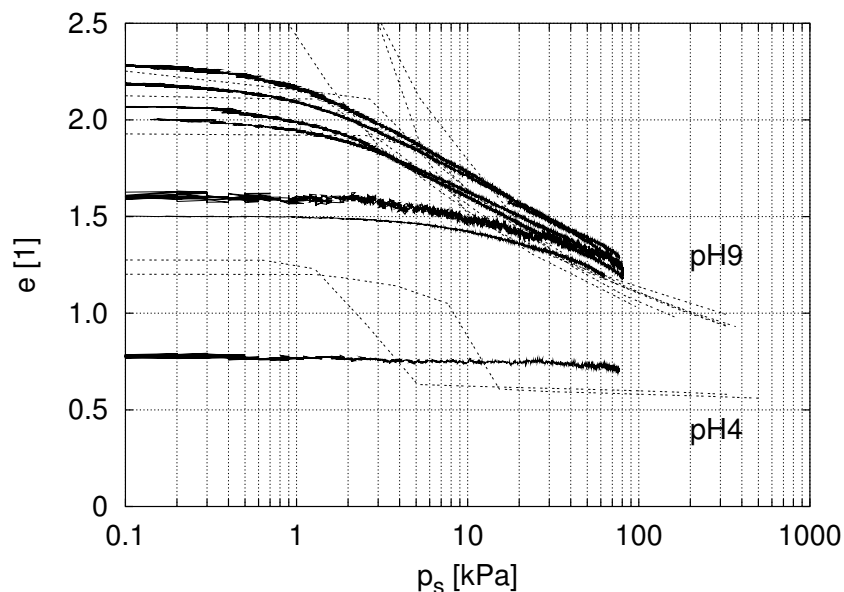
Figure 5.15: Comparison of oedometric and isotropic compression via the mean skeleton pressure p_s

compression is free of deviatoric stress, therefore a higher void ratio is obtained for the same p_s as compared with oedometric compression (cf. Sec. 1.2).

5.4 Drained shear tests

Tests in the direct shear device (Sec. 4.7) were executed to investigate the mechanical behaviour under drained shearing up to a critical state and to determine the critical friction angle, both with dependence on pH.

5.4.1 Drained shearing resistance with uncharged and charged particles

Exemplarily, test results are presented for aluminium oxide peloids at pH4 and pH9 with constant vertical pressure $\sigma'_v = 44$ kPa by plots of the shearing resistance τ and the vertical settlement Δh versus the horizontal displacement s (Fig 5.16). Other tests yielded similar results.

For both pH the shearing resistance is initially increasing with horizontal displacement up to a certain limit and then remains constant with further shear deformation, which indicates that the critical state was reached within the specimen. In order to reach the critical state, less shear deformation is required at pH4 than at pH9.

Fig. 5.16 shows that shear deformation with constant vertical pressure first yields a remarkable densification of the pH9-peloid, but after sufficient shear deformation no further densification can be observed. At pH4 a minor densification occurs, which is then reversed with ongoing deformation so that the density at the end of the test almost equals the initial one. Since there were no further changes in specimen volume observable after a sufficient shear deformation, it is assumed that a critical state was reached for both the pH9 and pH4 specimens.

In Fig. 5.17 the critical shear strength τ_f is presented versus σ'_v. Proportionality between τ_f and σ'_v can be concluded with independence of pH. A line of best fit through the origin of the coordinate system can be found. Its inclination yields the angle of friction in critical states

$$\varphi_c = \arctan \frac{\tau_f}{\sigma'_v} = 38° \quad , \tag{5.3}$$

which is independent of pH. An effective cohesion c' was not registered, consequently.
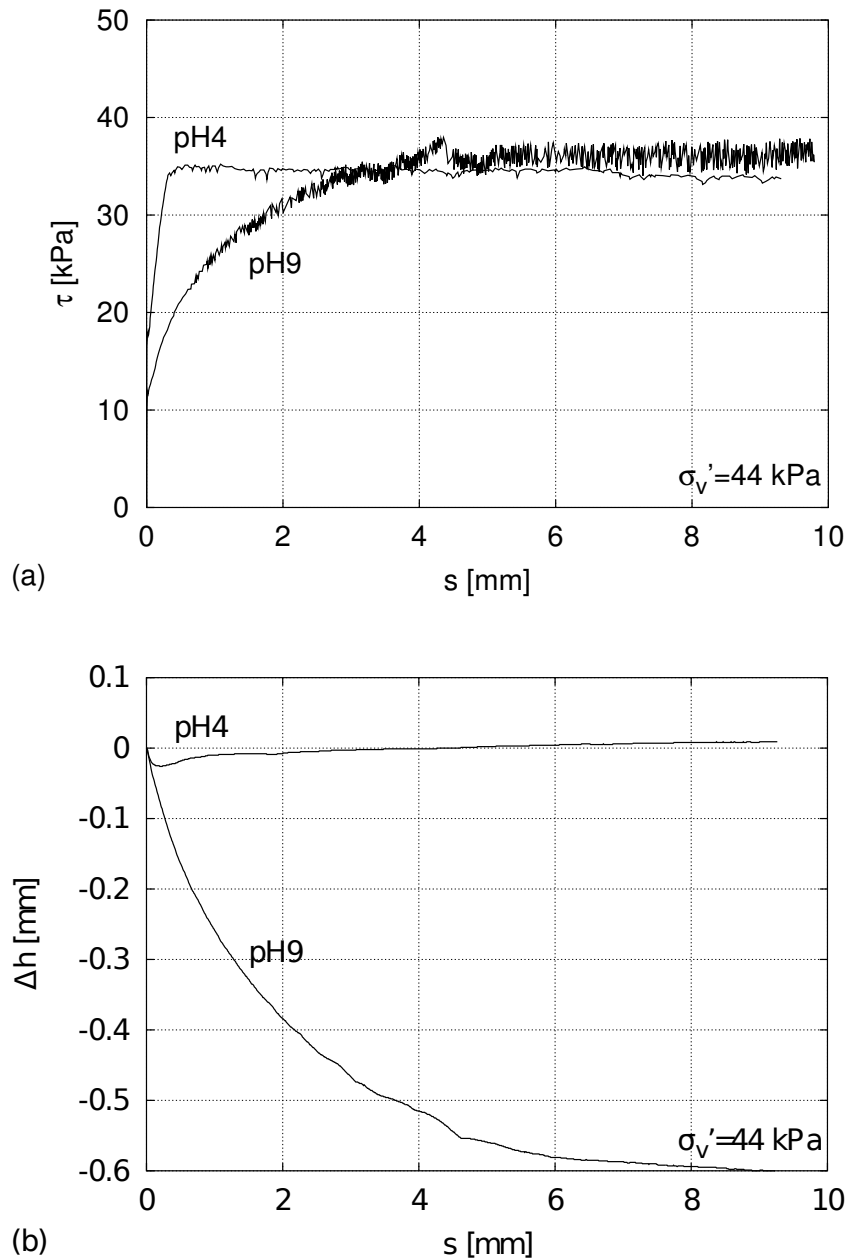
Figure 5.16: Shearing resistance τ (a) and vertical settlement Δh versus horizontal displacement s (b) of aluminium oxide peloids at pH4 and pH9 in drained shear tests.

Several attempts were made to determine critical void ratios e_c at the end of the tests. One procedure for the determination of e_c was via the dry mass and the dimensions of the specimen. Another procedure was the determination via the water content at the end of the test under assumption of full saturation. Both procedures yielded inconsistent results with each other and with the results of oedometric and isotropic compression. A further method of buoyancy weighting failed during the coating with paraffin wax due to fracture
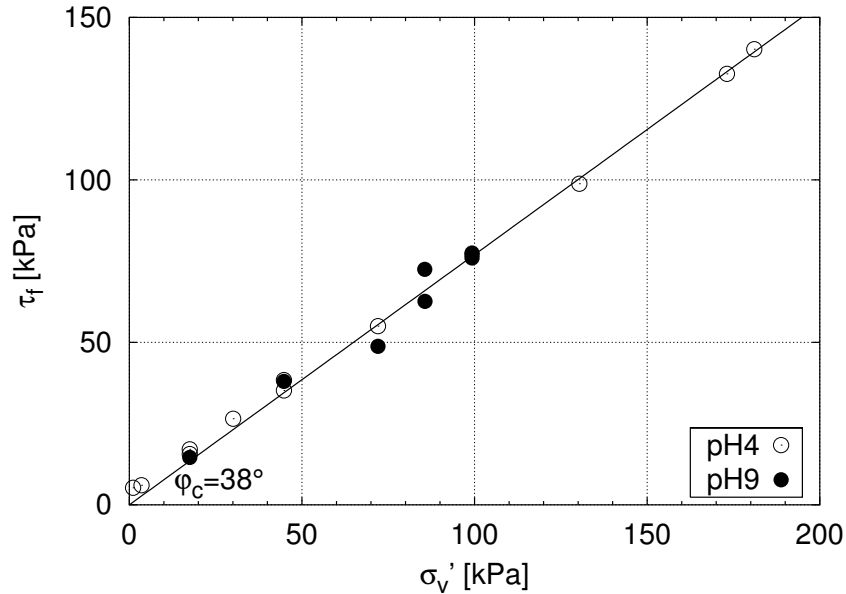
Figure 5.17: Shear strength τ_f versus vertical effective pressure σ_v' of aluminium oxide peloids at pH9 and pH4, respectively.

of the thin and fragile specimens. Therefore critical void ratios as for drained shearing could not be reliably determined.

5.4.2 Interpretation

Drained shearing of aluminium oxide peloids with uncharged particles (pH9) shows a densification due to the rearrangement of the particle fabric. Since the latter consists of lattices made of primary and secondary particles, this fragile three-dimensional particle network (cf. Fig. 5.3b) is successively brought to collapse by extensive horizontal shearing under simultaneous vertical loading. Drainage in conjunction with low shear rates allows the pore water to flow out. After sufficient shear deformation a steady state is reached with a densified and more homogeneous particle network. Then the existence of macropores is very unlikely. Fluctuation in shear resistance τ with ongoing deformation could represent a successive creation and decay of force-chain assemblies.

Drained shearing of aluminium oxide peloids with charged particles (pH4) initially yields a minute densification (contractancy) and subsequent reversal (dilatancy). No significant overall densification is obtained due to large shear deformation, i.e. the void ratio remains nearly unchanged. This behaviour is attributed to the comparatively dense and homogeneous particle assembly (cf. Fig. 5.3a) and to the oedometrical loading of the specimen before the shear deformation. During initial oedometric loading steps a small deviatoric

shear stress is sufficient for a rearrangement of the repulsive particles towards a critical void ratio (Sec. 5.3.3). Further load increment results in a successive minute compaction with the fundamental consequence of particle contact. The existence of particle contact is proved by the subsequent behaviour under shearing, which is characterized by typical friction as described by the law of Amontons and Coulomb (e.g. PERSSON 2000).

The presented results show that in a critical state the shearing resistance is proportional to the effective pressure. The critical friction angle φ_c is a material constant and independent of pH. A true cohesion c', i.e. shearing resistance at vanishing σ'_v, was not detected for critical states. This suggests the assumption that attractive (pH9) or repulsive (pH4) pressures due to particle surface interactions are in the range of diagram resolution or below. The observed deviation of data points in the very low σ'_v-range is attributed to parasitary friction of the shearing device.

Though e_c could not be determined experimentally, it can be estimated qualitatively from the contractant or dilatant shear behaviour. At pH9 a remarkable contractancy was observed, indicating an e_c far below the initial void ratio e_0. At pH4, dilatancy almost compensates initial contractancy, suggesting that e_c is very close to e_0. At least in the low effective vertical stress range, the critical void ratio at pH9 is expected to be higher than at pH4, since interparticle attraction at pH9 supports a minute dilatancy even in a critical state.

5.5   Undrained shear tests

For the investigation of the undrained shear strength of aluminium oxide peloids, cone penetration and vane shearing tests were executed. The tests focused at the influence of the void ratio e (or solid volume fraction $\alpha_s = 1/(1+e)$), of pH and of the ion concentration n_f.

5.5.1   Undrained shearing resistance with respect to the particle charge

The undrained shearing resistance c_u of aluminium oxide peloids was investigated by cone penetration tests (Sec. 4.5). Therefore several specimens were prepared with different pH and solid volume fraction α_s and were subsequently tested.

Results are presented in Fig. 5.18 as a 3D-plot. This plot is based on numerous single test results with interpolated intermediate values. The maximum $c_u \approx 2$ kPa is obtained
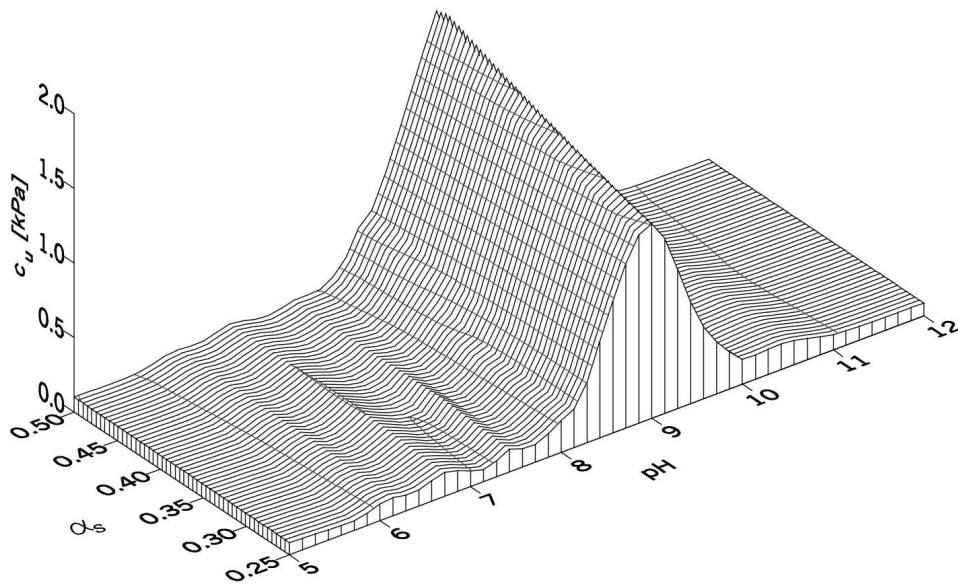
Figure 5.18: Undrained shearing resistance c_u of aluminium oxide peloids with respect to pH and the solid volume fraction α_s

at pH9 and $\alpha_s \approx 0.5$. For pH above or below pH9, a drastic decrease of c_u is registered. Below pH8 and above pH10 c_u almost vanishes. In the range of pH8 to pH10 an increase of c_u with increasing solid volume fraction is registered.

5.5.2   Undrained shearing resistance with respect to the ion concentration

The influence of NaCl on the undrained shearing resistance c_u of aluminium oxide peloids was investigated with positively charged particles (pH4) only. Tests with uncharged particles (pH9) were not considered, since it was already shown that the ion concentration then has no influence on the interparticle forces (Sec. 5.2.3). The specimens were prepared with water of different ion concentrations and subsequently subjected to cone penetration tests.

Test results are presented in Fig. 5.19. For constant void ratio the increase of ion concentration yields an increase of the undrained shearing resistance. Above a certain ion concentration no further increase of c_u can be obtained. For lower void ratios, this c_u-limit is reached at lower ion concentration. For a given ion concentration c_u increases with decreasing void ratio. A certain c_u can be reached either by a combination of low void ratio and low ion concentration or by a combination of high void ratio and high ion
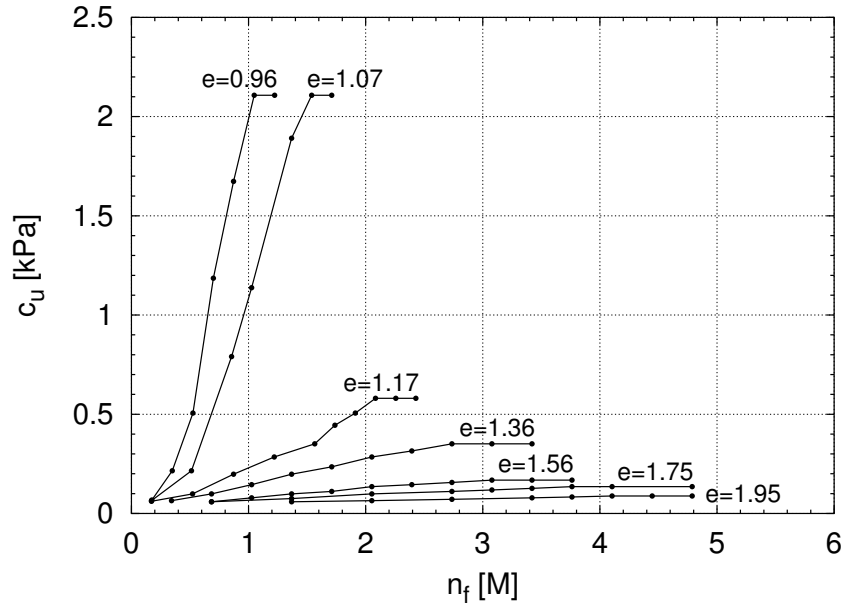
Figure 5.19: Undrained shearing resistance c_u of charged aluminium oxide peloids (pH4) with respect to the ion concentration n_f of NaCl and the void ratio e

concentration, but the entire c_u-range cannot be covered by an arbitrary combination of void ratio and ion concentration.

5.5.3   Interpretation

The undrained shearing resistance of aluminium oxide peloids was investigated in a much lower skeleton pressure range than in the drained direct shear tests (Sec. 5.4). There it shows a high dependency on the particle charge, which can be explained by the DLVO-interaction (Sec. 2.5.3).

At pH9 the DLVO-interaction is maximally attractive. Since the particles are in contact, friction at the particle contacts then generates a maximal c_u, even though the particle network is loose and contains large macropores. With a higher solid volume fraction, the number of particle contacts increases, and consequently c_u increases. A change of pH down to pH7 or up to pH10 yields an increase of the absolute value of the ζ-potential. Therefore the particle attraction is reduced, resulting in a lower c_u. Below pH7 and above pH10 the DLVO-interaction becomes repulsive and the particle are not in contact, and consequently c_u vanishes.

From the tests results the skeleton pressure p_s due to attractive DLVO-interaction can be

estimated. The undrained shearing resistance

$$c_u = p_s \tan \varphi_c \qquad (5.4)$$

depends on this skeleton pressure and the critical friction angle φ_c. Since $\varphi_c = 38°$ is already known from drained shearing tests (Sec. 5.4), inversion of (5.4) yields $p_s = p_{att} = c_u / \tan \varphi_c \approx 3.5$ kPa with $c_u = 2$ kPa at pH9. In contrast, the skeleton pressure due to repulsive DLVO-interaction is zero, since the particles are separated according to the distance of the local minimum of the particle interaction potential (cf. Sec. 2.5.3).

For aluminium oxide peloids at pH4 the addition of NaCl yields a screening of the particle charge. Therefore, the initially repulsive particles become attractive if the ion concentration is above the critical coagulation concentration of $n_f \approx 2 \cdot 10^{-1}$ M (cf. Fig. 3.4). Therefore the tests were executed with this n_f and above. Results show that the same maximum $c_u \approx 2$ kPa like for uncharged particles can be reached if a sufficient amount of NaCl is added and the void ratio is comparatively low. Then, the number of particle contacts contribute to the same $p_s = 3.5$ kPa. Further increase of the ion concentration yields no further increase of c_u, i.e. a maximum screening of the particle charge is already reached.

5.6   Other tests

In this section test are listed which could not be performed successfully. Possible causes are named and, if available, related improvements are suggested.

5.6.1   Coupled tumble-shrink tests

Coupled tumble-shrink tests (Sec. 4.8) aimed at a maximum possible density for a given p_s. During test execution, formation of an unsaturated crust on top of the specimen was registered. The crust showed a high stiffness, was acting like a rigid disc and therefore was preventing a homogeneous cyclic deformation of the entire cylindrical specimen.

This phenomenon occurs if the evaporation rate is too high. Then, a flow of sufficient pore water from inside the specimen towards the surface cannot be provided due to the low permeability and the corresponding consolidation delay. The high evaporation rate is attributed to the relative motion between the specimen's surface and the ambient air due to continuous cyclic deformation. Therefore the formation of a laminar boundary layer of almost water-saturated air on top of the specimen is restricted. Consequently, the actual

vapour pressure in the utmost proximity of the specimen's surface is reduced, and the evaporation rate remarkably decreases due to the higher relative humidity.

Therefore, future tests should be executed with control of the relative humidity within a climate chamber. Then, formation of an unsaturated crust can be avoided and the coupled tumble-shrink test could be successful.

5.6.2   Cyclic densification

Direct shear tests with cyclic shear amplitudes (Sec. 4.7) were executed to observe the densification of aluminium oxide peloids towards a maximum possible density. The effectiveness of the method is illustrated with Fig. 5.20a, showing the decrease of specimen's height with increasing number of shear cycles.
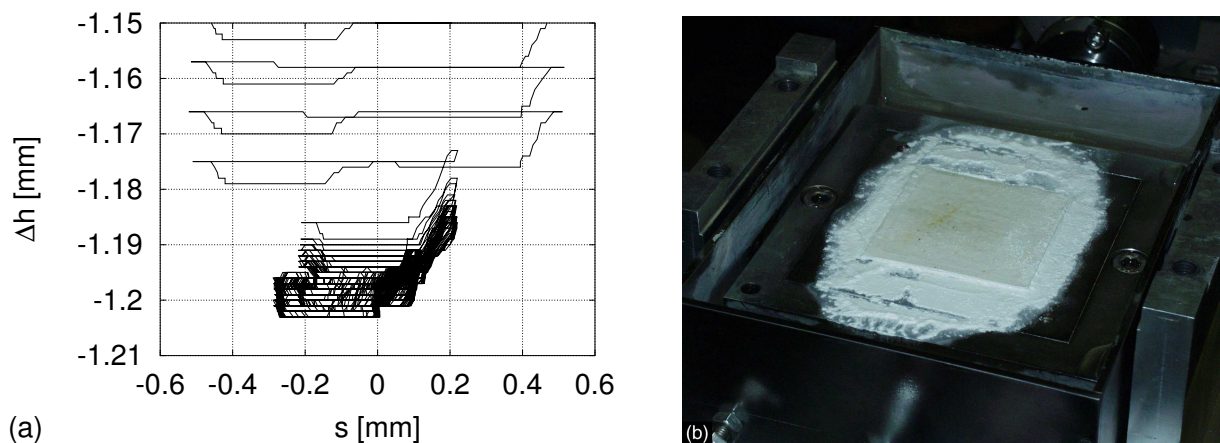
Figure 5.20: Cyclic densification of an uncharged aluminium oxide peloid (pH9): Specimen height vs. shearing amplitude (a), sample after end of the test (b)

Problems were faced during test execution with material passing through the gap between the upper and the lower frame (Fig. 5.20b), and the amount of escaped material was increasing with the number of shear cycles.

No effective sealing method could be found to prevent this effect of cyclic mobility. Preliminary tests with sand demonstrated the basic functionality of this densification method, but successful tests can only be executed with specimens of particle sizes in the range of the clearance and above.

5.7 Summary of aluminium oxide peloid properties

The above presented findings of the mechanical behaviour of aluminium oxide peloids can be summarized as follows:

- Aluminium oxide particles of rather spherical shape appear to have a rather uniform charge distribution at the surface.

- The surface charge depends on pH. At pH9 the surface is uncharged, at pH4 the surface is positively charged.

- The surface charge is shielded by surrounding ions, making the particles to appear less charged than they are at the surface. For uncharged particles the presence of ions has no effect.

- Particle interaction is due to Coulomb repulsion and van-der-Waals attraction. Coulomb repulsion depends on the surface charge and its shielding. Van-der-Waals attraction is ubiquitous and independent of the surface charge.

- Particle interactions can be superimposed. Net attraction is obtained for uncharged, less charged or high charged and ion-shielded particles. Net repulsion is obtained for high charged or high charged and less ion-shielded particles.

- Particle interaction determines the settlement behaviour of a suspension. Net attraction yields agglomeration and fast aggregate settlement. Net repulsion prevents agglomeration and yields slow settlement.

- Particle interaction determines the sediment structure. Net attraction yields a loose honeycomb-like sediment. Net repulsion yields a dense and homogeneous sediment.

- Compression of a peloid with net attraction yields a high compressibility. Compression of a peloid with net repulsion yields a low compressibility. The void ratio of a peloid with net attraction is much higher than the one of a peloid with net repulsion for the same effective pressure level.

- For the same effective vertical pressure level, the void ratio under isotropic compression is higher than the one for oedometric compression.

- The critical friction angle is independent of the particle interaction.

- Drained shearing of a peloid with net attraction is contractant, and the corresponding critical void is ratio far below of the one of oedometric compression. Drained

shearing of a peloid with net repulsion is without significant volume change, and the critical void ratio is about the one of oedometric compression at the same effective vertical pressure level. At least in the low effective vertical pressure level range, the critical void ratio of a peloid with net attraction is higher than the one of a peloid with net repulsion.

- The undrained cohesion of a peloid with net attraction close to the peloid's surface is significant. The undrained cohesion of a peloid with net repulsion is vanishing. The undrained cohesion can be attributed to the particle interaction.

- Net attraction at the sediments surface is in the range of $p_n \approx 3.5$ kPa, net repulsion means $p_n \leq 0$ (c.f. RICHTER 2006).

Chapter 6

Experimental results with laponite peloids

In this section experimental results with laponite peloids are presented. First observations during the preparation of laponite peloids are described in Sec. 6.1. Results of oedometric compression tests are presented in Sec. 6.2, followed by the description of the behaviour under undrained shearing in Sec. 6.3. Other tests which could not be performed successfully are also reported (Sec. 6.4).

6.1 Observations during the sample preparation

The peculiarity of laponite peloids was impressively observed already during the preparation process. Focus was set on the dispersion process of laponite in water with respect to the ion concentration of NaCl (Sec. 6.1.1), and with respect to the order of adding material (Sec. 6.1.2).

6.1.1 Dispersion of laponite in water with different ion concentration

For the preparation of this test series, deionized water was initially adjusted to pH10 by the adding of NaOH and to the desired ion concentration by adding of NaCl. Subsequently, dry laponite powder was poured in, and the slurry was mixed for some minutes. Finally, dispersion was awaited for approx. 12 hours without further stirring.
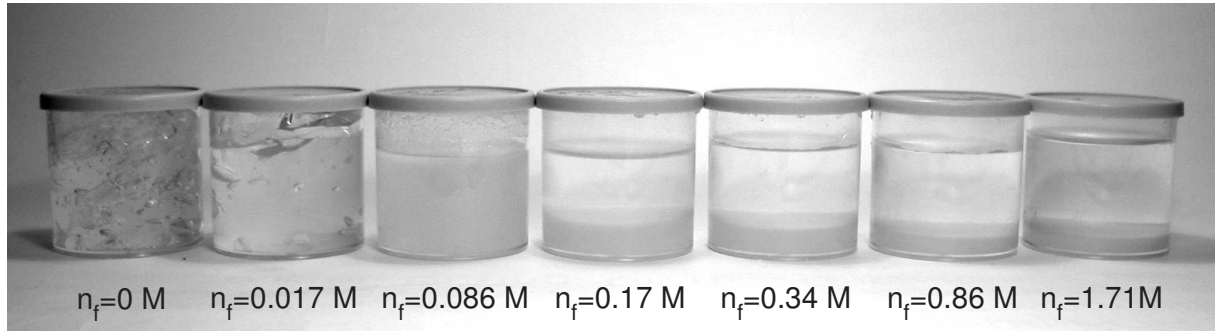
Figure 6.1: Dispersions of laponite powder in deionized water with different ion concentration n_f of NaCl (pH10, solid mass fraction $c = 5$m%)

Results are shown in Fig. 6.1. Without salt a transparent gel with the inclusion of large gas bubbles is obtained. The presence of salt with a low ion concentration of $n_f = 0.017$ M yields a similar dispersion, but the amount of included gas bubbles is far lower. For ion concentrations of $n_f = 0.086$ M and above, the dispersion is opaque. Sedimentation occurs for $n_f \geq 0.17$ M, showing a decrease in sediment height with increasing ion concentration.

Corresponding void ratios e of the gels and the sediments (Fig. 6.2) were determined via the geometry and the solid mass, and under the assumption of full saturation for lack of alternatives. For $n_f \leq 0.086$ M, $e = 54$ is obtained. Minute increase of the ion concentration to $n_f = 0.17$ M yields a drastic decrease of the void ratio down to $e \approx 17$. Further increase of the ion concentration up to $n_f = 1.71$ M results in a successive decrease of the void ratio down to $e \approx 8$.
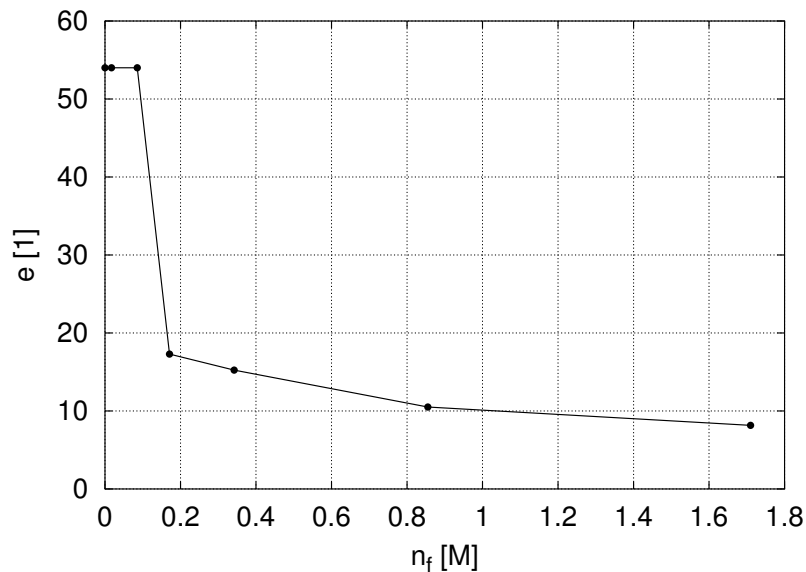
Figure 6.2: Void ratio e of the specimens of Fig. 6.1 with respect to the ion concentration

6.1.2 Dispersion of laponite in water with respect to the order of adding material

Further tests were carried out to investigate the influence of the order of adding material on the flocculation of laponite peloids. Fig. 6.3 shows the state of two laponite peloids with identical mass fraction of $c = 5\text{m}\%$ and identical ion concentration of $n_f = 0.86$ M NaCl after intensive stirring for ca. 15 minutes. Though the composition of the specimens is the same, preparation procedure yields remarkable differences. Fig. 6.3a illustrates the result of adding first salt and then laponite, whereas Fig. 6.3b shows the result of adding first laponite and then salt.
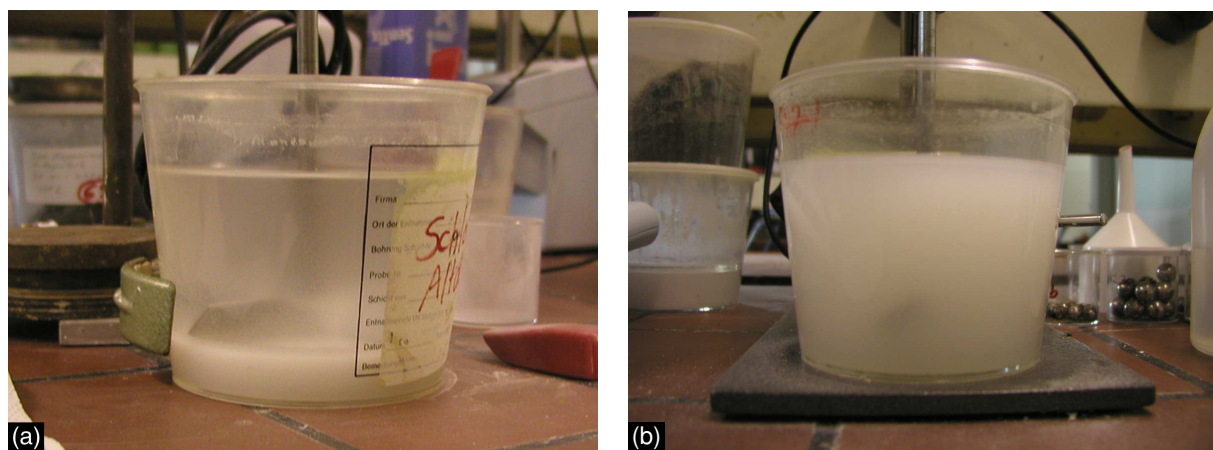
Figure 6.3: Different types of flocculation of laponite peloids with respect to the order of adding material: (a) water-salt-laponite, (b) water-laponite-salt (mass fraction $c = 5\%$, ion concentration $n_f = 0.86$ M NaCl)

The order of adding material has consequences for the settlement behaviour and the resulting peloid. If laponite is added to salty water, rapid settlement is observed with the consequence of a comparatively dense peloid. If salt is added to a laponite suspension, no settlement or segregation is observable and a comparatively disperse peloid is obtained.

6.1.3 Interpretation

Laponite particles at pH10 show a charge distribution of negatively charged faces and positively charged edges (Sec. 2.1 and 3.2). A sufficient ion concentration n_f of Na$^+$ and Cl$^-$ leads to the shielding of the negative charges at the particle faces by sodium cations and to the shielding of the positive charges at the particle edges by choride anions.

If laponite powder is poured into water with a low n_f, dispersion of the particles will be initiated. This process is enhanced by stirring, but some larger aggregates still remain after stirring. At a solid mass concentration of 5 % the dispersed particles are arranged in a nematic gel, i.e. with even particle orientation (Fig. 3.7) and without particle contacts. Transparency indicates that light waves of approx. 400 to 800 nm wavelength can pass the gel, which is only possible for a fairly low mass concentration in conjunction with a good dispersion of primary particles (particle diameter 25 nm, cf. Sec. 3.2.1). Larger dry aggregates of primary particles, which were not dispersed during stirring, are successively dispersed with time. The gas enclosed by the added powder joins to larger gas bubbles, which remain enclosed in the gel structure.

If laponite powder is poured into water with a higher n_f, the Na$^+$ and Cl$^-$ ions are attracted towards the particle faces and edges, respectively. Hence, the particle surface charges are shielded. For $n_f \geq 0.017$ M, termination of stirring enables the coagulation of primary particles, and the resulting secondary particles settle rather rapidly. The obtained sediment thus shows a higher density for higher n_f.

The above test results can be depicted in the phase diagram of Fig. 3.7 (Fig. 6.4). Tests without addition of NaCl are usually represented by $n_f = 10^{-4}$ due to ubiquitous impurities. All points are located in the corresponding phase area, the one with $n_f = 0.017$ M being close to the transition between nematic gel and flocculation.
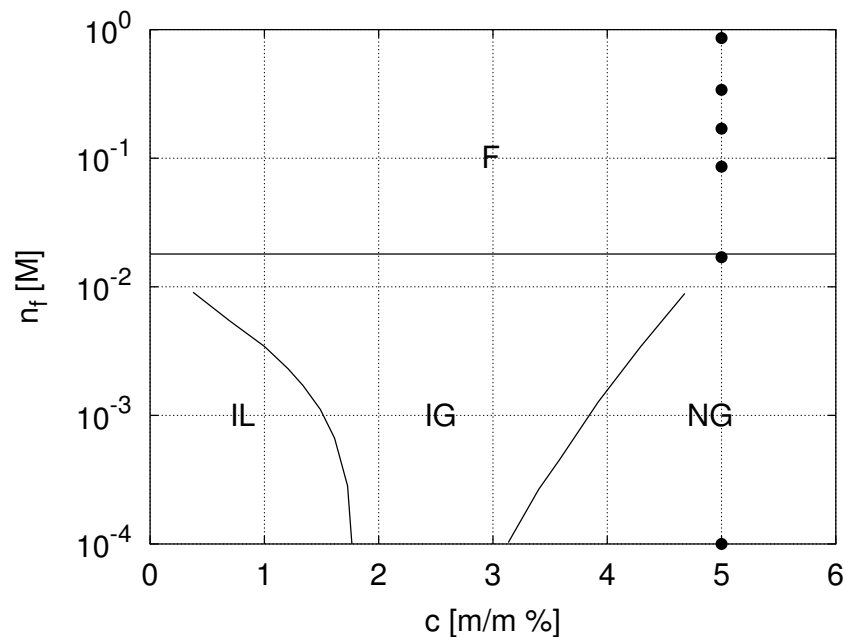
Figure 6.4: Test results of Fig. 6.1 illustrated in the phase diagram of Fig. 3.7 (pH10, $c = 5$ m%)

The order of material addition is not covered by the phase diagram. This is substantiated by Fig. 6.1, showing different sediment structures for the same point in the phase diagram (Fig. 6.5). Addition in the order of salt and laponite presumably generates a kind of crust around the agglomerated particles immediately after immersion. With this crust, the particle charge is shielded by the ions, making the particles attractive. By further wetting of the agglomerate, water and ions penetrate towards the agglomerate's centre. Hence, the inner particles become attractive, and the existing structure is strengthened. Stirring of such agglomerates does not result in a noticeable dispersion, so the agglomerates settle rapidly just after the end of stirring.
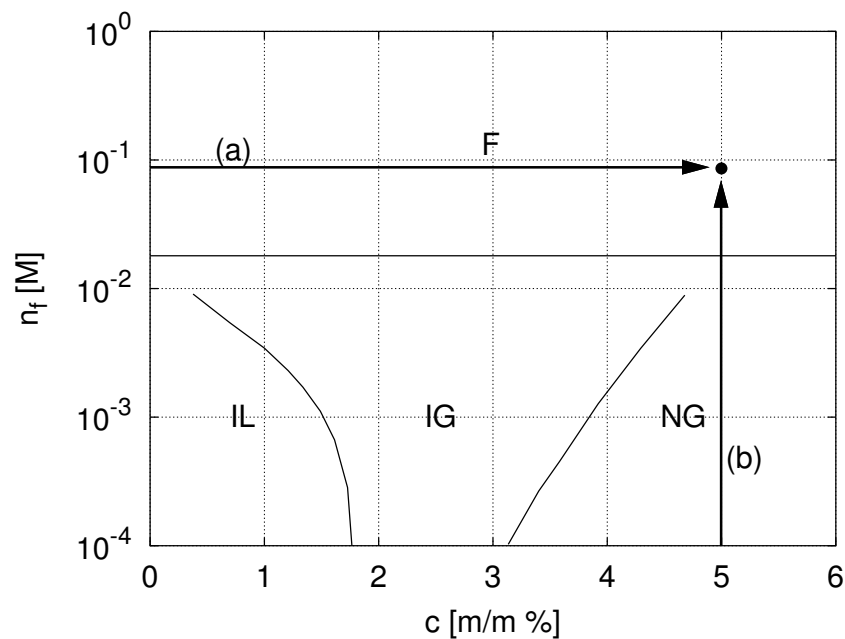
Figure 6.5: Illustration of the preparation paths of Fig. 6.3 in the phase diagram of Fig. 3.7

Mixing of laponite and water causes the dispersion of laponite aggregates. The subsequent addition of salt leads to a shielding of the particle charges, so the particles become attractive. After the end of stirring, the particles agglomerate and settle, forming a macroporous loose peloid of small agglomerates with net attraction.

This dependency on the preparation paths is not represented by the phase diagram of Fig. 3.7.

6.2   Oedometric compression tests

The oedometric compression behaviour of laponite peloids was investigated principally with the same devices and procedures as the ones employed for aluminium oxide peloids

(Sec. 5.2). Typical beakers of 76 mm and 100 mm in diameter were used with an initial height of the specimen of approx. 20 mm. Due to the high compressibility of laponite peloids, which was expected in consequence of the high initial void ratios after preparation, the oedometer device reached its kinematic limits. Therefore a procedure was developed to enable a shifting of the top plate during the tests. Since the reference level of the dial gauge was not affected by this procedure, the readings of the specimen height could be taken continuously. Shifting of the top plate during constant loading was carried out very sensitively in order to avoid a disturbance of the specimen. Nevertheless, in later tests the time-consuming consolidation process was shortened by reducing the initial height of the specimen to 10 mm, which was within the kinematic range of the device so that a shifting of the top plate was no longer required.

Problems with the expulsion of material through the gaps of the device were also faced in tests with laponite peloids. Consequently, the bottom filter plate and the horizontal ring were replaced by a beaker, and a precise tailoring of the upper filter paper with allowance for horizontal spreading due to wetting was applied. Nevertheless, in some tests an expulsion of material was observed even through the drainage channels of the top plate. This observation indicates that laponite particles were able to pass the filter paper and the porous filter stone. Remedy was partially achieved by the use of two sheets of filter paper. An expulsion of material through the gap of the top plate and the ring and through the filter stone occurred in several tests. Such tests had to be left aside.

6.2.1   Oedometric compression without adding salt

The specimen was prepared with a mass fraction of 5 % (i.e. initial void ratio $e_0 = 54$) and poured into the oedometric device in a liquid state immediately after the preparation procedure. Subsequent formation of the gel phase was awaited for. Finally, the upper filter paper was set, the top plate lowered and test execution started.

Initial vertical loading up to $\sigma_v \approx 10$ kPa yielded only a minor compression (Fig. 6.6a), i.e. a comparatively high stiffness of the specimen. The corresponding time-settlement behaviour (Fig. 6.6b) indicates that this compression was delayed by the dissipation of excess pore water pressure. With successive stepwise vertical loading up to $\sigma'_v = 100$ kPa, a remarkable compression was observed with a compaction of the specimen down to $e \approx 10$. During these load steps, a full consolidation was not reached even after an observation time of 10^5 s. Subsequent stepwise loading up to $\sigma'_v \approx 600$ kPa yielded only minor further compression, this time a full consolidation was achieved.
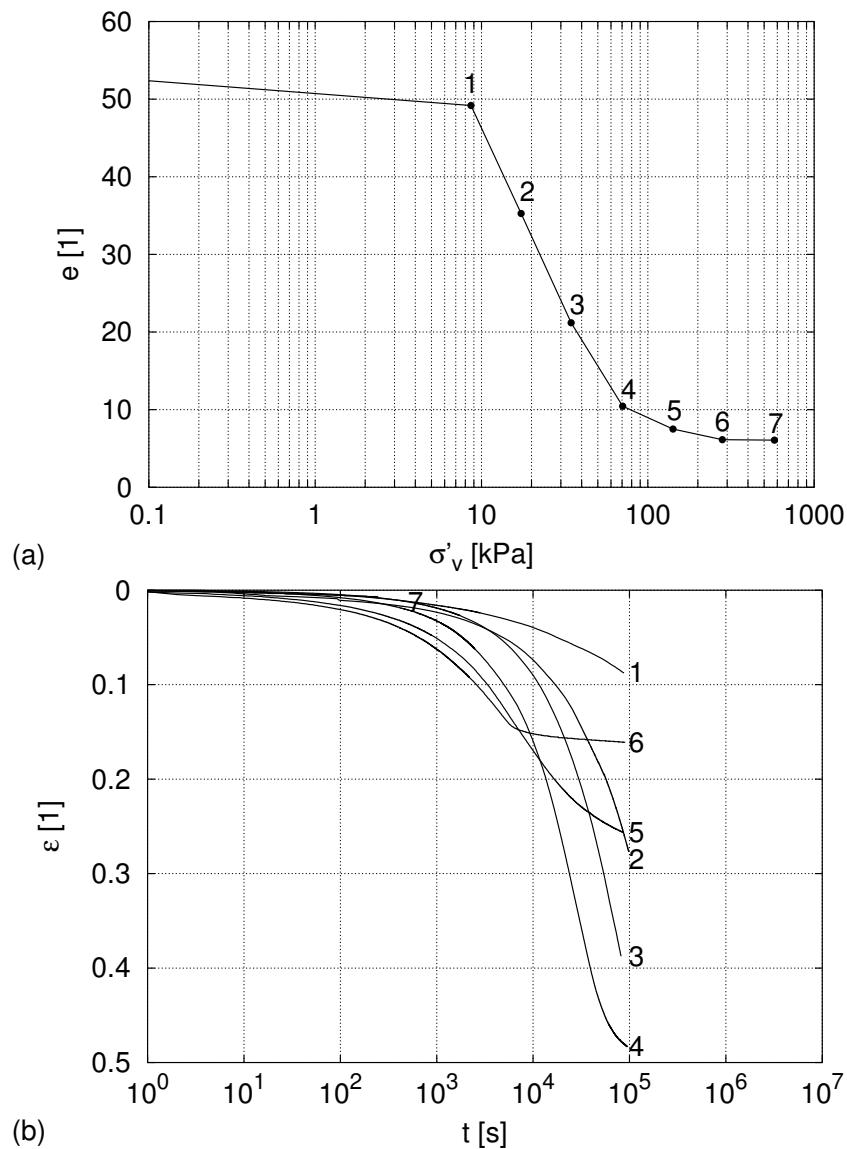
Figure 6.6: Void ratio e vs. effective vertical pressure σ'_v (a) and vertical strain ε vs. time t (b) of a laponite peloid without salt (pH10)

6.2.2 Oedometric compression with NaCl added

For the investigation of the oedometric compression behaviour in the presence of NaCl, the specimen was prepared by stirring laponite powder in salt water with the desired ion concentration. This resulted in a sediment according to Fig. 6.3a, which then was poured into the oedometer cell. The outer ring of the oedometer was filled with water of the same ion concentration, and the test was initiated.

The results in Fig. 6.7a show that the initial void ratio $e_0 = 10.7$ is in good agreement with Fig. 6.2. Stepwise vertical loading yielded a successive compression of the speci-
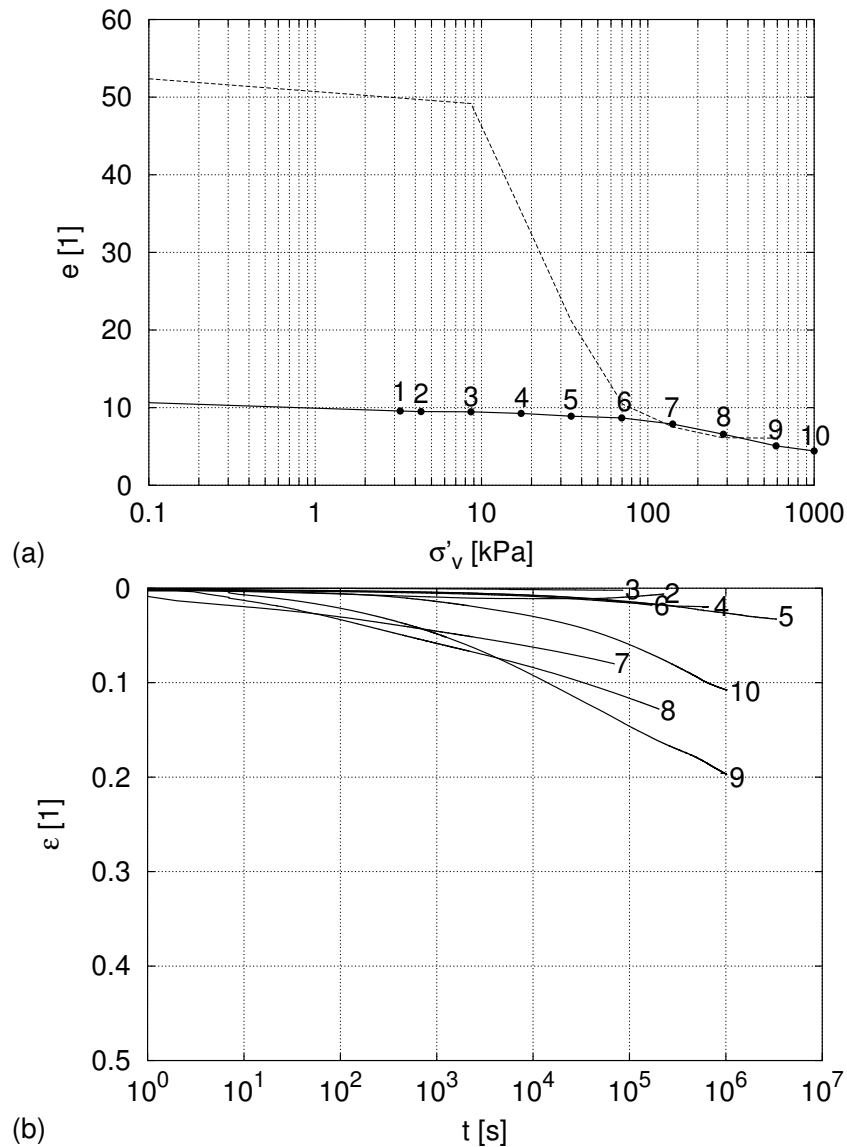
Figure 6.7: Void ratio e vs. effective vertical pressure σ'_v (a) and vertical strain ε vs. time t (b) of a laponite peloid with NaCl ($n_f = 0.86$ M, pH10)

men throughout the attained σ'_v-range, showing a considerably lower compressibility than without salt. Above $\sigma'_v \approx 100$ kPa the compression curve coincides with the one obtained without salt (added grey in Fig. 6.7).

Though the observation period of the vertical strain ε was prolonged up to $3.4 \cdot 10^6$ s per load step (Fig. 6.7b), a transition from primary consolidation to creep could not be determined within a 39 days (!) duration. Presumably creep processes were prevailing, and primary consolidation was negligible.

6.2.3 Oedometric compression with CaCl$_2$ added

An investigation of the oedometric compression behaviour in the presence of CaCl$_2$ was executed in analogy to Sec. 6.2.2.
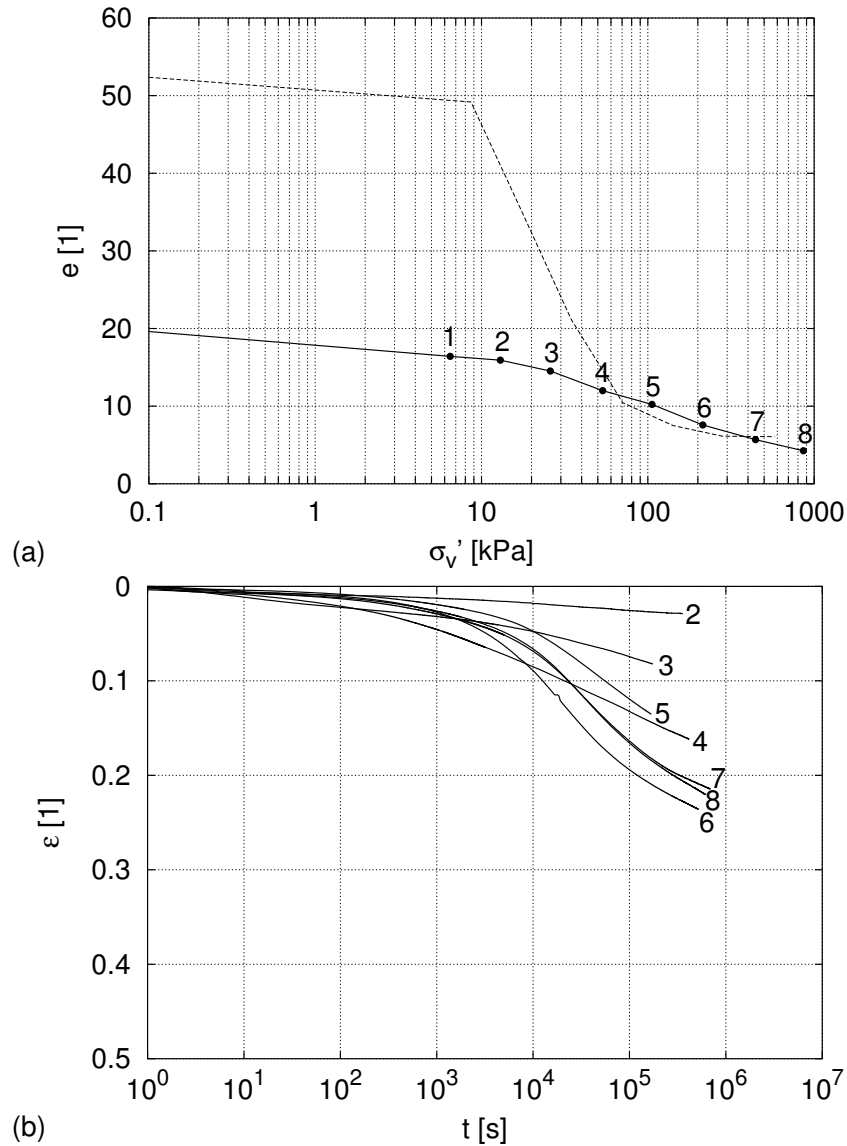
Figure 6.8: Void ratio e vs. effective vertical pressure σ'_v (a) and vertical strain ε vs. time t (b) of a laponite peloid with CaCl$_2$ ($n_f = 0.01$ M, pH10)

The test results in Fig. 6.8a show that the initial void ratio of the sediment $e_0 = 21$ is higher than the one obtained with NaCl. With the first two load steps a lower compressibility is obtained than with subsequent load steps, and the compression curve coincides with the one without salt for $\sigma'_v \approx 100$ kPa and above.

The vertical strain ε was observed up to $6 \cdot 10^5$ s per load step (Fig. 6.8b). In this period

of time, equalling 7 days, again no transition from primary consolidation to creep could be clearly identified. Only during the last three load steps the development of an S-type curve was registered.

6.2.4   Interpretation

Oedometric compression without salt was executed with an initial mass concentration of 5 % ($e = 54$), viz. with laponite in a nematic gel state. Vertical loading up to $\sigma'_v \approx 600\,\text{kPa}$ yielded an increase of the mass concentration up to 45 % ($e \approx 6$). This high e-range of laponite is neither covered by the phase diagram of laponite (Fig.3.7) nor discussed elsewhere in the literature.

Test results can be interpreted as the compression of a nematic gel, mainly consisting of evenly-orientated primary particles which are separated by interparticle repulsion. Compression of the particle assembly is therefore due to the overcoming of the interparticle repulsion. The compression is accompanied by a remarkable consolidation delay. At first sight this is surprising, since consolidation of a very loose particle network should be completed within a rather short time. Actually, squeezing out of water is hindered by the interaction with charged particles surfaces and ions (cf. Sec. 2.4), this causes a delay of consolidation.

Oedometric compression with salt starts from an agglomerated state, i.e. lower initial void ratios (cf. Fig 6.2). Shielding of the particle charges by ions is mainly relevant for the decrease of the repulsive face-to-face interaction, therefore a decrease in this long-range interaction enables the formation of a house-of-card-like structure. Its compressibility is far lower than with a nematic gel structure. Time-dependent compression shows a prevailing creep, indicating a thermally activated particle rearrangement of the house-of-card-like structure under constant load and a rather unhindered drainage of excess pore water.

6.3   Undrained shear tests

The undrained shearing resistance of the specimens presented in Sec. 6.1 was investigated with cone penetration tests. In order to assess the viscous properties of laponite, vane shear tests were performed (Sec. 6.3.3).

6.3.1 Undrained shearing resistance with respect to the solid mass fraction

The influence of the mass fraction on the undrained cohesion c_u of laponite peloids at pH10 without salt was investigated by cone penetration tests.
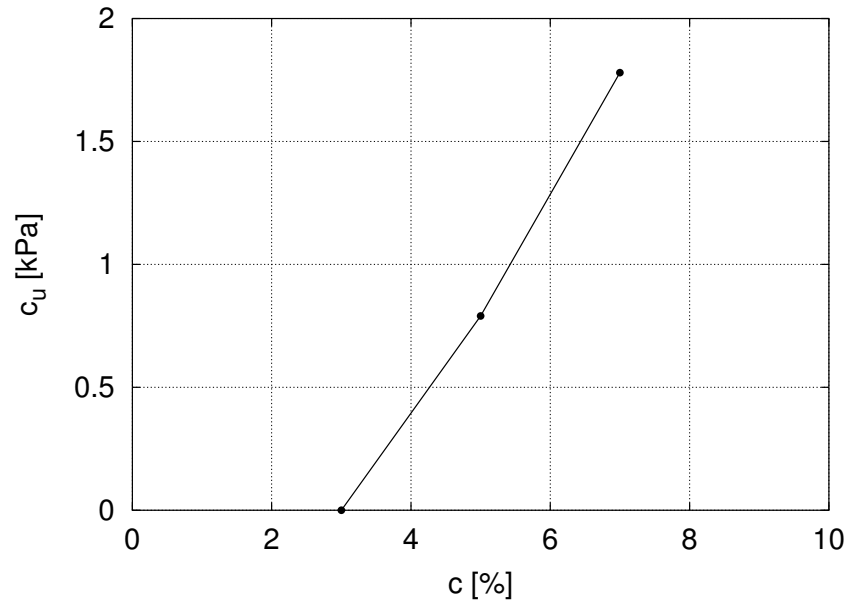
Figure 6.9: Undrained cohesion c_u of laponite peloids without salt and with respect to the solid mass fraction c (pH10)

Test results are given in Fig. 6.9. Below a solid mass fraction of 3 % there was no measurable undrained cohesion ($c_u \approx 0$), this means that the peloid was in a liquid state. Above 3 %, c_u increased linear with the solid mass fraction, and $c_u = 1.8$ kPa was reached at 7 %. Above this solid mass fraction there are no more test results available since the peloid could not be homogeneously prepared any longer.

6.3.2 Undrained shearing resistance with respect to the salt ion concentration

The influence of the ion concentration of NaCl on the undrained cohesion c_u of laponite peloids at pH10 was again investigated by cone penetration tests. See Fig. 6.1 for a photograph of these specimens.

Test results (Fig. 6.10) show a constant $c_u \approx 0.8$ kPa for ion concentrations up to $n_f = 0.017$ M. Minute increase of the ion concentration up to $n_f = 0.034$ M yields a drastic reduction of c_u up to its total loss. With further n_f-increase $c_u = 0$ remains.
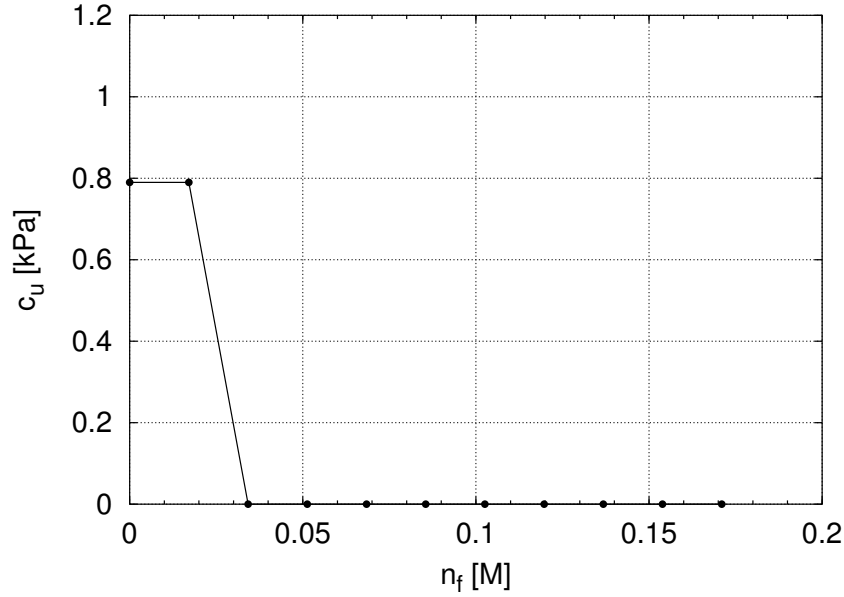
Figure 6.10: Undrained cohesion c_u of the laponite sediment with respect to the NaCl concentration (pH10, solid mass fraction $c = 5$ %)

6.3.3   Undrained shearing resistance with respect to deformation and deformation rate

Vane shear tests of laponite peloids were performed to investigate the undrained shearing resistance c_u under large monotonous deformation. These tests were performed with a modified rotational viscosimeter (Sec. 4.6), since the expected c_u was below the range of the standard lab vane shear device.

Two sets of test were performed with a solid mass fraction of 3 % and 6 %, respectively. To investigate the viscous properties of the material, each set was executed at different revolution speeds $n_0 = 8 \cdot 10^{-4}$ s^{-1}, $n_1 = 10n_0$ and $n_2 = 100n_0$.

Test results yielded a peak in c_u at a small deformation and a subsequent decrease of c_u by ongoing deformation for both mass fractions (Fig. 6.11). A stationary state is almost reached, but only for very large deformations. The sensitivity $S_t = c_{u,p}/c_{u,r}$, i.e. the ratio of the peak and residual shear strength, equals $S_t = 0.105/0.035 = 3$ for 3 % and $S_t = 1.25/0.55 = 2.3$ for 6 %.

Viscous properties of laponite peloids are revealed by the dependency of c_u on the revolving speed n of the vane. For higher n, a higher c_u is obtained. Calculation of the viscosity
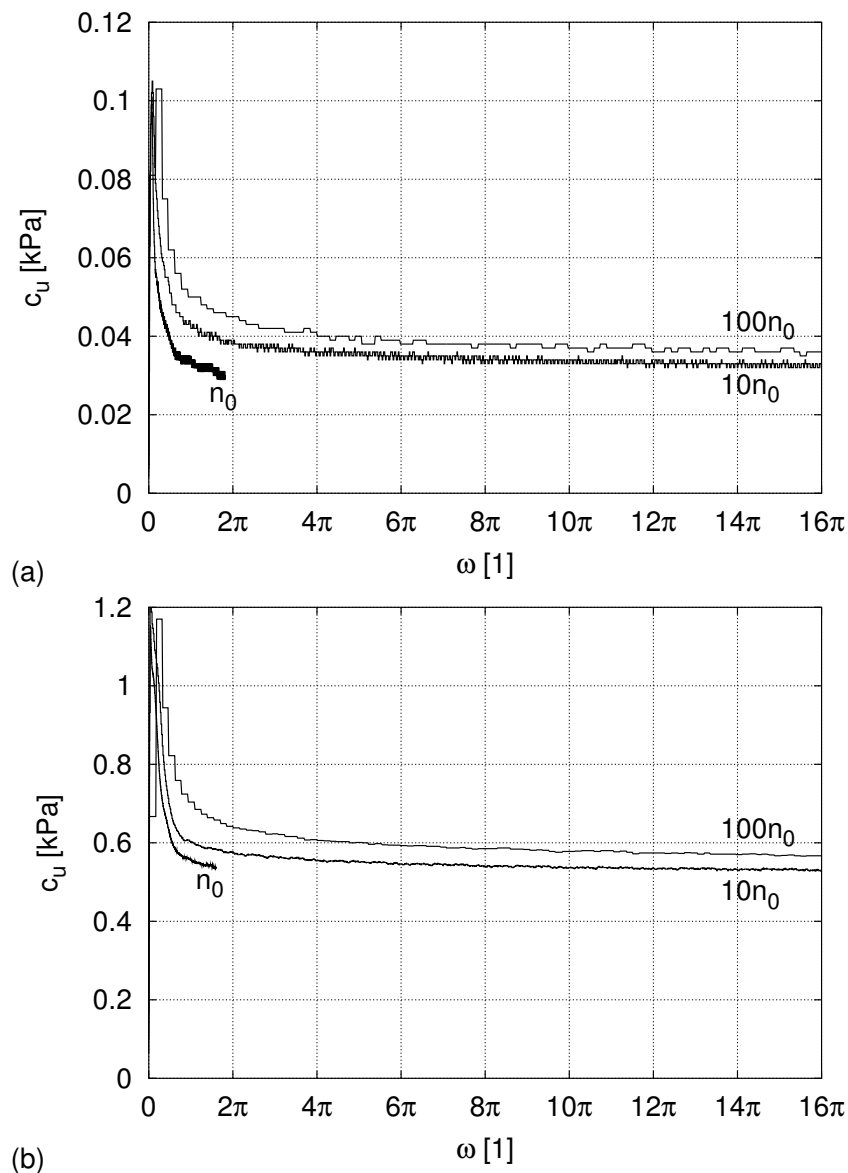
Figure 6.11: Undrained cohesion c_u of laponite peloids of (a) 3 % and (b) 6 % mass fraction with respect to the vane's angular torsion ω and revolution speed n

index I_v (LEINENKUGEL 1976)

$$I_v = \frac{\dfrac{c_u}{c_{u0}} - 1}{\ln\left(\dfrac{n}{n_0}\right)} \tag{6.1}$$

is in a strict sense only valid for stationary, i.e. residual states. Since the courses of c_u for different n are affine, I_v may also be determined if the residual state isn't already reached. I_v is almost independent of the reference rate.

Table 6.1: Viscosity index I_v of laponite peloids as calculated from the vane shear tests

solid fraction 3m%				solid fraction 6m%			
c_u [kPa]	c_{u0} [kPa]	$\ln(n/n_0)$	I_v [%]	c_u [kPa]	c_{u0} [kPa]	$\ln(n/n_0)$	I_v [%]
0.040	0.030	2.303	14.5%	0.583	0.536	2.303	3.8%
0.046	0.030	4.605	11.6%	0.685	0.536	4.605	6.0%
0.046	0.040	2.303	6.5%	0.685	0.583	2.303	7.6%
0.036	0.032	2.303	5.4%	0.567	0.531	2.303	3.0%

The viscosity index for both solid fractions is presented in Tab. 6.1. The first three data rows contain the calculation of c_u for shearing by $\omega \approx 1.6\pi$. In the last data row, I_v was calculated for the residual state, i.e. for $\omega = 16\pi$.

6.3.4   Interpretation

The solid mass fraction dependency of the undrained shearing resistance can be illustrated with the phase diagram of laponite (Fig. 3.7). For a mass fraction below ca. 2 m%, laponite exists in an isotropic liquid phase, consisting of aggregates in suspension. It was anticipated that cone penetration tests do not yield any measurable shearing resistance. For a mass fraction approximately between ca. 2 % and 3 %, laponite exists in an isotropic gel phase, consisting of chain aggregates with randomized particle orientation. The vanishing undrained shearing resistance indicates that there is no conjunction of these chain aggregates in the isotropic gel. For mass fractions above ca. 3 m%, laponite exists in a nematic gel phase, consisting of evenly-orientated and well-dispersed particles. This gel structure is due to electrostatic particle stabilization and obviously shows a remarkable resistance against particle dislocations, which increases with the solid mass concentration.

The dependence of the undrained shearing resistance on the ion concentration for a constant solid mass fraction of 5 % is explained with the transition from the nematic gel phase to the flocculated phase. For ion concentrations of $n_f = 0.017$ M and above, the number of ions is sufficient for shielding of the particle surface charges so that the particles are no longer electrostatically stabilized. A nematic gel structure cannot be formed, instead the particles flocculate and settle, resulting in a separation of solid and liquid. The undrained shearing resistance, determined with the cone penetration test on top of the specimen, is then $c_u = 0$ (cf. Fig. 6.1).

Vane shear test results show similar peak values for the undrained shear resistance like

obtained with cone penetration tests, i.e. the results are consistent. The loss in shearing resistance with ongoing deformation, expressed by the sensitivity, is ascribed to the disturbance of the nematic gel structure within a shear zone. After termination of the shearing process, a re-orientation of the particles towards a nematic gel structure is expected with an accompanied recovery of the peak values. Regarding the rate-dependency of the vane shear test, results show a wide viscosity index range of $3.8 \% \leq I_v \leq 14.5 \%$. This is rather nontypical, since the determination of the viscosity index of natural soils usually yields a rather robust I_v, e.g. for montmorillonites between 5 and 6 %.

Above findings are relevant for the description of the mechanical behaviour of laponite peloids, but the general question arises whether these results can be transferred to natural clays. Due to the comparatively small particle size, the large specific surface area and the surface charge at the particle's faces and edges, a homogeneous preparation of laponite peloids is only possible in a low solid mass fraction range. In this range, the undrained shearing resistance vanishes if the salt concentration exceeds a threshold so that the nematic state goes over to the flocculated state. Natural clay shows also a reduction of the undrained cohesion with increasing salt concentration, but at higher solid mass fractions and presumably without a phase transition.

6.4 Other tests

Due to the low particle size of laponite and the extremely high water content difficulties were faced in the execution of some test types. This section reports on tests which could not be performed successfully.

6.4.1 Isotropic compression tests

The isotropic compression behaviour of laponite peloids was investigated with the same procedure and device (Sec. 4.4) like the earlier presented tests with aluminium oxide peloids. It was intended to variate the initial solid mass fraction and ion concentration.

Regarding the variation in solid mass fraction there was only a small range suitable for the testing procedure. According to Sec. 6.1, the specimen could only be prepared homogeneously for a mass fraction of up to 7 %. Additionally, for the installation of the specimen with a semi-spherical shape a minute shear resistance was required, which was only obtained with mass fractions of 3 % or higher (Fig. 6.9). For this reason the initial solid fraction could only be varied within the range of 3 to 7 %.

According to the high initial water contents, the specimens underwent large volume decreases during the long-lasting shrinkage process. Hereby, a non-uniform drying of the specimen was observed, with the development of radial cracks heading down to the base plate and the filter stone. Consequently, a decay of the specimen into minor fragments occurred. During the tests, no applicable suction pressure data could be recorded for a subsequent analysis. At the end of the test, dismantling of the pressure transducer yielded the presence of laponite gel in the dead volume of the transducer; laponite particles had passed the filter stone and redispersed within the transducer.

Regarding the variation of salt content, for the installation of the specimen in hemispherical shape again a minute shearing resistance was required, but could not be provided according to Fig. 6.10. Since there were similar problems expected like described above, and there were no results available on the isotropic compression behaviour without salts, the execution of isotropic compression tests was abandoned.

6.4.2　Drained shear tests

Drained thin-layer shear tests also were hardly practicable with laponite peloids, since the material was expulsed through the gaps between the upper and the lower frame, between the filter plates and the frame, and through the pores of the filter plates. The expulsion of material occurred during the consolidation and the shearing stage.

For avoiding the expulsion of material during the consolidation stage, one specimen was externally preconsolidated in the oedometer device. It was prepared with an initial solid mass fraction of 5 % at pH10 and then filled into the oedometer beaker with an initial height of ca. 20 mm. After stepwise vertical loading up to $\sigma'_v = 100$ kPa, consolidation was awaited for (cf. Sec. 6.2.1). At the end of compression, a specimen height of ca. 4 mm was obtained. This height appeared as not sufficient for the subsequent direct shear test, since by experience from natural clays an initial height of 3 mm was required for the prevention of mechanical damage, and neither the settlement due to contractancy nor the amount of expulsed laponite gel could be predicted. Consequently, the loading was relieved and additional material was filled into the oedometer beaker. After subsequent reloading in the above described manner, a specimen of ca. 7 mm height was obtained. The specimen was then detached from the oedometer and pricked out to fit the dimensions of the shear frame. Subsequently, the specimen was set into the shear device, reloaded with the same $\sigma'_v = 100$ kPa and subjected to shearing with a horizontal velocity of $\dot{s} = 4.57$ mm/d.

Test results are presented in Fig. 6.12. With horizontal shearing, τ reached a peak and afterwards decreased, but a steady state was not achieved. The corresponding settlement
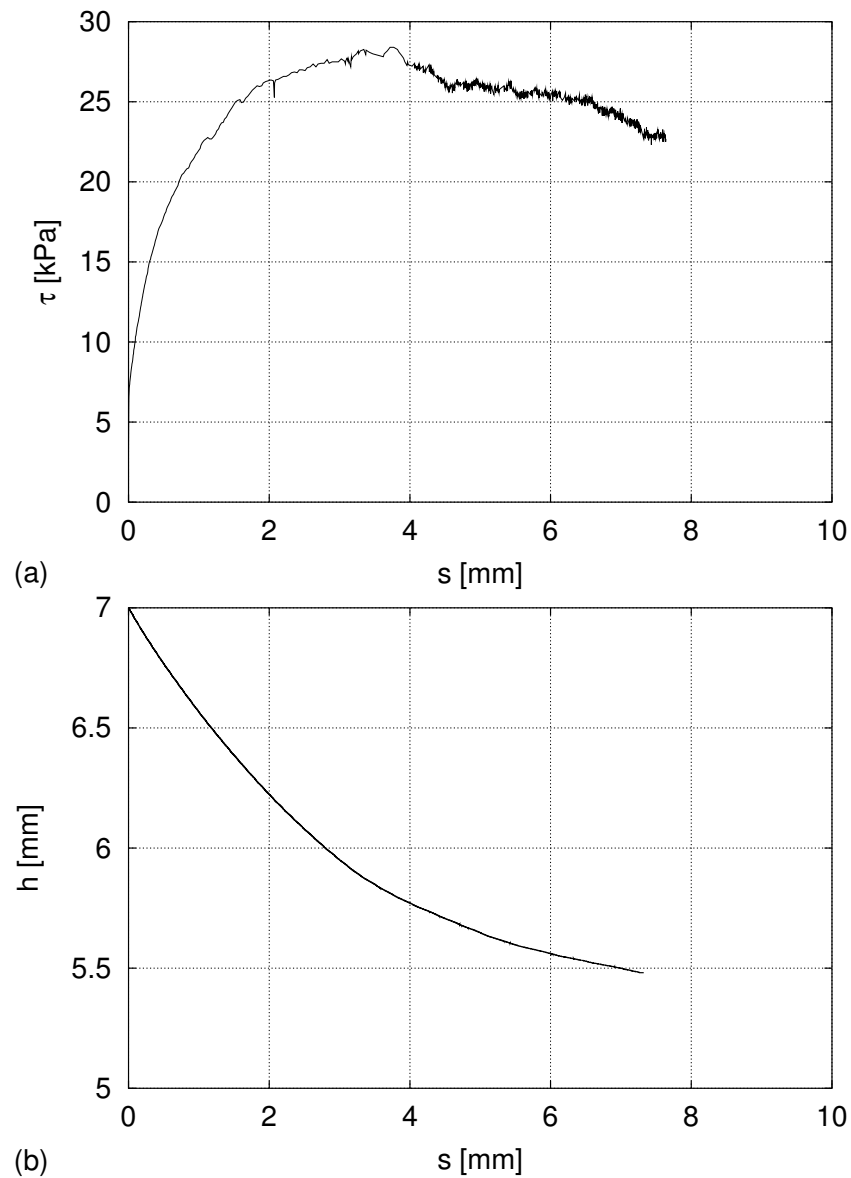
Figure 6.12: Direct shear test of laponite peloid of estimated initial void ratio $e_0 \approx 11$

shows a monotonous decrease in specimen height. During the test, again an expulsion of laponite gel through all gaps was observed. The resulting friction angle at the end of the test $\varphi_c = 15.9°$ is only given with reservation.

6.4.3 Biaxial tests

Biaxial tests aimed at the investigation of density changes of the pore water by execution of isochoric shear tests with open drainage. In the tests performed earlier by TOPOLNICKI (1987) with kaoline clays, a saturated specimen was subjected to shear while the total

volume of the specimen maintains constant. Under assumption of a sufficient precision of the device, no expulsion or inhibition of pore water at the drainage should be observed if the density of the grains and the pore water remains constant and full saturation is still maintained.

Biaxial tests with water only

Preliminary tests were performed with *water* enclosed by the rubber membrane under back pressure of 500 kPa in order to check the accuracy of the biaxial device.

Volumetric changes of the specimen as detected by the dial gauges during isochoric shear tests are below ± 0.05 ml (Fig. 6.13a). A volume change of up to 0.6 ml (flow-in) was observed at the burette (Fig.6.13b) with a decrease with strain, and two superposed wave-like interferences with wavelengths of ca. 1 mm and 10 mm, respectively.

The volumetric change detected by the dial gauges meets the requirements, whereas the deviation in volumetric change observed at the burette is far higher than expected. Since these observations cannot be attributed to solid adsorption, they are probably due to the following effects:

(α) Leakage through the rubber membrane: Investigations revealed a constant leakage rate summing up to ca. 0.4 ml during a test. This can be allowed for in the analysis.

(β) Fluctuation of back pressure level: Alternating supply pressure levels of ca. ± 5 kPa resulted in elastic deformations of the apparatus of ca. $\Delta V_{Pip} \approx \pm 0.1$ ml. Consequently, the pressure control device was improved.

(γ) Wrinkling of the rubber membrane: Inclusion of air in wrinkles at the outer surface gives rise to flow-out of water during the test if the membrane is perfectly smooth initially. Flow-in and flow-out may arise if the membrane is already wrinkled initially. Both is avoidable by using membranes which are overstretched during the whole test.

TOPOLNICKI (1987) allowed for (α) in his investigations. (β) is ascribed to ageing of the air regulator's sealing. Whether TOPOLNICKI (1987) also allowed for (γ) in his analysis, cannot be reliably assessed. Comparison of Fig. 6.13 and Fig. 2.14 suggests that he didn't. For clarification, Topolnicki's tests with kaolin clay were repeated.
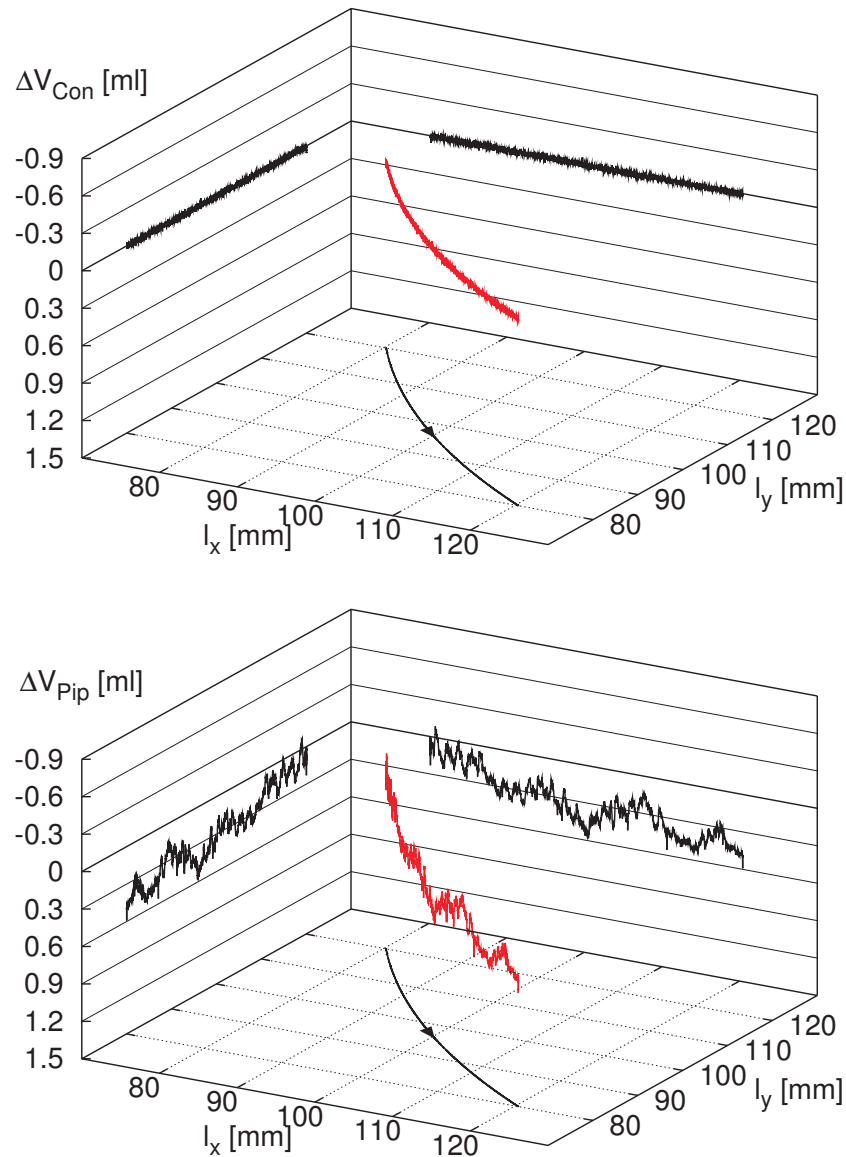
Figure 6.13: Isochoric biaxial deformation of water with open drainage. Volume changes (a) due to the control program, (b) as measured at the burette (KÜLZER & GUDEHUS 2005)

Biaxial tests with kaolinite peloids

For the re-assessment of Topolnicki's results, biaxial tests with kaolinite peloids were repeated with the same procedure as described by TOPOLNICKI (1987).

Analysis of the tests data with allowance for leakage yielded similar results (Fig. 6.14) as observed by Topolnicki (Fig. 2.14). With an overstretched membrane a neutral over-all pore volume change was observed in passive tests, with an intermediate pore water flow-in
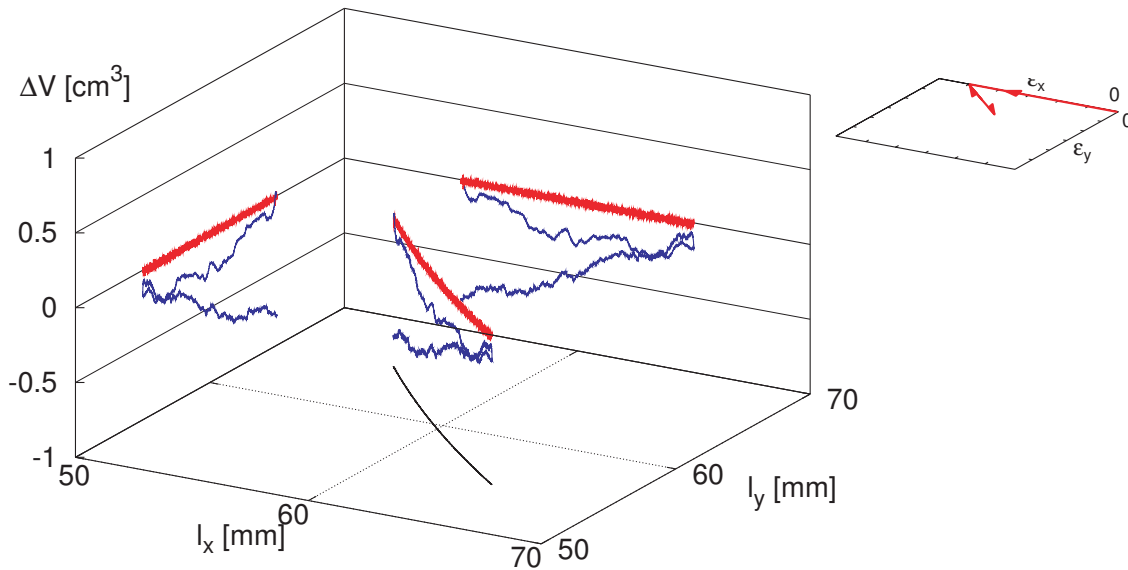
Figure 6.14: Isochoric biaxial deformation of kaolinite peloids with open drainage

of ca. 0.25 ml. In a subsequent active test, an almost immediate pore water flow-in of ca. 0.8 ml was registered. From this test it is concluded that wrinkling may also occur for overstretched membranes. The wrinkling is assumed to occur preferably close to the steel plate corners.

For an objective evidence of the pore water expansion, this type of tests should be performed with a material of higher specific surface area and charge, so that the amount of pore water volume changes exceeds the effects of wrinkling explicitly. Therefore, execution with the three-layer mineral laponite instead of the two-layer mineral kaoline was aimed at.

Biaxial tests with laponite peloids

For the execution of a biaxial tests with laponite peloids, the procedure of specimen preparation was changed. The dispersity of laponite particles in water was utilized by sucking a laponite suspension into the rubber membrane.

After 24 hours of resting time for the dispersion of the laponite peloid, consolidation was initiated. In Fig. 6.15 the volume changes of the specimen and changes in burette level are shown during consolidation. Within the observed time interval the specimen volume decreased by ca. 3.1 ml, but at the burette almost no changes in expressed pore water volume were registered. Instantaneous search for leakage yielded no result. By attempting to lower the water level in the burette via a bypass system, no changes in water level could be accomplished. By closer look it was realized that the entire pore water system
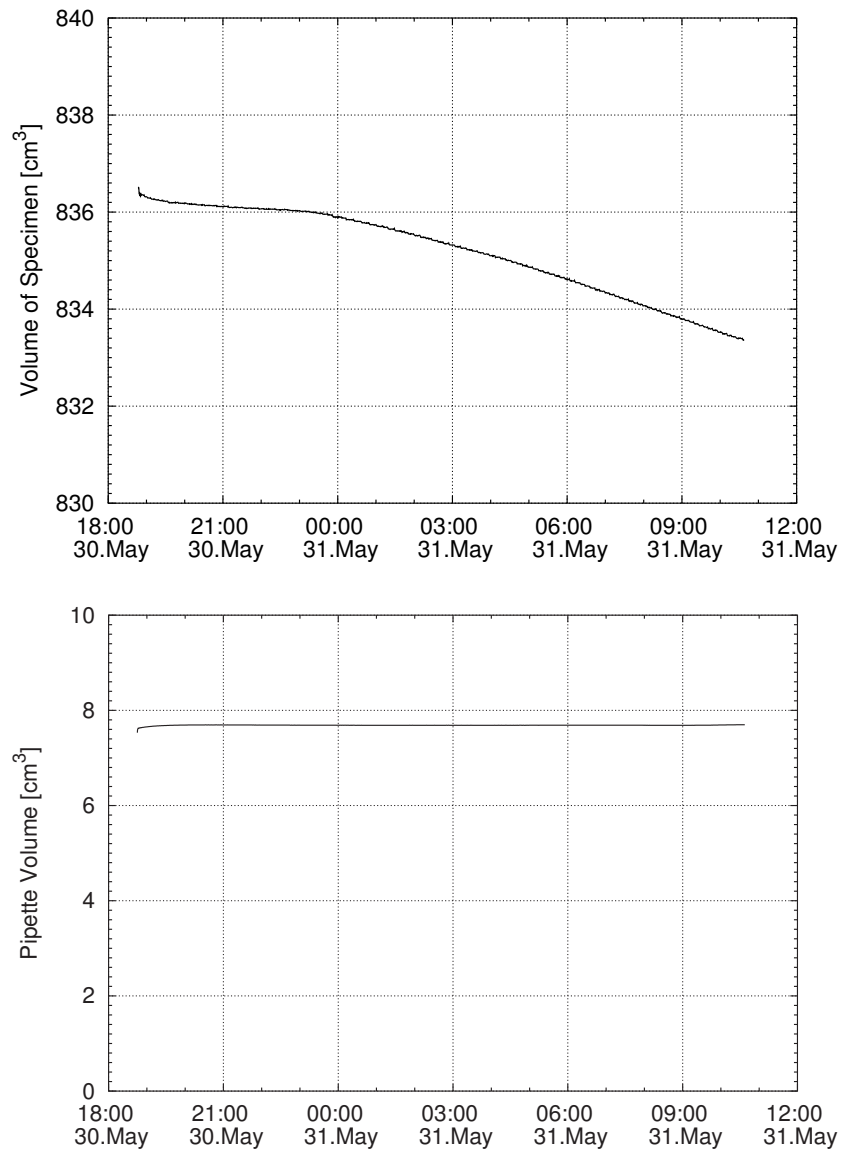
Figure 6.15: Biaxial consolidation of laponite peloids. Volume change (a) of the specimen, (b) as measured at the burette.

of burette, tubes and pressure transducers was filled by a transparent laponite solution. Raising of the water level in the burette via the bypass system was possible, but the readings taken by the differential pressure transducer remained unchanged.

Consequently, the tiny laponite particles were able to pass the filter paper and filter stone at the bottom of the specimen, to spread over the entire pore water control system and to form a gel for the irritation of the burette level readings. Therefore another three-layer mineral of substantially larger particle size had to be chosen for subsequent tests.

Biaxial tests with bentonite

With Na-bentonite MX-80, a suitable material was found for subsequent tests. It consists of ca. 75% of the three-layer mineral Montmorillonite, with an upper grain size limit of ca. 0.1 mm and about 76 m% below 0.2 μm. The specific gravity counts $\gamma_s = 2.755$ kNm^{-3} and the specific surface area is in the range of $S_m = 550$ m^{2}g^{-1} (MÜLLER-VONMOOS & KAHR 1983). The material was obtained from Süd-Chemie AG, Moosburg, Germany.

Material preparation was adopted from preceded tests with kaoline. Initial consolidation was intended to be executed with $\varepsilon_x = \varepsilon_y$ and constant strain rate. During the consolidation stage, severe mechanical problems with the biaxial device were faced.
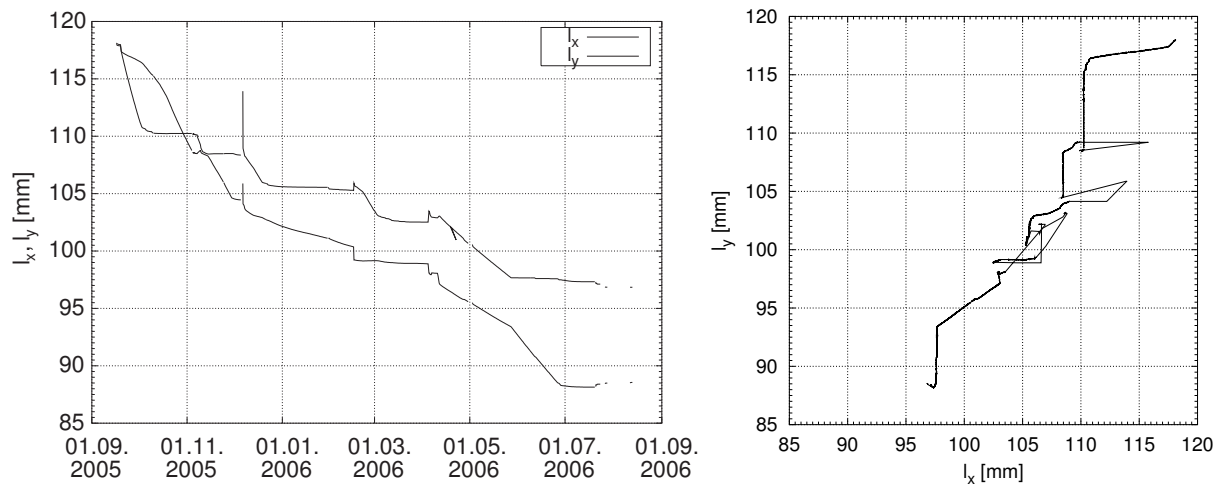
Figure 6.16: Mechanical problems of the biaxial device during the consolidation of bentonite peloids: (a) time-dependent dimensions l_x and l_y of the specimen, (b) l_x versus l_y

Fig. 6.16a illustrates the course of the specimens dimensions l_x and l_y over the entire testing time of almost one year. In Fig. 6.16b l_y is plotted over l_x. Consolidation was started with the initial dimensions $l_{x0} = 118.00$ mm and $l_{y0} = 118.12$ mm and could first be executed as scheduled. Then an unexpected decrease of the deformation rate $\dot{\varepsilon}_x$ was registered, which could be attributed to oil on the lining of the safety clutch. Since the function of the safety clutch is the limitation of the driving torque, the oiling line led to slippage of the clutch with the consequence of reduced $\dot{\varepsilon}_x$. The oil was originating from minute leakage of the gear box, which is required for the transformation of the rotating motion of the vertical drive axis into longitudinal motion of the horizontal load rod. Due to the device's age of almost 30 years, spare parts for the gear box and the safety clutch were no longer available. Therefore remedy was found by cleaning the rod and the clutch lining, but due to the type of construction there was no way for a durable protection of the

rod from oil. Consequently, the remedy was only of temporary effect, and it was decided to bypass the safety clutch. In the course of time also the lower situated electromagnetic clutch for the disconnection of drive and gear box was unavoidably affected by the oil, associated with a further decrease of the driving torque.

Simultaneously to the described dilemma with the oil leakage, a series of other problems occurred during the test. The velocities v_x and v_y had to be applied in a very low range in order not to exceed the maximum total stress limit of the device due to consolidation delay. In this very low velocity range the electrical control was not operating precisely, with the consequence of fluctuation in v_x and v_y. Due to residual magnetism of a contactor of the electrical drive control, the contactor had to be replaced by a one of modern design with the consequence of a comprehensive re-wiring of the electrical unit. Furthermore, several sudden crashes of the operating system of the ancient personal computer occurred, and no logfiles were stored for subsequent trouble-shooting. Due to all the problems and remedial actions, the test execution was explicitly delayed. Within an almost one-year period of consolidation, ochring of the filter stone led to a reduction of its permeability with the consequence of a further prolongation of the consolidation process.

In consideration of all these troubles, the test execution had to be finally given up. Until further biaxial tests can be scheduled, extensive maintenance of the entire device with particular attention to the drive unit is required for the prospect of successful test execution. Regrettably, no new findings on the density changes of pore water could be obtained by the author due to the above described technical problems of the device, but a continuation of the investigations appears nevertheless advisable in general.

6.5 Summary of laponite peloid properties

The above presented findings on the mechanical behaviour of laponite peloids can be summarized as follows:

- Laponite particles are of platey shape and carry different charges at the faces and the edges.

- The surface charge depends on pH. At pH10 the faces are negatively and the edges are positively charged. Since laponite is chemically stable only at pH10, the method of pH-alteration is not applicable for the manipulation of the surface charge.

- The surface charge is shielded by surrounding ions, making the particles to appear less charged than they are at the surface.

- Particle interaction is due to van-der-Waals–attraction and either Coulomb repulsion or Coulomb attraction. Van-der-Waals attraction is ubiquitous and independent of the surface charge, Coulomb repulsion or attraction depends on the surface charge and its shielding and on the sign of the charges of the related surfaces.

- The DLVO-theory is not applicable for plate-like particles with different charge distributions on face and edge.

- The particle interaction can be derived from an experimentally obtained phase diagram. For low ion concentrations, an increasing solid mass content yields an isotropic liquid, an isotropic gel and a nematic gel. For ion concentrations above a certain threshold, transition of these phases towards a flocculated phase occurs.

- Oedometric compression of laponite peloids at low ion concentration (nematic gel) starts from a very high initial void ratio and shows a high compressibility with large consolidation delay. In comparison, oedometric compression at high ion concentration (flocculated phase) starts from a rather low initial void ratio and shows a low compressibility and intensive creep. The corresponding void ratios coincide for vertical effective pressures above approx. 100 kPa.

- The undrained shearing resistance at low effective pressure vanishes for the isotropic liquid, increases with the mass fraction for the isotropic and nematic gel and again vanishes for the flocculated phase. Continued shear deformation yields a drastic reduction of the undrained shear resistance for the nematic gel.

- Above findings are relevant for the description of the mechanical behaviour of laponite peloids. It is generally questionable, however, whether the obtained results can be simply transferred to natural clays.

- Earlier biaxial tests taken from literature, targeting at the density change of the pore water, were re-executed in the same device. It could be shown that these results are erroneous due to systematic errors of the device. Therefore density changes of bound pore water could neither be approved nor disproved.

Chapter 7

Conclusions

According to the findings presented in Chs. 5 and 6, state limits of aluminium oxide and laponite peloids have to be treated separately. This necessity emerges from the difference in particle shape and size and the corresponding distribution of surface charges.

7.1 State limits of aluminium oxide peloids

State limits of aluminium oxide peloids are illustrated in Fig. 7.1, based on the previous obtained experimental results (solid lines) and on reasonable assumptions (dashed lines). Two extreme cases, maximum repulsive particle interaction (index r) and maximum attractive particle interaction (index a) are displayed.

For maximum repulsive particle interaction, the highest void ratio $e_{i,r}$ is obtained by isotropic compression (Sec. 5.3.2). Oedometric compression yields $e_{o,r}$ below $e_{i,r}$ due to the unavoidable portion of deviatoric stress (Sec. 5.2.2). The critical void ratio $e_{c,r}$ is assumed to be slightly below $e_{o,r}$ (Sec. 5.4.1). The void ratio at maximum density $e_{d,r}$ can only be assumed with respect of the described difficulties in its experimental determination (Sec. 5.6.2). In general, the aluminium oxide peloid with charged particles represents a fine-grained non-cohesive soil without macropores. Therefore determination of the parameters of Bauer's formula (Sec. 1.2) is possible, yielding the solids hardness $h_s = 100$ GPa and the exponent $n = 0,167$. For non-cohesive soils, so far the maximum solid hardness $h_s = 32$ GPa was obtained for Hochstetten gravel (HERLE 1997), which now is more than three times outshined by the one of aluminium oxide. This is attributed to the extreme hardness of the aluminium oxide mineral (corundum).

For maximum attractive particle interaction, $e_{i,a}$ is obtained from isotropic compression (Sec. 5.3.1) and $e_{o,a}$ from oedometric compression (Sec. 5.2.1). The critical void ratio $e_{c,a}$
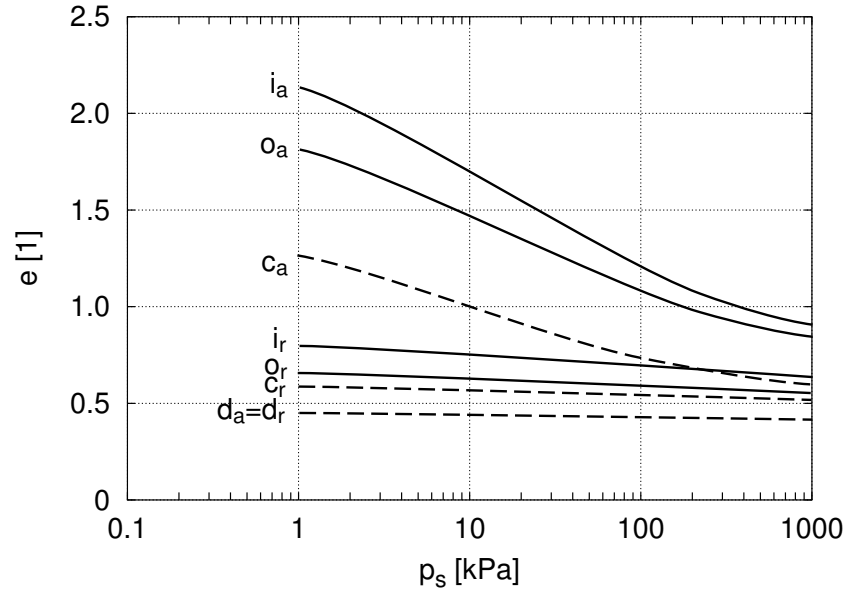
Figure 7.1: State limits of aluminium oxide peloids according to the experimental results (solid line) and to assumption (dashed lines). i = isotropic, o = oedometric, c = critical (steady state), d = dense; a = attractive, r = repulsive particles.

is only assumed, but its course can be outlined due to the following consideration: The upper limit of $e_{c,a}$ will be below $e_{o,a}$, and the lower limit of $e_{c,a}$ will be above $e_{c,r}$. Whereas the upper limit of $e_{c,a}$ is easy to accept, the lower limit of $e_{c,a}$ requires the dependency of the critical void ratio on the interparticle interaction. The latter is substantiated by the findings in Sec. 5.4.1, stating that the critical void ratio increases with the interparticle attraction due to the support of a minute local dilatancy. The void ratio at maximum density $e_{d,a}$ is identical with $e_{d,r}$ as per first approximation. Determination of the solid hardness h_s and the exponent n for the use of Bauer's formula mathematically failed due to the non-compliance of the precondition of a simple grain skeleton.

The large difference between the state limits of attractive and repulsive particle interaction, even at high p_s, results with rather low absolute values of net attraction p_a and net repulsion p_r. In Sec. 5.5, $p_a \approx 3.5$ kPa and $p_r < 0$ was determined; RICHTER (2006) obtained the net interaction $p_n = p_a - p_r \approx -6$ kPa, i.e. $p_r \approx -10$ kPa from resonant column tests with the same material. Aside from the apparent contradiction of interparticle attraction yielding a loose and interparticle repulsion a dense grain skeleton (Sec. 5.1), it is astonishing that such a comparatively low particle attraction causes a stabilization of the grain skeleton up to a high effective pressure range (Sec. 5.2).

For the understanding of the stabilizing mechanism it is helpful to study the compression behaviour of dry and partially saturated glass beads. In these tests, earlier executed

by the author (KÜLZER 1998), glass beads with diameters ranging between 0.25 and 0.50 mm were subjected to oedometric compression in dry and partially water-saturated state. Van-der-Waals–attraction and Coulomb repulsion were fully negligible, but the partially saturated glass beads showed an interparticle attraction due to the action of capillary forces. Flooding of the partially saturated specimen at a certain σ'_v-level caused a loss of capillary forces and therefore of interparticle attraction.
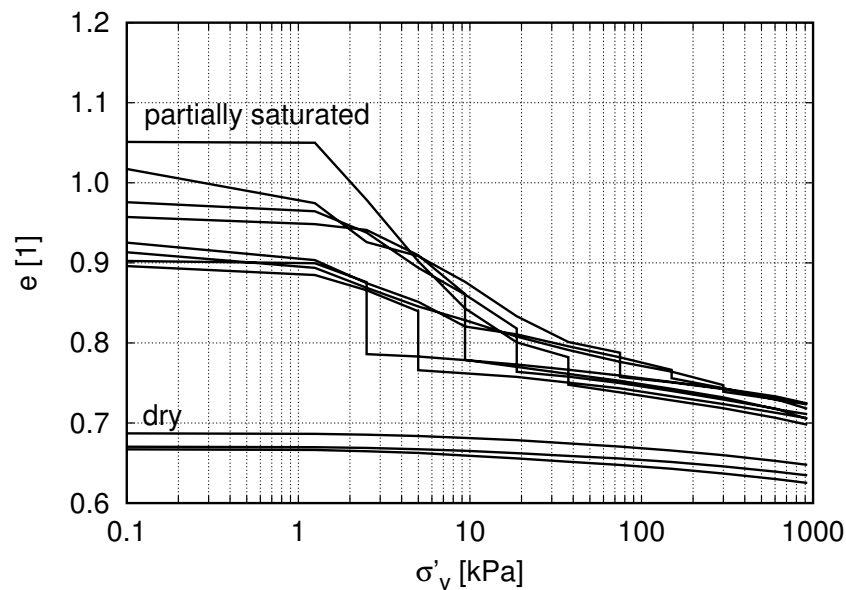
Figure 7.2: Oedometric compression of dry and partially saturated glass beads with intermittent flooding (KÜLZER 1998)

Test results are presented in Fig. 7.2. For dry specimens, placed in loosest density into the oedometer beaker, the initial void ratio is lower than the one of partially saturated specimens. The latter include macropores, which are stabilized by interparticle attraction at the particle contacts due to capillarity and dry friction. Compression of the dry specimens yields a comparatively stiff compression behaviour, whereas the partially saturated specimens show a lower stiffness, again attributed to macropores. Flooding of the partially saturated specimen at a certain σ'_v-stage eliminates the interparticle attraction, causing a sudden densification of the specimen. Further σ_v-increase leads to a further densification, but the lower void ratios of the dry specimen are not achieved even in the high σ'_v-range.

It is concluded that interparticle attraction is required for the formation of macropores and its stabilization in the low effective pressure range. In the medium and high effective pressure range, sudden neutralization of the interparticle attraction causes the macropores to collapse. The corresponding particle rearrangement is hindered due to friction at the

particle contacts and due to remaining gas bubbles in the macropores. Therefore the corresponding void ratio of the dry glass beads cannot be reached.

Compared with the results obtained for aluminium oxide peloids, the similarity of the compression curves is eye-catching. The behaviour of dry glass beads can be associated with the one of charged aluminium oxide particles (pH4), the behaviour of partially saturated glass beads with the one of uncharged aluminium oxide particles (pH9). It can be deduced that interparticle attraction is required for the genesis of a macroporous structure, and the absolute value of interparticle attraction is correlating with the porosity of the sediment. With increasing effective pressure, interparticle attraction is still contributing to the stabilization of the particle structure, but at higher effective pressure level the interparticle attraction is no longer the key aspect - it is rather the particle assembly and the enclosed gas bubbles which determine the mechanical behaviour. For isotropic compression it is expected that $e_{i,a}$ only reaches $e_{i,r}$ if particle fracture occurs (Fig. 7.1), whereas $e_{c,a}$ will reach $e_{c,r}$ within a reasonable effective pressure range by a shear-induced particle rearrangement.

Nevertheless, the contribution of interparticle attraction or repulsion to the skeleton pressure p_s has to be allowed for according to

$$p_s = \underbrace{p - (p_w - p_{atm})}_{\text{Terzaghi}} + \underbrace{p_a - p_r}_{\text{physico-chemical}} , \qquad (7.1)$$

representing an extension of Terzaghi's law of effective pressures. It becomes relevant for the determination of the skeleton pressure especially in the low pressure range, since there $p_a - p_r$ is contributing remarkably. As outlined above, the extension of Terzaghi's law is not sufficient, however, for the explanation of the state limits of repulsive and attractive particle interaction. It appears that a kind of fabric factor or tensor is required, incorporating aspects like the fabric genesis and history.

7.2 Transferability of the results to quartz minerals

The transferability of the results with aluminium oxide peloids is exemplarily shown by the sedimentation and oedometric compression of quartz peloids, with quartz being the most common mineral. Herein, the line of argument is qualitatively the same like for aluminium oxide, if the ζ-potential is allowed for. For quantification, other specific material parameters like Hamaker constant A, surface potential ψ_0, ion concentration ρ_∞ and valency z_i of the electrolyte, relative dielectricity constant ε_r and particle radius R have to be taken into account.

In the subsequently presented tests, quartz powder Mikrosil LS300 and LS500 was used (Euroquarz GmbH, Dorsten, Germany). It consists of particles with very angular shape, a Moh's hardness of 7 and a grain density of $\rho_s = 2.65$ gcm^{-3}. The grain size distribution, given in Fig. 7.3, enables the quartz powder to be classified as silt. The specific surface area counts $S_m = 0.55$ m^{2}g^{-1} for LS300 and $S_m = 0.87$ m^{2}g^{-1} for LS500. The mineralogical composition of quartz was earlier presented in Sec. 2.1.3. The quartz powder is chemically composed of >99.5m% SiO$_2$ with traces of Al$_2$O$_3$, Fe$_2$O$_3$ and TiO$_2$.
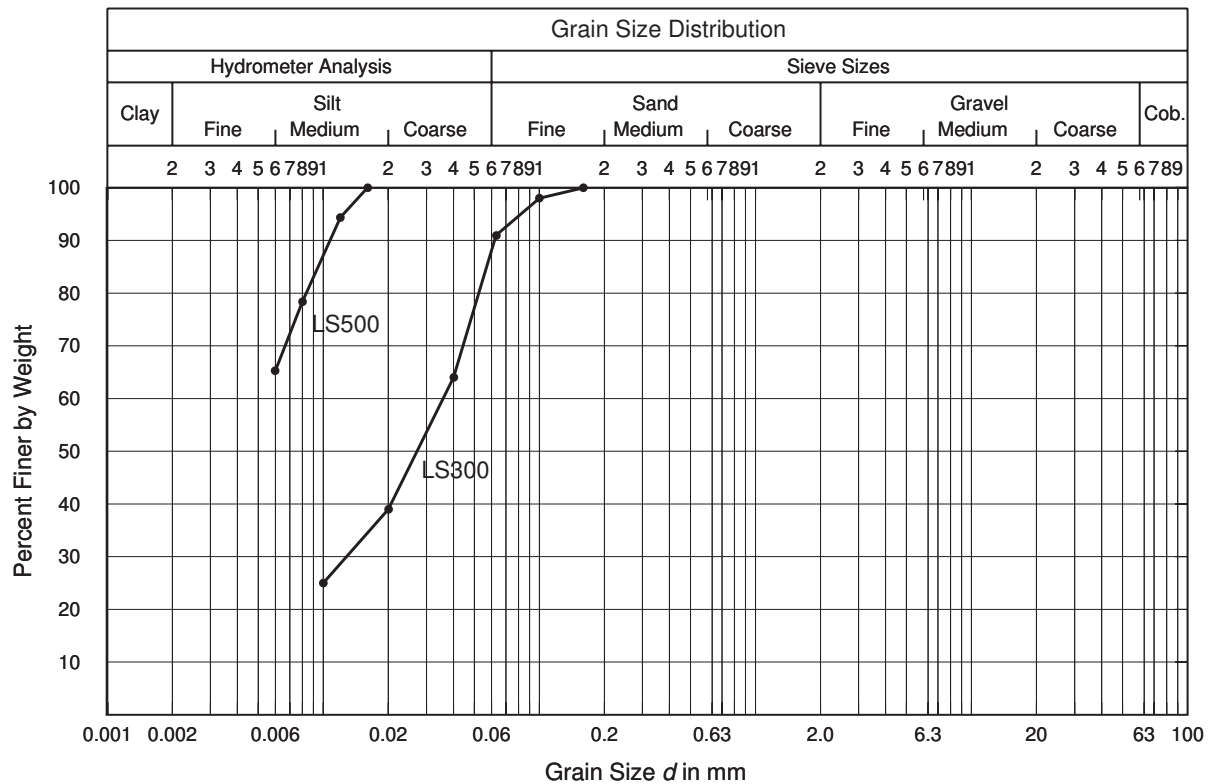
Figure 7.3: Grain size distribution of quartz powder Mikrosil LS300 and LS500 (Euro-quarz 2006)

There was no ζ-potential data for NaCl-electrolytesin literature but only for various concentrations of KCl-electrolytes (Fig. 7.4). This is sufficient for an interpretation, as potassium and chlorine represent non-potential-determing ions (Sec. 2.4.3) and therefore will not qualitatively affect the course of the ζ-potential and the location of the IEP.

Fig. 7.4 yields electrical neutrality of quartz particles at pH3 and an increasingly negative surface charge for increasing pH up to pH8. With a further increase of pH the ζ-potential remains constant. For quartz peloids mixed with neutral water, the particles therefore will be negatively charged, even if a minor shifting of pH towards the IEP due to the surface reactions described in Sec. 2.3.1 is allowed for.
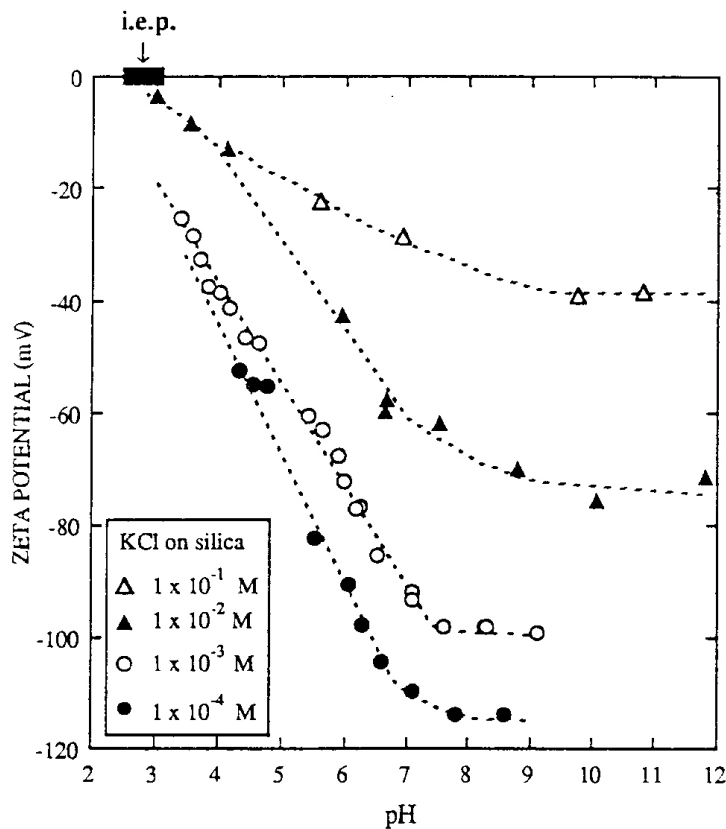
Figure 7.4: ζ-potential of quartz (HEANEY *et al.* 1994)

An example of transferability is given by Fig. 7.6, showing the time-dependent settlement behaviour of quartz suspensions (LS500). In these tests, the suspensions were settling in perspex cylinders while the corresponding solid concentration was determined in several height levels via the transmission of visible light. One test was performed without adding NaCl, whilst in the other test an ionic concentration $n_f = 0.26$ M NaCl was presetted.

Results show a decrease in solid concentration with column height and time like expected for settling of suspensions. Mind the difference between the settlement behaviour without and with salt: Without salt the settlement process takes a longer period of time as compared to the one with salt; comparison of the time lags show that without salt the settlement is roughly ten times slower than with salt.

This difference in settlement rate can be explained with the screening of the negative ($\approx$pH7) particle surface charge by Na^+ counterions. The latter are attracted towards the particle surface, yielding a compression of the double layer (cf. Fig. 2.16) with the consequence of decreasing ζ-potential (Fig. 7.4). The Coulombic repulsion is reduced, hence the unaffected van-der-Waals–attraction is dominant, causing an agglomeration
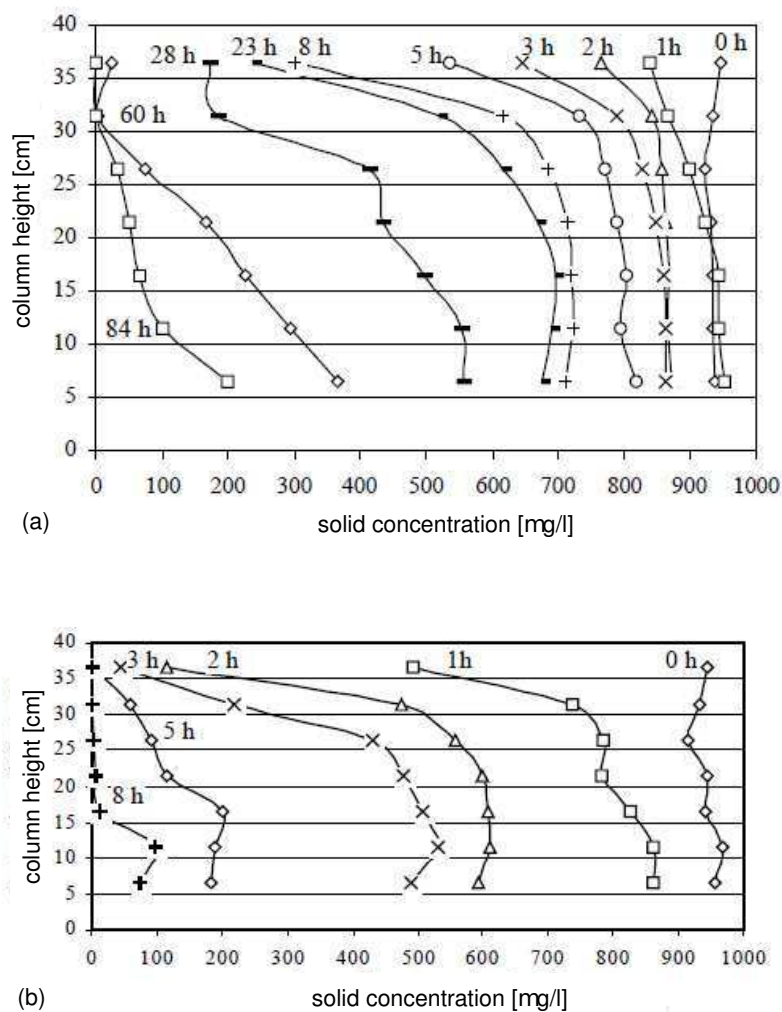
Figure 7.5: Time-dependent solid concentration of quartz peloids settling in cylindrical columns with respect to the ion concentration: (a) 0 M, (b) 0.26 M NaCl (KIM 2004)

of particles and a comparatively rapid sinking of large aggregates. Without salt the ζ-potential is higher, and the DLVO-like interaction of Coulombic repulsion and van-der-Waals–attraction yields a comparatively slow sinking of individual particles.

In comparison with the settling of aluminium oxide peloids (Sec. 5.1), the observed behaviour and the mechanical explanation of the settling process is qualitatively the same, although the particle surface charge was controlled by different mechanisms: while the surface charge of aluminium oxide was adjusted via pH (potential-determing ions), the surface charge of quartz was given by the pH of the water and then screened by the adding of NaCl (non-potential-determining ions).

The next example of transferability is given by the density of the sediment resulting from
the settling of quartz suspensions (LS300). In these tests, a number of perspex cylinders
were filled with quartz suspensions of the same solid concentration but different ion con-
centration of NaCl and CaCl$_2$. After the complete settling of the suspended particles,
the density of the sediment was determined via the volume of the sediment and the solid
mass. The corresponding void ratio versus the ion concentration is shown in Fig. 7.6.
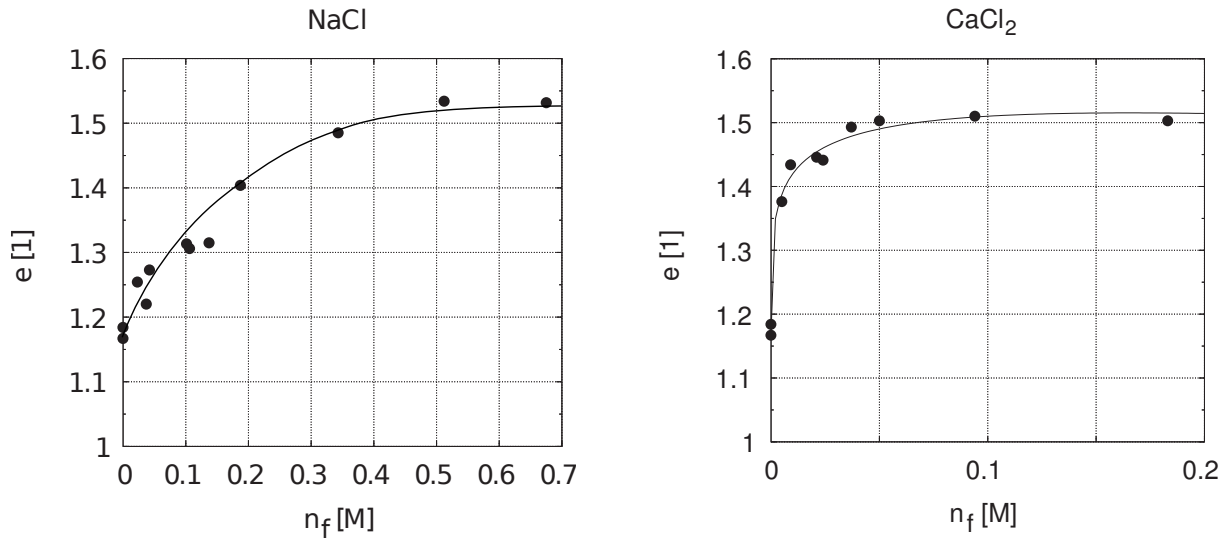
Figure 7.6: Void ratio of a quartz-sediment with respect to the NaCl- and CaCl$_2$-
concentration (KÜLZER 1999)

Results yield a successive increase in void ratio for increasing ion concentration. Beyond
a certain ion concentration saturation is achieved so that the void ratio remains constant
with further increase of the ion concentration. Comparison between NaCl and CaCl$_2$
shows that more monovalent Na$^+$ counterions are required than bivalent Ca^{2+} in order
to achieve the same void ratio, but the highest attainable void ratio at saturation is
practically equal for both salts.

In analogy with the sedimentation behaviour of aluminium oxide (Sec. 5.1), particles
with a high surface charge settle to a denser fabric. Since the particle interaction potential
according to the DLVO-theory (Fig. 2.21c) shows a local energy barrier, the particles won't
agglomerate and settle with unhindered translational and rotational motion. If the surface
charge is screened by counterions, particles with shielded surface charge agglomerate
during settling and form a loose honeycomb-like sediment. Regarding the influence of
the ion species, bivalent counterions yield a disproportionately higher compression of the
double layer according to (2.7) than monovalent counterions, with the consequence that
low ion concentration of bivalent counterions may yield a stronger screening of the particle
surface charge than a high concentration of monovalent counterions.

Another example of transferability is given by the oedometric compression of quartz peloids (LS300), performed with NaCl- and CaCl$_2$-electrolytes of different concentration (Fig. 7.7).
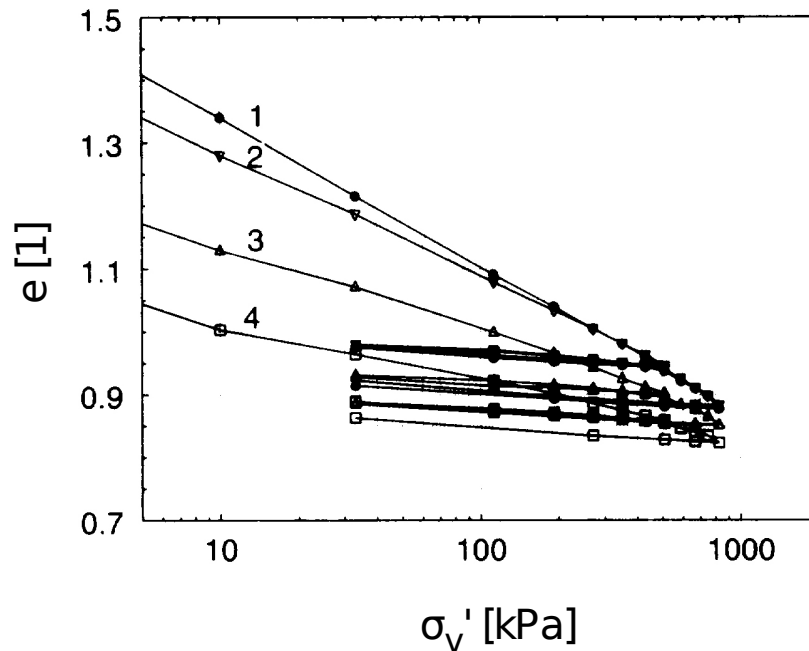
Figure 7.7: Void ratio e versus vertical pressure σ_v' of quartz peloids with respect to the NaCl- and CaCl$_2$-concentration. 1: 10^{-1} M CaCl$_2$, 2: $1.4 \cdot 10^{-2}$ M CaCl$_2$, 3: $5 \cdot 10^{-1}$ M NaCl, 4: $5 \cdot 10^{-2}$ M NaCl (Zou 1998)

Results show different initial void ratios according to the ion species and concentration. CaCl$_2$ yields a larger e_0 than NaCl. For both ion species a higher ion concentration yields a larger e_0. Regarding the behaviour due to the increase of σ_v', the compressibility is higher for a larger e_0. In case of CaCl$_2$, the compression curves for both ion concentrations converge and coincide for $\sigma_v' > 200$ kPa. In case of NaCl, the compression curves for both ion concentrations converge as well, but do not coincide in the investigated σ_v'-range.

Now particularities of the oedometric compression tests with quartz peloids are discussed. Comparison of the particular NaCl and CaCl$_2$ concentrations preset by Zou (1998) and the sediment density of quartz peloids implies higher ion concentrations ($5 \cdot 10^{-1}$ M NaCl and 10^{-1} M CaCl$_2$) were chosen since they represent the transition to saturation (cf. Fig. 7.6), and lower ion concentrations ($5 \cdot 10^{-2}$ M NaCl and $1.4 \cdot 10^{-2}$ M CaCl$_2$) were arbitrarily chosen to approx. 1/10 of the former values. The initial void ratios of the compression tests can hardly be compared with the void ratios of the sediment, since the compression curves are only displayed from $\sigma_v' = 5$ kPa on and an increase of σ_v' up to this level already yields a corresponding decrease of e_0. A crude estimation of e_0 of the com-

pression tests indicates that the $CaCl_2$-tests were performed with a quartz peloid almost in a sedimented state, whereas the NaCl-tests were performed with a lower e_0 than obtained by sedimentation. Therefore the oedometric compression curve of the quartz peloid with high $CaCl_2$ concentration can be interpreted as a succession of oedometric state limits, and the compression curve of high NaCl concentration indicates a path towards the same state limit.

7.3   State limits of laponite peloids

From the four significant state limits of isotropic and oedometric compression, critical state and maximum density, only the state limits of oedometric compression could be successfully determined for laponite peloids. In Fig. 7.8 these state limits are plotted for two extreme cases, the one without salts o_0 and the one with a sufficient ion concentration for the maximum shielding of the surface charges o_{n_f}.
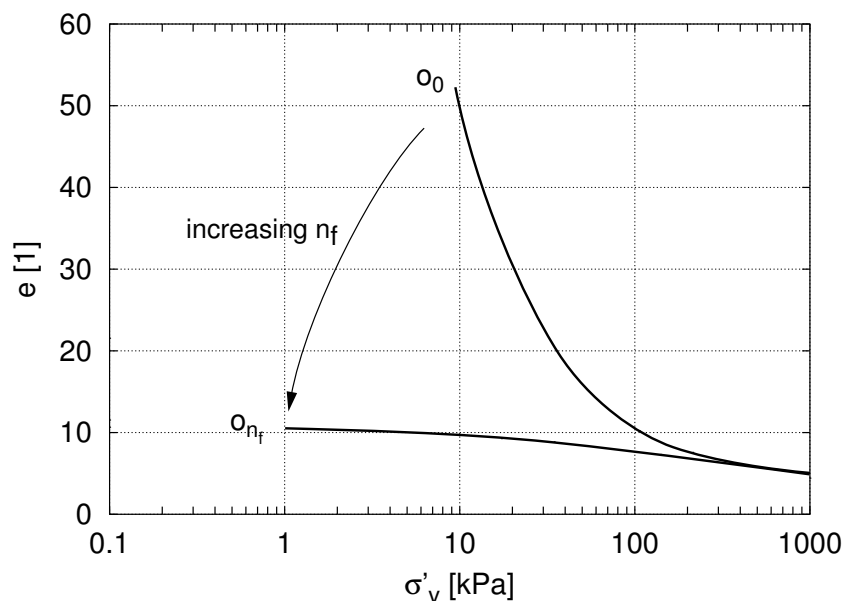
Figure 7.8: State limits of laponite peloids according to the experimental results

By presetting of the ion concentration and the vertical pressure, each state enclosed by an upper and a lower state limit can be reached. It is noticeable that for maximum shielded surface charges the *lower* boundary of the oedometric state limit is attained. This is in contrast to the findings with aluminium oxide peloids, reaching the *upper* boundary of the oedometric state limit for maximum shielded surface charges, and is attributed to the uneven charge distribution of the plate-like particles. The coincidence of the upper and

lower state limit for vertical pressures above approx. 200 kPa can only be explained with bending or even fracture of the laponite particles in this stress range.

A similar behaviour can be found, e.g., in the oedometric compression of kaolinite (Fig. 7.9). Herein, kaolinite peloids were prepared with different ion concentration and species of the pore water and were subsequently subjected to oedometric compression.
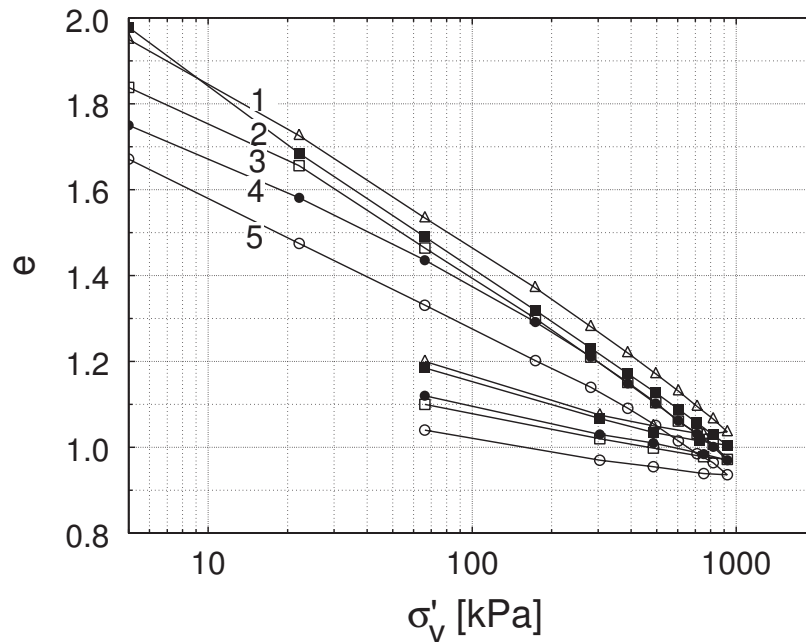
Figure 7.9: Oedometrical compression of kaolinite (ZOU 1998): (1) 10^{-3} M $CaCl_2$, (2) 10^{-2} M $CaCl_2$, (3) 10^{-1} M $CaCl_2$, (4) $5 \cdot 10^{-3}$ M NaCl, (5) $5 \cdot 10^{-1}$ M NaCl.

Results show in general that with increasing ion concentration the oedometric compression curve is lower, which is in qualitative agreement with the results of laponite. On the other hand it was expected that the influence of $CaCl_2$ is higher than the one of NaCl, which could not be confirmed by the test results.

Regarding the mineralogy it is generally questionable why kaolinite shows any sensitivity with respect to the ion concentration, since pure kaolinite minerals are electrically neutral, i.e. uncharged (cf. Sec. 2.1.3). Hence it is concluded that the examined kaolinite contained impurities either in its mineralogical structure or in terms of constituents of other minerals.

7.4 Interpretation of the Rissa landslide

GREGERSEN (1981) explained the formation of quick clay by the sedimentation of clay particles in salt water, uplift due to the melting of glaciers and a subsequent reduction of

salinity by fresh water, yielding a collapsible skeleton of hydrolysed particles (cf. Sec. 1.1). On the other hand, own observations with the extreme clay mineral laponite yielded quite the opposite behaviour (cf. Sec. 6): a comparatively dense sediment with low undrained cohesion at high salinity (representing the conditions during sedimentation in salt water) and a comparatively loose sediment with high undrained cohesion at low salinity (representing the conditions after reduced salinity by fresh water). Consequently, the formation and mechanical behaviour of Rissa quick clay cannot be explained with the findings for laponite clay particles of the present treatise.

The term 'quick clay' implies the material mainly consists of clay particles. For the Rissa quick clay, water contents of $w \approx e\gamma_w/\gamma_s = 32$ % and $w_L \approx e_{LL}\gamma_w/\gamma_s = 25$ % have been reported (GREGERSEN 1981). However, the liquid limit of $w_L = 25$ % is exceptionally low for a clay material and could rather be explained by a significant fraction of silt. OSTERMAN (1963) states that the quick clay structure consists of coarser, non-argillaceous grains surrounded by or embedded in clay, and that clay mixtures which are artificially converted to a quick clay system, the incorporation of a quantity of coarser grains of non-argillaceous material, apart from the material in the clay fraction, has been found to contribute to the process and, in some cases, to be essential to it. According to OSTERMAN (1963), the Norwegian clays are generally coarser than the Swedish and Finnish clays, with the latter generally containing quartz or feldspar and showing a lack of plastic properties.

Consequently, the following interpretation of the Rissa landslide by means of state limits is based on a mechanically dominating silt fraction: With the formation by sedimentation in salt water with almost neutral pH, the negative surface charge (Fig. 7.4) of the quartzite particles is shielded by the presence of salt ions (Fig 2.20). Consequently, Coulomb repulsion is decreased and attractive van der Waals particle interaction (Fig. 2.21b) causes an agglomeration of the particles and a rapid sinking of the aggregates. This yields a loose sediment (cf. Fig 7.6). With ongoing sedimentation, the sediment is consolidated and oedometrically compacted by the weight of the overburden, but macropores remain. After the uplift of the sediment above sea level by the melting of glaciers, leaching of salts by fresh water leads to a decrease in the shielding of the surface charge (Fig. 7.4), and re-gained Coulomb repulsion leads to a DLVO-like particle interaction (Fig. 2.21a to c) with time. In the beginning, attractive particle interaction is maintained, since the DLVO-theory also yields attraction for very low separation of charged particles (Fig. 2.21c). This results in a very fragile, meta-stable and almost fully saturated sediment.
Subsequent excavation activities are causative for the generation of additional shear stresses in the sediment, initiating a shear deformation of the grain skeleton. During the corresponding particle rearrangement, pairs of particles are separated with the con-

sequence of a sudden transition of the attractive to a repulsive particle interaction (first zero-crossing in Fig. 2.21c2). A local loss of shear resistance is initiating a cascading process of further shear deformation, particle rearrangement and loss of shear resistance. Simultaneously, the collapse of macropores with the corresponding generation of excess pore water pressure is contributing to the total loss of shear resistance.

Thus the phenomenon of the quick clay liquefaction is attributed to the transition of attractive to repulsive particle interaction of the mechanically dominating silt fraction and a corresponding alteration of the state limits in terms of Fig. 1.2f.

Chapter 8

Summary and outlook

8.1 Summary

In the present treatise the influence of particle interaction on the course of state limits was investigated. *State limits* are understood as triples of values $(e,\ p_s,\ \tau)$, which are asymptotically achieved by monotonous deformation with constant deformation rate and which are significant for a specific soil. Four state limits are of relevance, resulting from isotropic and oedometric compression, shearing up to the critical state and cyclic shearing up to maximum density. The concept of state limits includes the conventional limit states w_L, w_P and w_S, but goes far beyond. The term *peloids* describes mixtures of hydrophilic fine-grained minerals, water, ions and possibly gas bubbles and additives, i.e. cohesive soils in the conventional sense. They can differ from non-cohesive soils by exhibiting a true cohesion, which can be related to ubiquitous van-der-Waals–attraction and the electrostatic (Coulomb) repulsion in the near-field of charged particle surfaces. In the present treatise it is shown that these particle interactions have a substantial influence on state limits.

The theoretical section of the treatise is to demonstrate that the particle surface undergoes reversible acid/base reactions as soon as the particles are connected with water. With dependence on the mineralogy and pH, the achieved chemical equilibrium determines the surface charge in density and distribution. By formation of a so-called electrical double layer the surface charge is shielded by dissociated ions in the adjacent water, the more the higher the ion valency and concentration. Viewn from outside, the particles then appear as less charged. The interaction of a pair of evenly charged neighboured particles is electrostatically repulsive. This Coulombic repulsion is counteracted by the ubiquitous van-der-Waals–attraction. With the DLVO-theory the function of the interaction force

with respect to the particle separation can be described by the superposition of Coulomb repulsion and van-der-Waals–attraction. Plate-like particles have different face and edge charges, so they exhibit Coulombic face-rim attraction but face-face and rim-rim repulsion as far the charges are not shielded by attached ions. In particular cases (and these are relevant for fine-grained soils) the interaction force from Coulomb repulsion and van-der-Waals–attraction vanishes for two distinct particle separations. The larger of these two distinct particle separations is of particular interest, since for higher separation the particle interaction is attractive and for (slightly) lower separation the particle interaction is repulsive. Hereby it can be explained, e.g., why a suspension is not settling over a long period of time in spite of gravity.

In the experimental section two fine-particle granulates, aluminium oxide and laponite, were investigated with regard to the mechanical behaviour under the influence of aforementioned particle interactions. Due to the mineralogy and the grain shape and size, aluminium oxide powder represents a pronounced silt and laponite powder a pronounced clay. These model materials are synthetic and therefore provide the advantage of a well-defined composition as compared with natural soils. Since the experiments were partly executed with specimens of an initial liquid state, an improvement of existing and the development of new testing devices was required. Test execution mainly targeted at the settlement behaviour of suspensions, the behaviour during isotropic and oedometric compression and during drained and undrained shearing with respect to the particle charge and the ion species and concentration in the pore water. Furthermore, drained isochoric biaxial tests were executed to investigate density changes of bound pore water during shear deformation, a phenomenon which is rarely treated in the literature.

Experimental results show that the settlement behaviour of aluminium oxide peloids depends on the pH- and salt-dependent particle charge. For uncharged particles the particle interaction is attractive with the consequence of the agglomeration of suspended particles, the comparatively rapid settlement of so-called secondary particles and the formation of a loose, honeycomb-like sediment with included macropores. For charged particles the particle interaction is repulsive, yielding the particles to be suspended for a longer period of time, a comparatively low sedimentation rate and the formation of a relatively dense and homogeneous sediment. Isotropic and oedometric compression of these sediments show the dependency of the corresponding state limits on the particle interaction. For uncharged particles the compressibility is high, for charged particles the compressibility is low. Even at high effective pressures an identical void ratio is not achieved. Drained shearing yields an unique critical friction angle which is independent of the particle interaction. Undrained shearing and back-calculation yields a net attraction of approx. 3.5 kPa for uncharged particles and a net repulsion for charged particles.

Laponite peloids could only be investigated in a low mass fraction range, since only in this range a homogeneous preparation of the specimens was possible. Highly charged particles form different gel structures with dependence on the mass fraction. If the particle charge is shielded by sufficient presence of ions, flocculation occurs. Oedometric compression yields a high compressibility for charged particles and a low compressibility for particles of shielded surface charge. Consequently, the particle charge has an opposite influence on the compression behaviour of aluminium oxide and laponite peloids.

The transferability of the results to natural silts is exemplarily shown for quartz powder. The mechanical behaviour of the suspension, during settlement and due to oedometric compression can be explained with the same theoretical concept, if the surface charge and the ion species and concentration is allowed for and if the related material parameters are adjusted to quartz. For laponite it is questionable whether the test results are transferable by implication to natural clays, since the size of laponite particles is far below the one of natural clay particles with the consequence of a far higher specific surface area. Therefore the influence of the particle interaction of laponite emerges much more dominant than for natural clays. Nevertheless, the experimental results obtained with laponite are helpful with regard to the interpretation of the particle interaction of natural clays. Regarding the density changes of bound pore water due to shear deformation, biaxial tests could demonstrate that the test results of biaxial tests taken from literature are misleading, since they rely on errors due to the wrinkling of the latex membrane required for the sealing of the specimen. Consequently, with this test setup no experimental evidence for the density change of the bound pore water could be obtained. The applicability of the concept of peloid state limits was finally shown for the prominent case of the Rissa landslide.

8.2 Outlook

In the present treatise theoretical fundamentals of the particle interaction of peloids were presented for the case of spherical particles with homogeneous charge distribution. Herewith the opportunity is provided to incorporate these fundamentals to the formulation of constitutive laws for fine-grained soils of compact particle shape. This is not provided so far for clay minerals of plate-like particles, since the clay particles carry charges at its faces and edges which differ in density and sign. An extension of the theoretical fundamentals towards clay minerals is therefore still missing.

During the investigations, some questions regarding the course of the isotropic and oedometric state limits with respect to the particle interaction could be clarified. Due to

the mentioned difficulties in the determination of the void ratios in critical state and at maximum density, the course of the corresponding state limits could not be determined explicitly; hence these points still need clarification. A possible opportunity could be the investigation of specimens by computer tomography, but this would first require an improvement of this method with respect to resolution. Regarding the state limits with plate-like clay minerals, a synthetic model material with particle sizes in the range of natural minerals and with comparable surface charge would be desirable. In relation with the above-mentioned advantages of a synthetic product, the investigation could be executed in conventional testing devices without significant further efforts. Additionally, the corresponding void ratio is expected in a more geotechnical regime, which is helpful for the transfer of the findings to natural soils. The question of density changes of the bound pore water still remains. Although biaxial tests taken from the literature could be disproved, the basic theoretical idea and other citations are not affected by the disproval. Laponite could be a suitable model material for further investigations, but an appropriate
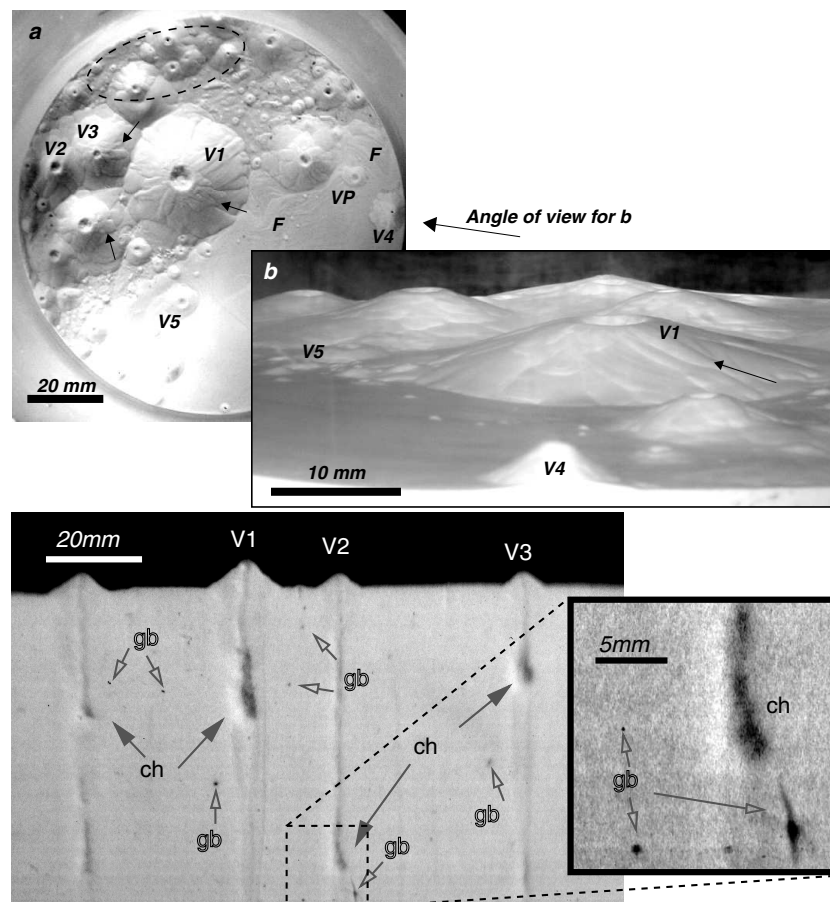
Figure 8.1: Quartz powder volcanoes evolved from model-scale column and slope tests (PRALLE, KÜLZER & GUDEHUS 2003)

test setup has to be found first.

The treatise can also find practical application, e.g., in the stabilization of trench walls, boreholes or tunnel faces by suspensions and their potential collapse, in the fields of mud avalanches onshore and offshore (turbidites), the transport or disposal of muds in mining, the maintenance of seaports and inland waterways or the phenomenon of mud expulsion (cold volcanism) on construction sites and in the lithosphere (e.g. Fig. 8.1).

Chapter 9

Zusammenfassung und Ausblick

9.1 Zusammenfassung

In der vorliegenden Arbeit mit dem Titel "Zustandsgrenzen von Peloiden" wird der Einfluss von Partikelwechselwirkungen auf den Verlauf von Zustandsgrenzen untersucht. Unter *Zustandsgrenzen* werden Wertetripel (e, p_s, τ) verstanden, welche aufgrund monotoner Deformation mit vorgegebener Deformationsrate asymptotisch erreicht werden und deren Verlauf für einen Boden kennzeichnend sind. Vier Zustandsgrenzen sind von Relevanz, die sich infolge isotroper bzw. oedometrischer Kompression, Scherung bis zum kritischen Zustand und zyklischer Scherung bis zur größtmöglichen Dichte ergeben. Das Konzept der Zustandsgrenzen beinhaltet damit auch die Konsistenzgrenzen w_L, w_P und w_S, geht aber weit darüber hinaus. Der Begriff *Peloide* beschreibt Gemische aus hydrophilen feinkörnigen Mineralen, Wasser und Ionen sowie eventuell vorhandenen Gasblasen und Additiven, im herkömmlichen Sinne also bindige Böden. Diese grenzen sich von den nichtbindigen Böden dadurch ab, dass sie eine echte Kohäsion besitzen, welche i. W. auf der allgegenwärtigen van-der-Waals–Anziehung und der elektrostatischen (Coulomb-) Abstoßung im Nahfeld geladener Partikeloberflächen beruht. In der vorliegenden Arbeit wird gezeigt, dass diese Partikelwechselwirkungen einen nachhaltigen Einfluss auf den Verlauf der Zustandsgrenzen haben.

Im theoretischen Teil der Arbeit wird dargelegt, dass an der Partikeloberfläche reversible Säure/Base-Reaktionen ablaufen, sobald die Partikel in Wasser gegeben werden. Je nach Mineralogie und pH stellt sich ein Reaktionsgleichgewicht ein, welches die Oberflächenladung in Dichte und Verteilung festlegt. Durch Bildung einer sog. elektrischen Doppelschicht schirmen im Wasser dissoziierte Ionen die Oberflächenladung um so stärker ab, je höher deren Ionenwertigkeit und -konzentration ist. Von außen gesehen erscheinen

die Partikel dadurch weniger stark geladen. Die Wechselwirkung zweier benachbarter, gleichnamig geladener Partikel ist somit elektrostatisch abstoßend. Dieser Coulomb'schen Abstoßung wirkt die allgegenwärtige van-der-Waals–Anziehung entgegen. Mit der DLVO-Theorie kann die Kraft-Abstandsfunktion der superponierten Coulomb-Abstoßung und van-der-Waals–Anziehung beschrieben werden. Oft ist diese Kraft- Abstandsfunktion rein attraktiv oder rein repulsiv. In Sonderfällen (und diese sind für feinkörnige Böden die Regel) weist die Kraft-Abstandsfunktion aber zwei Nulldurchgänge auf, d.h. es existieren zwei Partikelabstände, für welche die Summe von Coulomb-Abstoßung und van-der-Waals-Anziehung verschwindet. Der größere dieser beiden Partikelabstände mit Nulldurchgang in der Kraft-Abstandsfunktion ist von besonderem Interesse, da für größere Partikelabstände die Interaktion attraktiv, für (etwas) kleinere Partikelabstände die Interaktion repulsiv ist. Hiermit kann z.B. erklärt werden, weshalb sich eine Suspension trotz Wirkung der Erdschwere auch über lange Zeiträume nicht vollkommen absetzt.

Im experimentellen Teil wurden zwei Feinstgranulate, Aluminiumoxid und Laponit, hinsichtlich ihres mechanischen Verhaltens unter dem Einfluss o. g. Partikelwechselwirkungen untersucht. Aufgrund der Mineralogie sowie der Kornform und -größe repräsentiert das gewählte Aluminiumoxidpulver einen extremen Schluff und Laponit einen extremen Ton. Diese Modellmaterialien sind synthetisch und bieten damit gegenüber natürlichen Böden den Vorteil einer definierten Zusammensetzung. Da die Versuche teilweise mit anfangs suspensionsartigen Proben durchgeführt wurden, war es erforderlich, bestehende Versuchsgeräte zu verbessern bzw. neue Versuchsgeräte zu entwickeln. Die durchgeführten Untersuchungen zielten i. W. auf das Absetzverhalten von Suspensionen, das Verhalten bei isotroper und ödometrischer Kompression und das Verhalten bei drainierter und undrainerter Scherung in Abhängigkeit von der Partikelladung und der Ionenspezies und -konzentration im Porenwasser. Darüber hinaus wurde mit drainierten isochoren Biaxialversuchen der Frage nach der Dichteänderung von gebundenem Wasser infolge Scherdeformation nachgegangen, einem Phänomen, welches selten in der Literatur beschrieben ist.

Die experimentellen Ergebnisse zeigen, dass das Absetzverhalten von Aluminiumoxid-Suspensionen stark abhängig ist von der durch pH vorgegebenen Partikelladung. Für ungeladene Partikel ist die Partikelinteraktion attraktiv, weshalb die suspendierten Partikel agglomerieren, sich als sog. Sekundärpartikel vergleichsweise schnell absetzen und ein lockeres, wabenartiges Sediment unter dem Einschluss von Makroporen bilden. Für geladene Partikel ist die Partikelinteraktion repulsiv, weshalb die Partikel lange in Suspension bleiben, sich vergleichsweise langsam absetzen und ein relativ dichtes und homogenes Sediment bilden. Isotrope und oedometrische Kompression dieser Sedimente zeigt, dass die entsprechenden Zustandsgrenzen ebenfalls stark von der Partikelinteraktion abhängen.

Für ungeladene Partikel ist die Kompressibilität hoch, für geladene Partikel ist die Kompressibilität gering. Auch für vergleichsweise große Effektivdrücke wird keine einheitliche Porenzahl erhalten. Drainierte Scherung liefert dagegen einen einheitlichen kritischen Reibungswinkel, der nicht von der Partikelinteraktion abhängt. Undrainierte Scherung liefert durch Rückrechnung eine Nettoattraktion von ca. 3,5 kPa für ungeladene Partikel und eine Nettorepulsion für geladene Partikel. Laponit-Peloide konnten nur im Bereich kleiner Massenanteile untersucht werden, da nur hier eine homogene Aufbereitung der Proben möglich war. Bei starker Partikelladung bilden sie verschiedene Gelstrukturen aus, welche vom Massenanteil abhängen. Wird die Partikelladung durch ausreichende Ionenkonzentration abgeschirmt, wird eine Ausflockung beobachtet. Oedometrische Kompression liefert eine hohe Kompressibilität für geladene Partikel und eine geringe Kompressibilität für Partikel mit abgeschirmter Ladung. Die Partikelladung hat als einen gegensätzlichen Einfluss auf das Kompressionsverhalten von Aluminiumoxid- und Laponit-Peloiden.

Die Übertragbarkeit der Versuchsergebnisse auf natürliche Böden konnte für Aluminiumoxidpeloide am Beispiel von Quarzpulver gezeigt werden. Dessen mechanisches Verhalten in Suspension, infolge Sedimentation und bei oedometrischer Kompression konnte unter Berücksichtigung der Partikelladung und der Ionenspezies und -konzentration mit demselben theoretischen Konzept erklärt werden, sofern die Materialparameter von Aluminiumoxid durch diejenigen für Quarz ersetzt werden. Für Laponitpeloide erscheint es fraglich, ob die Übertragbarkeit der Versuchsergebnisse auf reale Tone ohne weiteres möglich ist, da die Laponitpartikel im Vergleich zu natürlichen Tonpartikeln erheblich kleiner sind und daher eine wesentlich größere spezifische Oberfläche besitzen. Infolgedessen tritt der Einfluss der Partikelwechselwirkungen für Laponit noch deutlicher hervor als für natürliche Tone. Nichtsdestotrotz sind die Beobachtungen mit Laponit in Bezug auf die Interpretation der Partikelwechselwirkungen von natürlichen Tonen hilfreich. Bzgl. der Dichteänderung von gebundenem Wasser infolge Scherdeformation zeigen eigene Biaxialversuche, dass der Literatur entnommene Ergebnisse von Biaxialversuchen irreführend sind, da sie auf systematischen Fehlern infolge Faltenbildung der die Probe einschließenden Latexmembran beruhen. Daher konnte mit dieser Anordnung kein experimenteller Beweis für eine Dichteänderung des gebundenen Wassers geliefert werden. Die Anwendung des Konzepts der Zustandsgrenzen wurde schließlich für den prominenten Fall des Rissa-Erdrutsches dargelegt.

9.2   Ausblick

In der vorliegenden Arbeit wurden die theoretischen Grundlagen zur Partikelwechselwirkung bei Peloiden für den Fall kugelförmiger Partikel mit homogener Ladungsverteilung dargelegt. Damit bietet sich die Möglichkeit, diese Grundlagen in die Formulierung von Stoffgesetzen für feinkörnige Böden mit gedrungener Partikelform einfließen zu lassen. Für Tonminerale mit plättchenartiger Partikelform sind diese Voraussetzungen nicht mehr gegeben, da die Tonplättchen an ihren Flächen und Kanten eine in Dichte und Vorzeichen unterschiedliche Ladung aufweisen. Eine Erweiterung der theoretischen Grundlagen auf plättchenartige Tonminerale steht damit noch aus.

Im Zuge der Untersuchungen konnten wichtige Fragen bzgl. des Verlaufs der isotropen und der oedometrischen Zustandsgrenzen unter Berücksichtigung von Partikelwechselwirkungen für gedrungene Feinstpartikel geklärt werden. Aufgrund der beschriebenen Schwierigkeiten in Zusammenhang mit der Bestimmung der Porenzahlen im kritischen Zustand und bei maximaler Dichte war der Verlauf der zugehörigen Zustandsgrenzen nicht eindeutig bestimmbar, daher besteht in diesen Punkten noch Klärungsbedarf. Eine denkbare Möglichkeit wäre die Untersuchung von Proben im Computertomographen, was allerdings zunächst eine technische Weiterentwicklung des Verfahrens in Hinblick auf dessen minimale Auflösung voraussetzt. Bzgl. der Zustandsgrenzen von plättchenförmigen Tonmineralen wäre es wünschenswert, ein synthetisches Modellmaterial zu finden, welches eine Partikelgröße im Bereich von realen Tonmineralen und eine vergleichbare Oberflächenladung aufweist. In Verbindung mit den bereits aufgeführten Vorzügen eines synthetischen Produkts könnten die Untersuchungen ohne großen zusätzlichen Aufwand in konventionellen Versuchsgeräten erfolgen. Darüber hinaus wird erwartet, dass die sich einstellenden Porenzahlen in einem realistischeren Porenzahlregime liegen, wodurch die Übertragbarkeit der Versuchsergebnisse auf natürliche Böden erleichtert wird.

Die Frage nach der Dichteänderung des gebundenen Porenwassers infolge Scherung bleibt weiterhin offen. Zwar wurden der Literatur entnommene Ergebnisse von Biaxialversuchen widerlegt, aber sowohl der theoretische Grundgedanke als auch die anderen Literaturstellen haben dadurch immer noch Bestand. Für weitergehende Untersuchungen scheint Laponit ein geeignetes Modellmaterial darzustellen, allerdings muss eine geeignete Versuchsanordnung gefunden werden.

Die Arbeit kann auch Anwendung finden z.B. bei der Suspensionsstützung von Schlitzwänden, Bohrlöchern oder der Ortsbrust im Tunnelbau und deren möglichen Kollaps, bei Schlammlawinen über und unter Wasser (Turbidite), dem Transport und der Entsorgung von Schlämmen im Bergbau, dem Unterhalt von Seehäfen und Binnenwasserstraßen oder
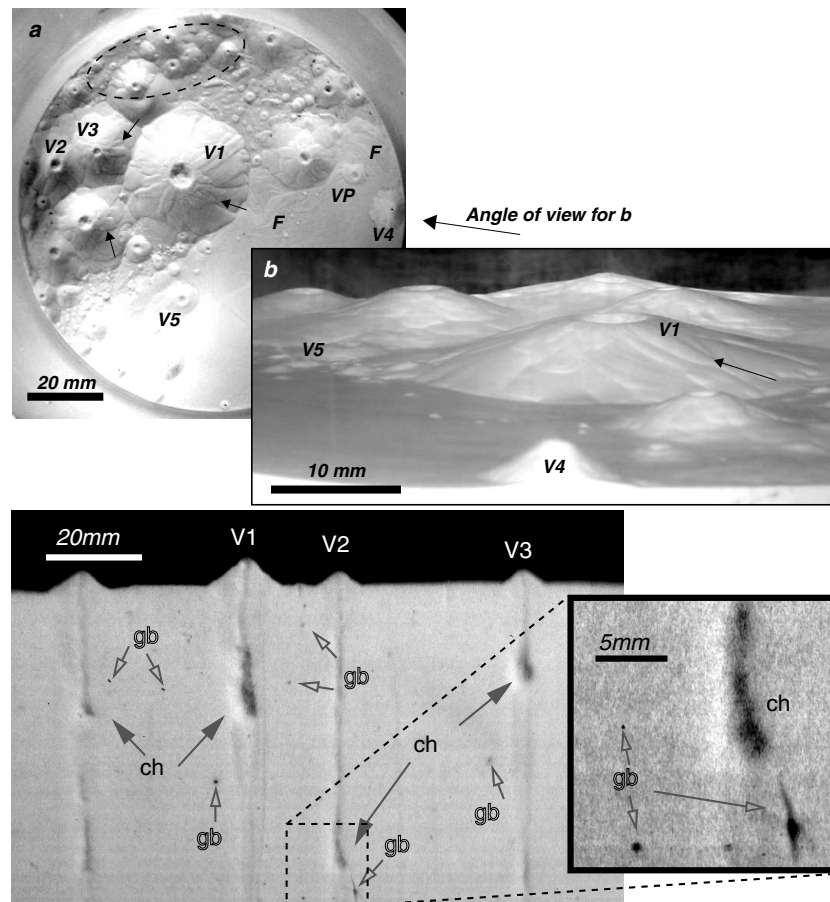
Figure 9.1: Vulkane aus Quarzpulver, aufgetreten in modellmaßstäblichen Säulen- und Böschungsversuchen (PRALLE, KÜLZER & GUDEHUS 2003)

dem Phänomen von Schlammausbrüchen (kalter Vulkanismus) auf Baustellen und in der Lithospäre (vgl. Fig. 9.1).

Bibliography

[1] ALCOA (1998): Calcined and Reactive Aluminas for the Ceramic Industry. *Product Data Sheet and Security Data Sheet.* Alcoa GmbH, Ludwigshafen, Germany.

[2] ATKINS, P.W. (1996): Physikalische Chemie. VCH Verlagsgesellschaft mbH, Weinheim, 2nd Edition.

[3] BAADER, F.H. (1995): Enzymkatalysiertes Formgebungsverfahren für Aluminiumoxid-Keramiken. Dissertation, ETH Zürich.

[4] BAUER, E. (1996): Calibration of a Comprehensive Hypoplastic Model for Granular Materials. *Soils and Foundations* **36** (1), pp. 13-26. Japanese Geotechnical Society.

[5] BAUMGART, W., DUNHAM, A.C. and AMSTUTZ, G.C. (1984): Process Mineralogy of Ceramic Materials. Enke-Verlag, Stuttgart.

[6] BRUNAUER, S., EMMETT, P.H. and TELLER, E. (1938): Adsorption of Gases in Multimolecular Layers. *Journal of the American Chemical Society* **60** (2), pp. 309-319.

[7] BUGGISCH, H. (2003): Institute for Mechanical Process Engineering and Mechanics, University of Karlsruhe, Germany. *Personal communication.*

[8] CASAGRANDE, A. (1936): Characteristics of Cohesionless Soils Affecting the Stability of Slopes and Earth Fills. *Journal of the Boston Society of Civil Engineers* **23** (1), pp. 13-32.

[9] DERJAGUIN, B.V. and CHURAYEV, N.V. (1971a): Investigation of the Properties of Water II. *Journal of Colloid and Interface Science* **36** (4), pp. 415-426. Academic Press.

[10] DERJAGUIN, B.V. and CHURAYEV, N.V. (1971b): Anomalous Water. *Nature Physical Science* **232**, August 9th, p. 131.

[11] DERJAGUIN, B.V. and CHURAYEV, N.V. (1973): Nature of 'Anomalous Water'. *Nature* **244**, August 17th, pp. 430-431.

[12] DERJAGUIN, B.V., KARASEV, V.V. and KHROMOVA, E.N. (1986): Thermal Expansion of Water in Fine Pores. *Journal of Colloid and Interface Sciences* **109** (2), pp. 586-587.

[13] EUROQUARZ (2006): Product Data Sheets of Mikrosil Typ 300 and Typ 500. Euroquarz GmbH, Dorsten, Germany.

[14] FRIPIAT, J., CASES, J., FRANCOIS, M. and LETELLIER, M. (1982): Thermodynamic and Microdynamic Behaviour of Water in Clay Suspensions and Gels. *Journal of Colloid and Interface Science* **89** (2), pp. 378-400. Academic Press.

[15] GREGERSEN, O. (1981): The Quick Clay Landslide in Rissa, Norway. *Proceedings of the 10th International Conference on Soil Mechanics and Foundation Engineering, Stockholm* **3**, pp. 421-426. Balkema, Rotterdam.

[16] GRAULE, T.J., BAADER, F.H. and GAUCKLER, L.J. (1994): Shaping of Ceramic Green Compacts direct from Suspension by Enzyme Catalyzed Reactions. cfi/Ber. DKG, **71** (6), pp. 317-323.

[17] GRIM, R.E. (1962): Applied Clay Mineralogy. *International Series in the Earth Sciences.* McGraw-Hill Book Company, New York.

[18] GUDEHUS, G. (1996): A Comprehensive Constitutive Equation for Granular Materials. *Soils and Foundations* **36** (1), pp. 1-12. Japanese Geotechnical Society.

[19] GUDEHUS, G. (2004): A Visco-hypoplastic Constitutive Relation for Soft Soils. *Soils and Foundations* **44** (4), pp. 11-23. Japanese Geotechnical Society.

[20] GUDEHUS, G. and MAŠÍN, D. (2009): Graphical Representation of Constitutive Equations. *Géotechnique* **52** (2), pp. 147-151.

[21] GUDEHUS, G. (2011): Physical Soil Mechanics. *Advances in Geophysical and Environmental Mechanics and Mathematics.* Springer-Verlag, Berlin Heidelberg.

[22] HANSBO, S. (1957): A New Approach to the Determination of the Shear Strength of Clay by the Fall Cone Test. *Proceedings of the Royal Swedish Geotechnical Institute, Stockholm* **14**, pp. 1-47.

[23] HEANEY, P.J., PREWITT, C.T. and GIBBS, G.V. (1994): Silica – Physical Behavior, Geochemistry and Materials Applications. *Reviews in Mineralogy* **29**. Mineralogical Society of America, Washington, D.C.

[24] HEIM, D. (1990): Tone und Tonminerale – Grundlagen der Sedimentologie und Mineralogie. Enke Verlag, Stuttgart.

[25] HENKEL, D.J. (1956): The Effect of Overconsolidation on the Behaviour of Clays During Shear. *Géotechnique* **6**, pp. 139-149.

[26] HICHER, P.Y., WAHYUDI, H. and TESSIER, D. (1994): Microstructural Analysis of Strain Localization in Clay. *Computers and Geotechnics* **16**, pp. 205-222.

[27] HIDBER, P.C. (1993): Zusammenhang von Struktur und Wirkung von Carbonsäuren als Verflüssiger für wässrige α-Aluminiumoxidsuspensionen. Dissertation, ETH Zürich.

[28] HOLZ, M. (2002): Institute for Physical Chemistry and Electrochemistry, University of Karlsruhe. *Personal communication.*

[29] HORN, R. (1990): Surface Forces and Their Action in Ceramic Materials. *Journal of the American Ceramic Society* **73** (5), pp. 1117-1135.

[30] HUNTER, R.J. (1993): Introduction to Modern Colloid Science. Oxford University Press, New York.

[31] HVORSLEV, M.J. (1937): Über die Festigkeitseigenschaften gestörter bindiger Böden. *Ingeniorvidenskabelige Skrifter* A, No.45. Danmarks Naturvidenskabelige Samfund, Kobenhavn.

[32] ISRAELACHVILI, J.N. (1991): Intermolecular and Surface Forces. *Academic Press*, 2nd Edition.

[33] KIM, J.-W. (2004): Mobilisierung und Immobilisierung von mineralischen Feinstkornaggregaten an Gewässersohlen. Dissertation, Institut für Wasserbau und Kulturtechnik, Universität Karlsruhe.

[34] KLEIN, C. and HURLBUT, C.S. (1993): Manual of Mineralogy. *John Wiley & Sons*, 21nd edition.

[35] KOLYMBAS, D. (1977): Ein nichtlineares viskoplastisches Stoffgesetz für Böden. *Veröff. Inst. Bodenmech. u. Felsmech., Univ. Karlsruhe*, Heft 77.

[36] KOLYMBAS, D. (2000): Introduction to Hypoplasticity. *Advances in Geotechnical Engineering and Tunnelling.* Balkema.

[37] KÜLZER, M. (1998): Kompressionsverhalten feuchter Granulate. Vertieferarbeit am Institut für Bodenmechanik und Felsmechanik, Universität Karlsruhe.

[38] KÜLZER, M. (1999): Setzungsfließen im Modellversuch. Diplomarbeit am Institut für Bodenmechanik und Felsmechanik, Universität Karlsruhe.

[39] KÜLZER, M. and GUDEHUS, G. (2005): Density Changes of the Pore Water of Saturated Clay. *Proc. Powders and Grains 2005* **2**, pp. 1087-1090. A.A.Balkema Publishers.

[40] KUNTSCHE, K. (1982): Materialverhalten von wassergesättigtem Ton bei ebenen und zylindrischen Verformungen. *Veröff. Inst. Bodenmech. u. Felsmech., Univ. Karlsruhe*, Heft 91.

[41] KRIEG, S. (2000): Viskoses Bodenverhalten von Mudden, Seeton und Klei. *Veröff. Inst. Bodenmech. u. Felsmech., Univ. Karlsruhe*, Heft 150.

[42] LAGALY, G. (1993): Tonminerale und Tone: Struktur, Eigenschaften, Anwendungen und Einsatz in Industrie und Umwelt. Steinkopff-Verlag, Darmstadt.

[43] LAGALY, G. (1997): Dispersionen und Emulsionen: Eine Einführung in die Kolloidik feinverteilter Stoffe einschließlich der Tonminerale. Steinkopff-Verlag, Darmstadt.

[44] LAPORTE (2000): Laponite. *Product Brochure*. Laporte Industries Ltd., Widnes, Cheshire, UK.

[45] LEINENKUGEL, H.J. (1976): Deformations- und Festigkeitsverhalten bindiger Erdstoffe. Experimentelle Ergebnisse und ihre physikalische Deutung. *Veröff. Inst. Boden- u. Felsmech., Univ. Karlsruhe*, Heft 66.

[46] LEVITZ, P., LECOLIER, E., MOURCHID, A., DELVILLE, A. and LYONNARD, S. (2000): Liquid-solid Transition of Laponite Suspensions at Very Low Ionic Strength: Long-range Electrostatic Stabilsation of Anisotropic Colloids. *Europhysics Letters*, **49** (5), pp. 672-677.

[47] MARTIN, R.T. (1962): Adsorbed Water on Clay: A Review. *Clays and Clay Minerals. Proceedings of the 9th National Conference on Clay Minerals*, pp. 28-70.

[48] MOURCHID, A. and LEVITZ, P. (1998): Long-term Gelation of Laponite Aqueous Dispersions. *Physical Review E*, **57** (5), pp. R4887-R4890.

[49] MOURCHID, A., Lécolier, H., Van Damme, H. and LEVITZ, P. (1998): On Viscoelastic, Birefringent, and Swelling Properties of Laponite Clay Suspensions: Revisited phase diagram. *American Chemical Society* **14** (17), pp. 4718-4723.

[50] MÜLLER-VONMOOS, M. and KAHR, G. (1983): Mineralogische Untersuchungen von Wyoming Bentonit MX-80 und Montigel. *Nagra, Technischer Bericht*, Heft 83-12.

[51] NEY, P. (1973): *Zeta-Potentiale und Flotierbarkeit von Mineralien.* In: Fréchette, V.D., Kirsch, H., Sand, L.B. and Trojer, F. (Eds.): *Applied Mineralogy* **6**. Springer-Verlag.

[52] OSTERMAN, J. (1963): Studies on the Properties and Formation of Quick Clays. *Clays and Clay Minerals* **12** (1), pp. 87-108.

[53] PERSSON, B.N.J. (2000): Sliding Friction. Springer-Verlag, 2nd Edition.

[54] PRALLE, N., KÜLZER, M. and GUDEHUS, G. (2003): *Experimental Evidence on the Role of Gas in Sediment Liquefaction and Mud Volcanism.* In: Subsurface Sediment Mobilization. Geological Society of London, Special Publications SP 216, ISBN 1-86239-141-6.

[55] REED, J.S. (1995): Principles of Ceramics Processing. John Wiley & Sons, 2nd Edition.

[56] REINSHAGEN, J. (2000): Institute for Ceramics in Mechanical Engineering, University of Karlsruhe, Germany. *Personal communication.*

[57] RENDULIC, L. (1937): Ein Grundgesetz der Tonmechanik und sein experimenteller Beweis. *Bauingenieur* **18** (31|32), pp. 459-467.

[58] RICHTER, S. (2006): Mechanical Behavior of Fine-grained Model Materials During Cyclic Shearing. *Veröff. Inst. Bodenmech. u. Felsmech., Univ. Karlsruhe*, Heft 167.

[59] ROSCOE, K.H., SCHOFIELD, A.N. and WROTH, C.P. (1958): On the Yielding of Soils. *Geotechnique* **8**, pp. 22-53.

[60] ROSENQVIST, I. TH. (1966): Norwegian Research into the Properties of Quick Clay - A Review. *Engineering Geology* **1** (6), pp. 445-450. Elsevier, Amsterdam.

[61] ROSENQVIST, I. TH. (1972): Quickton. *Bild der Wissenschaft* **9**, pp. 1293-1299.

[62] SCHOFIELD, A. (2002): Re-appraisal of Terzaghi's Soil Mechanics. *Proc. XVth ICSMGE 4*, pp. 2473-2482.

[63] SCHOFIELD, A. and WROTH, P. (1968): Critical State Soil Mechanics. McGraw Hill, London.

[64] SCHUBERT, H. (1982): Kapillarität in porösen Feststoffsystemen. Springer-Verlag Berlin, Heidelberg.

[65] SILVESTRI, V., AUBERTIN, M. and CHAPUIS, R. (1993): A Study of Undrained Shear Strength using various Vanes. *Geotechnical Testing Journal* **16** (2), pp. 228-237.

[66] STRUNZ, H. and NICKEL, E.H. (2001): Strunz Mineralogical Tables. Chemical-Structural Classification System. Schweizerbart, Stuttgart, 9th Edition.

[67] TERZAGHI, K. (1920): New Facts about Surface Friction. *Physical Review* **16** (1), pp. 54-61.

[68] TERZAGHI, K. (1925): Erdbaumechanik auf bodenphysikalischer Grundlage. Deuticke-Verlag, Leipzig, Wien.

[69] TOPOLNICKI, M. (1987): Observed Stress-strain Behaviour of Remoulded Saturated Clay and Examination of two Constitutive Models. *Veröff. Inst. Bodenmech. u. Felsmech., Univ. Karlsruhe*, Heft 107.

[70] ZOU, Y. (1996): A Non-linear Permeability Relation depending on the Activation Energy of Pore Liquid. *Géotechnique* **46** (4), pp. 769-774.

[71] ZOU, Y. (1998): Der Einfluss des gebundenen Wassers auf die Leitfähigkeit und die mechanischen Eigenschaften feinkörniger Böden. *Veröff. Inst. Bodenmech. u. Felsmech., Univ. Karlsruhe*, Heft 144.